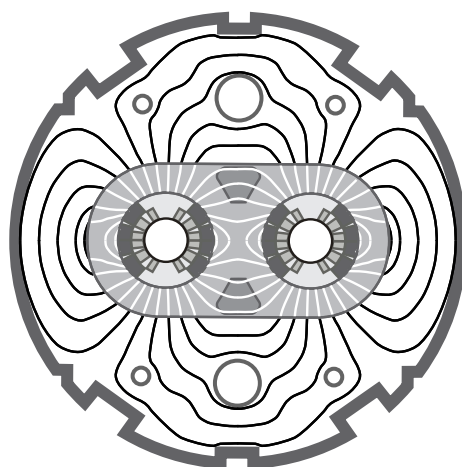


QUENCH PROTECTION AND POWERING IN A STRING OF SUPERCONDUCTING MAGNETS FOR THE LARGE HADRON COLLIDER

Günter Krainz

CERN-THESIS-2002-003

01/02/1997



Quench Protection and Powering in a String of Superconducting Magnets for the Large Hadron Collider

Dissertation

zur Erlangung des Grades

Doktor der technischen Wissenschaften

vorgelegt an der Fakultät für Elektrotechnik
der Technischen Universität Graz
von

Dipl.-Ing. Günter Krainz

Graz, Februar 1997

Acknowledgements

The work presented in this thesis has been carried out in the LHC/ICP group at CERN in the framework of a collaboration with the University of Technology Graz, Austria.

I wish to express my gratitude and appreciation to Professor Hansjörg Köfler, head of the Department of Electrical Machines and Drives, University of Technology Graz, for his advises and fruitful discussions. His expert opinion and support has been valuable and encouraging.

I wish to express my gratitude to Dietrich Hagedorn, who initiated the work and under whose direction this research has been carried out.

I would like to thank Professor Hans Michael Muhr, head of the Department of High Voltage Engineering, University of Technology Graz, for the great interest he has shown for this thesis.

I would like to thank the people I have worked most closely with during my stay at CERN: Rüdiger Schmidt and Felix Rodriguez-Mateos. I appreciated the help of people of the LHC String Team for the general support during performing experiments.

I wish to express my gratitude to Leslie Coull and Al McInturff for their advises and for correcting my English language.

Last but obviously not least I would like to thank my family and friends for their help and encouragement.

Günter Krainz

Contents

1	Introduction	1
1.1	Principles of Accelerators	2
1.2	The LHC design	3
1.2.1	Overview	3
1.2.2	Electrical Powering Scheme and Quench Protection	6
2	Superconductivity	9
2.1	Superconducting Materials	9
2.1.1	Niobium-Titanium Superconductors	11
2.1.2	Niobium-Tin Superconductors	11
2.2	Superconducting Cable	11
2.2.1	Losses in Superconducting Cables	12
2.2.2	Normal State Transition	13
2.3	Magnets in Superconducting Accelerators	16
3	The LHC Test String	19
3.1	The LHC Test String Configuration	20
3.2	Main Components of the LHC Test String	21
3.2.1	Main Dipole Magnets	21
3.2.2	Main Quadrupole Magnets	24
3.2.3	String Feed Box and String Return Box	25
3.2.4	Power Converter	25
3.2.5	Discharge Circuit	25
3.3	Magnet Protection System	31
3.3.1	Cold Diodes	32
3.3.2	Quench Heaters	32
3.3.3	Quench Relief Valves	33
3.3.4	Quench Detectors and Interlock Matrix	34
3.3.5	Programmable Logic Controller	36
3.4	Instrumentation	36
3.4.1	Voltage Taps	36
3.4.2	Temperature Sensors	36
3.4.3	Pressure Sensors	38
3.5	Cooling System	38
3.6	Data Acquisition	39

4	Electrodynamic Model	41
4.1	Transient Model	41
4.1.1	System of Differential Equations	41
4.2	Program Algorithm	47
4.3	Model Parameters	50
4.3.1	Input Parameters	50
4.3.2	Calculated Output Parameters	51
4.4	Model Structure	52
4.5	Stability of the Transient Model	55
4.6	Validation of the Model	57
4.6.1	Deduced Results from Model Calculations	60
4.7	Modelling Quench Propagation through Bus-bars	63
4.7.1	Numerical Model	63
4.7.2	Heat Propagation along Bus-bar	66
5	String Experiments and Test Results	69
5.1	Measurement Errors	69
5.1.1	Error Margin in Voltage Measurement	70
5.1.2	Error Margin in Temperature Measurement	71
5.2	Single Dipole Quench Behaviour	71
5.3	Quench Behaviour of the LHC Test String	78
5.3.1	Heater Provoked Quench	78
5.3.2	Natural Quench	84
5.4	Inter-magnet Quench Propagation	87
5.4.1	Set-up of Quadrupole Quench Propagation Experiments	87
5.4.2	Quadrupole Quench Propagation Experiments	88
5.5	Quench Heater Performance Tests	95
5.6	Balancing the Quench Detectors	96
5.7	Contact Resistance Measurement	97
6	Outlook for the LHC Magnet Protection	101
6.1	Final Design of Magnets for the LHC Machine	101
6.2	Extrapolation for the LHC Dipole Magnets	101
6.2.1	Quench Simulations	102
6.2.2	Coil Voltage Distribution	116
6.2.3	Variation of Parameters	117
7	Conclusions	127
A	Calculations	129
A.1	Inductance Calculation	129
A.2	Approximation of Diode Characteristics	136
B	Magnet Parameters	139
C	Quench Detection Scheme	143

D	Material Properties	145
D.1	Specific Heat	145
D.2	Electrical Resistivity	146
D.3	Thermal Conductivity	147
E	List of Symbols	149

List of Figures

1.1	Schematic layout of accelerators at CERN side	4
1.2	Experimentation areas on the circumference of the LHC machine	4
1.3	Schematic layout of the LHC half-cell	5
1.4	Powering scheme with current sources at even points and energy extractions at odd and even points	6
2.1	Magnetic flux density versus magnetisation for Type I superconductors (left side) and Type II superconductors (right side)	9
2.2	Typical current densities of NbTi and Nb ₃ Sn superconductors	10
2.3	Superconducting/resistive phase transition surface of niobium-titanium . . .	13
2.4	Heat balance in a quenching mono-filamentary strand	14
2.5	Generation of pure dipole (m=1), quadrupole (m=2), and sextupole (m=3) fields by current distributions	17
2.6	Coil cross section of a 10 m prototype dipole magnet	17
3.1	Assembly of the LHC Test String containing one superconducting quadrupole and two superconducting dipole magnets used for STRING RUN 2	20
3.2	Principle electrical scheme of the LHC Test String without quenching the magnets	21
3.3	Cross section of main lattice dipole (LHC Version 1)	22
3.4	Insulation of the LHC cable used for Version 1 prototype dipole magnets, consisting of polyimide and glass-fibre tape.	23
3.5	Cross section of main lattice quadrupole (LHC Version 1)	24
3.6	Simplified electrical scheme for a slow discharge of the LHC Test string . . .	26
3.7	Electrical circuit to calculate the maximum reverse voltage across the by-pass diodes in case of a discharge	27
3.8	Electrical circuit to estimate the maximum temperature in the small cross-sectional auxiliary bus-bar in case of emergency	28
3.9	Auxiliary bus-bar temperature versus dump resistance R_{dm} with initial quench currents as parameter	28
3.10	$\int i^2 dt$ for 1 mm ² cross-section area versus temperature for copper ($RRR = 100$)	30
3.11	Location of stainless steel quench heater strips on the outer layer of the dipole magnet	33
3.12	Simplified powering scheme of quench heater strips for quadrupole (left side) and for dipole (right side)	34
3.13	Block diagram of the quench detector module for the LHC Magnet String . .	35
3.14	Temperature and Pressure instrumentation of the main dipole end volumes .	37

3.15	Voltage and temperature instrumentation in the cold mass of the short straight section	37
3.16	Principle cooling scheme of the LHC Test String	38
4.1	Simplified electrical scheme of the LHC Test String	42
4.2	Magnet scheme with by-pass diode	43
4.3	Structure of the program to simulate the electrodynamic behaviour	53
4.4	Deviation in temperature calculation versus iteration time interval Δt to verify the stability of the model	56
4.5	Current decay versus time for a heater provoked quench at 13.1 kA	58
4.6	Aperture voltage versus time across the dipole MB1 for a heater provoked quench at 13.1 kA	58
4.7	Aperture voltage versus time across the dipole MB2 for a heater provoked quench at 13.1 kA	59
4.8	Aperture voltage versus time across the dipole MB3 for a heater provoked quench at 13.1 kA	59
4.9	Deduced average MIIT's evolution versus initial quench current for the outer layer coils in the magnets	61
4.10	Calculated average temperature of the small cross-section auxiliary bus-bar as a function of increasing heater delay between dipole magnets	62
4.11	Net for calculating the temperature distribution across bus-bar	64
4.12	Bus bar dimensions for simulating heat propagation	66
4.13	Temperature profile versus time across the bus-bar leading from the diode triplet to the adjacent dipole	67
5.1	Chain of components for voltage measurement across coils and bus-bars . . .	70
5.2	Chain of components for temperature measurement	71
5.3	Electrical scheme of a twin-aperture LHC dipole	72
5.4	Measured magnet current versus time after a heater provoked quench in dipole MB3 at 13994 A	73
5.5	Deduced magnet current decay rate versus time after a heater provoked quench in dipole MB3 at 13994 A	73
5.6	Voltage across the outer layer coil of pole 1 after a heater provoked quench at 13994 A (inductive voltage deduced from current decay)	75
5.7	Voltage across the inner layer coils of pole 1 after a heater provoked quench at 13994 A (inductive voltage deduced from current decay)	75
5.8	Resistance of the outer layer coil and the inner layer coil of pole 1 after a heater provoked quench at 13994 A	76
5.9	Deduced temperature versus time in the outer and inner layer coil after a heater provoked quench at 13994 A	76
5.10	Possible number of resistive conductors in the dipole coils after a heater provoked quench at 13994 A	77
5.11	Simplified electrical scheme of a dipole magnet	77
5.12	Coil voltage distribution in dipole MB 3 after a heater provoked quench at 13994 A	77
5.13	String current decay versus time after a heater provoked quench at 13.1 kA .	78

5.14	Magnet voltages versus time after a heater provoked quench at 13.1 kA . . .	79
5.15	Development of magnet voltages after firing the quench heaters at 13.1 kA (zoom of Fig. 5.14)	79
5.16	Simulated magnet currents versus time for a heater provoked quench at 13.1 kA	80
5.17	Simulated diode current versus time for a heater provoked quench at 13.1 kA (Note: Current across dipole MB1 is zero)	81
5.18	Simulated average magnet resistance versus time for a heater provoked quench at 13.1 kA	82
5.19	Simulated average temperature in the resistive sections of the magnet coils versus time for a heater provoked quench at 13.1 kA	82
5.20	Simulated maximum bus-bar current versus heater delay time after a quench at 12400 A	83
5.21	Simulated maximum temperature of the auxiliary bus-bar leads for different heater delay times after a quench at 12400 A	84
5.22	Measured output voltage of the bridge quench detector across aperture A of dipole MB2 during a natural quench at 13283 A	85
5.23	Resistance development in pole 1 of dipole MB2 during a natural quench at 13283 A	85
5.24	Chronology of quench detection	86
5.25	Adiabatically calculated hot-spot temperature in the outer layer coil at dif- ferent quench detection levels after a natural quench at 13283 A	86
5.26	Short Straight Section with protection diodes and instrumentation	88
5.27	Simplified electrical scheme for quadrupole quench propagation experiments	89
5.28	Pressure and temperature versus time for a quench at 5 kA and closed quench relief valves	90
5.29	Pressure and temperature versus time for a quench at 7 kA by limiting the cold mass pressure to about 12 bar.	91
5.30	Pressure and temperature versus time for a quench at 7 kA by opening the relief valve on MB3 after 35 s.	91
5.31	Pressure and temperature versus time for a quench at 7 kA and open relief valve on MB3	92
5.32	Pressure and temperature versus time for a quench at 13.1 kA by opening the relief valve on MB3 about 5 s after initiating a quench in the quadrupole . .	93
5.33	Current versus time after provoking a quadrupole quench with quench heaters at different initial current levels	94
5.34	Voltage versus time across the transition of the stabilised and non-stabilised bus-bar section in the dipole at different initial current levels	94
5.35	Measured time delays from protection heater firing until resistance in the superconducting coil appears	95
5.36	Quench detector output voltage signal versus time before (solid line) and after (dashed line) modification	96
5.37	Input circuit for dipole main bus-bar quench detectors	97
5.38	Connection of two superconducting cables by soldering	98
5.39	Electrical circuit of the LHC Test String with the number of splices along the main circuit	99

6.1	Cross section of main lattice dipole (LHC version 4)	102
6.2	Electrical scheme of a single twin-aperture dipole magnet with a by-pass diode in parallel	103
6.3	Magnet current versus time ($RRR_A = RRR_B = 100, t_{hA} = t_{hB}=50$ ms) . . .	105
6.4	Average coil resistance of outer layer coils and inner layer coils versus time ($RRR_A = RRR_B = 100, t_{hA} = t_{hB}=50$ ms)	105
6.5	Voltages versus time in Aperture A ($RRR_A = RRR_B = 100, t_{hA} = t_{hB}=50$ ms)	106
6.6	Voltages versus time in Aperture B ($RRR_A = RRR_B = 100, t_{hA} = t_{hB}=50$ ms)	106
6.7	Average temperatures of outer layer and inner layer coils versus time ($RRR_A = RRR_B = 100, t_{hA} = t_{hB}=50$ ms)	107
6.8	Hot-spot temperatures of outer layer and inner layer coils versus time ($RRR_A = RRR_B = 100, t_{hA} = t_{hB}=50$ ms)	107
6.9	Magnet current versus time ($RRR_A = RRR_B = 100, t_{hA}=50$ ms, $t_{hB}=70$ ms)	109
6.10	Average coil resistance of outer layer coils and inner layer coils versus time ($RRR_A = RRR_B = 100, t_{hA}=50$ ms, $t_{hB}=70$ ms)	109
6.11	Voltages versus time in Aperture A ($RRR_A = RRR_B = 100, t_{hA}=50$ ms, $t_{hB}=70$ ms)	110
6.12	Voltages versus time in Aperture B ($RRR_A = RRR_B = 100, t_{hA}=50$ ms, $t_{hB}=70$ ms)	110
6.13	Average temperatures of outer layer and inner layer coils versus time ($RRR_A = RRR_B = 100, t_{hA}=50$ ms, $t_{hB}=70$ ms)	111
6.14	Hot-spot temperatures of outer layer and inner layer coils versus time ($RRR_A = RRR_B = 100, t_{hA}=50$ ms, $t_{hB}=70$ ms)	111
6.15	Magnet current versus time ($RRR_A = 70, RRR_B = 130, t_{hA} = t_{hB}=50$ ms) .	113
6.16	Average coil resistance of outer layer coils and inner layer coils versus time ($RRR_A = 70, RRR_B = 130, t_{hA} = t_{hB}=50$ ms)	113
6.17	Voltages versus time in Aperture A ($RRR_A = 70, RRR_B = 130, t_{hA} = t_{hB}=50$ ms)	114
6.18	Voltages versus time in Aperture B ($RRR_A = 70, RRR_B = 130, t_{hA} = t_{hB}=50$ ms)	114
6.19	Average temperatures of outer layer and inner layer coils versus time ($RRR_A = 70, RRR_B = 130, t_{hA} = t_{hB}=50$ ms)	115
6.20	Hot-spot temperatures of outer layer and inner layer coils versus time ($RRR_A = 70, RRR_B = 130, t_{hA} = t_{hB}=50$ ms)	115
6.21	Electrical scheme of coil connections in a dipole magnet	116
6.22	Simulated coil voltage distribution in a 14.2 m dipole magnet after a quench at 11.5 kA for different values of RRR and heater delay combinations	116
6.23	Hot-spot temperature versus differences in heater response time at different values of RRR (same in both apertures)	119
6.24	Maximum voltages versus differences in heater response time at different values of RRR (same in both apertures)	119
6.25	Hot-spot temperature versus differences in heater response time at an average RRR of 100 (different in apertures)	120
6.26	Maximum voltages versus differences in heater response time at an average RRR of 100 (different in apertures)	120
6.27	Hot-spot temperature versus RRR with Δt_h as parameter	121

6.28	Maximum voltage versus RRR with Δt_h as parameter	121
6.29	Hot-spot temperature versus ΔRRR with average RRR as parameter at uniform heater delay of $\Delta t_{hA} = \Delta t_{hB} = 50$ ms	122
6.30	Maximum voltage to ground versus ΔRRR with average RRR as parameter at uniform heater delay of $\Delta t_{hA} = \Delta t_{hB} = 50$ ms	122
6.31	Hot-spot temperature versus Cu/Sc -ratio with Δt_h as parameter	123
6.32	Maximum voltage versus Cu/Sc -ratio with Δt_h as parameter	123
6.33	Hot-spot temperature versus Cu/Sc -ratio with ΔRRR as parameter	124
6.34	Maximum voltage versus Cu/Sc -ratio with ΔRRR as parameter	124
A.1	Configuration of two parallel double lines to calculate the mutual inductance	129
A.2	Image mirror method to consider the effect of the iron	131
A.3	Cross-section of the superconducting cable	132
A.4	Dipole coil designation for calculating self and mutual inductances	132
A.5	Quadrupole coil designation calculating the self and mutual inductances	132
A.6	Measured forward voltage versus temperature at different current levels for a single diode of the triplet; (o) $i = 460$ A, (+) $i = 8000$ A, (*) $i = 15000$ A and approximations	138
A.7	Forward voltage versus temperature at different current levels for a single diode of the quadruplet; (o) $i = 460$ A, (+) $i = 8000$ A, (*) $i = 15000$ A and approximations	138
C.1	Quench protection scheme for the LHC Test String	144
D.1	Specific heat versus temperature for copper and niobium-titanium	145
D.2	Electrical resistivity versus temperature for copper with RRR as parameter	146
D.3	Thermal conductivity versus temperature for different materials	147

List of Tables

1.1	LHC performance parameters	5
2.1	Typical properties of copper and niobium-titanium at 10 K	15
3.1	Diode parameters for triplet and quadruplet diodes	32
4.1	Cases of current sharing in the superconducting magnets of the LHC Test String during a discharge	49
4.2	Temperature increase as a function of temperature at $\Delta t = 50 \mu s$	56
4.3	Input parameters for the simulation deduced from experiment <i>RUN0525</i> to validate the model	57
4.4	Deduced hot-spot temperature in dipole conductors, simulated for different quench currents	61
5.1	Relative error in voltage measurement of a quench detector module (gain= 1.2)	70
5.2	Experimental parameters of a heater provoked quench in dipole MB3 after the 2 nd thermal cycle	72
5.3	Results deduced from a simulation of a heater induced quench at 13.1 kA (<i>RUN0525</i>)	83
5.4	List of quench propagation experiments	89
5.5	Summary of the contact resistance measurement on the LHC Test String performed with electrical and calorimetric method	98
6.1	Input parameters for quench simulation by considering equal conditions for both aperture dipoles	104
6.2	Input parameters for quench simulation by considering different heater delays for both aperture dipoles	108
6.3	Input parameters for quench simulation by considering different values of RRR for both aperture dipoles	112
A.1	Centre co-ordinates of the conductors in the first quadrant of the LHC prototype dipole magnet	133
A.2	Centre co-ordinates of the conductors in the first quadrant of the LHC prototype quadrupole magnet	134
A.3	Self- and mutual inductances of the LHC dipole	135
A.4	Self- and mutual inductances of the LHC prototype quadrupole	135
A.5	Typical forward voltage measured on a single triplet diode versus temperature with the current as parameter	136

A.6	Typical forward voltage measured on a single quadruplet diode versus temperature with the current as parameter	136
A.7	Parameters to fit the diode triplet characteristics	137
A.8	Parameters to fit the diode quadruplet characteristics	137
B.1	Main quadrupole parameters for LHC version 1 and LHC version 4	139
B.2	Main dipole parameters for the first and final version of LHC magnets	140
B.3	Main parameters of the quench heater strips for the prototype quadrupole and prototype dipoles in the LHC Magnet String	141
C.1	Threshold and gain adjustment of quench detector modules for the LHC Test String	143

Chapter 1

Introduction

The Large Hadron Collider LHC will be the next research instrument at CERN to further the extraordinary progress in understanding the structure of matter. The design, based on the experience in superconducting accelerator projects attained from TEVATRON, RHIC, HERA, and SSC, aspires to accelerate and collide protons, heavy ions and electron-protons in the multi-TeV energy range. It will mainly consist of a ring of high field magnets installed in the existing tunnel of the LEP collider. To bend protons with a beam energy of 7 TeV along the circular trace, the main dipole magnets will operate at about 8.4 T flux density and the quadrupoles at 220 Tm^{-1} field gradient. Niobium-titanium superconductors have been chosen to generate these high magnetic fields. Therefore, the superconducting magnet coils have to operate close to their physical limits at 1.9 K in superfluid helium in order to reach the high magnetic field.

The LHC magnet system will be one of the largest applications of superconductivity. The tunnel with a circumference of 26.8 km long ring is sectorized in octants. In each octant the superconducting main dipole magnets will be powered in series. At a flux density of 8.4 T the magnets in an octant store an energy of about 1.2 GJ. In case of quench, the stored energy should not cause over-voltages or overheating of the machine components. This requires a fast and reliable magnet protection system composed of quench detectors and quench heaters.

After detecting a quench, heater strips on the superconducting coils of the quenched magnet are fired in order drive large fractions of the magnet coils normal and so to distribute the dissipated energy over the whole magnet length. The current in the quenched magnet decays according to the magnet inductance and magnet coil resistance in less than one second. The still superconducting magnets in the octant will be discharged with a time constant of about 100 s, guiding the decaying current in the octant around the quenched magnet by use of by-pass diodes.

To obtain experience in operating a system of superconducting magnets and to study the cryogenic and electro-magnetic behaviour, a chain of one superconducting quadrupole and three superconducting dipoles, the so-called *LHC Test String*, has been installed and tested at CERN.

A reliable quench protection system requires actions in case of a quench to keep the hot-spot temperature in the quench origin and the maximum voltage between coils and ground below their critical values.

The thesis treats with

- the analysis of the electrodynamic behaviour in the LHC Test String, in particular the transients after a quench,
- the development of a model to deduce critical parameters for the quench protection, and
- the analysis of quench propagation experiments between magnets in the LHC Test String.

The equations to describe the transients contain the specific heat and electrical resistivity of the conductor materials, which are non-linear functions of temperature. Since after a magnet quench the temperature in the resistive coil sections increases by about two orders of magnitude, the temperature dependencies of the material properties have to be taken into account. Initially it was foreseen to describe the transients by some simple equations which would allow the estimation of essential parameters. Considering the properties as constant or linear functions of temperature is not sufficient and gives wrong results.

Diodes as by-pass elements of the magnets complicate the analytical description of the transient model. After a quench the diodes turn on depending on the voltages across the single magnets in the LHC Test String. Since this conditions may change during the discharge, an iterative solution gives the most reliable results.

However based on the analytical description of electrodynamics, a transient model was developed to calculate numerically the parameters which cannot be directly measured during experiments. By choosing time intervals between iterations small enough, the properties can be assumed as constant during an interval.

Some parameters are fixed, like inductance, magnetic length, values of residual resistivity ratio of copper, copper to superconductor ratio of the cable, number of conductors, etc. Others like heater delay between magnets, difference in heater response time between magnet apertures may endanger the operation of the LHC Test String. By use of the transient model, predictions of critical values after changing the magnet design and worst case situations can be simulated. Since the final version magnets for the LHC machine [13] are not yet built, measures in advance can be adopted to keep this development within safe limits.

In order to understand the quench propagation from the quenched magnet to the adjacent magnets, a series of experiments were performed on the LHC Test String. The analysis is discussed. These results of the quench propagation experiments on the LHC Test String are essential in order to estimate the maximum number of neighbouring magnets which quench until the quench dies out.

1.1 Principles of Accelerators

Particle accelerators are mainly known for their application as research tools in nuclear and high energy particle physics requiring the largest and highest energy facilities. They are based on the interaction of the electric charge with static and dynamic electro-magnetic fields. The technical realisation of this interaction leads to the different types of particle

accelerators. All particle accelerators consist of two basic units, the particle source or injector and the main accelerator. The particle source comprises all components to generate the desired type of particles. Particle beams are accelerated in linear or circular accelerators. A linear accelerator consists of a linear sequence of many accelerating units where accelerating fields are generated and timed such that particles absorb and accumulate energy from each acceleration unit. Most commonly used linear accelerators consist of a series of cavities excited by radio frequency sources to high accelerating electric fields. For very high beam energies linear accelerators become very long and costly. Such practical problems are avoided in circular accelerators where the beam is held on a circular path by magnetic fields in bending magnets. The particles pass repeatedly every turn through accelerating sections, similar to those in linear accelerators. At each turn the particles gain energy from the cavities and reach the maximum energy while the fields in the bending magnets are increased in synchronism. Such a circular accelerator is called synchrotron. In addition to the bending dipoles, a synchrotron contains also elements for orbit corrections, betatron tunes, chromaticity correction, etc.

The basic principles to accelerate particles of different kinds are similar for protons, ions, and electrons. Technically the accelerators differ more or less to adjust to the particular beam parameters which have mostly to do with the particle momentums.

After acceleration in a linear accelerator or synchrotron the beam can be directed onto a target to study high energy interactions with the target protons. In the past such fixed target experiments dominated nuclear and high energy particle experiments. To increase the centre-of-mass energy for basic research, particle beams are aimed not at fixed targets but to collide head on with another beam. This is a main goal for the construction of colliding beam facilities or storage rings. Because the interactions between counter orbiting particles are very rare, storage rings are designed to allow the beams to circulate for many turns with beam life times of several hours to give the particles ample opportunity to collide with another counter rotating particles [32].

1.2 The LHC design

1.2.1 Overview

The existing accelerator infrastructure of CERN (see Fig. 1.1) will be able to provide the injection beams with the required characteristics by only a few additions to the present installations.

The LHC will be installed in the existing tunnel of the Large Electron Collider LEP whereas the ring diameter is already fixed. In two separated beam channels the proton bunches accelerate in opposite directions up to an energy of 7 TeV.

For reasons of space limitations, imposed by the cross-section of the LEP tunnel, and for economy, a compact *twin-aperture* structure, incorporating the two beam channels in the same yoke and cryostat, has been adopted for the main dipoles and main quadrupoles. Over the circumference, the beams are crossed over at the points where they collide in order to have an identical path length (see Fig. 1.2). Before and after collision, the beams are brought together or separated by separation/recombination dipole magnets.

Two kinds of detectors will be used in LHC. Toroid magnets bend charged particle

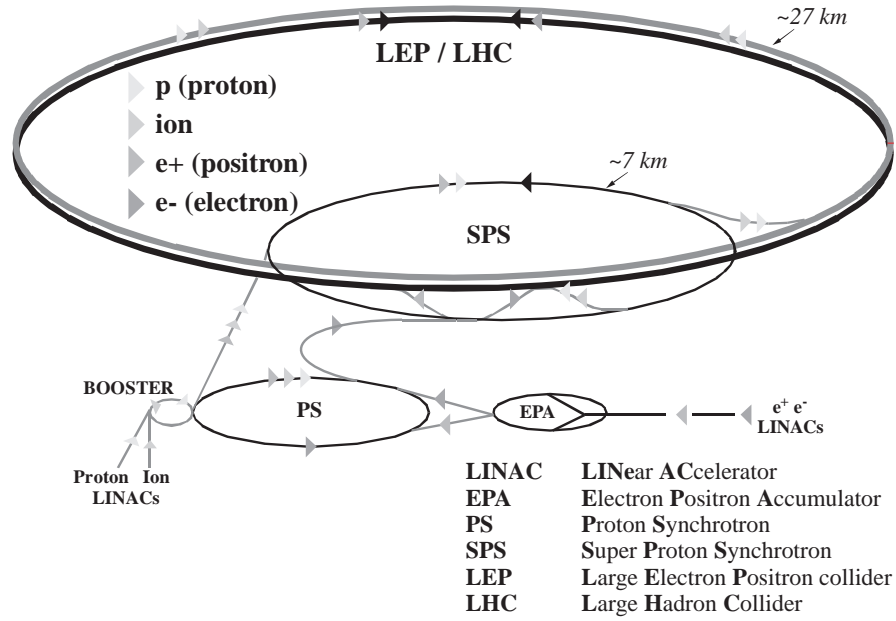


Figure 1.1: Schematic layout of accelerators at CERN side

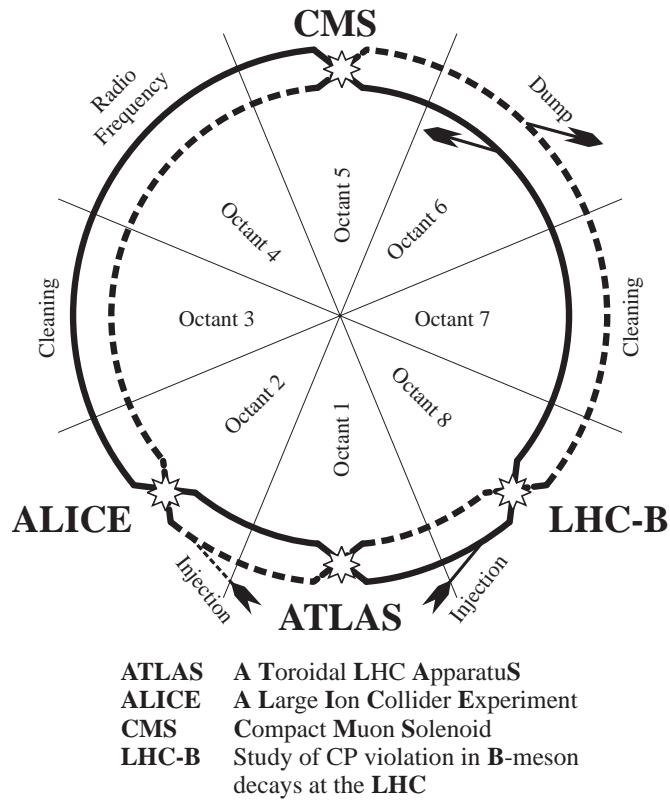


Figure 1.2: Experimentation areas on the circumference of the LHC machine

tracks longitudinally along the beam line while solenoid magnets bend them in a plane perpendicular to the beam line.

In addition to proton-proton operation, the LHC will be able to collide heavy nuclei (Pb-Pb) produced in the existing CERN accelerator complex, giving an energy of 1150 TeV in the centre of mass.

The performance parameters for the LHC machine are listed in Table 1.1 [13].

Table 1.1: LHC performance parameters

	Units	proton-proton	Pb-ions
Expected operational energy	[TeV]	14.0	1148
Dipole field (max.)	[T]	8.4	8.4
Luminosity	[cm ⁻² s ⁻¹]	10 ³⁴	10 ²⁷
Luminosity at beam-beam limit	[cm ⁻² s ⁻¹]	2.5·10 ³⁴	
Number of bunches		2835	608
Bunch spacing	[m]	7.5	37.4
	[ns]	25	124.8
Particles per bunch		10 ¹¹	9.4·10 ⁷
Particles per beam		2.8·10 ¹⁴	4.7·10 ¹⁰
β -value at interaction point	[m]	0.5	0.5
r.m.s radius at interaction point	[μ m]	16	15
r.m.s collision length	[mm]	54	54
Full crossing angle	[μ rad]	200	<100
Synchrotron Radiation (two beams)	[kW]	7.2	

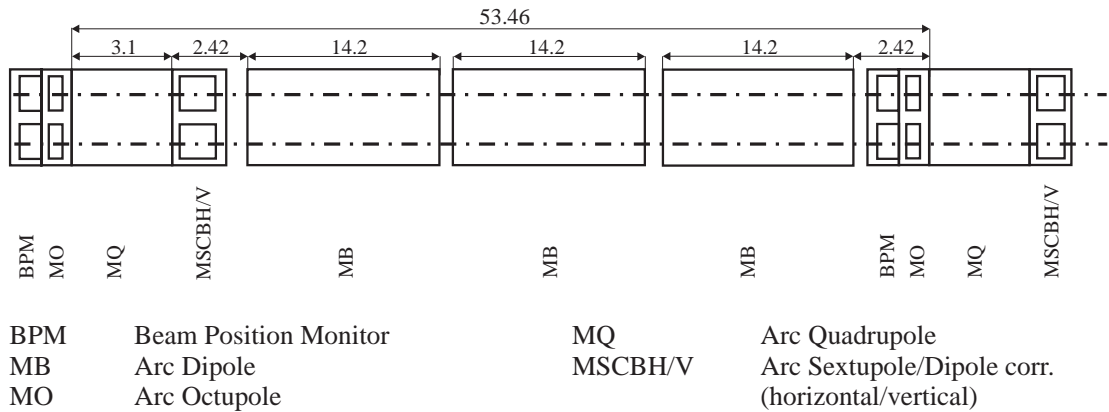


Figure 1.3: Schematic layout of the LHC half-cell

Each of the eight 2456 m long LHC sectors will be made up of 23 cells formed of two identical half-cells. They are bending/focusing configurations (Fig. 1.3) composed of three 14.2 m long twin-aperture main dipoles and a short straight section housing one 3.1 m long main quadrupole, a combined sextupole/dipole corrector, an octupole or a skew quadrupole or a trim quadrupole and a beam position monitor. The main dipoles and quadrupoles are all of the twin-aperture design, while corrector magnets are independent for each beam [23].

As the circumference of the LHC machine is given by the existing tunnel, a bending field of about 8 T is required to reach the design energy. This high field can be reached reliably and economically in such a massive application only by use of the well understood niobium-titanium superconductor technology. Therefore, the magnets have to be cooled to a very low temperature, below 2 K, to increase the current carrying capacity versus field of that conductor. Below 2.17 K, helium is in the superfluid state with extremely low viscosity and very high thermal conductivity. Niobium-tin superconductors at 4.2 K would require impregnated coils. For beam loss and ac-loss, helium transparent windings are needed which cannot be obtained easily with impregnated coils. Further, niobium-tin superconductors are still too expensive and too risky for a large application such as the LHC magnets.

1.2.2 Electrical Powering Scheme and Quench Protection

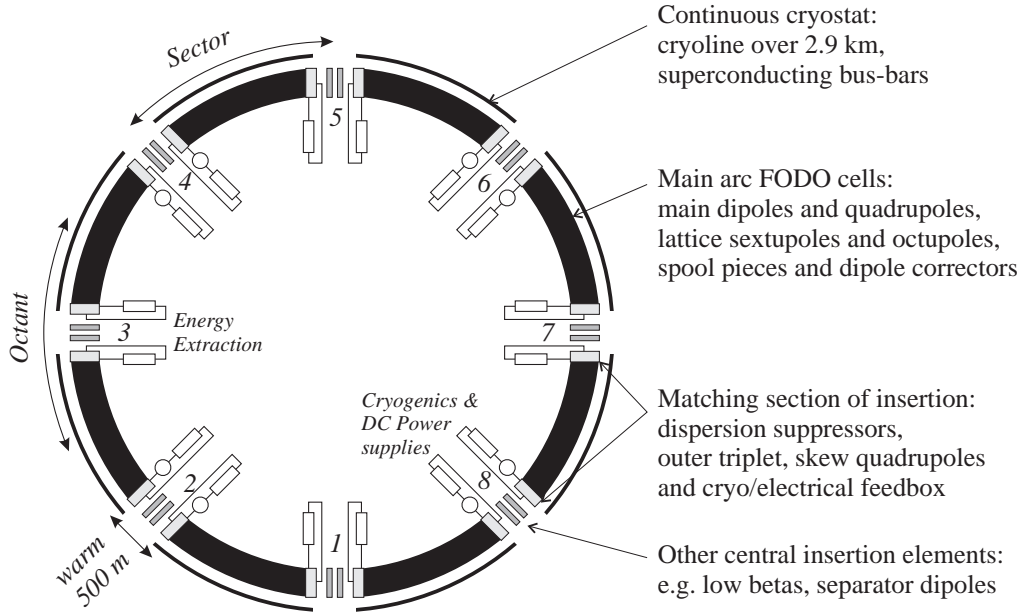


Figure 1.4: Powering scheme with current sources at even points and energy extractions at odd and even points

The powering of the machine is concentrated in the even points, as depicted in Fig. 1.4, where the existing power supplies and cooling towers of LEP can be re-used. From the even points, all main lattice magnets, and also a number of insertion magnets, are fed using superconducting bus-bars running through the magnet cold masses and cryostats. Main quadrupoles and dipoles are powered separately to give maximum tune flexibility to the machine [25]. In the odd and even points, energy extraction resistors are installed to dissipate the magnetic stored energy during fast discharges.

Without precautions in a series connection of high-field superconducting magnets, if one magnet quenches then the magnetic stored energy of all the other magnets will be dissipated in the quenching magnet therefore destroying it.

A quench protection system, containing quench detectors, quench heaters on the superconducting magnet coils, by-pass diodes across each single magnet, and external energy dump resistors, is required in order to avoid such accidents. The large stored energy of 520 kJm^{-1} at 8.4 T and the relatively low quench propagation speed, between 10 and 20 ms^{-1} , make it necessary to detect a quench quickly and fire the strip heaters which spread the quench over a sufficiently large part of the coil volume to absorb the energy without excessive heating. Silicon diodes are located in the cold mass to by-pass the quenching magnets and safely discharge the still superconducting magnets.

The advantage of the electrical segmentation is a reduction in the total quenching voltage, rapid discharge of only 1/8 of the machine in case of a magnet quench, no risk of a complete machine avalanche quench, and better static and dynamic control of the machine. The drawback of the electrical segmentation is the need of a strongly synchronized power converter control.

Chapter 2

Superconductivity

Some pure metallic elements and alloys become zero-resistive conductors when they are cooled down to very low temperatures. This superconducting state corresponds to a thermodynamic phase which is stable within a given range of temperature, magnetic flux density, and current density. Outside this range the superconductor becomes resistive. Since the discovery of the superconducting state, several attractive superconductors (metallic compounds and ceramics) were found. The niobium-titanium alloy became a leading role in superconducting applications due to the well established manufacture of conductors. While current flows without loss during steady state conditions, different a.c. losses occur in the superconductor during current or field changes.

In this chapter the properties of superconducting metallic compound materials are briefly discussed with respect to their application in superconducting accelerator magnets.

2.1 Superconducting Materials

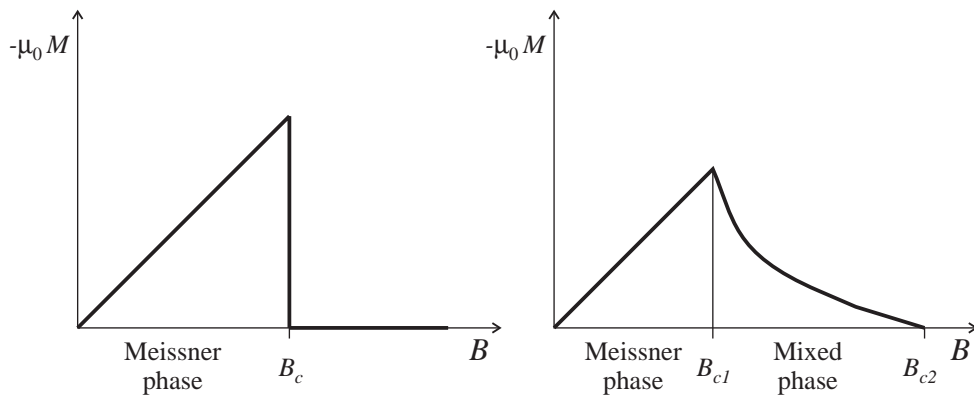


Figure 2.1: Magnetic flux density versus magnetisation for Type I superconductors (left side) and Type II superconductors (right side)

Metallic superconductors are classified in Type I and Type II superconductors. Type I superconductors, which comprise most of pure-elements, have a sharp transition to the superconducting state and a total screening of magnetic flux within the bulk (Meissner-effect).

With the exception of some electronics applications, Type I superconductors have few practical magnet uses because of their rather low critical flux density B_c . They are determined by the parameters of critical temperature T_c and critical magnetic flux density B_c .

Type II superconductors are much more useful because of their higher critical flux density and transition temperature. The structure of Type II superconductors, sometimes referred to as 'hard' superconductors, is more complex.

The distinction between Type I and Type II superconductors lies in the magnetic behaviour as shown in Fig. 2.1. In a Type I superconductor magnetic flux is totally excluded for $B < B_c$. A Type II superconductor allows penetration of magnetic flux under certain circumstances which brings small regions into a normal state. Such behaviour, which is a deviation from the Meissner state, is referred to as the mixed state in Type II superconductivity. It has two critical flux densities B_{c1} and B_{c2} . Because of flux penetration, the Type II superconductor in the mixed state is no longer perfectly diamagnetic. The lower critical flux density B_{c1} represents the transition from the Meissner state to the mixed state. The upper critical flux density B_{c2} marks the maximum field for which any superconducting behaviour is present. Although the critical temperature T_c may be only slightly higher than that of some Type I materials, while B_{c2} is often orders of magnitudes larger than B_c .

An important step in the history of superconductivity was the discovery of high temperature superconductors. Depending on the ceramic compound, transition temperatures beyond 100 K are possible, but the fabrication of wires and cables is difficult [29].

Most of the superconductor applications today use metallic superconductors. The most practical superconducting alloy is niobium-titanium (NbTi).

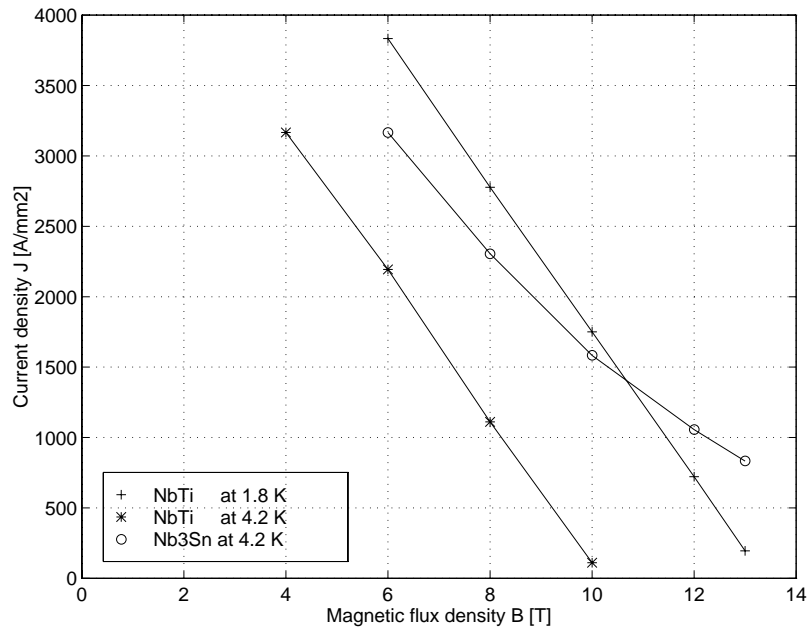


Figure 2.2: Typical current densities of NbTi and Nb₃Sn superconductors

Fig. 2.2 shows the comparison of current densities for NbTi and Nb₃Sn superconductors. Both materials are practically equivalent provided the NbTi is cooled to 1.8 K. Thus, two design strategies have to be distinguished. Either Nb₃Sn superconductors are used with a

relatively simple cryogenic system at 4.2 K with the drawback of a very brittle material which is difficult to handle. Or to use NbTi superconductors which are simple to handle, but with the drawback of a more complex cryogenic system working in superfluid helium below 2 K [24].

2.1.1 Niobium-Titanium Superconductors

In addition to the good superconducting properties of NbTi alloys, the excellent combination of mechanical and metallurgical properties make this alloy important for technical applications. The transition temperature T_c and the upper critical flux density B_{c2} depend on the alloy. To keep T_c and B_{c2} constant over the length of the superconducting wire, the alloy composition must be kept constant during melting. The basic alloys and the influence of impurities must be carefully controlled. The critical current density J_c is structure dependent and depends strongly on density, size and distribution of imperfections [15].

The critical current density can be improved by alternating sequences of cold work and heat treatment. Cold reduction of the wire reduces the size of the dislocation cells in a direction perpendicular to the drawing direction. Heat treatment causes any dislocations which might be in the centre of the superconductor to migrate to the walls, thereby increasing the difference in properties between cell wall and interior. The applications of such superconductors are limited to magnetic flux densities up to about 8 T at 4.2 K and 10 T at 2 K.

2.1.2 Niobium-Tin Superconductors

A commercial superconducting material suitable for use at higher magnetic flux densities and at higher temperatures is the inter-metallic compound Nb₃Sn. It consists of a body centred cubic lattice of tin atoms with two niobium atoms on each face of the cube. This unusual structure causes the niobium atoms to approach each other more closely than in elemental niobium and is thought to be the reason behind the excellent superconducting properties [33]. Pure strain-free Nb₃Sn of stoichiometric composition has a critical temperature of 18.5 K and an upper critical flux density B_{c2} of about 28 T. Unfortunately this inter-metallic compound can be deformed only about 0.2 % in tension before it fractures and becomes useless in superconducting wires. Since coils wound with niobium-tin superconductors have to be fully impregnated, helium transparency is not present. These conditions facilitates premature quenching of the conductor due to heat building as a result of beam and ac-losses.

2.2 Superconducting Cable

The LHC superconducting accelerator magnet design foresees niobium-titanium (NbTi) superconductors operated at a current level of 11500 A. A single composite NbTi wire of 1 mm strand diameter typically carries about 500 A in magnetic field of about 8 T. Therefore it is necessary to use many wires in parallel. To ensure that the wires share current equally, they must be combined in a form of a twisted, two-dimensionally transposed cable. The Rutherford type cable has been chosen because of its superior mechanical properties. Between 20 and 40 strands are bundled together with a transposition pitch length which is about 6 to 8

times the cable width [34]. Each strand itself is twisted with a pitch length of 25 mm [13]. In order to obtain the desired coil configuration, the rectangular cable has a small keystone angle. The cable is kept slightly porous in magnet windings so that the helium may penetrate to provide additional stability by increasing the minimum quench energy.

During operation the maximum temperature of the helium in the interior of the cable should not exceed the transition temperature of 2.17 K, in order to benefit from the high thermal conductivity and low viscosity of superfluid helium.

2.2.1 Losses in Superconducting Cables

Any change in the current automatically implies a change in the field pattern of the superconductor which principally causes a power loss. A close relationship exists between the flux-jump stability of a multi-filamentary conductor and its hysteretic loss in an applied a.c. field. The flux-jump stability of a given composite is maximised if the filaments are decoupled by twisting. Likewise the hysteretic a.c. loss is minimised, since it becomes simply the sum of the hysteretic losses of the individual filaments.

When the current flows in the wire wound in a coil, the field change is enlarged by the local field in the windings. Eventually external time varying magnetic fields are present. Considering this the occurring losses can be classified into the following components:

- Hysteresis loss in the superconducting filaments due to the alternating field and current changes.
- Coupling current loss due to induced normal currents in the copper matrix by a $\partial B/\partial t$.
- Self-field loss due to $\partial I/\partial t$ in the superconductor.

In a practical situation all three loss components interact. A simple analysis becomes impossible. If the conductor is exposed to a time varying external magnetic field, flux penetrates from the outside of the conductor while the interior will remain field-free due to screening currents. A local self-field in the conductor occurs. Losses associated to this are not able to be reduced by twisting, since the self field rotates with the twist. Self-field loss may be minimised by filament transposition, an important element in conductor design. In addition to hysteretic loss, the conductor is subject to Joule heating associated with the normal-state eddy currents that cross the matrix between the filaments. At sufficiently high frequencies these eddy currents, which flow longitudinally along the skin of the conductor, have the effect of coupling the filaments therein into a solid superconducting shell [4][33]. High current de-ramp rates after a quench in any section of the superconducting cable may cause quenching of still superconducting sections of the cable. This effect is called quench-back.

To a first approximation, the frequency dependence of a.c. loss may be divided into two regimes separated by a characteristic frequency F_c , related to the conditions for the inter-filamentary coupling. With $F \ll F_c$ all of the filaments are fully decoupled, the hysteretic power loss \dot{Q}_h is minimal, since it increase proportional to F and may be treated separately from the matrix eddy current loss \dot{Q}_e , which has an F^2 frequency dependence. The a.c. power loss \dot{Q} can be determined by the superposition of hysteretic power loss \dot{Q}_h and eddy current power loss \dot{Q}_e .

$$\dot{Q} = \dot{Q}_h + \dot{Q}_e = a \cdot F + b \cdot F^2 \quad (2.1)$$

in which a and b are constants.

2.2.2 Normal State Transition

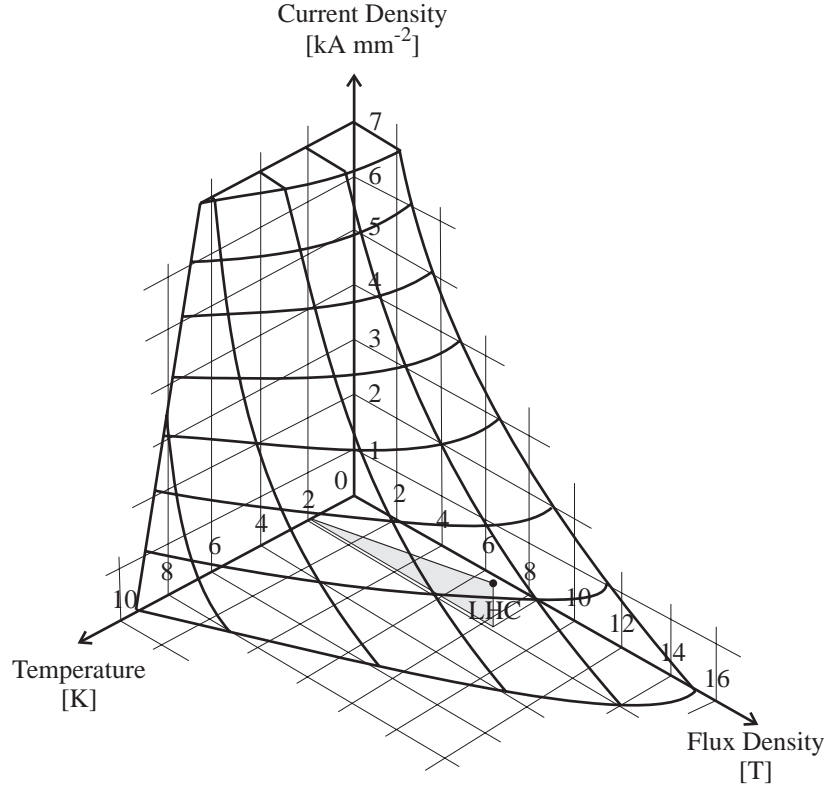


Figure 2.3: Superconducting/resistive phase transition surface of niobium-titanium

The superconducting state only exists when materials are maintained below the critical temperature. This temperature depends on many parameters, including the amount of current carried by the conductors and the magnetic field to which the conductor is subjected. A three-dimensional surface, called the *critical surface*, is defined by the boundaries of critical temperature T_c , critical magnetic flux density B_c , and critical current density J_c , as shown in Fig. 2.3. Superconductivity vanishes for any set of two parameters, if the third parameter increases beyond the critical surface. This transition process where the superconductor changes from the superconducting state to the normal resistive state is called *quench*.

If the temperature is below the critical value, the current density in the copper matrix

$$J_{Cu} = \frac{i_{Cu}}{f \cdot A} \quad (2.2)$$

will be zero. $A = A_{Cu} + A_{Sc}$ is the conductor cross section area. The factor

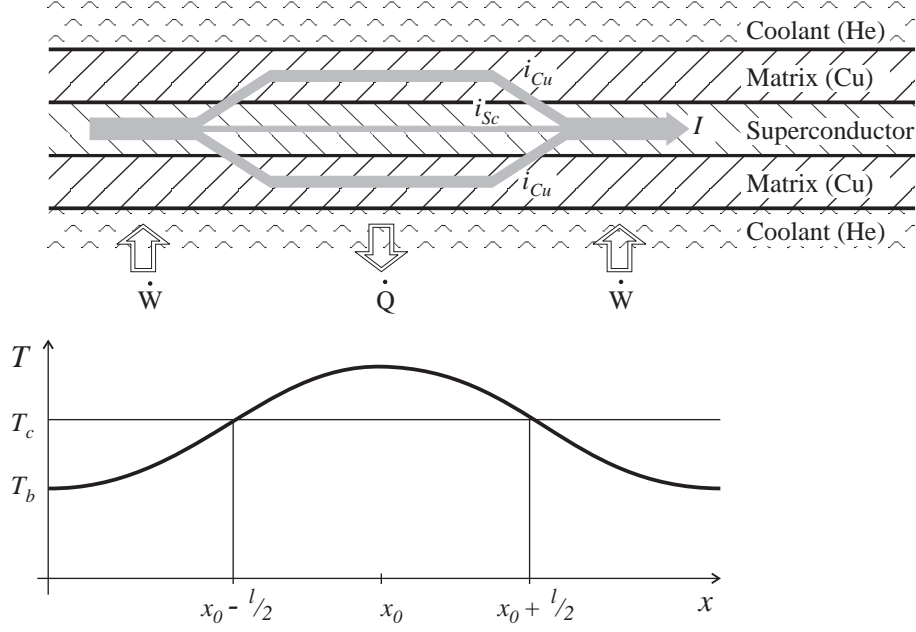


Figure 2.4: Heat balance in a quenching mono-filamentary strand

$$f = \frac{A_{Cu}/A_{Sc}}{1 + A_{Cu}/A_{Sc}} \quad (2.3)$$

considers the copper-matrix fraction of the wire.

The current entirely flows in the superconductor with a density

$$J_{Sc} = \frac{i_{Sc}}{(1 - f) \cdot A}. \quad (2.4)$$

Wire motions in the magnetic field, cracking epoxy, and eddy currents generate heat. Fig. 2.4 shows a resistive section of a mono-filamentary strand in a superconducting cable. The origin of the quench is marked with x_0 .

The thermal energy varies along the strand because of the heat flow. Close to the critical surface some flux in the superconducting strand starts moving. The changing total flux through the superconductor induces an electrical field. The resistances of the flux flow and of the matrix act in parallel. The so called current-sharing model states that the superconductor carries as much current as possible up to the critical current density. Any additional current flows through the matrix. Due to the finite resistance of copper, heat Q is generated in the matrix where the current is passing.

The whole conductor is cooled by the surrounding helium. All energy variations result in a local change of thermal energy. In a piece of conductor of length dx yields the heat balance

$$c_p(T) \frac{\partial T}{\partial t} = \frac{\partial}{\partial x} \left(\lambda(T) \frac{\partial T}{\partial x} \right) + Q(T) + g(t, x) - W(T). \quad (2.5)$$

Specific heat c_p , thermal conductivity λ , Joule heating Q , and energy absorbed by the coolant W determine the change in temperature. The cooling of the conductor depends on the temperature difference and the heat transfer coefficient, which varies with temperature and cooling conditions.

Both, cooling and heat capacity of the conductor determine the stability against temperature disturbances. The heat propagates with a certain velocity along the conductor which is included in the term g . Its extension in space and time and the temperature distribution will determine whether the zone of disturbance grows or decreases. The balance between generated and removed heat defines the length of the 'minimum propagation zone'

$$l_{MPZ} = \sqrt{\frac{2 \cdot \lambda (T_c - T_b)}{J^2 \cdot \rho}}. \quad (2.6)$$

with T_c the critical temperature of the superconductor and T_b the bath temperature. This normal zone will expand for $l > l_{MPZ}$ and will shrink for $l < l_{MPZ}$.

Complete cryogenic stability of a superconductor is guaranteed if cooling will always dominate over heat generation. A coil then can basically not quench provided enough coolant is available. But full cryogenic stabilisation tends to be uneconomic for magnets with small apertures, like accelerator magnets. Such magnets have to be protected against irreversible damage by overheating of the conductor, the insulation materials and further structural materials. Once a normal zone has started to grow it will continue as long as the current density and the magnetic field are high enough.

The low heat conductivity of the insulation and the latent heat of the helium in the cable results in slow propagation to neighbour turns. Therefore the normal zone will propagate dominantly along the cable.

Table 2.1: Typical properties of copper and niobium-titanium at 10 K

Property	Unit	Copper	NbTi
Electrical Resistivity ρ	Ωm	$3 \cdot 10^{-10}$	$6 \cdot 10^{-7}$
Specific Heat c_p	$\text{J} \cdot \text{kg}^{-1} \cdot \text{K}^{-1}$	0.84	4.3
Thermal Conductivity λ	$\text{W} \cdot \text{m}^{-1} \cdot \text{K}^{-1}$	7000	0.5
Density δ	$\text{kg} \cdot \text{m}^{-3}$	8960	6630

Above the critical temperature T_{c2} , the electrical resistivity of niobium-titanium becomes three magnitudes higher than that of copper [11]. Table 2.1 compares the material properties of copper and niobium-titanium just above the critical temperature of the superconductor.

The voltage across the resistive section between $x_0 - l/2$ and $x_0 + l/2$ (Fig.2.4) is

$$u = i_{Cu} \cdot \frac{\rho_{Cu} \cdot l}{A_{Cu}} = i_{Sc} \cdot \frac{\rho_{Sc} \cdot l}{A_{Sc}}. \quad (2.7)$$

With $\alpha = A_{Cu}/A_{Sc}$, the copper to superconductor ratio, yields for the current in the copper matrix

$$i_{Cu} \approx \frac{6 \cdot 10^{-7}}{3 \cdot 10^{-10}} \cdot \alpha \cdot i_{Sc} = 2 \cdot 10^3 \cdot \alpha \cdot i_{Sc}, \quad (2.8)$$

whereas the current through the superconducting filament can be neglected. In a quenched superconductor section almost all heat

$$Q = \int_{t=0}^{\infty} \frac{\rho_{Cu}(T, B) \cdot l}{A \cdot f} \cdot i^2(t) \cdot dt. \quad (2.9)$$

is generated in the copper matrix. For the dissipated energy in the superconducting strand

$$Q = l \cdot \int_{T_1}^{T_2} [\delta_{Cu} \cdot c_{pCu}(T) \cdot A \cdot f + \delta_{Sc} \cdot c_{pSc}(T) \cdot A \cdot (1 - f)] \cdot dT, \quad (2.10)$$

both heat capacities of copper and niobium-titanium have to be considered.

The increase in temperature can be calculated under adiabatic conditions for a given time interval dt by combining the energy equations Eq. (2.9) and Eq. (2.10)

$$dT = \frac{i^2(t) \cdot \rho_{Cu}(T, B)}{\delta_{Cu} \cdot c_{pCu}(T) \cdot A^2 \cdot f^2 + \delta_{Sc} \cdot c_{pSc}(T) \cdot A^2 \cdot f(1 - f)} \cdot dt. \quad (2.11)$$

Heat capacity c_p and electrical resistivity ρ are non linear functions of temperature. The electrical resistivity also changes with magnetic field.

The copper to superconductor ratio of the superconducting strands has to be chosen mainly with the magnet protection parameters. The superconductor cross section A_{Sc} is a function of magnetic field, temperature, and current density. The copper matrix stabilises the superconducting strand and reduces the hot-spot temperature in case of a quench.

2.3 Magnets in Superconducting Accelerators

Before superconductors became available, accelerator magnets used fields below 2 T. The magnetic saturation of the iron gave the economical upper limit. The TEVATRON at Fermilab and HERA at DESY have proved that magnets with superconducting coils can produce fields in the range of 5 T with sufficient safety margin. Future hadronic machines under consideration aim at even much higher fields. SSC had been designed for 6.6 T and LHC is designed for 8.4 T. The upper limit for the field in both machines is determined by a compromise between physical need and the economical limits. The energy of a synchrotron is proportional to both the field and the radius of the machine. One has the choice of having either a large radius with a more expensive tunnel and a low field with cheaper magnets, or the opposite situation. In the LHC case the machine is to be built in the existing LEP tunnel. Therefore, the beam energy of 7 TeV can only be reached with magnetic dipole fields

of about 8.4 T. This field is an ambitious goal and is certainly close to the upper physical limit that can be reached today with existing technology.

The coil configuration for accelerator magnets is chosen to obtain the field quality requirements of the machine optics. A line current

$$I(\phi) = I_0 \cdot \cos(m\phi) \quad (2.12)$$

distributed on a circular cylindrical surface as a function of the azimuthal angle ϕ generates a pure $2m$ -pole field inside the circular aperture (see Fig. 2.5).

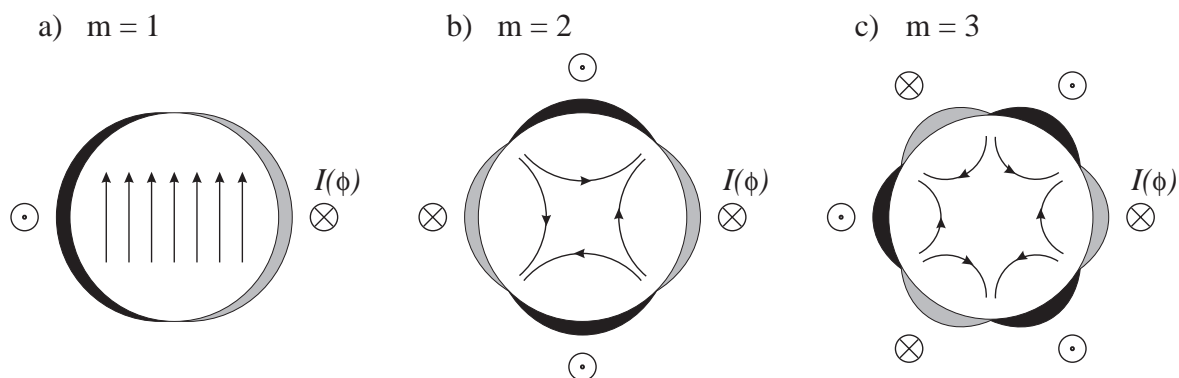


Figure 2.5: Generation of pure dipole ($m=1$), quadrupole ($m=2$), and sextupole ($m=3$) fields by current distributions

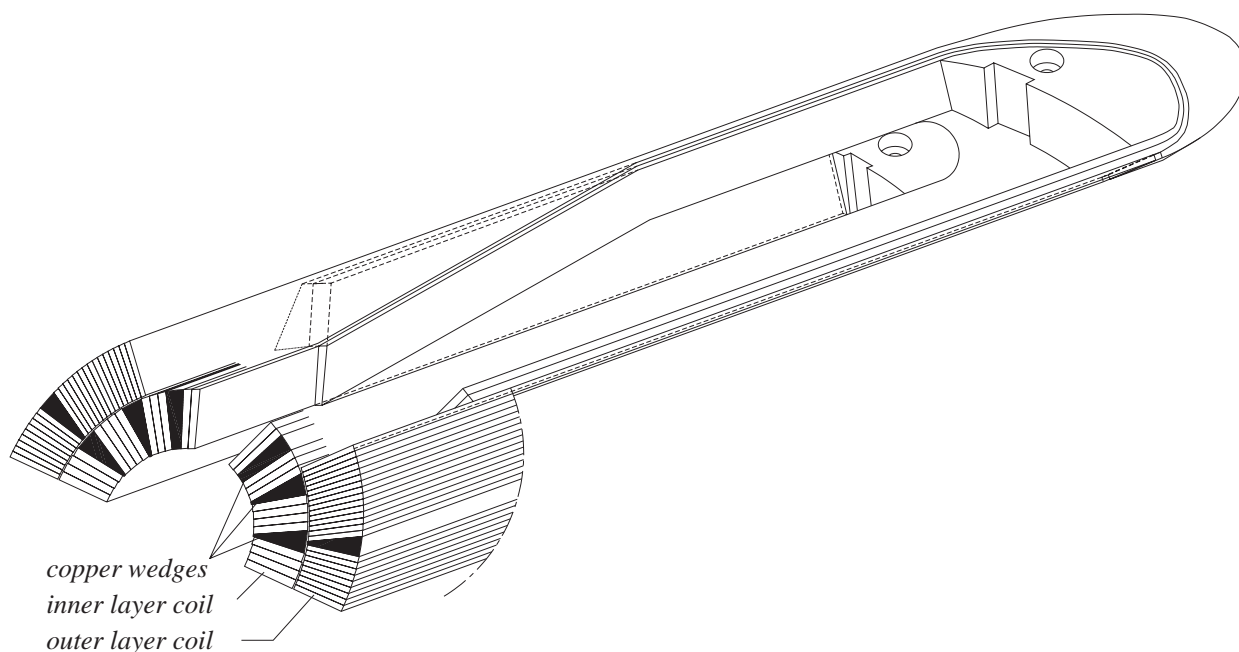


Figure 2.6: Coil cross section of a 10 m prototype dipole magnet

A pure dipole generates a homogeneous field. Pure higher order magnets (quadrupoles, sextupoles, octupoles, etc.) generate gradient fields where the field in the centre is zero.

Since a perfect $\cos(m\phi)$ current distribution can never be technically achieved, other multipole components are present which are referred to as harmonics distortions or field errors. The distortions are corrected by using tuning quadrupole-, sextupole-, and other higher-order magnets [31]. Fig. 2.6 shows the pole cross section of a two layer dipole coil.

High field magnets for the LHC are designed in the so-called *two-in-one* structure, incorporating the two beam channels in the same yoke and cryostat [30].

In order to obtain magnetic flux densities above 8 T with sufficient margins, the magnet coils, made of NbTi superconductor cables, are cooled down below 2.17 K (see Fig. 2.3).

The cable insulation has to withstand high voltages which may appear during a quench while on the other hand it should be sufficiently porous to allow permeation of helium.

Superconducting prototype magnets of the first LHC version [12] were assembled and tested. The dipole magnets of this version are 9 m long and have a design field of 10 T. Some of them are installed in the LHC Test String, which is subject of the following chapters.

After design changes, the magnets of the final version are described in the *Yellow Book* [13]. The main dipole magnets are 14.2 m long in order to reduce the flux density to 8.4 T. Using the experience accumulated in the study of the previous versions, these parameters appear to be a good compromise between an industrially achievable dipole length and aperture diameter.

Chapter 3

The LHC Test String

The superconducting accelerator magnets in the LHC machine are grouped in half-cells, composed of one main lattice quadrupole and three main dipoles. Each octant contains 23 cells in which all main dipole magnets are powered in series. During operation each LHC main dipole stores an magnetic energy of about 8 MJ. In case of quench a fast energy dump has to be performed. To de-excite the dipole magnets in an octant ($L = 23 \cdot 6 \cdot 0.108 \text{ H} \approx 15 \text{ H}$) after a quench in less than one second through an external dump resistor would require a dump resistance of about $75 \text{ } \Omega$. At a current level of 12.4 kA, a voltage across the dump resistor of $75 \text{ } \Omega \cdot 12.4 \text{ kA} = 930 \text{ kV}$ would appear. Hence, dumping the stored magnetic energy after a quench in an external resistor is impossible. The superconducting magnets are designed to be able to dissipate their stored energy into the cryo-system through the magnet coils.

In the first design proposal for magnet protection [12] it was foreseen to protect each complete half-cell by a set of diodes across it. A similar magnet protection scheme was already used for the *Accelerator System String Test* (ASST) at SSC. Quench experiments on the ASST configuration have shown unexpected high voltages up to 1700 V between coil and ground. Also a non-uniform energy dissipation in the ASST half-cell magnets was observed, closely related to the *RRR* of the superconducting cables and non-uniform heater firing [3][20][27]. Magnets with a $RRR \approx 100$ absorbed about twice the energy of magnets with a $RRR \approx 170$.

With an inductance of about 75 mH per dipole and a nominal current of 6500 A, the stored magnetic energy in each SSC magnet is about 1.6 MJ. Since the LHC magnets will be operated at higher fields and at higher current levels, the stored energy is about five times higher than in the SSC magnets.

Special arrangements were necessary in order to avoid non uniform energy distributions and high voltage peaks in the LHC half-cell. Auxiliary by-pass leads, foreseen to power correction magnets, have been adapted to connect one diode parallel to each dipole magnet in the LHC Test String. They help to limit the magnet voltages in one direction only to the forward voltages of the by-passing diodes and permit an individual internal current decay in the quenched magnet.

Many experiments on the superconducting dipole magnets (heater provoked quenches and magnet training with and without energy extraction) can be only performed efficiently

on the magnet bench¹ and not on the LHC Test String. The influence of other magnets is not given and so does not effect the measurements.

To operate the LHC machine, experience has to be attained in powering and de-exciting of a serial chain of superconducting magnets. The possibility is given for checking the reliability of the quench protection system. Knowledge about inter-magnet quench propagation has to be obtained in order to minimise the possibility of quenching adjacent magnets due to heat transport through the coolant and through the copper stabilised bus-bars. Studies on quench heater performance and the influence of RRR have been performed in order to optimise the quench protection system.

From the cryogenics point of view the cooling performance of the string, the pressure and temperature development in case of a quench, the recovery after magnet quenches, and the heat in-leaks have been studied.

Weak points in the mechanical structure due to thermal and electrical cycles and material fatigue can be found out after more than two years operation of the LHC Test String.

This chapter gives an overview about the main components of the LHC Test String. The quench protection system is discussed in detail and considerations for dimensioning the external discharge circuit are given. The cryogenic system is discussed briefly.

3.1 The LHC Test String Configuration

Fig. 3.1 shows the assembly of the LHC superconducting magnet string, composed of a superconducting quadrupole magnet *QP*, located in the Short Straight Section *SSS*, three superconducting bending dipole magnets *MB1*, *MB2*, *MB3*, a String Feed Box *SFB*, and a String Return Box *SRB*. The electrical main circuit is depicted in Fig. 3.2. It shows the physical location of the magnets and protection elements in the LHC Test String. The twin-aperture structure is represented by the two rows of in series connected magnets. All protection diodes are located in the cold mass of the *SSS*. Since the corrector magnets were not installed in the string, the auxiliary bus-bars have been used to connect one diode parallel to each magnet. This arrangement reduces high voltages to ground and permits a uniform distribution of the dissipated energy in case of a quench.

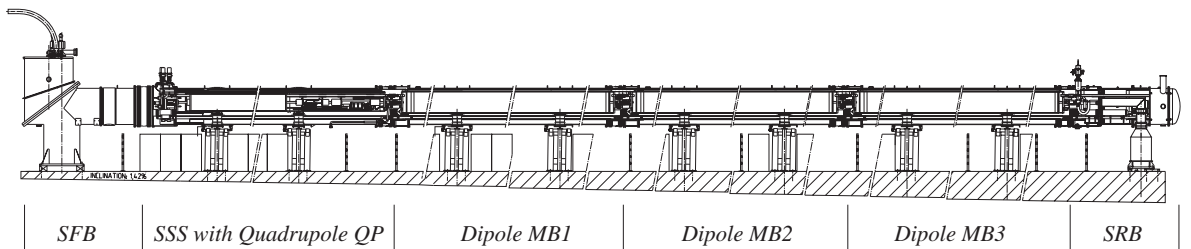


Figure 3.1: Assembly of the LHC Test String containing one superconducting quadrupole and two superconducting dipole magnets used for STRING RUN 2

¹Test facility for single magnets

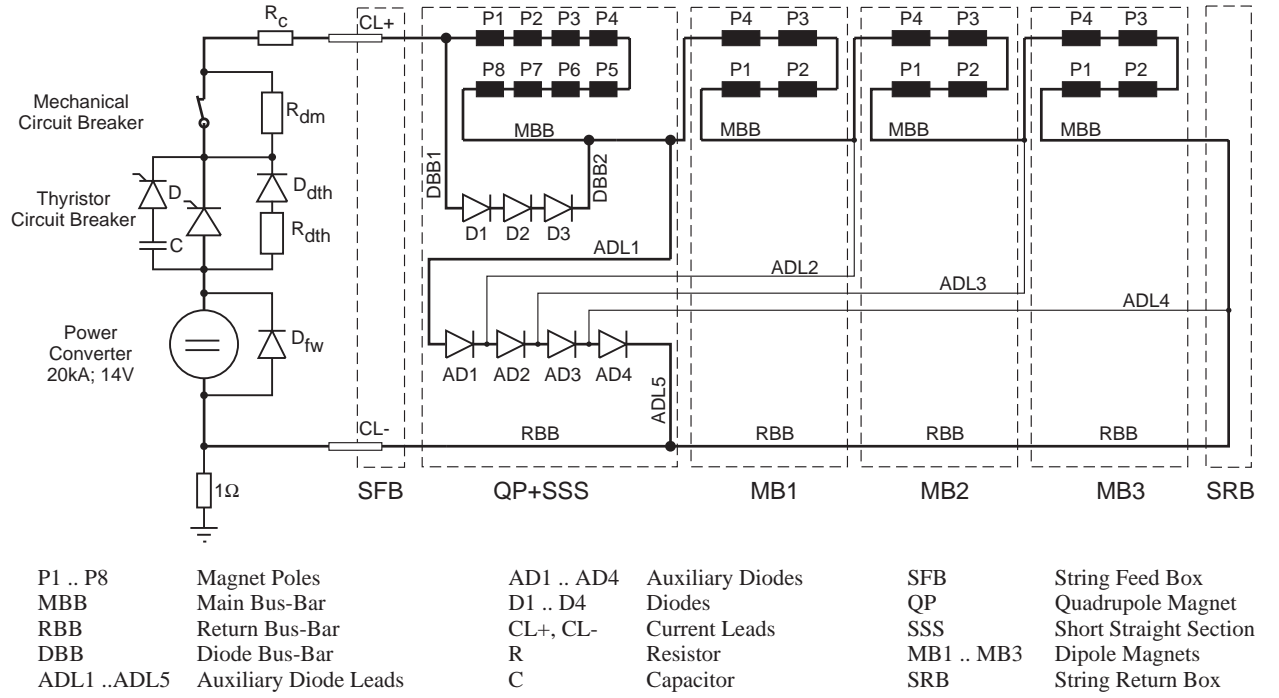


Figure 3.2: Principle electrical scheme of the LHC Test String without quenching the magnets

3.2 Main Components of the LHC Test String

The main components described in this section belong to the LHC Test String used for experiments in STRING RUN 2A and 2B. The magnet design corresponds to the specification of the pink book [12].

3.2.1 Main Dipole Magnets

The superconducting dipole magnets consist mainly of three main parts (Fig. 3.3):

- the *cold mass* composed of the superconducting coils, non-magnetic collars, iron yoke, and a shrinking cylinder,
- the *thermal insulation* to minimise heat radiation, and
- the *vacuum vessel* to provide the insulation vacuum in order to reduce heat inleaks.

Cold Mass

Superconducting coils: The superconducting coils are formed of two shells, as shown in Fig. 2.6, made with keystones cables of same width but of different thickness, resulting from the desired grading of current density for optimum use of the superconducting material. The copper to superconductor ratio in the strands, different in the inner and outer layer, results from stability and protection considerations. The conductors of each coil run parallel to the beam line over the longest part of the magnet and are guided across only the relatively short coil heads. Wedge-shaped copper spacers are inserted between blocks of conductors to produce the desired field quality and to ap-

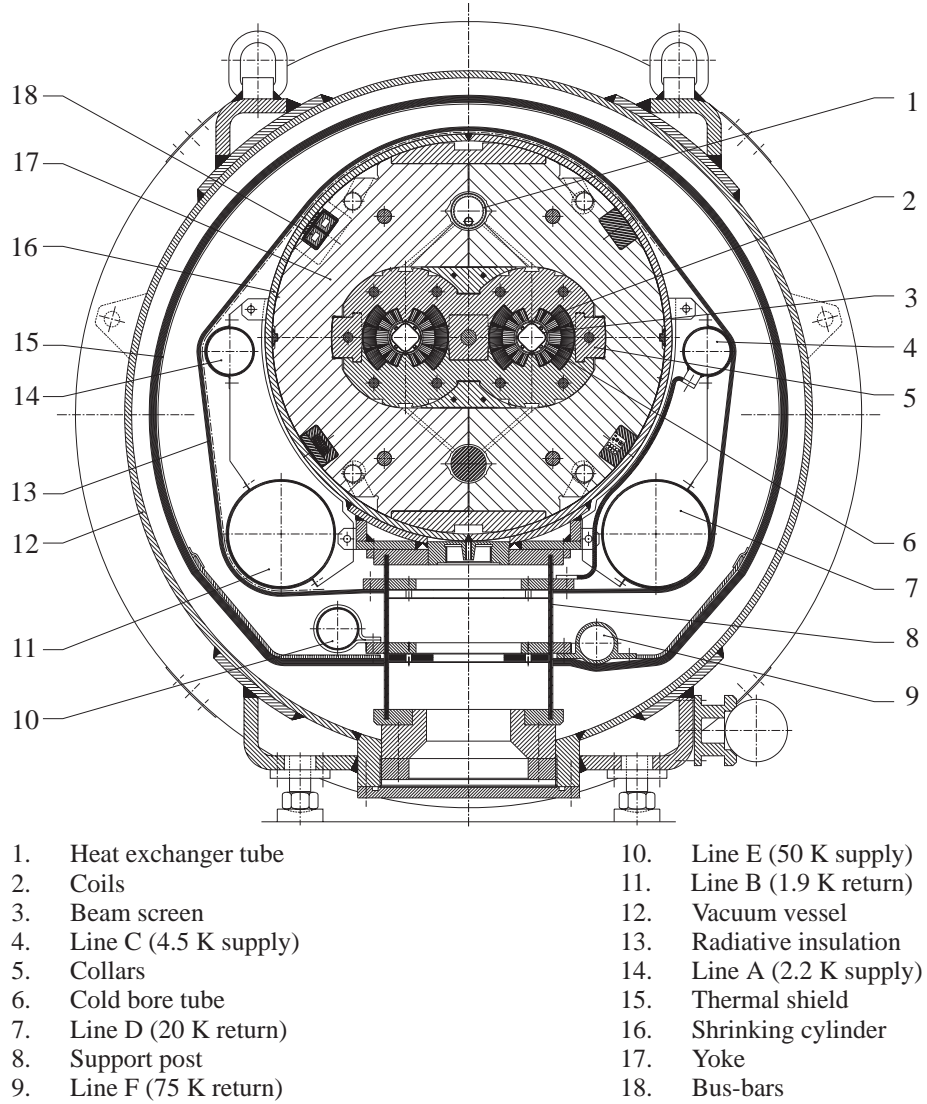


Figure 3.3: Cross section of main lattice dipole (LHC Version 1)

proximate a quasi-circular coil geometry, compensating for the insufficient key-stoning of the cables. These spacers are continued at the coil ends by saddle-shaped pieces which allow the winding and the mechanical confinement of the cables.

The cables are insulated by a half-overlapped layer of polyimide tape with a thickness of $25\ \mu\text{m}$ and one layer of $125\ \mu\text{m}$ thick glass-fibre adhesive, already pre-impregnated by epoxy resin with spaces of $2.5\ \text{mm}$ between successive turns, as shown in Fig. 3.4. The spacing increases the porosity of the coil by forming helium flow channels without affecting the mechanical support between the turns. Helium comes into direct contact with a large proportion of the cable surface and penetrates the interior of the cable. The insulation to ground is composed of superposed polyimide film layers and includes the quench protection heaters (Fig. 3.11).

Collars, iron yoke, and shrinking cylinder: The electro-magnetic forces become extremely high in the superconducting magnets. Even small sudden movements of the superconducting

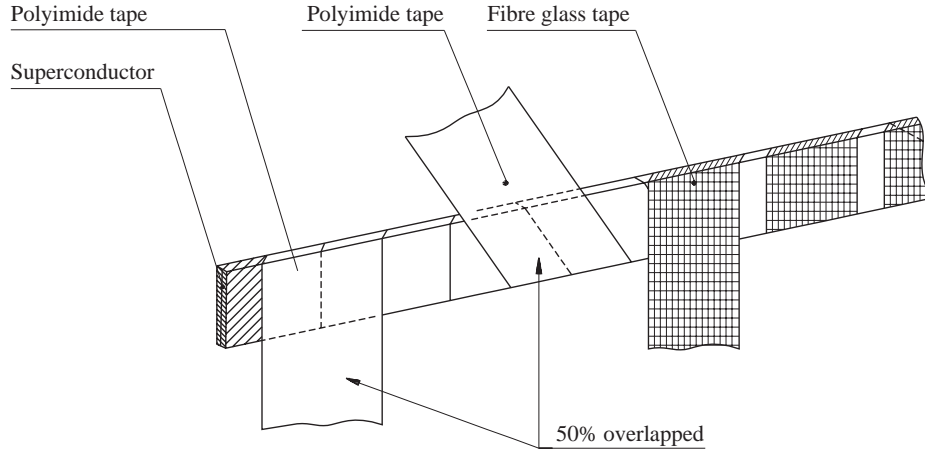


Figure 3.4: Insulation of the LHC cable used for Version 1 prototype dipole magnets, consisting of polyimide and glass-fibre tape.

cable or cracking of the insulation may generate enough heat to raise local parts of the superconductor above the critical temperature due to the very low heat capacity [22].

A mechanical support structure around the superconducting magnet coils has to ensure proper control of the Lorentz forces. The force containment structure consists of coil clamping elements, the collars, the iron yoke, and the shrinking cylinder. It produces the necessary azimuthal pre-compression in the coils and prevents tensile stresses from arising in the coils under the action of the electro-magnetic forces.

The shrinking cylinder is at the same time the outer shell of the helium tank, while the inner wall forms the beam vacuum chamber. The assembly between these two cylindrical walls, the cold mass, is kept at 1.9 K.

The cold mass is closed at the ends by covers, welded to the shrinking cylinder. The covers have passages for the beam vacuum chambers, a heat exchanger tube, and two pipes containing the main and the auxiliary electrical connections. The cover on the magnet electrical connections side (front end) also leaves a passage for a pipe leading to a pressure relief valve located in the junction space between the magnet units. All these pipes are welded to the end covers.

Thermal Insulation

In order to reduce the heat load on the low-temperature cryogenic system, the heat generated by the proton beams and the effect of beam induced currents in the resistive wall is intercepted by a shield. This is inserted within the vacuum chamber and is cooled by helium circulating in a range between 5 and 20 K (Fig. 3.3).

Two thermal shields are installed to minimise heat inleaks to the cold mass at 1.9 K. The inner radiation screen uses multi-layer superinsulation operating between 5 and 10 K, enclosing the cold mass. The outer thermal shield, which intercepts the largest fraction of incoming heat at 50 to 70 K, consists of a self-supporting screen covered with multi-layer superinsulation.

Support posts are made of composite material to carry the cold mass and permit their adjustment in the cryostat.

Vacuum Vessel

The outer vacuum vessel is a cylindrical stainless steel tube which covers the cold mass and thermal insulation. The space between the vessel and the shrinking cylinder of the cold mass is pumped to about 10^{-6} mbar.

3.2.2 Main Quadrupole Magnets

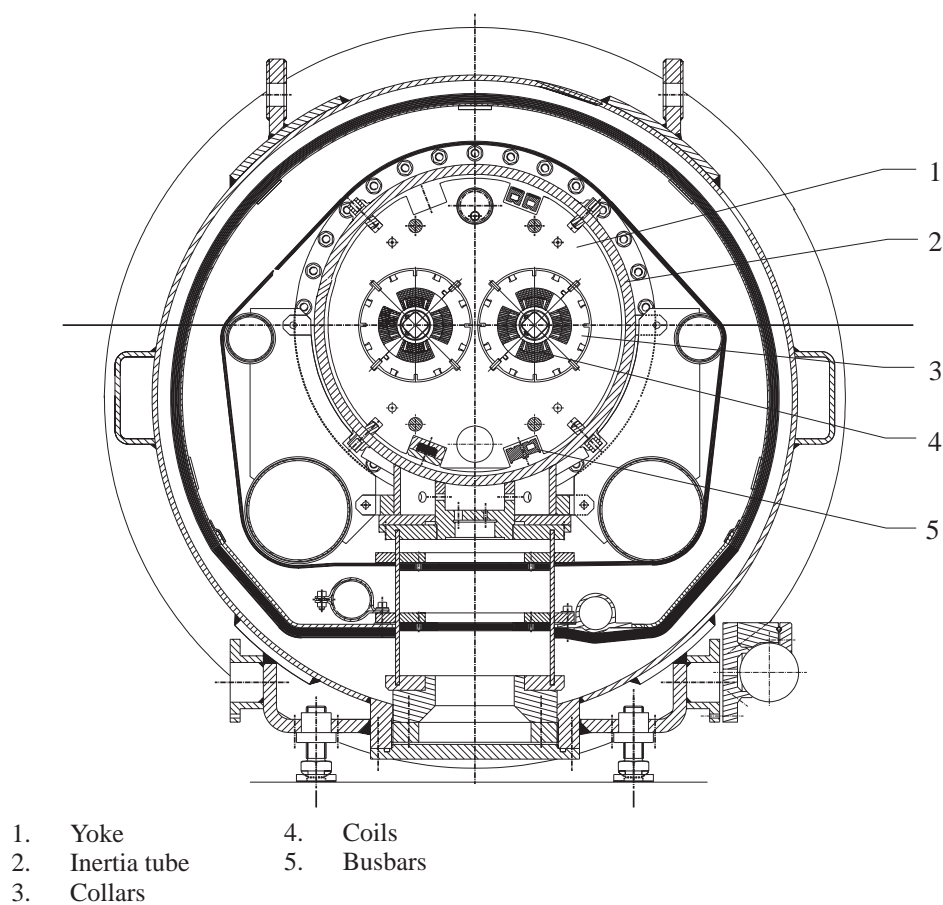


Figure 3.5: Cross section of main lattice quadrupole (LHC Version 1)

Fig. 3.5 shows the cross section of the quadrupole. The electro-magnetic design is governed by considerations similar to those for the dipole magnets. In contrast to the dipole coil design, the lattice quadrupole coils are not graded in current density. The winding of the two layers of each coil is made from the same cable in the double-pancake style. This avoids the inner layer splices which, being numerous in the quadrupole, would be a significant source of heat generation. The turn of the inner block of the conductors in the inner layer are spaced with respect to each other over the end region which avoids too high peak fields in this mechanically sensitive part of the coils. The electro-magnetic forces in the main quadrupoles

are considerably smaller than those in the main dipole magnets, which allows to contain the forces by the collar structure alone.

The cryostat of the Short Straight Section in the LHC Test String contains the twin-aperture quadrupole magnet and the protection diodes for quadrupole and dipole magnets in the half-cell. The cryostat of the Short Straight Section in the final LHC version houses the twin aperture quadrupole, two octupoles, two combined sextupole-dipole correctors, and the quench protection diodes for the quadrupoles. The magnets and the diodes are mounted in a common inertia tube with end covers, forming the cold mass and thus the helium vessel, filled with pressurised helium II at 1.9 K [12][13].

3.2.3 String Feed Box and String Return Box

The principal components of the cryogenic system for the LHC Test String are the String Feed Box (SFB), the String Return Box (SRB), and the saturated superfluid helium circuit coupled to the pressurised (1 bar) superfluid helium bath through a corrugated heat exchanger tube.

The SFB contains the main cryostat, used to distribute the liquid helium to different circuits in order to perform refrigeration and transient phases, i.e. cool-down and warm-up. The cryostat is equipped with several pairs of current leads for powering the superconducting magnets (15 kA) and correction magnets (50, 250, 500, and 1600 A). Furthermore, the SFB contains a gas counter-flow heat exchanger, a liquid/gas heat exchanger, a very low pressure liquid sub-cooler, as well as the instrumentation and valves necessary for the cryogenic operation [2].

The SRB is the end module of the LHC Test String and is used to close the cryogenic loops as well as the insulation vacuum. A vacuum barrier in the SRB is installed in order to validate the heat inleaks and to test the insulation behaviour.

3.2.4 Power Converter

The power converter is a 12-phase thyristor-controlled rectifier with free-wheeling diodes and a passive filter. It supplies the LHC Test String with DC current up to 20 kA at a voltage of up to 14 V. The current measurement is with a high precision DCCT and a current stability of better than 0.01 % is achieved [28].

3.2.5 Discharge Circuit

A thyristor circuit breaker and a mechanical circuit breaker are connected in series (see Fig. 3.2). The thyristor circuit breaker is composed of six parallel thyristors with forced commutation while the mechanical switch consists of six industrial fast-switching d.c. circuit breakers in parallel [28]. Dump resistors are connected parallel to each circuit breaker.

Slow discharge experiments on the LHC Test String are performed by opening the thyristor circuit breaker and switching off the power converter. The stored energy in the magnet dissipates in the dump resistance, connected parallel to the thyristor circuit breaker.

An emergency arrangement was judged necessary since at low current levels the quench heaters become less effective. At currents below 1.5 kA they may not force anymore quenching the superconducting magnets. In order to perform a secure de-excitation from low current levels, the dump resistance has been defined within the following boundaries.

On one hand a de-excitation of the LHC Test String has to be performed *fast* enough to avoid overheating of the auxiliary bus-bar leads.

On the other hand the de-excitation has to be *slow* enough in order to not exceed the maximum reverse voltage of by-pass diodes parallel to the still superconducting magnets.

Both, mechanical and thyristor circuit breaker open in case of quench.

Dimensioning of the dump resistor in parallel to the thyristor switch:

The dump resistor across the thyristor circuit breaker is dimensioned for slow discharge experiments. During the de-ramping procedure the magnets are expected to remain superconducting. The time constant of about 100 s corresponds to the time constant specified in the LHC machine which causes a current decay rate of about 120 As^{-1} . It is long enough to avoid quench back (see section 2.2.1) in the superconducting magnet coils. Experiments on LHC superconducting prototype magnets have shown the effect of quench back at current rates higher than 150 As^{-1} .

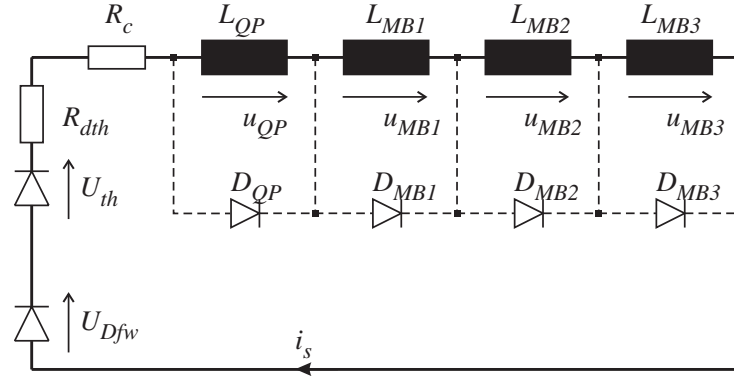


Figure 3.6: Simplified electrical scheme for a slow discharge of the LHC Test string

The dump resistance R_{dth} in Fig. 3.6 is deduced from the differential equation

$$(L_{QP} + L_{MB1} + L_{MB2} + L_{MB3}) \cdot \frac{di_s(t)}{dt} + (R_c + R_{dth}) \cdot i_s(t) = U_{Dfw} + U_{th} \quad (3.1)$$

with the maximum current decay rate at $t = 0$.

Initial string current	$i_s(0) = I_0$	=	12400 A
Maximum current decay rate	$\left(\frac{di_s(t)}{dt}\right)_{max}$	=	-150 As^{-1}
Diode forward voltages	U_f	=	$U_{Dfw} + U_{th}$
		=	0.6 V + 0.6 V = 1.2 V
Inductance	L	=	$L_{QP} + L_{MB1} + L_{MB2} + L_{MB3}$
		=	8 mH + 57 mH + 57 mH + 57 mH = 179 mH
Cable resistance	R_c	=	0.16 m Ω .

$$R_{dth_{max}} = \frac{U_f - L(di_s/dt)_{max}}{I_0} - R_c \approx 2.3 m\Omega. \quad (3.2)$$

Higher values of R_{dth} may lead to quenches caused by di/dt . In order to have about the same discharge time constant than in the LHC machine, R_{dth} was set to 0.7 m Ω .

Dimensioning of the dump resistor in parallel to the mechanical switch:

The following procedure describes the dimensioning of the dump resistances.

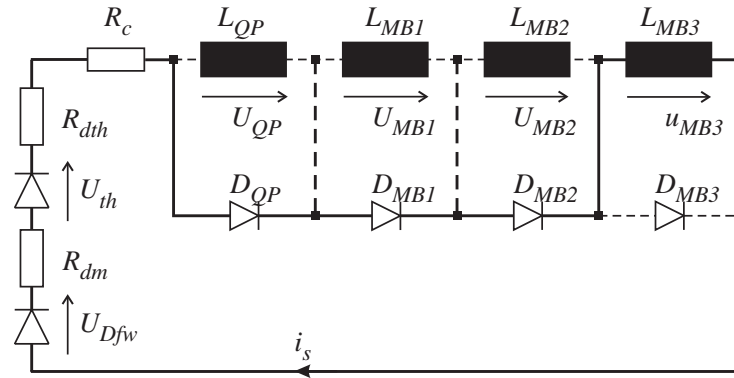


Figure 3.7: Electrical circuit to calculate the maximum reverse voltage across the by-pass diodes in case of a discharge

- *Dimensioning the dump resistance with respect to the maximum diode reverse voltage:* Danger for a protection diode is given in case of a quench, if the heaters in only one magnet (e.g. MB3 in Fig. 3.7) are not efficient to drive the magnet coils normal. The inductive voltage across the remaining superconducting magnet must not exceed the permissible reverse voltage $U_{rev} = 120 \text{ V}$ (see Table 3.1) of the parallel connected protection diode. At $t = 0$ the maximum inductive voltage across the dipole (e.g. MB3) becomes

$$u_{MB3} = L_{MB3} \cdot \frac{di_s}{dt} = -U_f - i_s \cdot (R_{circ} + R_{dm}). \quad (3.3)$$

With

Initial string current	$i_s(0)$	=	$I_0 = 12400 \text{ A}$
Diode forward voltages	U_f	=	$u_{QP} + u_{MB1} + u_{MB2} + U_{th} + U_{Dfw}$
		\approx	$1.2 \text{ V} + 1.2 \text{ V} + 1.2 \text{ V} + 0.6 \text{ V} + 0.6 \text{ V} \approx 4.8 \text{ V}$
Inductance	L_{MB3}	=	57 mH
Circuit Resistance	R_{circ}	=	$R_{dth} + R_c \approx 0.7 + 0.16 \approx 0.86 \text{ m}\Omega$

The maximum value for the dump resistance R_{dm} gives

$$R_{dm_{max}} = -\frac{U_f + U_{rev}}{I_0} - R = -\frac{4.8 \text{ V} - 120 \text{ V}}{12400 \text{ A}} - 0.86 \text{ m}\Omega \approx 8.4 \text{ m}\Omega. \quad (3.4)$$

Higher values of R_{dm} extend the time constant of the decaying current and hence increase the reverse voltage in such a case of emergency.

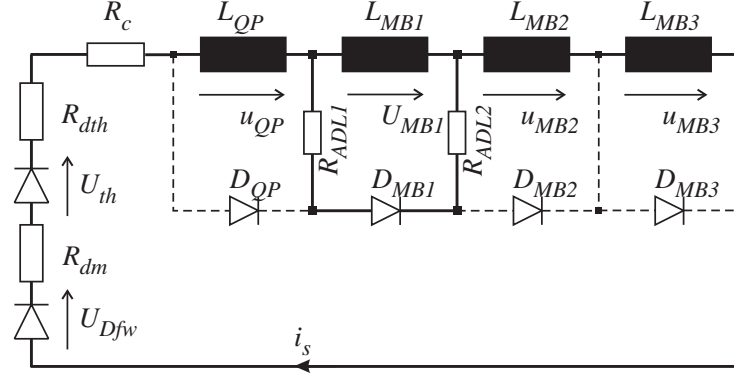


Figure 3.8: Electrical circuit to estimate the maximum temperature in the small cross-sectional auxiliary bus-bar in case of emergency

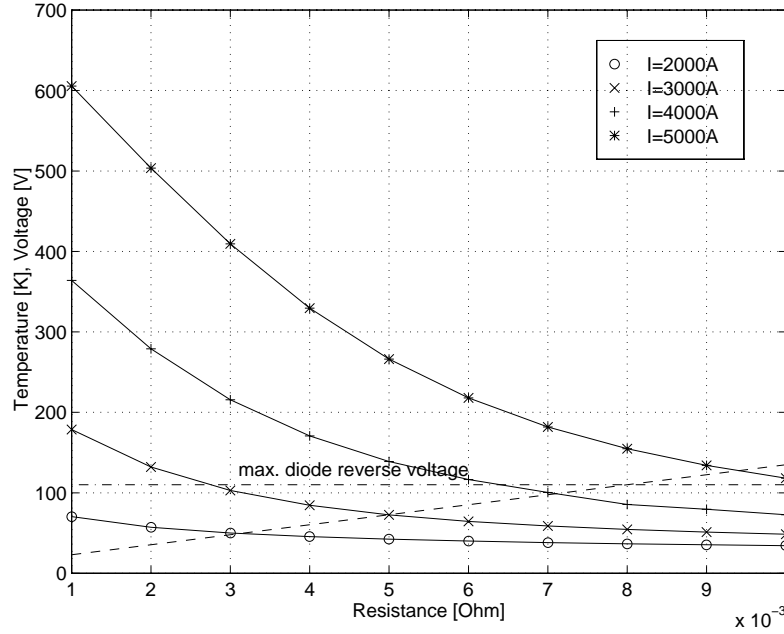


Figure 3.9: Auxiliary bus-bar temperature versus dump resistance R_{dm} with initial quench currents as parameter

- *Dimensioning the dump resistance with respect to the maximum temperature in the auxiliary bus-bars:* If the quench heaters only in the quenched magnet become effective, the

decaying current will be by-passed over the diode connected parallel to this magnet. The other magnets are assumed superconducting during the de-excitation (see Fig. 3.8). Due to the absence of liquid helium or by exceeding the critical current density, the superconductor in the auxiliary bus-bars may become resistive. Most of the by-passed current flows through the stabilising copper section. The auxiliary bus-bars *ADL1* and *ADL5* have about 10 times more copper section than *ADL2* to *ADL4*. Only the auxiliary bus-bars with small copper cross sections have been considered for calculating the resistance and temperature rise, since they constitute a weak part in the magnet protection scheme.

The graph in Fig. 3.9 shows the influence of the external dump resistance on the auxiliary bus-bar temperature. The higher the dump resistance across the mechanical circuit-breaker the lower becomes the end temperature of the auxiliary bus-bar due to the faster current decay [14].

In the following a quasi-analytical method is presented to estimate the auxiliary bus-bar temperature as a function of the external dump resistance $R_d = R_{dm} + R_{dth}$. By considering adiabatic conditions, the temperature rise in the resistive auxiliary bus-bars is governed by the heat balance equation

$$i^2(t) \cdot \frac{\rho(T)}{A_{Cu}} \cdot dt = \delta_{Cu} \cdot A_{Cu} \cdot c_{pCu}(T) \cdot dT. \quad (3.5)$$

Since the auxiliary bus-bars have a copper to superconductor ratio of 19:1, the superconductor cross-section can be neglected for the calculation.

The parameters $\rho(T)$, $c_{pCu}(T)$, and δ_{Cu} are related to copper. Hence, after separating time and temperature dependent parameters and integrating Eq. (3.5) yields

$$\int_{t=t_1}^{t_2} i^2(t) \cdot dt = A_{Cu}^2 \cdot \delta_{Cu} \int_{T=T_1}^{T_2} \frac{c_{pCu}(T)}{\rho(T)} \cdot dT. \quad (3.6)$$

Tables and graphs for the right hand integral in Eq. (3.6) exist (see Fig. 3.10). Only the characteristic of the current decay has to be determined in order to evaluate the maximum bus-bar temperature. According to Fig 3.8 the string current $i_s(t)$ is calculated by solving the differential equation

$$L \cdot \frac{di_s(t)}{dt} + R(T) \cdot i_s(t) = -U_D \quad (3.7)$$

with $L = L_{QP} + L_{MB2} + L_{MB3}$ as the actual inductance, $R(T) = R_c + R_{dth} + R_{dm} + R_{ADL2}(T)$ as the overall circuit resistance, and $U_D = U_{Dfw} + U_{Dth} + U_{DMB1}$ as the diode forward voltages in the circuit.

By assuming constant temperature T , which is valid for short iteration intervals, the Laplace transform applied to Eq. (3.7) gives

$$L [s \cdot I(s) - I_0] + R(T) \cdot I(s) = -U(s). \quad (3.8)$$

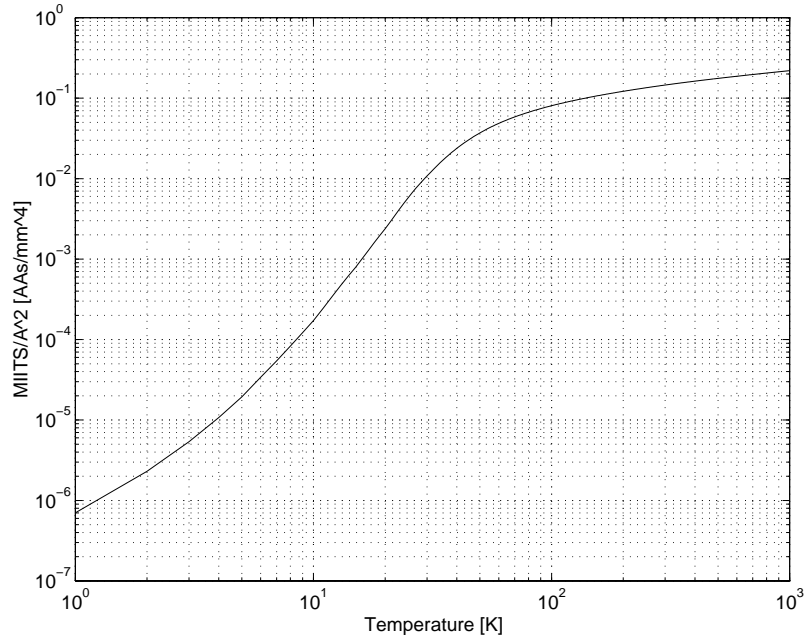


Figure 3.10: $\int i^2 dt$ for 1 mm² cross-section area versus temperature for copper ($RRR = 100$)

After each iteration step the temperature and further the resistance $R(T)$ have to be updated. For the current follows

$$I(s) = \frac{I_0 \cdot L}{R(T) + s \cdot L} - \frac{U}{s [R(T) + s \cdot L]} \quad (3.9)$$

or expressed in partial fractions

$$I(s) = \frac{I_0}{R(T)/L + s} - \frac{U}{R(T) \cdot s} + \frac{U}{R(T) \cdot [R(T)/L + s]}. \quad (3.10)$$

Applied the inverse Laplace transform to the string current leads back to the current in time domain

$$i_s(t) = A + B \cdot e^{-t/\tau} \quad (3.11)$$

with the expressions

$$A = -U/R(T), \quad (3.12)$$

$$B = U/R(T) + I_0, \quad (3.13)$$

$$\tau = L/R(T). \quad (3.14)$$

The left-hand integral in Eq. (3.6) becomes

$$\begin{aligned}
 & \int_{t=t_1}^{t_2} i_s^2(t) \cdot dt \\
 &= \int_{t=t_1}^{t_2} \left[A^2 + 2 \cdot A \cdot B \cdot e^{-t/\tau} + B^2 \cdot e^{-2t/\tau} \right] \cdot dt \\
 &= A^2 \cdot t - 2 \cdot \tau \cdot A \cdot B \cdot e^{-t/\tau} + 2 \cdot \tau \cdot A \cdot B - \frac{B^2 \cdot \tau}{2} \cdot e^{-2t/\tau} + \frac{B^2 \cdot \tau}{2} \quad (3.15)
 \end{aligned}$$

During the time interval $\Delta t = t_2 - t_1$ the temperature in the auxiliary bus-bar rises from T_1 to T_2 . The accuracy in calculating Eq. (3.15) can be increased by decreasing the time interval Δt and updating the material parameters to evaluate the bus-bar resistance $R(T)$ as a function of temperature.

The graphs in Fig. 3.9 are calculated with the following parameters:

Initial string current	$i_s(0)$	=	$I_0 = 12400 \text{ A}$
Diode forward voltage	U	=	$U_{Dfw} + U_{th} + U_{MB1} = 1.2 \text{ V}$
Inductance	L	=	$L_{QP} + L_{MB2} + L_{MB3} = 122 \text{ mH}$
Length of aux. diode line	l_{ADL2}	=	1.25 m
Aux diode line cross section	A_{ADL2}	=	27 mm^2
Aux. diode line resistance	$R_{ADL2}(T)$	=	$\frac{\rho_{Cu}(T) \cdot l_{ADL2}}{A_{ADL2}}$
Cable resistance	R_c	=	$0.16 \text{ m}\Omega$
Dump resistance (mech. switch)	R_{dm}	=	$1 \dots 10 \text{ m}\Omega$
Dump resistance (thyr. switch)	R_{dth}	=	$0.7 \text{ m}\Omega$
Resistance	$R(T)$	=	$R_c + R_{dth} + R_{dm} + R_{ADL2}(T)$

The upper value of the dump resistance $R_{dm} = 8 \text{ m}\Omega$ is fixed by the resistance calculated for limiting the diode reverse voltage U_{rev} to a safe level below 120 V. The lower limit of R_{dm} is governed by the minimum quench current of magnets with heaters (Fig. 5.35) and the maximum expected auxiliary bus-bar temperature. Experiments on the LHC magnet bench have shown that quench heaters are efficient at quench currents down to about 4 kA. Below 4 kA, coil sections may remain superconducting after firing the heaters. In order to keep the maximum temperature in the auxiliary bus-bars as small as possible, the dump resistance is fixed to $R_{dm} = 8 \text{ m}\Omega$ for the experiments on the LHC Test String.

3.3 Magnet Protection System

The magnet protection of the main lattice dipole and quadrupole magnets is based on the so-called *cold diode* concept [13]. Since there is no practical way to extract the magnetic energy from a quenching magnet which is connected in series with other superconducting magnets, each magnet must be independently protected. This is achieved by diodes which serve as a by-pass around the quenching magnets and strip heaters mounted on the outer shell of each magnet coil.

The quench detection system for the LHC Test String is composed of isolation amplifier circuits for voltage measurement and quench detection, an interlock matrix, and a programmable logic controller (PLC).

3.3.1 Cold Diodes

Diodes located inside the cryostat reduce heat loads because of the absence of additional current leads. These diodes are not easily accessible for replacement and they have to withstand the radiation generated by the beams when they are installed in the LHC machine.

In the LHC Test String, two packages of cold diodes, a triplet and a quadruplet, are situated inside the cryostat of the short straight section. The triplet is composed of three in series connected diodes which act as by-pass elements for the quadrupole in the LHC Test String. Each dipole magnet has its own by-pass diode, located in the quadruplet package. As part of the cold mass the diodes are operated at helium-II temperature. The type of diodes are different for the triplet and quadruplet (see Table 3.1). The triplet is composed of radiation resistant epitaxial diodes while diffusion diodes are used in the quadruplet.

Table 3.1: Diode parameters for triplet and quadruplet diodes

	Units	Triplet diode	Quadruplet diode
Operating temperature	[K]	1.9	1.9
Turn-on voltage	[V]	~ 1.5	~ 4.8
max. reverse voltage ²	[V]	80...120	~ 120

All protection diodes have to be able to carry a peak current of more than 12 kA decaying exponentially with a time constant of about 100 s. This requires copper heat sinks to absorb the out-pointed energy of about 1.8 MJ. Before installation the diodes were pre-tested with 15 kA and 100 s.

Under normal discharge conditions, the diode reverse voltage is about 10 V per diode. In case of a discharge after a quench it can be much higher. A rating of at least 100 V at liquid helium temperature is required.

For the LHC the diodes should be radiation resistant at liquid helium temperatures up to a dose of 50 kGy and neutron fluencies of 10^{15} neutrons per cm^2 during a period of 10 years [9].

3.3.2 Quench Heaters

The extremely high energy density of the LHC main lattice magnets, coupled with the relatively slow heat propagation of about 20 ms^{-1} along the conductor inside the winding can lead to excessive heating at the origin of the quench. Quench heater strips, located on the outer shell of each magnet coil, reduces the hot-spot problem by driving a sufficient large coil volume into the resistive state. The quench heater strips for the dipole magnets are composed of 15 mm wide and $25 \mu\text{m}$ thick stainless steel strips with polyimide insulation. Four quench heater strips are placed on the outer layer coils covers 12 turns of each pole along the entire length of the magnet (see Figures 2.6 and 3.11).

The heaters are powered by capacitor discharge. In order to keep the voltage low without losing heater efficiency, the stainless heater strips are section-wise copper clad on one side with high RRR copper of $1.5\ \mu\text{m}$ thickness, such as to alternate 25 cm. This almost halves the resistance of the strips and gives a quasi multiple spot heating along the coils. Due to subsequent conductor quenching, longitudinal spreading is almost as effective as heating over the full length [9]. Results from one-metre model tests have shown that at high magnet current a specific initial heater power of $36\ \text{kWm}^{-2}$ is sufficient to drive the outer layer coils resistive within a heater response time of less than 35 ms [18].

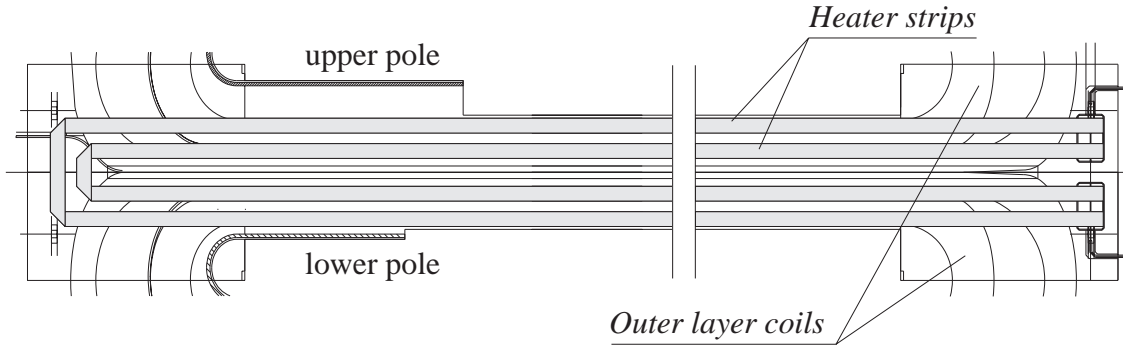


Figure 3.11: Location of stainless steel quench heater strips on the outer layer of the dipole magnet

The heater strips for the quadrupole are fabricated similar to that of the dipole. The parameters of the heater strips for the quadrupole and dipole magnets are listed in Table B.3.

Each heater power supply contains four channels composed of a capacitor battery and a thyristor switch, as shown in Fig. 3.12. The maximum charging voltage of the capacitor battery is fixed to 400 V in order to not endanger the electrical insulation during powering the quench heater strips.

To drive the outer layers in both aperture magnets resistive, even if one heater power supply fails, half of the heater strips in an aperture magnet are connected to one power supply module while the other two are connected to an other powers supply in order to have redundancy. A voltage of 400 V is sufficient to distribute enough heat to quench the outer layer coils of the quadrupole down to quench current levels of about 1.5 kA. Since the dipole is longer than the quadrupole, more energy is required to quench the outer layer coils along the whole magnet length. To avoid exceeding the permissible voltage between heater strips and ground, two power supplies of different polarity are connected in series, with a midpoint connection to ground.

3.3.3 Quench Relief Valves

The LHC Test String contains two quench relief valves, located at the front end and at the rear end of the magnet chain. Their function is to limit the generated pressure in the cold mass after a quench to a level below the specified maximum value of 20 bars.

The quench relief valves open either if the helium pressure becomes higher than the defined threshold or by receiving a logical signal from the interlock system. Taking into account that the hydraulic diameter of the valve is 50 mm and the pressure rises with about $30\ \text{bar s}^{-1}$, the valves have to open in less than 500 ms [5].

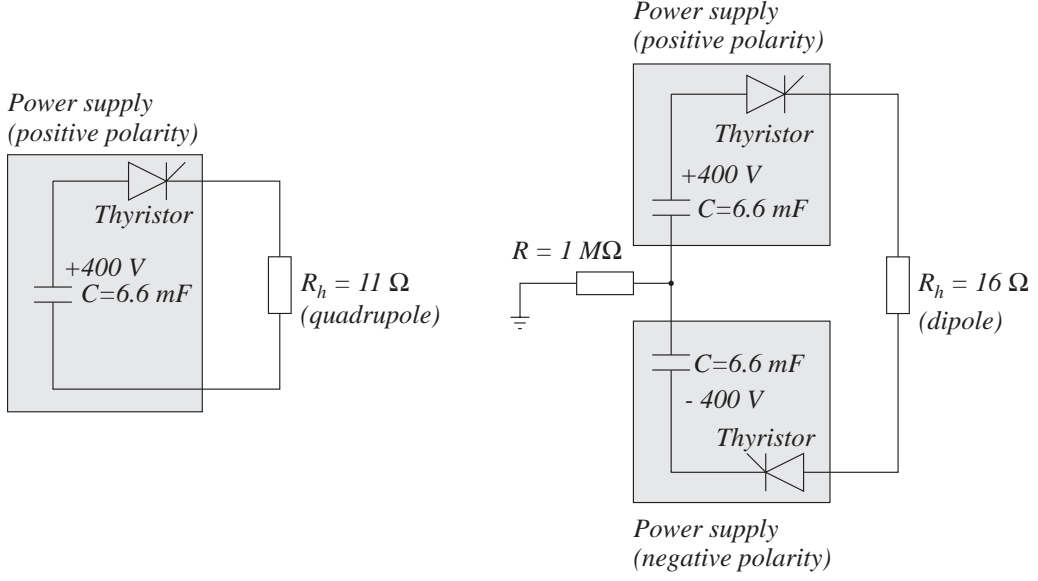


Figure 3.12: Simplified powering scheme of quench heater strips for quadrupole (left side) and for dipole (right side)

3.3.4 Quench Detectors and Interlock Matrix

A quench detector module, used for the LHC Test String, contains two individual input channels which are mainly based on analogue electronics components. Fig. 3.13 shows a block diagram of the quench detector circuit.

Resistors R_p of about 500Ω in series with the voltage sensing wires protect the cables in case of an external short circuit. The input signal u_{in} on the quench detector module represents either a differential voltage from a bridge circuit or a potential difference between two voltage taps. Usually in the acquisition electronics the voltages are related to a common ground. In order to permit voltage measurements between different voltage taps, isolation amplifiers perform a galvanic separation of input and acquisition circuit. Moreover, they condition the incoming signals to voltages within a range of $\pm 10 \text{ V}$ for data transmission and reduce the sensitivity of the acquisition electronics to transmitted high voltage peaks.

A logic quench trigger signal u_l is deduced from the analogue output signal u_{out} by comparing it with a defined threshold voltage u_{thr} . As long as u_{out} is below u_{thr} , the comparator output u_l is logic high. If u_{out} exceeds u_{thr} over more than 10 ms, a quench trigger signal u_{trig} is created on the output of the integrator circuit. Voltage spikes smaller than 10 ms do not trigger the magnet protection system.

Due to the input circuit structure of the quench detectors, the modules are able to operate in two different modes.

Bridge circuit mode: In this mode the circuit compares the voltage drop across a conductor or coil section in respect to their midpoint 0.

Amplifier mode: Selected as amplifier, the channel measures the voltage drop between two voltage tap locations and amplifies the signal with the gain, selected on the isolation amplifier.

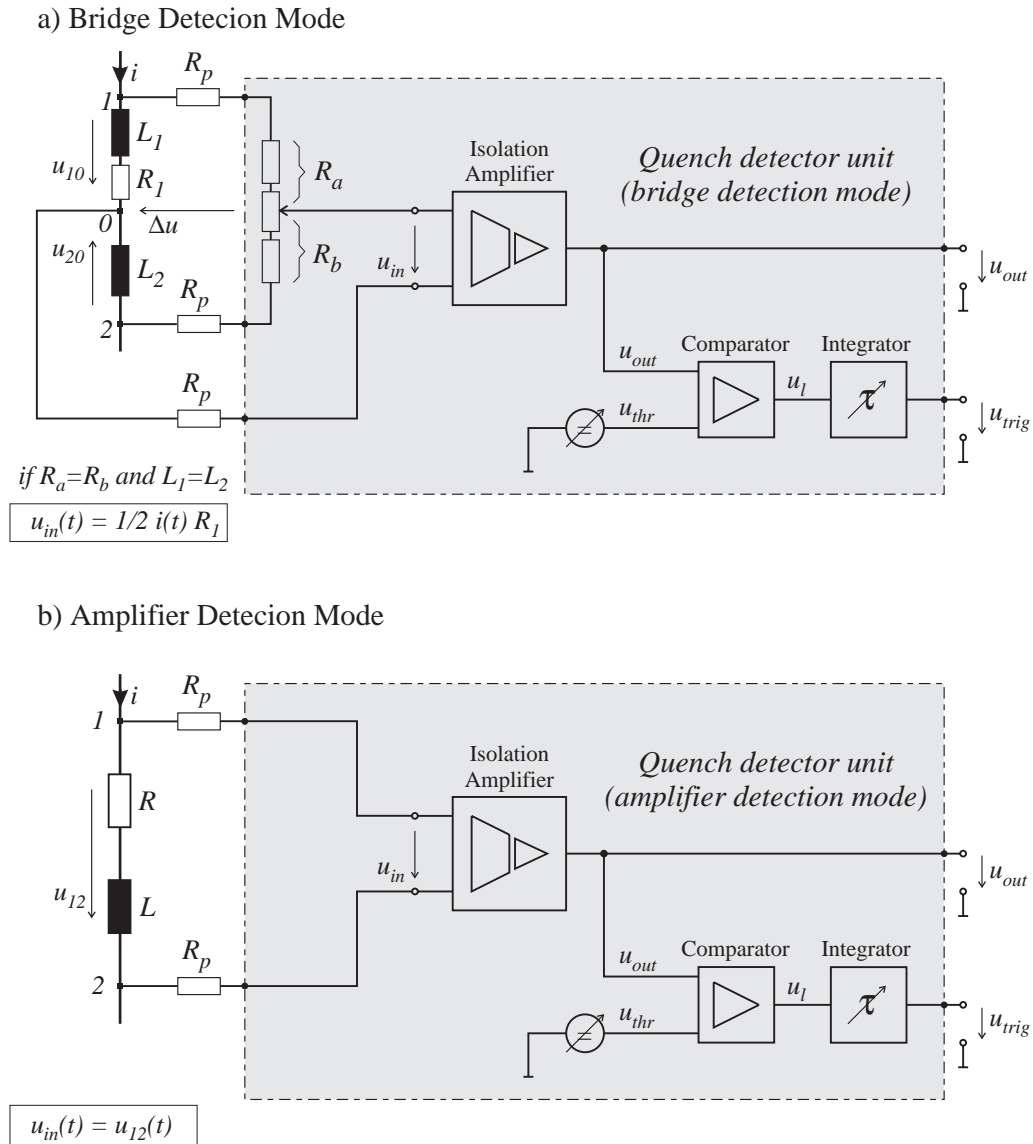


Figure 3.13: Block diagram of the quench detector module for the LHC Magnet String

Due to the measurement of voltage differences in bridge circuit mode, inductive voltages of the same order in both bridge branches are compensated. The output signal of detectors operating in bridge circuit mode then is equivalent to the resistive voltage.

All analogue outputs of the quench detector modules are connected to a data recording system. Each section of the main circuit of the LHC Test String has to be monitored by quench detection circuits. Magnet coils and most of the interconnections between magnets are observed with a certain redundancy. The scheme in Fig. C.1 shows the quench detectors which observe each section of the main circuit.

Magnet coils are monitored with a redundancy in different levels. In the first level, the quench detectors monitor the unbalance between the pole voltages, while quench detectors in the second level compare the voltage difference between two aperture magnets. A third redundancy level exists for the dipole magnets by monitoring the difference in voltage between two magnets. But due to the length of measurement wires the signal becomes very

noisy. The threshold level for these detectors has to be set relatively high, as depicted in Table C.1.

3.3.5 Programmable Logic Controller

Additional to the electronic interlock circuit a Programmable Logic Controller (PLC) is installed to monitor the status of some parameters. Most of these parameters are used specially for the system start-up. The permission to operate the LHC Test String is given as soon as the parameters, listed below, are within their specified ranges:

- Cryogenic temperatures and levels.
- Water-flow in the water cooled cables between the power converter and the current leads.
- Temperatures at 90 % height of both current leads.
- Voltage drop across both current leads.
- Mechanical and thyristor circuit breaker have to be closed and armed.
- All quench heater power supplies have to be charged.

Otherwise the operation inhibited by sending a fault output signal to the interlock matrix.

3.4 Instrumentation

The magnets in the LHC Test String have all the same type of standard instrumentation, including voltage taps, temperature sensors, and pressure sensors. Additional to that, flow-meters, liquid level sensors, and distance sensors are installed for special cryogenics and displacement measurements.

3.4.1 Voltage Taps

Voltage taps are located at the beginning and at the end of each pole coil winding of the magnets, in the bus-bars, at the cold diodes, and on both ends of each current lead. Voltage sensing wires, connected to each voltage tap, are led through capillary tubes to the feed-through connectors either at the top of each magnet or at the string feed box (SFB). Fig. C.1 shows the electrical scheme with all voltage taps and their designations.

3.4.2 Temperature Sensors

Two different types of temperature sensors are used to measure the temperature from about 300 K down to the operating point of 1.9 K. Carbon resistor thermometers are calibrated individually in a range between 1.7 and 25 K. Platinum resistor thermometers, operating above 20 K, are used with a standard calibration curve.

Inside the cold mass both type of sensors are located on the end volumes of each magnet (Fig. 3.14), on the heat sink of the triplet diodes, and in the bus-bars of the short straight section (Fig. 3.15).

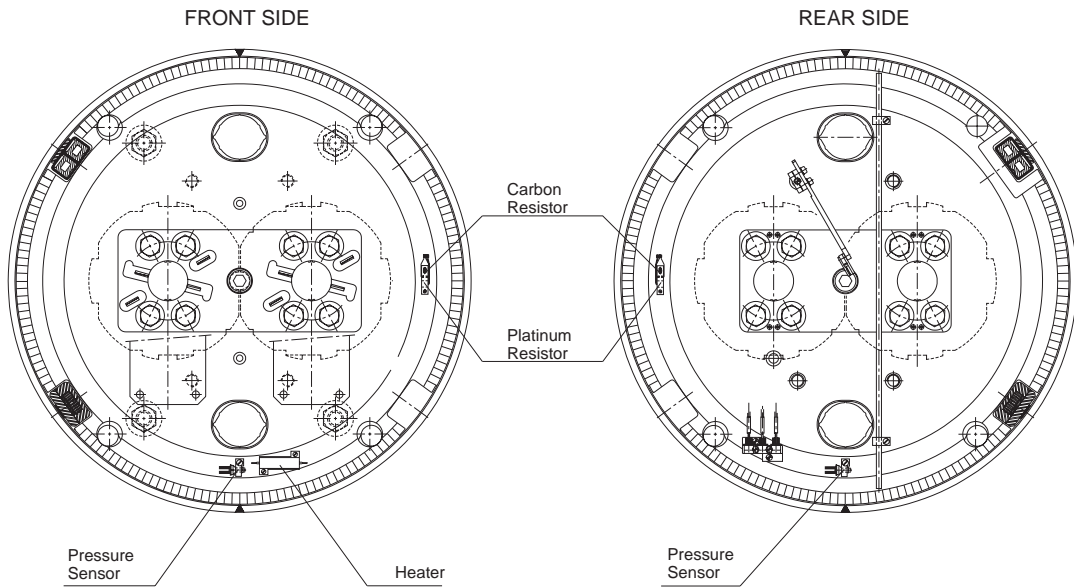


Figure 3.14: Temperature and Pressure instrumentation of the main dipole end volumes

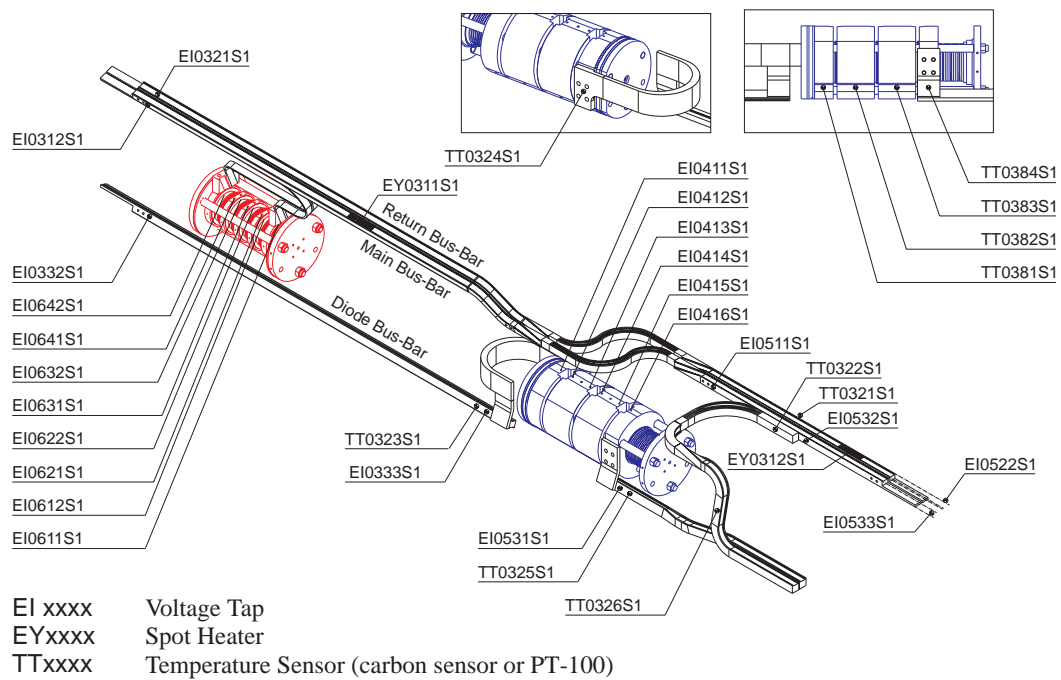


Figure 3.15: Voltage and temperature instrumentation in the cold mass of the short straight section

3.4.3 Pressure Sensors

Temperature compensated pressure sensors, strain-gauge type, are located on the end volumes of the cold masses to measure the helium transient pressure. Their location is visible in Fig. 3.14.

3.5 Cooling System

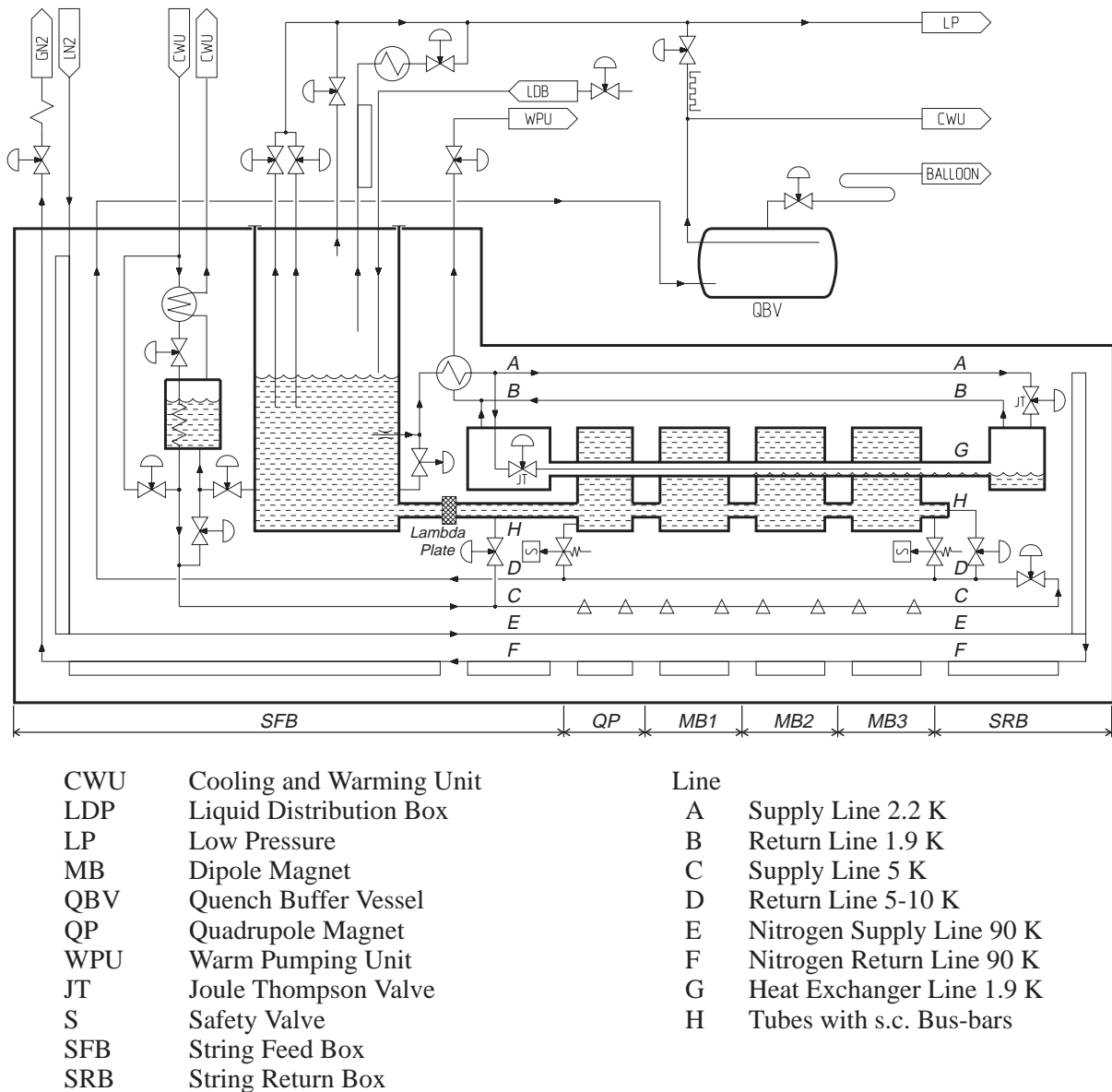


Figure 3.16: Principle cooling scheme of the LHC Test String

The cooling scheme is implemented in independent cooling loops, each extending over the total length of the LHC Test String (Fig. 3.16).

The cooling procedure is performed in three steps:

1. Cool-down from 300 K to 80 K
2. Cool-down from 80 K to 4.5 K
3. Cool-down from 4.5 K to 1.8 K

In the first phase the temperature will be decreased from room temperature to about 80 K with pressurised helium gas, pre-cooled in a nitrogen heat exchanger. A fixed gradient of 60 K between the quadrupole inlet and the last dipole outlet limits the mechanical stress and possible magnet deformation [26].

The next phase, cooling from 80 K to 4.5 K, is achieved by filling the magnets either with liquid or supercritical helium.

The third phase of cooling starts when the cold masses are filled with about 800 litres of liquid helium. Then the temperature is lowered by pumping on saturated helium, flowing and evaporating in a longitudinal heat exchanger. The heat exchanger is coupled to the pressurised helium bath permeating the yoke, collars and superconducting windings of the magnets [2].

For the whole duration of cold experiments, the LHC Test String is maintained at 1.9 K with temperature excursions of short duration caused by quenches or other experimental effects.

3.6 Data Acquisition

A 600 channel data acquisition system continuously monitors temperature, pressure, helium flow, and position parameters. It also acts as a transient recorder to observe the magnet string during a quench with a sampling rate of 1 kHz. VME crates, containing the 16-bit Analogue/Digital Converter (ADC) modules and a communication module, transfer the data to a SUNTM workstation.

The workstation runs a LabViewTM application which presents the data to the user in form of strip charts and stores the data on a local disk. Each channel acquires data with 16-bit resolution in the range ± 10 V. A number of signal conditioners and filters are installed between the transducers and the ADC's.

In archiver mode, the data acquisition system samples once per second every channel and compares each value with the last acquired value. If they differ by more than an individually programmable amount the last value is stored, otherwise it is discarded.

The transient recorder operates like a digital oscilloscope. However, the data is acquired at two adjustable frequencies

- *high frequency (up to 1 kHz)*: before and short time after the quench,
- *low frequency*: observation of the signal tail.

Typically, voltage signals received from voltage amplifiers and quench detectors are recorded at 1 kHz during 500 ms before the quench and during 2 s after the quench. Further 8 s are recorded with a lower sampling rate of 100 Hz.

Each channel can be observed by using the archiver and transient recorder. In order to allow a correlation between transient data, each transient recorder acquisition is absolute

time stamped with a time resolution of ± 1 ms. Both, the archiver and transient data are transferred to a central data base, from where they are accessible on any network computer for viewing and further analysis [1][28].

Chapter 4

Electrodynamic Model

This chapter contains a mathematical description of the electrical circuit of the LHC Test String. In a first step an analytical solution of the differential equations is attempted. Due to the non linear dependencies of electrical resistivity and heat capacity on temperature, a numerical solution of the transient behaviour is preferred. The numerical model helps to find parameters which cannot be directly measured (current sharing between magnet coils and the diode by-pass during the discharge after a quench, bus-bar temperatures, hot-spot temperatures in the quench origin, energy dissipated in magnets, etc.). It is also a useful tool for verifying the transient behaviour of in-series connected superconducting magnets in case of design changes [7] (see chapter 6).

4.1 Transient Model

The model for simulating the electrodynamic behaviour is based on a simplified network (Fig. 4.1), composed of in series connected magnets.

Each magnet is represented by the magnet inductance L_m , including self inductance and mutual inductance (see appendix A.1), and the magnet resistance R_m of the normal conducting sections. The subscripts 1 to 4 in Fig. 4.1 correspond to the location of the magnets in the LHC Test String, where the first magnet is the quadrupole followed by three dipole magnets. Each dipole magnet is by-passed by a single diode, while the quadrupole has a series connection of three diodes in the parallel path. A free-wheeling diode D_{fw} parallel to the power converter carries the whole string current i_s during the discharge. R_{dm} is the dump resistance parallel to the mechanical circuit breaker and R_{dth} is the dump resistance parallel to the thyristor circuit breaker. The inductance of superconducting bus-bars is neglected, since the influence is small in comparison to the coil inductances. Measurements have shown that the inductance of a bus-bar along a dipole is about 20 to 60 times lower than the pole inductance of a dipole. Capacitive effects in the coils and bus-bars are neglected because they become effective at frequencies only above 100 Hz.

4.1.1 System of Differential Equations

At the beginning of the discharge an initial current I_0 flows through the circuit. In the simulation, the external dump resistors R_{dm} and R_{dth} become effective with a time delay

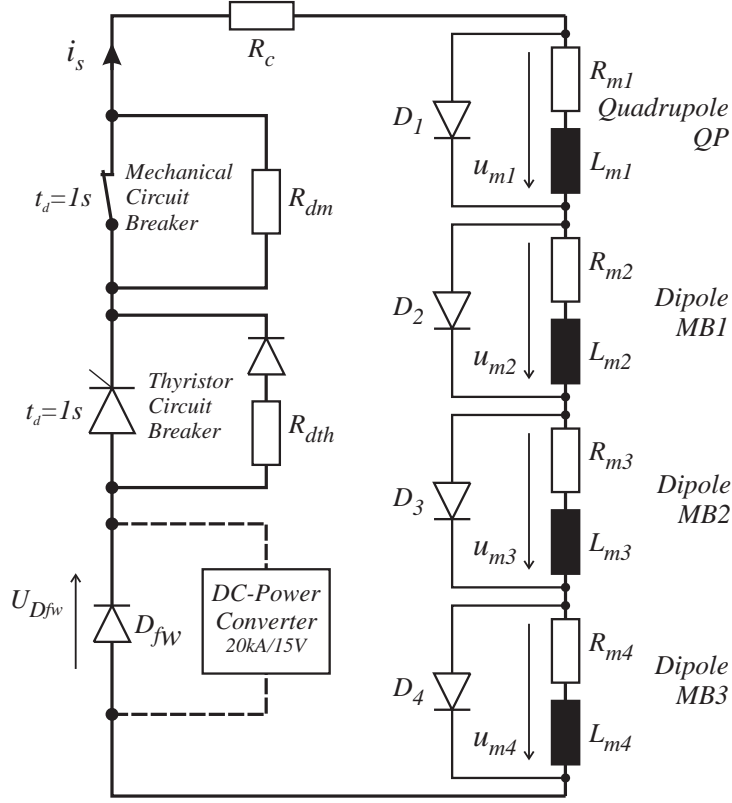


Figure 4.1: Simplified electrical scheme of the LHC Test String

$t_d = 1$ s. The resistor R_c represents the average resistance of the water cooled cable and the current lead resistance.

The model solves the electrical network, represented by the equation

$$\sum_{k=1}^4 u_{m,k}(t) + i_s(t) \cdot R_e + U_{Dfw} + U_{dth} = 0 \quad (4.1)$$

with $u_{m,k}(t)$ the voltage across the k -th magnet, $i_s(t)$ the main current through the LHC Test string, U_{Dfw} the forward voltage of the free-wheeling diode in parallel to the power converter, and $R_e = R_{dm}(t - t_d) + R_{dth}(t - t_d) + R_c$ the external resistance of the circuit. Both, R_{dm} and R_{dth} open with a delay time t_d after initiating the discharge.

Each magnet has at least one diode in parallel (see Fig. 4.2). Generally the current $i_s(t)$ splits up into a current through the magnet $i_{m,k}(t)$ and a current through the diode $i_{D,k}(t)$.

As long as the magnet voltage $u_{m,k}(t)$ is below the turn-on voltage of the by-pass diode across the magnet, the entire string current flows through the magnet coils. The diode current $i_{D,k}(t)$ is zero. The magnet voltage then is given by the differential equation

$$u_{m,k}(t) = \frac{di_s(t)}{dt} \cdot L_{m,k} + i_s(t) \cdot R_{m,k}(T). \quad (4.2)$$

If $u_{m,k}(t)$ becomes equal to the turn-on voltage of the by-passing diode, then the diode across this magnet starts conducting in order to clamp the magnet voltage $u_{m,k}(t)$ to the

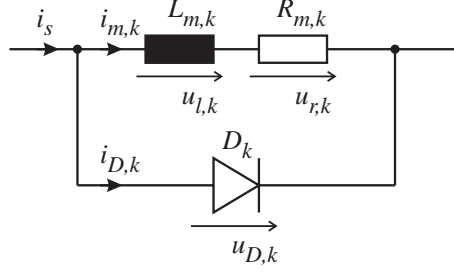


Figure 4.2: Magnet scheme with by-pass diode

diode forward voltage $U_{D,k}(T_D, i_D)$. Diode forward voltage and coil resistance are assumed as time independent functions.

The current through a single magnet is

$$i_{m,k}(t) = \left[I_{m0} - \frac{U_{D,k}(T_D, i_D)}{R_{m,k}(T)} \right] \cdot e^{-\frac{R_{m,k}(T)}{L_{m,k}} \cdot t} + \frac{U_{D,k}(T_D, i_D)}{R_{m,k}(T)} \quad (4.3)$$

with I_{m0} as the initial current in the magnet. The solution is valid for $R_{m,k}(T) = \text{const.}$, which is not the case here.

A unique solution of Eq. (4.1) does not exist due to the effect of by-pass diodes. Dependent on the quench behaviour of each single magnet which is mainly caused by the heater response time and the RRR of the magnet coils, different solutions have to be considered. In the following a selection of reasonable results of Eq. (4.1) is presented.

- *Non by-passed magnets:*

This case is given as long as the voltages across each single magnet are below the turn-on voltage of their by-passing diode.

$$\frac{di_s(t)}{dt} \cdot \sum_{k=1}^4 L_{m,k} + i_s(t) \left[\sum_{k=1}^4 R_{m,k}(T) + R_e \right] + U_{Dfw} + U_{dth} = 0. \quad (4.4)$$

Deduced from Eq. (4.4) the string current is

$$i_s(t) = \left[I_0 + \frac{U_{Dfw} + U_{dth}}{\sum_{k=1}^4 R_{m,k}(T) + R_e} \right] e^{-\frac{\sum_{k=1}^4 R_{m,k}(T) + R_e}{\sum_{k=1}^4 L_{m,k}} t} - \frac{U_{Dfw} + U_{dth}}{\sum_{k=1}^4 R_{m,k}(T) + R_e}. \quad (4.5)$$

The full current flows through the magnet coils. The case $R_m(T) = 0$ describes a magnet discharge through the external dump resistor, e.g. a fast discharge of the LHC Test String by opening the thyristor circuit breaker only.

$$i_s(t) = \left[I_0 + \frac{U_{Dfw} + U_{dth}}{R_c + R_{dth}} \right] e^{-\frac{R_c + R_{dth}}{4} t} - \frac{U_{Dfw} + U_{dth}}{R_c + R_{dth}}. \quad (4.6)$$

- *One by-passed magnet:*

If the voltage across one magnet, e.g. QP ($k = 1$), reaches the turn-on voltage, then the magnet voltage across this magnet is clamped to the forward voltage of the by-passing diode. Eq. (4.1) becomes

$$\frac{di_s(t)}{dt} \cdot \sum_{k=2}^4 L_{m,k} + i_s(t) \left[\sum_{k=2}^4 R_{m,k}(T) + R_e \right] + U_{D,1}(T_D, i_D) + U_{Dfw} + U_{dth} = 0 \quad (4.7)$$

and has the solution

$$i_s(t) = \left[I_0 + \frac{U_{D,1}(T_D, i_D) + U_{Dfw} + U_{dth}}{\sum_{k=2}^4 R_{m,k}(T) + R_e} \right] e^{-\frac{\sum_{k=2}^4 R_{m,k}(T) + R_e}{\sum_{k=2}^4 L_{m,k}} t} - \frac{U_{D,1}(T_D, i_D) + U_{Dfw} + U_{dth}}{\sum_{k=2}^4 R_{m,k}(T) + R_e}. \quad (4.8)$$

- *Two by-passed magnets:*

In case of two by-passed magnets, e.g. QP and MB1 ($k = 1, 2$), the differential equation Eq. (4.1) is written in the form

$$\begin{aligned} \frac{di_s(t)}{dt} \cdot \sum_{k=3}^4 L_{m,k} + i_s(t) \left[\sum_{k=3}^4 R_{m,k}(T) + R_e \right] + \\ + \sum_{k=1}^2 U_{D,k}(T_D, i_D) + U_{Dfw} + U_{dth} = 0 \end{aligned} \quad (4.9)$$

with the solution

$$i_s(t) = \left[I_0 + \frac{\sum_{k=1}^2 U_{D,k}(T_D, i_D) + U_{Dfw} + U_{dth}}{\sum_{k=3}^4 R_{m,k} + R_e} \right] e^{-\frac{\sum_{k=3}^4 R_{m,k} + R_e}{\sum_{k=3}^4 L_{m,k}} t} - \frac{\sum_{k=1}^2 U_{D,k}(T_D, i_D) + U_{Dfw} + U_{dth}}{\sum_{k=3}^4 R_{m,k} + R_e}. \quad (4.10)$$

- *Three by-passed magnets:*

The string current decay rate is determined by the one magnet which has not reached the turn-on voltage, e.g. MB3 ($k = 4$).

$$\frac{di_s(t)}{dt} \cdot L_{m,4} + i_s(t) [R_{m,4}(T) + R_e] + \sum_{k=1}^3 U_{D,k}(T_D, i_D) + U_{Dfw} + U_{dth} = 0. \quad (4.11)$$

The solution is

$$i_s(t) = \left[I_0 + \frac{\sum_{k=1}^3 U_{D,k}(T_D, i_D) + U_{Dfw} + U_{dth}}{R_{m,4} + R_e} \right] e^{-\frac{R_{m,4}(T) + R_e}{L_{m4}} t} - \frac{\sum_{k=1}^3 U_{D,k}(T_D, i_D) + U_{Dfw} + U_{dth}}{R_{m,4} + R_e}. \quad (4.12)$$

- *All magnets by-passed:*

In case of by-passing the current across all magnets, the protection diodes lead current only in forward direction. The voltage across the diodes is counted positive (from the anode to the cathode).

$$i_s(t) \cdot R_e + \sum_{k=1}^4 U_{D,k}(T_D, i_D) + U_{Dfw} + U_{dth} = 0. \quad (4.13)$$

Hence, the string current is

$$i_s(t) = -\frac{\sum_{k=1}^4 U_{D,k}(T_D, i_D) + U_{Dfw} + U_{dth}}{R_e}. \quad (4.14)$$

Since the current decays from a positive level I_0 , the case of all magnets by-passed is excluded. In reality such a case may appear if the inductive voltage across the bus-bars is able to compensate the sum of diode forward voltages and the voltage across the resistive sections of the circuit (external bus-bars, current leads, superconductor joints, etc.).

In general, the string current decays according to the equation

$$i_s(t) = \left[I_0 + \frac{\sum_p U_{D,p}(T_D, i_D) + U_{Dfw} + U_{dth}}{\sum_q R_{m,q}(T) + R_e} \right] e^{-\frac{\sum_q R_{m,q}(T) + R_e}{\sum_q L_{m,q}} t} - \frac{\sum_p U_{D,p}(T_D, i_D) + U_{Dfw} + U_{dth}}{\sum_q R_{m,q}(T) + R_e}. \quad (4.15)$$

The subscripts p and q mark magnets with different behaviour.

p : Magnets, where part of the string current is by-passed through the parallel connected diode(s). For the magnet voltage yields

$$U_{D,p}(T_D, i_D) = u_{m,p}(t). \quad (4.16)$$

The magnet voltage is clamped to the forward voltage of the by-passing diode.

q : Magnets, carrying the whole string current, since the magnet voltage is below the diode forward voltage (by-pass diodes are blocked).

$$U_{D,q}(T_D, i_D) > u_{m,q}(t). \quad (4.17)$$

With use of Kirchhoff's first law, the current through the by-passing diode is

$$i_{D,k}(t) = i_s(t) - i_{m,k}(t). \quad (4.18)$$

The forward voltage $U_{D,k}(T_D, i_D)$ of the by-pass diode across a single magnet is a non-linear function of temperature and current. Therefore, an approximation formula

$$u_{D,k}(T_D, i_D) = [a_n + b_n \cdot i_D(t)] \cdot e^{-(c_n + d_n \cdot i_D(t)) \cdot T} \quad (4.19)$$

has been developed. It fits well with the measured data in Tables A.5 and A.6 for the triplet and quadruplet diodes. The adjustment parameters a_n , b_n , c_n , and d_n for triplet and quadruplet diodes are listed in Tables A.7 and A.8.

The fact that the coil resistance is very non-linear with temperature makes a global analytical solution of the differential equations with a certain precision almost impossible. Under adiabatic conditions, which can be considered worst than real conditions, the average coil temperature in the k -th magnet is given by integrating Eq. (2.11)

$$T_{m,k} = \int_{t=0}^{\infty} \frac{i_{m,k}^2(t) \cdot \rho_{Cu,k}(T)}{\delta_{Cu} \cdot c_{pCu}(T) \cdot A^2 \cdot f_{m,k}^2 + \delta_{Sc} \cdot c_{pSc}(T) \cdot A^2 \cdot f_{m,k} (1 - f_{m,k})} \cdot dt. \quad (4.20)$$

While by-passing current through the diode of the k -th magnet, heat is generated according to the dissipated energy

$$W_{D,k} = \int_{t=0}^{\infty} u_{D,k}(T_D, i_D) \cdot i_{D,k}(t) \cdot dt \quad (4.21)$$

In order to avoid overheating of the diodes while passing current, copper heat sinks mounted on the diodes have to absorb most of the energy.

For heater provoked quenches the discharge is so fast that the heat transfer to the surrounding helium can be neglected and adiabatic conditions can be considered for the calculation.

The adiabatic temperature in the diode section is

$$T_{D,k} = \int_{t=0}^{\infty} \frac{u_{D,k}(T_D, i_D) \cdot i_{D,k}(t)}{m_{Cu,k} \cdot c_{pCu}(T)} \cdot dt \quad (4.22)$$

with m_{Cu} the mass and c_{pCu} the specific heat of the copper heat sinks. Actually exists also a time dependent diffusion process from the wafer to the heat sinks, by means of which the diode wafer temperature is higher than the heat sink temperature.

Temperature and field dependent parameters can be deduced from tables or calculated with approximation formulas. The electrical resistivity of copper is for instance calculated by use of the approximation formula Eq. D.1. The specific heat of copper and niobium-titanium, both functions of temperature, are tabulated and presented in diagrams (see Fig. D.1).

4.2 Program Algorithm

The numerical solving algorithm requires a transformation of the differential equations Eq. (4.1) into difference equations. The network equations are solved for each iterative time step $\Delta t = t_n - t_{n-1}$. Parameters which are non-linear functions of temperature or field, are deduced from approximation formulas or tables.

$$\begin{aligned}
\rho_{Cu}(T, B) &= \rho_{Cu,n} \\
c_{pCu}(T) &= c_{pCu,n} \\
c_{pNbTi}(T) &= c_{pNbTi,n} \\
U_D(T_D, i_D) &= U_{D,n}.
\end{aligned}$$

At each sample n the string current i_s is calculated by the equation

$$i_{s,n} [R_c + R_{dth,n-\tau} + R_{dm,n-\tau}] + u_{m1,n} + u_{m2,n} + u_{m3,n} + u_{m4,n} + U_{Dfw} = 0. \quad (4.23)$$

For each single magnet ($k = 1 \dots 4$) yields

$$\begin{aligned}
u_{mk,n} &= \frac{[i_{s,n} - i_{s,n-1}]}{\Delta t} \cdot L_{mk} + i_{s,n} \cdot R_{mk,n} \quad \text{if } u_{mk,n} < U_{Dk,n} \\
u_{mk,n} &= U_{D,n} \quad \text{if } u_{mk,n} = U_{Dk,n}.
\end{aligned} \quad (4.24)$$

As long as a part of the current flows through the diode, the magnet voltage is clamped to the forward voltage of the by-passing diode.

Dependent on differences in quench heater response time between magnets and increase of magnet coil resistances, different cases for the evaluation of the electrodynamic behaviour have to be considered (see Table 4.1). The string current i_s either flows fully through the magnet coil $i_s = i_{mk}$ or it splits up to $i_s = i_{mk} + i_{Dk}$.

Since the model does not consider the inductances of external cables and bus-bars, case 16 in Table 4.1 is not used for calculating the transients (see Eq. (4.14)).

A general form of Eq. (4.23) which also takes into account the different cases in Table 4.1 is

$$\begin{aligned}
i_{s,n} \left[\sum_q R_{q,n} R_c + R_{dth,n-m} + R_{dm,n-m} \right] + \\
+ \frac{i_{s,n} - i_{s,n-1}}{\Delta t} \sum_q L_q + \sum_p U_{p,n} + U_{Dfw} + U_{dth} = 0. \quad (4.25)
\end{aligned}$$

Voltages marked with p represent magnet voltages clamped to the forward voltage of their by-pass diode. Inductances and resistances marked with q represent magnets which have not reached the forward voltage of the by-passing diodes. The string current is

$$i_{s,n} = \frac{\frac{i_{s,n-1}}{\Delta t} \sum_q L_q - \sum_p u_{p,n} - [U_{Dfw} + U_{dth}]}{\frac{1}{\Delta t} \sum_q L_q + \sum_q R_{q,n} + R_c + R_{dth,n-\tau} + R_{dm,n-\tau}}. \quad (4.26)$$

Table 4.1: Cases of current sharing in the superconducting magnets of the LHC Test String during a discharge

Case	Quadrupole	Dipole MB1	Dipole MB2	Dipole MB3
1	i_{m1}	i_{m2}	i_{m3}	i_{m4}
2	i_{m1}	i_{m2}	i_{m3}	$i_{m4} + i_{D4}$
3	i_{m1}	i_{m2}	$i_{m3} + i_{D3}$	i_{m4}
4	i_{m1}	i_{m2}	$i_{m3} + i_{D3}$	$i_{m4} + i_{D4}$
5	i_{m1}	$i_{m2} + i_{D2}$	i_{m3}	i_{m4}
6	i_{m1}	$i_{m2} + i_{D2}$	i_{m3}	$i_{m4} + i_{D4}$
7	i_{m1}	$i_{m2} + i_{D2}$	$i_{m3} + i_{D3}$	i_{m4}
8	i_{m1}	$i_{m2} + i_{D2}$	$i_{m3} + i_{D3}$	$i_{m4} + i_{D4}$
9	$i_{m1} + i_{D1}$	i_{m2}	i_{m3}	i_{m4}
10	$i_{m1} + i_{D1}$	i_{m2}	i_{m3}	$i_{m4} + i_{D4}$
11	$i_{m1} + i_{D1}$	i_{m2}	$i_{m3} + i_{D3}$	i_{m4}
12	$i_{m1} + i_{D1}$	i_{m2}	$i_{m3} + i_{D3}$	$i_{m4} + i_{D4}$
13	$i_{m1} + i_{D1}$	$i_{m2} + i_{D2}$	i_{m3}	i_{m4}
14	$i_{m1} + i_{D1}$	$i_{m2} + i_{D2}$	i_{m3}	$i_{m4} + i_{D4}$
15	$i_{m1} + i_{D1}$	$i_{m2} + i_{D2}$	$i_{m3} + i_{D3}$	i_{m4}
16	$i_{m1} + i_{D1}$	$i_{m2} + i_{D2}$	$i_{m3} + i_{D3}$	$i_{m4} + i_{D4}$

It splits up into a diode current $i_{D,n}$ and a magnet current $i_{m,n}$ (see Fig. 4.2). The simulation program first assumes the whole string current flowing through the magnet coils. Dependent on the string current decay rate and the magnet coil resistance follows for the magnet voltage

$$u_{mk,n} = \frac{i_{mk,n} - i_{mk,n-1}}{\Delta t} \cdot L_{mk} + i_{mk,n} \cdot R_{mk,n}. \quad (4.27)$$

As long as the magnet voltage is below the turn on voltage of the by-passing diode, the whole string current flows through the magnet coils. In case of by-passing current through the parallel connected protection diode, the voltage across the magnet is clamped to the diode forward voltage, $u_{mk,n} = U_{Dk,n}$. Calculating the magnet current $i_{mk,n}$ from Eq. (4.27) gives

$$i_{mk,n} = \frac{U_{Dk,n} + \frac{i_{mk,n-1}}{\Delta t} \cdot L_{mk}}{R_{mk,n} + \frac{1}{\Delta t} \cdot L_{mk}}. \quad (4.28)$$

The magnet current is lower than the string current $i_{s,n}$. The remaining current flows through the diodes

$$i_{Dk,n} = i_{s,n} - i_{mk,n}. \quad (4.29)$$

With the splitting of string current $i_{s,n}$ into magnet current $i_{mk,n}$ and diode current $i_{Dk,n}$, the average adiabatic temperature development in the magnet coils and diodes can be calculated.

From Eq. (2.11) follows the rise in coil temperature

$$\Delta T_{mk,n} = \frac{i_{mk,n}^2 \cdot \rho_{Cu,n}}{A_k^2 [\cdot f_k^2 \cdot \delta_{Cu} \cdot c_{pCu,n} + f_k(1 - f_k) \cdot \delta_{NbTi} \cdot c_{pNbTi,n}]} \cdot \Delta t. \quad (4.30)$$

The average temperature of the resistive coil section becomes

$$T_{mk,n} = T_{mk,n-1} + \Delta T_{mk,n}. \quad (4.31)$$

Due to the diode current $i_{Dk,n}$ and the forward voltage $U_{Dk,n}$ the average temperature rise in the by-pass diodes is

$$\Delta T_{Dk,n} = \frac{U_{Dk,n} \cdot i_{Dk,n}}{\delta_{Cu} \cdot V_{Cuk} \cdot c_{pCu,n}} \cdot \Delta t_n. \quad (4.32)$$

For the adiabatic calculated diode temperature follows

$$T_{Dk,n} = T_{Dk,n-1} + \Delta T_{Dk,n}. \quad (4.33)$$

At each time step the actual calculated temperatures in the magnets $T_{mk,n}$ and in the by-pass diodes $T_{Dk,n}$ are used to update the values for specific heat and electrical resistivity.

4.3 Model Parameters

4.3.1 Input Parameters

The simulation requires a set of input parameters as listed below for calculating the transients.

- i_{max} : Current before the initiation of the decay.
- t_h : The thermal heater response time for each aperture magnet is usually deduced from experiments. It is the time difference between initiating the quench heater strips and the appearance of the resistive voltage in the magnet aperture.
- n : Number of conductors which become normal after firing the quench heaters (see Fig. 5.10). By considering the outer layer coils in the magnets becoming resistive, it can be assumed that n will be settled somewhere in the range between n_1 and n_2 (n_1 is the number of conductors covered by the heater strips and n_2 is the number of conductors of the whole outer layer coil).
- RRR : Residual resistivity ratio of copper of the conductors in the outer layer of each aperture magnet.

- L : Inductances, including self and mutual inductances, calculated for the inner and outer layer coils of each magnet.
- $A = A_{Cu} + A_{NbTi}$: Cross section of the non-insulated conductor of the coils in the different magnets.
- α : Copper to superconductor ratio for the conductors of the different magnets.
- l_m : Length of the straight section of the magnet coils, not including the coil heads in the ends.
- R_d : Resistance of the external dump circuit.

4.3.2 Calculated Output Parameters

The values of the following parameters are calculated for each time step and stored in a file:

- $i_s(t)$: Current in the LHC Test String, which can be also measured externally with current transducers.
- $i_{m,k}(t)$: Current, which flows through the magnet coils.
- Diode currents $i_{D,k}(t)$: Current, which flows through the cold diode in the magnet by-pass.
- $u_{m,k}(t)$: Magnet voltages (dipole or quadrupole).
- $u_{a,k}(t)$ and $u_{b,k}(t)$: Voltages across each single aperture magnet (dipole or quadrupole) in the twin-aperture magnets. The apertures are designated with a and b .
- $u_{r,k}(t)$: Voltage which appears across a magnet due to the resistive section of the coils after quenching.
- Inductive magnet voltage $u_{l,k}(t)$: Voltage induced in the magnet inductance in case of changing the current.
- $R_{m,k}(t)$: Average coil resistance after magnet quench, calculated by considering adiabatic conditions.
- T_k : Adiabatic average temperature of the resistive section of the coil, driven normal by the quench heater strips.
- $T_{h,k}(t)$: Adiabatic hot-spot temperature at the quench origin.
- $T_{D,k}$: Adiabatic average temperature of the diode heat sinks, generated by the dissipated heat in the diode during current by-passing.
- $E_{m,k}$: Energy dissipated in the resistive section of the magnet coils.
- $E_{D,k}$: Energy according to the diode forward voltage and diode current.
- $\int i_{m,k}^2 dt$: $MIIT$'s of the superconducting cable in each magnet.

In order to use the model for the calculation of parameters which cannot be directly measured, the initial current and the quench heater delays are taken from experiments. The RRR values of the superconducting cables in the LHC Test String are calculated from measurements performed at 10 K and 300 K.

The number of resistive conductors after firing the quench heaters can be estimated between the number of conductors covered by the heater strips and the number of conductors in the outer and inner layer coils (see Fig. 5.10).

In case of predictions and worst case calculations, all input parameters can be individually varied.

4.4 Model Structure

For modelling a network as shown in Fig. 4.1, different system analysis tools (SPICETM, SABERTM, etc.) exist. Especially the temperature dependencies may lead to limitations in modelling. The iterative model, written in MATLABTM code, has been chosen to get a feeling when changing parameters.

A rough structure of the transient model to calculate the electrodynamic behaviour is presented in Fig. 4.3. Bold characters mark vectors, normal characters are scalar values.

- Step 1:* The iterative calculation requires some initial values to start the simulation. In general these are the initial currents ($i_{s,0}$, $\mathbf{i}_{m,0}$, $\mathbf{i}_{D,0}$), the initial current decay $\Delta \mathbf{i}_{s,0}$, the flux density in the coil region $\mathbf{B}_{m,0}$, and the temperatures ($\mathbf{T}_{m,0}$, $\mathbf{T}_{D,0}$) before the event.
- Step 2:* Setting the relevant parameters for the calculation including the circuit dependent parameters (\mathbf{A}_m , \mathbf{f}_m , \mathbf{l}_m , \mathbf{L}_m , etc.) and run dependent parameters (\mathbf{t}_h , Δt , \mathbf{RRR}_m , etc.).
- Step 3:* Iteration loop. As long as the string current $i_{s,n}$ is greater than zero (or a defined minimum value), the network and heat balance equations are calculated sequentially.
- Step 4:* The variable n is used to count the number of time steps.
- Step 5:* Since the model solves the equations in discrete time steps, after each performed calculation cycle the time has to be increased by a specified Δt . The time interval Δt can be constant during the whole simulation or dependent on the increase in temperature.
- Step 6:* Dependent on the actual temperature and field, the material properties ($\rho_{Cu,n}$, $\mathbf{c}_{pCu,n}$, and $\mathbf{c}_{pNbTi,n}$) are updated.
- Step 7:* By assuming a number of conductors $\mathbf{w}_{m,n}$ resistive in the outer layer coils of each magnet, the coil resistance $\mathbf{R}_{m,n}$ is a function of coil temperature $\mathbf{T}_{m,n}$ and magnetic flux-density $\mathbf{B}_{m,n}$.
- Step 8:* For a first estimation the magnet voltages $\mathbf{u}_{m,n}$ are calculated by assuming the whole string current flowing through the magnet coils.
- Step 9:* The diode forward voltages $\mathbf{u}_{D,n}$ are estimated by use of a polynomial fit.

Initial conditions:	$i_{s,0}; \Delta i_{s,0}; i_{m,0}; i_{D,0}; T_{m,0}; T_{D,0}; B_{m,0}; \Delta t$	1					
Parameters:	$\Delta t_h; RRR_m; N_m; A_m; f_m; L_m; l_m; w_m; a; b; c; d$	2					
while $i_{s,n} > 0$			3				
Iteration counter:	$n = n + 1$	4					
Update time step:	$t_n = t_n + \Delta t$	5					
Material properties:	$\rho_{Cu,n}(T_{m,n}, B_{m,n}); c_{pCu,n}(T_{m,n}); c_{pNbTi,n}(T_{m,n})$	6					
Coil resistance:	$R_{m,n} = \frac{\rho_{Cu,n}(T_{m,n}, B_{m,n}) l_m w_m}{RRR_m A_m^2 f_m}$	7					
Estim. magnet voltage:	$u_{m,n} = R_{m,n} i_{s,n} + L_m \frac{i_{s,n} - i_{s,n-1}}{t_n - t_{n-1}}$	8					
Diode forward voltage:	$u_{D,n} = (a + b i_{D,n})e^{-(c + d i_{D,n})T_{D,n}}$	9					
Initialize parameters:	$u_x = 0; L_y = 0; R_y = 0$	10					
for k = 1 to N			11				
<table><tr><td colspan="2">$u_{mk,n} \geq u_{Dk,n} \mid i_{Dk,n-1} > -\Delta i_{mk,n-1}?$</td></tr><tr><td>YES</td><td>NO</td></tr></table>			$u_{mk,n} \geq u_{Dk,n} \mid i_{Dk,n-1} > -\Delta i_{mk,n-1}?$		YES	NO	12
$u_{mk,n} \geq u_{Dk,n} \mid i_{Dk,n-1} > -\Delta i_{mk,n-1}?$							
YES	NO						
Voltage: $u_x = u_x + u_{Dk,n}$		Inductance: $L_y = L_y + L_{mk}$	13				
		Resistance: $R_y = R_y + R_{mk,n}$	14				
String current:	$i_{s,n} = \frac{L_y \frac{i_{s,n-1}}{t_n - t_{n-1}} - U_{Dfw} - u_x}{L_y \frac{1}{t_n - t_{n-1}} + R_c + R_d + R_y}$		15				
String current difference:	$\Delta i_{s,n} = i_{s,n} - i_{s,n-1}$		16				
for k = 1 to N			17				
<table><tr><td colspan="2">$u_{mk,n} \geq u_{Dk,n} \mid i_{Dk,n-1} > -\Delta i_{mk,n-1}?$</td></tr><tr><td>YES</td><td>NO</td></tr></table>			$u_{mk,n} \geq u_{Dk,n} \mid i_{Dk,n-1} > -\Delta i_{mk,n-1}?$		YES	NO	18
$u_{mk,n} \geq u_{Dk,n} \mid i_{Dk,n-1} > -\Delta i_{mk,n-1}?$							
YES	NO						
Magnet current: $i_{mk,n} = \frac{L_{mk} \frac{i_{mk,n-1}}{t_n - t_{n-1}} + u_{Dk,n-1}}{L_{mk} \frac{1}{t_n - t_{n-1}} + R_{mk,n}}$		Magnet current:	19				
		$i_{mk,n} = i_{s,n}$	20				
Magnet current difference: $\Delta i_{mk,n} = i_{mk,n} - i_{mk,n-1}$		Magnet current difference:	21				
		$\Delta i_{mk,n} = \Delta i_{s,n}$					
Diode current: $i_{Dk,n} = i_{s,n} - i_{mk,n}$		Diode current:					
		$i_{Dk,n} = 0$					
Magnet voltage:	$u_{m,n} = R_{m,n} i_{m,n} + L_m \frac{i_{m,n} - i_{m,n-1}}{t_n - t_{n-1}}$		22				
Dissipated energy in magnets:	$W_{m,n} = (i_{m,n})^2 R_{m,n} \Delta t + W_{m,n-1}$		23				
Dissipated energy in diodes:	$W_{D,n} = i_{D,n} u_{D,n} \Delta t + W_{D,n-1}$		24				
MIITs in magnet coils:	$IIIt_{m,n} = (i_{m,n})^2 \Delta t + IIIt_{m,n-1}$		25				
Average magnet coil temperature rise:	$\Delta T_{m,n} = \frac{R_{m,n} (i_{m,n})^2 (t_n - t_{n-1})}{(\delta_{Cu} A_m^2 f_m^2 c_{pCu,n} + \delta_{NbTi} A_m^2 f_m (1 - f_m) c_{pNbTi,n}) l_m w_m}$		26				
Average magnet coil temperature:	$T_{m,n} = T_{m,n-1} + \Delta T_{m,n}$		27				
Average diode temperature rise:	$\Delta T_{D,n} = \frac{u_{D,n} i_{D,n} (t_n - t_{n-1})}{\delta_{Cu} V_{DCu} c_{pCu,n}}$		28				
Average diode temperature:	$T_{D,n} = T_{D,n-1} + \Delta T_{D,n}$		29				
Store data in file			30				

Figure 4.3: Structure of the program to simulate the electrodynamic behaviour

Step 10: For deducing the string current $i_{s,n}$ in *Step 15*, some initial parameters have to be reset. U_x is the sum of magnet voltages, clamped to the forward voltage of their by-pass diode. L_y and R_y are the sums of magnet inductances and coil resistances in magnets which have not yet reached the turn-on voltage of their by-pass diodes.

Step 11: Loop over each single magnet k , where N is the number of magnets in the LHC Test String.

Step 12: Each single magnet voltage $u_{mk,n}$ is compared with the actual forward voltage $U_{Dk,n}$ of the by-passing diode. If $u_{mk,n} < U_{Dk,n}$ and $i_{Dk,n} = 0$, the by-pass diode parallel to the magnet does not carry current. As soon as $u_{mk,n} = U_{Dk,n}$, the by-pass diode turns on and starts clamping the magnet voltage to their forward voltage. Since the string current decays, also the resistive voltage decreases at the end of the decay. If $u_{mk,n}$ becomes lower than $U_{Dk,n}$ while the diode current $i_{Dk,n}$ is still higher than the magnet current difference $\Delta i_{mk,n}$ since the last sample, the diode current will be reduced to lift up the magnet current $i_{mk,n}$ in order to clamp $u_{mk,n}$ to $U_{Dk,n}$. The diode turns off, as soon the magnet voltage $u_{mk,n}$ is below the diode forward voltage $U_{Dk,n}$ and the diode current $i_{Dk,n}$ is too low in order to lift the magnet voltage $u_{mk,n}$ up to the diode forward voltage $U_{Dk,n}$.

Steps 13 and 14: If the conditions in *Step 12* are fulfilled, then the forward voltage $U_{Dk,n}$ of this magnet will be added to U_x . Otherwise the magnet inductance L_{mk} is added to L_x and the magnet coil resistance $R_{mk,n}$ is added to R_x .

Step 15: The string current $i_{s,n}$ is calculated dependent on the network conditions. The resistance R_d contains the dump resistances across both, the mechanical and thyristor circuit breaker (R_{dm} and R_{dth}). Moreover, it considers the time delay for opening the circuit breakers.

Step 16: The change in string current $\Delta i_{s,n}$ during the time interval Δt is required to calculate the string current decay rate.

Step 17: See description of *Step 11*.

Step 18: See description of *Step 12*.

Step 19: If the conditions in *Step 18* are fulfilled (by-pass diode is turned on), the magnet current $i_{mk,n}$ decay depends on the magnet inductance L_{mk} , the coil resistance $R_{mk,n}$, and the forward voltage of the by-pass diode $U_{Dk,n}$. Otherwise the magnet current $i_{mk,n}$ decays in the same way than the string current $i_{s,n}$.

Step 20: Calculating the difference in magnet current since the last sample by considering the different conditions in *Step 18*.

Step 21: In case of by-passing current, the amount of diode current $i_{Dk,n}$ is the difference between string current $i_{s,n}$ and magnet current $i_{mk,n}$.

Step 22: Calculating the magnet voltage $u_{m,n}$ with the magnet current $i_{mk,n}$ obtained in *Step 19*.

Step 23: The dissipated energy in the magnets, $\mathbf{W}_{m,n}$, is the sum of generated heat in the resistive magnet coil sections during the finite time steps Δt .

Step 24: The dissipated energy in the protection diodes, $\mathbf{W}_{D,n}$, is the sum of generated heat in the diodes during the finite time steps Δt .

Step 25: The sum of the product $\mathbf{i}_{m,n}^2 \Delta t$ is a value which is used to deduce the adiabatic temperature generated in a resistive section of a conductor.

Step 26: The average change in magnet coil temperature $\Delta \mathbf{T}_{m,n}$ is calculated as a function of magnet current and material properties.

Step 27: Adding the change in temperature $\Delta \mathbf{T}_{m,n}$ to the previous deduced average temperature value $\mathbf{T}_{m,n-1}$ gives the new temperature value $\mathbf{T}_{m,n}$, used to update the material property values for the next iteration.

Step 28: Calculating the temperature rise $\Delta \mathbf{T}_{D,n}$ due to the generated heat in the current leading by-pass diodes.

Step 29: Updating the average diode temperature $\mathbf{T}_{D,n}$ by adding $\Delta \mathbf{T}_{D,n}$ to the previous diode temperature $\mathbf{T}_{D,n-1}$.

Step 30: For further analysis, the simulated data are stored in a matrix. The columns represent the signals while each line contains the result of a simulation run.

The transient model subdivides the magnets in apertures and poles to simulate the electrodynamic behaviour in more detail.

4.5 Stability of the Transient Model

The simulated change in temperature, voltage, resistance, etc. is coupled with time increment Δt , chosen between two calculated time steps. Heat capacity and electrical resistivity are non-linear functions of temperature. Accurate simulation results are achieved if the average temperature increase during a time interval Δt is lower than one Kelvin.

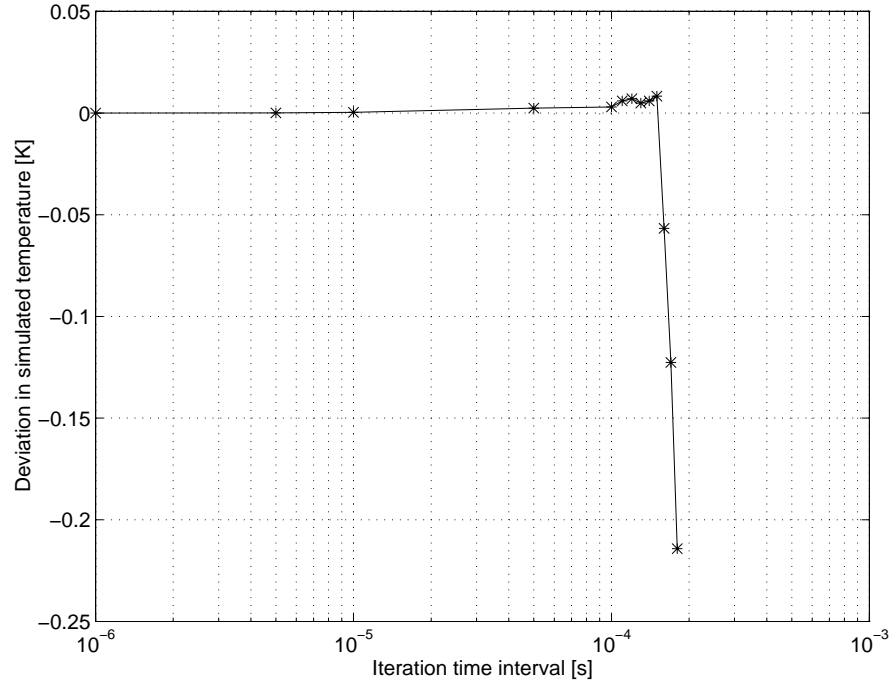
An estimation of temperature increase ΔT during a time interval can be determined by use of Eq. (4.30). Table 4.2 contains the values of electrical resistivity and specific heat of copper at different temperatures. The increase in temperature is calculated with the following parameters for a dipole magnet of the LHC Test String:

Magnet current	$i_{mk,n}$	=	11500	A
Conductor cross section	A_k	=	19.24	mm ²
Copper friction of conductor	f_k	=	0.655	
Density of copper	δ_{Cu}	=	8960	kg m ⁻³
Density of niobium-titanium	δ_{NbTi}	=	6630	kg m ⁻³
Time increment	Δt	=	50	μ s

Fig. 4.4 shows the deviation in temperature with increasing the iteration time interval Δt . Iteration steps in the μ s range lead to accurate results with the drawback of long simulation times. In case of the LHC Test String configuration, the choice of Δt between 10 and 50 μ s led to fast results by avoiding instabilities in the simulation. Increasing the time increment leads to temperature jumps in the beginning of the simulation, which falsifies the results.

Table 4.2: Temperature increase as a function of temperature at $\Delta t = 50 \mu s$

Temperature [K]	ρ_{Cu} [Ωm]	c_{pCu} [J kg ⁻¹ K ⁻¹]	c_{pNbTi} [J kg ⁻¹ K ⁻¹]	ΔT_{Cu} [K]
10	5.749e-10	0.848	4.269	0.9143
20	5.862e-10	6.049	24.33	0.1512
30	6.477e-10	25.83	67.76	0.0499
40	8.141e-10	54.06	122.7	0.0322
50	1.119e-9	88.28	174.2	0.0289
60	1.561e-9	124.3	217.3	0.0302
70	2.113e-9	159.2	246.7	0.0335
80	2.742e-9	191.3	276.1	0.0372
90	3.420e-9	219.6	294.9	0.0415
100	4.124e-9	244.0	313.7	0.0457
150	7.722e-9	317.3	359.7	0.0687
200	1.121e-8	342.4	381.0	0.0929
250	1.457e-8	349.6	393.5	0.1179
300	1.785e-8	352.7	402.7	0.1426
350	2.108e-8	356.9	410.0	0.1661
400	2.427e-8	364.3	416.6	0.1876

Figure 4.4: Deviation in temperature calculation versus iteration time interval Δt to verify the stability of the model

4.6 Validation of the Model

Some simulated parameters are available from measurements. A validation of the model is possible by comparing calculated versus measured data of the same signal.

The quench heater delays of the different magnets are deduced from experiment *RUN0525*, performed at an initial current of 13.1 kA. Table 4.3 contains the data which adapt the simulation to the measurement.

After a provoked firing of the quench heater strips in all superconducting magnets, the coils become resistive after some milli seconds (see Table 4.3).

Table 4.3: Input parameters for the simulation deduced from experiment *RUN0525* to validate the model

Magnet	Aperture	t_h	RRR
		[ms]	[-]
Quadrupole QP	A	8	92
	B	11	96
Dipole MB1	A	15	113
	B	18	109
Dipole MB2	A	22	91
	B	16	106
Dipole MB3	A	9	84
	B	13	86

The heater response time t_h is defined as the time interval between firing the quench heaters and detection of a resistive voltage signal across the coil section which is situated below the heater strip. Together with the RRR of the magnet coils, the heater response time is an essential input value for the simulation. The difference in t_h between apertures determines the maximum voltage from coil to ground and the hot-spot temperature.

Fig. 4.5 shows the comparison between measured and simulated current decay. The deviation between measured and simulated current data is less than 2.5 %.

The voltages across the dipole magnets apertures are shown in Figures 4.6 to 4.8. A comparison between measured and calculated signals is given. Deviations between measured and simulated voltages appear during the first 100 ms of voltage rise. As discussed in section 5.2, the peaks in the voltages across dipole apertures are caused by additional quenching the inner layer coils (due to quench back, too high dB/dt) and differences in longitudinal and transversal quench propagation velocities. Those effects are uniquely for each magnet. They are studied on a single magnet as described in the next chapter. In the model for simulating the electrodynamic behaviour of the LHC Test String, longitudinal and transversal quench propagation are not considered.

Voltage steps in the end of the graphs appear due to turning off of the by-passing diodes. As shown in Fig. 4.6, a deviation in time exists between appearance of this voltage step in the measurement and in the simulation. This is mainly due to the adiabatic calculation. This effect has low priority since it happens at very low current levels. Differences in thermal response between heater strips and outer layer coils are considered between apertures only,

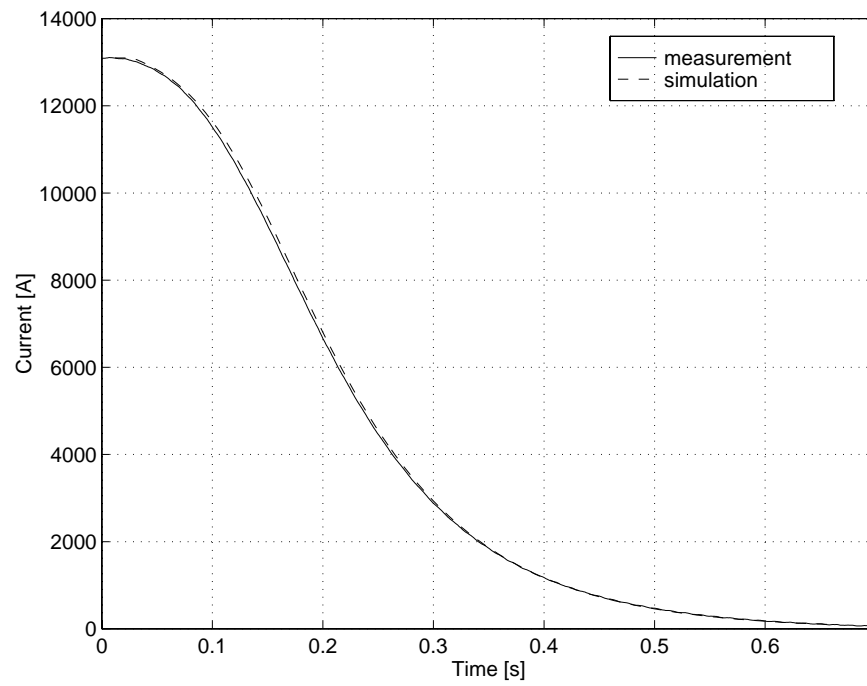


Figure 4.5: Current decay versus time for a heater provoked quench at 13.1 kA

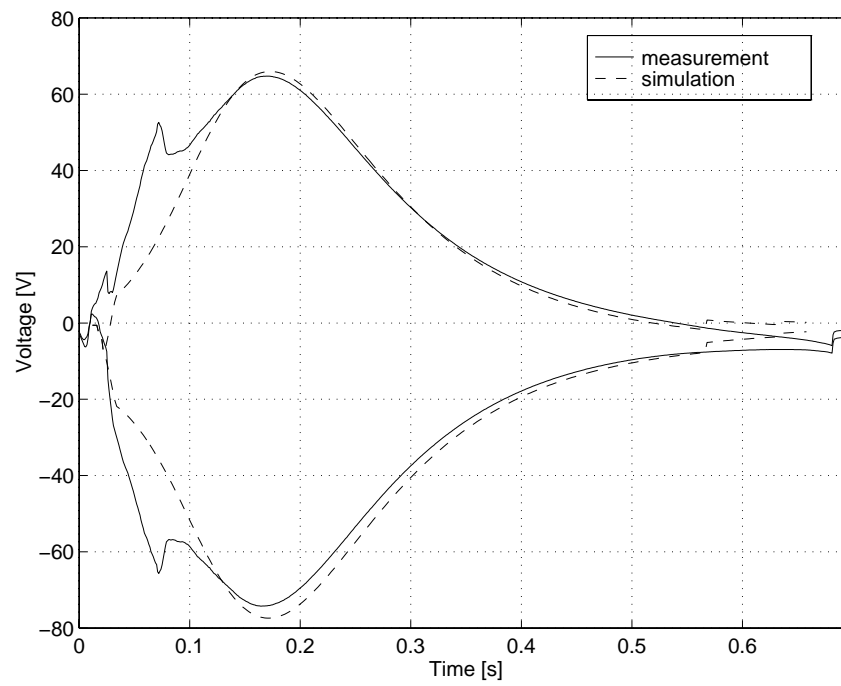


Figure 4.6: Aperture voltage versus time across the dipole MB1 for a heater provoked quench at 13.1 kA

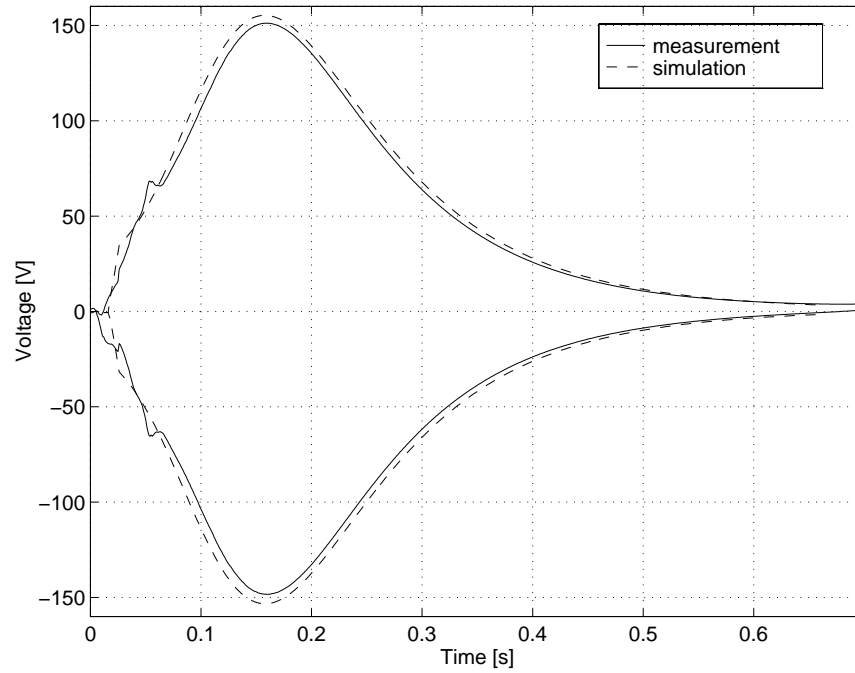


Figure 4.7: Aperture voltage versus time across the dipole MB2 for a heater provoked quench at 13.1 kA

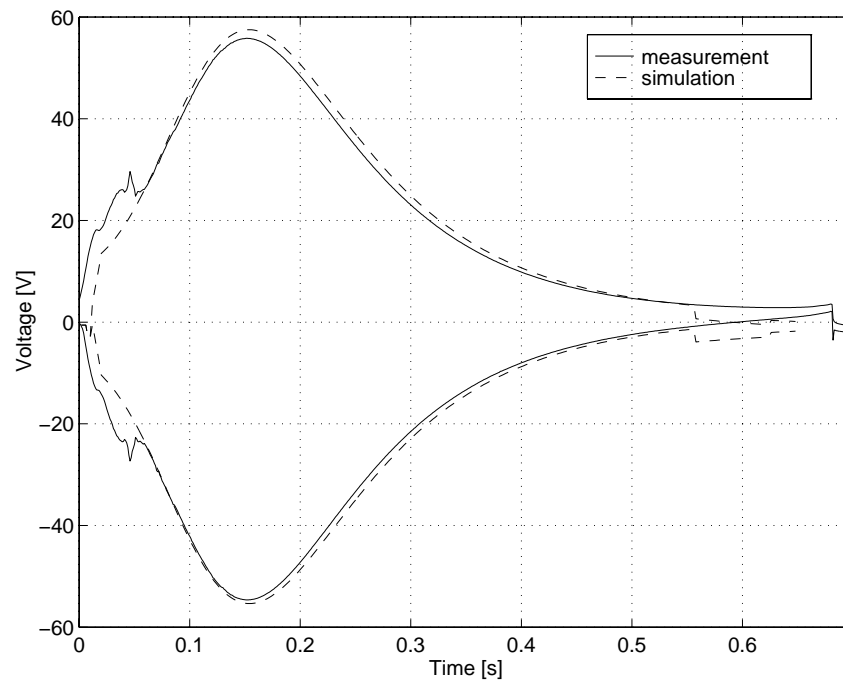


Figure 4.8: Aperture voltage versus time across the dipole MB3 for a heater provoked quench at 13.1 kA

but not between poles. After about 100 ms the deviation between measured and simulated values is in a range of $\pm 5\%$. The voltage development after a quench is analysed in the next chapter.

4.6.1 Deduced Results from Model Calculations

An advantage of a transient simulation model is to deal with different system parameters, which cannot be measured or changed in the real configuration. Some behaviours are easier to understand, if the parameters can be changed independently. In the following, results of different simulation runs are presented.

Evaluation of MIIT's Values from Experiments with Help of the Transient Model

The solution of the left side integral in Eq. (3.6) is often called MIIT's value (unit $[10^6 \text{A}^2\text{s}]$) and indicates the maximum temperature rise in the resistive part of a superconductor cable. In the present configuration of the LHC Test String, an independent measurement of magnet and diode current is not possible. As soon as the by-pass diode turns on, the MIIT's value in a magnet cannot be deduced anymore from the current measurement itself. By feeding the simulation program with the measured quench heater delay time and the initial current, the MIIT's values and further the hot-spot temperatures can be calculated.

Fig. 4.9 shows the MIIT's dependency from the quench current in the different magnets in the LHC Test String. The values are deduced from simulation runs, performed at initial currents levels. Dipole MB1 has the highest MIIT's value, because

- the outer layer coils of MB1 have the highest RRR of all magnets in the string
- the by-pass diode across MB1 did not turn on because of the high inductive voltage compared with the resistive voltage across the magnet
- MB1 has the slowest thermal quench heater response time.

The lower the RRR is in a magnet, the lower is the MIIT's value. A similar MIIT's characteristic exists from experiments at the SSC string [20]. The number of MIIT's in the quadrupole ($\approx 22 \text{ MA}^2\text{s}$) cannot be compared with the values deduced for the dipoles ($\approx 25 \text{ MA}^2\text{s}$) because of the lower stored energy in the quadrupole.

Differences in quench heater response time between the apertures of a magnet causes also in an increase of MIIT's since the magnet current decays slower as long one aperture is still superconducting.

Hot-spot Temperature in Magnet Coils

In case of a natural quench in a magnet, the temperature at the origin is higher than the average coil temperature. Experimental results show longitudinal quench propagation velocities of about 20 ms^{-1} [10]. The voltage across the resistive part of the cable increases due to propagation and temperature rise, until the detection level of 100 mV is reached. From this time on all outer layer conductors are considered as resistive and start also heating. Table 4.4 shows hot-spot temperatures, simulated for different quench currents.

Since the temperatures are calculated by assuming adiabatic condition they can be considered as worst case temperatures.

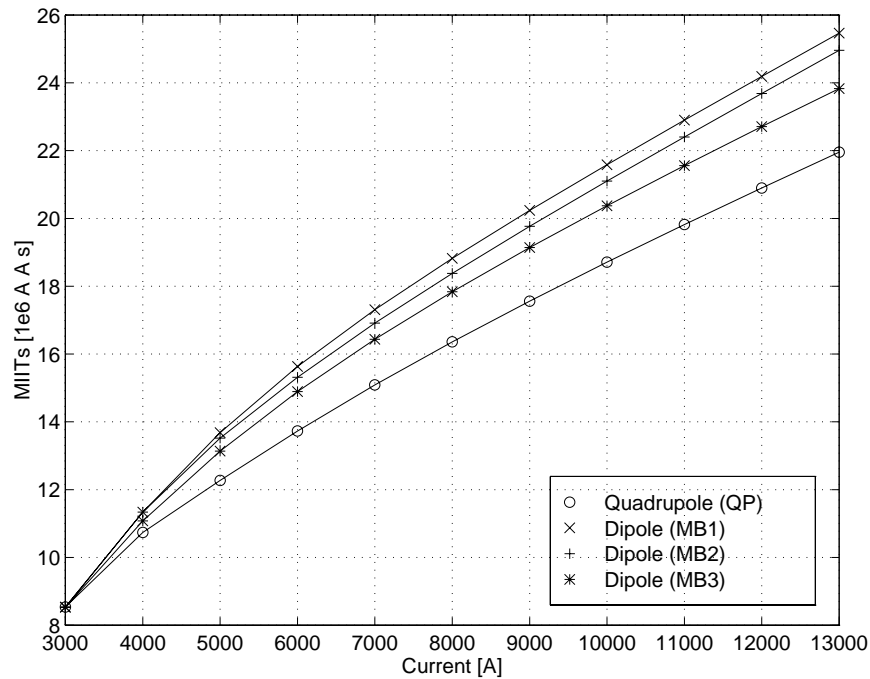


Figure 4.9: Deduced average MIIT's evolution versus initial quench current for the outer layer coils in the magnets

Table 4.4: Deduced hot-spot temperature in dipole conductors, simulated for different quench currents

RUN No.	Quench current	Hot-spot
	[A]	temperature [K]
RUN0517	5000	62
RUN0597	7000	86
RUN0522	10000	136
RUN0525	13100	174

Average Temperature in the Diode Bus-bars

The calculation of the temperature rise in the diode bus-bars is of interest specially for the LHC Test String, since some bus-bars in the dipole by-pass (ADL 2, ADL 3, and ADL 4) have a rather small copper cross-section area of about 27 mm^2 . After a quench they would not withstand a discharge from full current with a time constant of 100 s, as foreseen in the LHC machine. This fact limits experiments on quench propagation between dipole magnets, because of a limited time interval of firing heaters in the different dipole magnets.

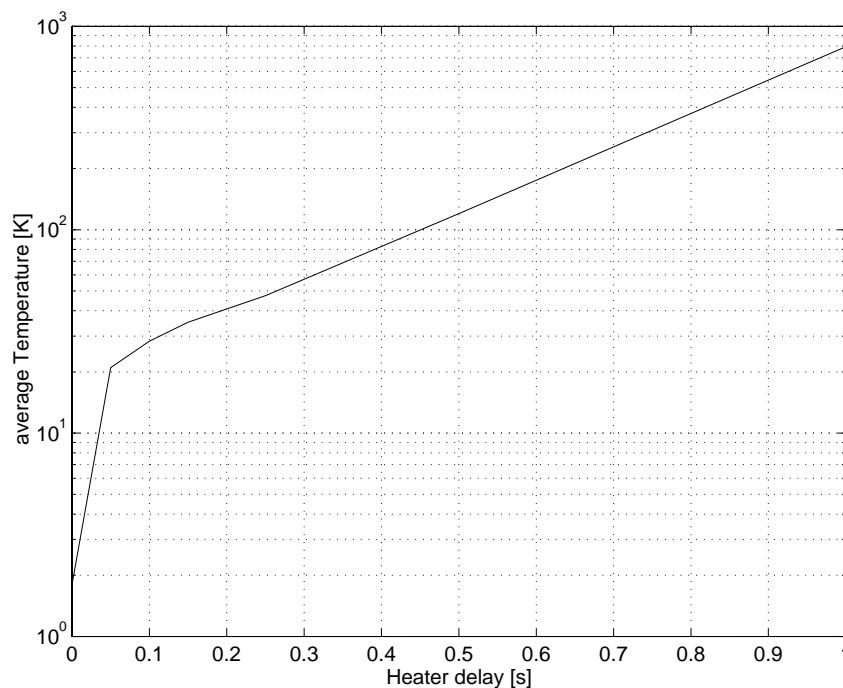


Figure 4.10: Calculated average temperature of the small cross-section auxiliary bus-bar as a function of increasing heater delay between dipole magnets

Fig. 4.10 shows the temperature rise in the small cross-section auxiliary diode bus-bars across the magnets MB1 and MB2, simulated for heater induced quenches in these dipoles at the same time, and delayed firing in dipole MB3. Already a firing of heaters with a delay of 0.8 s in the two still remaining dipoles would heat up the bus-bar temperature across the first quenched dipole to about 350 K. The calculation considers adiabatic conditions, whereas the real temperature can be lower due to cooling effects of the surrounding helium.

Conclusion

The transient model is realised as a macro program, written as a MATLABTM application, which solves the electrodynamic equations iteratively for constant defined time steps. Especially at low temperatures some material properties, e.g. specific heat and electrical resistivity, vary non-linearly with temperature. In order to avoid discontinuities in the calculation and to get results within $\pm 10\%$ deviation from deduced measurements, the interval between time steps should be below $50 \mu\text{s}$. This would result in an enormous amount of data

since a decay finishes, dependent on the initial current, after 0.6 and 3 s. The simulation program reduces the number of data to a sufficient amount for further analysis.

The validation of the model shows, that a change of just a few parameters is necessary to fit the simulation to a performed measurement. The same rules are used to describe the behaviour of the dipole magnets and deducing their discharge currents, magnet and aperture voltages, temperatures, $\int i^2 dt$, etc. Already the study of the dipole pole voltages after quenches at different current levels becomes quite difficult, because the magnets would need additional parameters to describe this behaviour.

More detailed calculations by implementing cable characteristics (e.g. hysteretic and eddy current loss, persistent currents, etc.), quench propagation velocity, and cryogenic effects (e.g. thermal conductivity, heat transfer, etc.) would just magnify the amount of input parameters and so complicate the model without increasing really the benefits. Essential values like hot-spot temperature, maximum voltage between coil and ground, etc. could be deduced with sufficient accuracy.

4.7 Modelling Quench Propagation through Bus-bars

Inter-magnet quench experiments (described in the next chapter) have been performed to study the heat propagation from a quenched magnet to the adjacent superconducting magnet. The effects on inter-magnet quench propagation are heat transport via helium and heat conduction through the copper stabilised bus-bars. Due to the dimensions of the diode bus-bars in the LHC Test String, quench propagation experiments could be performed only from quadrupole to dipole magnet without endangering the system. Therefore, the heat sink of the diode triplet in the short-straight-section, by-passing the quadrupole, generates mainly the heat to quench the adjacent dipole magnet.

A simplified analytical model has been developed in order to estimate the temperature of the highly copper stabilised bus-bars at the end close to the dipole by providing an exponentially increasing temperature T_c of the diode triplet heat sink.

4.7.1 Numerical Model

The initial temperature of the bus-bar T_b is assumed equal to the helium bath temperature. The heat flow in the copper stabilised bus-bar is governed by the partial differential equation

$$\delta_{Cu} \cdot c_{pCu}(T_{Cu}) \cdot A_{Cu} \frac{\partial T_{Cu}}{\partial t} = \frac{\partial}{\partial x} \left[\lambda(T_{Cu}) \cdot A_{Cu} \cdot \frac{\partial T_{Cu}}{\partial x} \right] + \frac{\rho_{Cu}(T_{Cu}) \cdot i^2(t)}{A_{Cu}} - p \cdot h \cdot [T_{Cu} - T_{He}], \quad (4.34)$$

where the propagation is assumed along the x -axis. T_{Cu} and T_{He} are the temperature of the copper bus-bar and the surrounding helium, λ_{Cu} is the heat conductivity, c_{pCu} is the heat capacity, ρ_{Cu} is the electrical resistivity, h is the heat transfer coefficient, p the wetted perimeter, and $i(t)$ is the time dependent current flowing through the copper section of the bus-bar.

One end of the bus-bar is connected to the diode triplet. In case of by-passing current across the quadrupole, the heat sinks heat up and distribute heat to the bus-bar. Therefore, the boundary condition is given by the temperature profile of the diode heat sink

$$T(0, t) = T_d \left[1 - e^{-t/\tau} \right] \quad (4.35)$$

with T_d the final diode heat sink temperature and τ the time constant to describe the heat sink temperature profile after the diodes turn on. The initial condition

$$T(x, 0) = T_b \quad (4.36)$$

considers, that the bus-bar is cooled with superfluid helium at the bath temperature $T_b = 1.8$ K.

The solution of Eq. 4.34 is determined by an iterative method because of the fact that heat capacity, thermal conductivity, heat transfer, and electrical resistivity are non-linear functions of temperature.

Fig. 4.11 shows a grid with different grid length Δx and Δt .

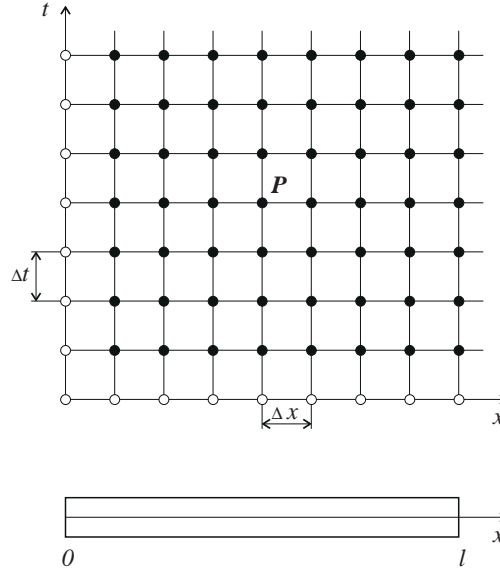


Figure 4.11: Net for calculating the temperature distribution across bus-bar

The nodes in the grid, in which the value of the function is given either by initial conditions or boundary conditions, are marked with circles, while nodes with unknown values are marked with points. The nodes have the co-ordinates $x_i = i \cdot \Delta x$, ($i = 0, 1, \dots, n$) and $t_j = j \cdot \Delta t$, ($j = 0, 1, 2, \dots$). The values of the function $T_{Cu}(x_i, t_j)$ are designated as $T_{Cu}^{(i,j)}$. To approximate the partial differential equation in point $P(x_i, t_j)$, the first derivative of t is exchanged by

$$\frac{\partial T_{Cu}}{\partial t} = T_t(P) \approx \frac{T_{Cu}^{(i,j+1)} - T_{Cu}^{(i,j)}}{\Delta t} \quad (4.37)$$

and the second derivative of x is exchanged by

$$\frac{\partial^2 T_{Cu}}{\partial x^2} = T_{xx}(P) \approx \frac{T_{Cu}^{(i+1,j)} - 2T_{Cu}^{(i,j)} + T_{Cu}^{(i-1,j)}}{(\Delta x)^2} \quad (4.38)$$

At $t = 0$, the values of the function are known by the initial conditions. Hence, equating Eq. 4.37 and Eq. 4.38 results in

$$\mathbf{T}_{Cu}^{j+1} = \mathbf{A} \cdot \mathbf{T}_{Cu}^j + \mathbf{b}_j, \quad (4.39)$$

where

$$\mathbf{T}_{Cu}^j = \begin{pmatrix} T_{Cu}^{1,j} \\ T_{Cu}^{2,j} \\ T_{Cu}^{3,j} \\ \vdots \\ T_{Cu}^{n-1,j} \\ T_{Cu}^{n,j} \end{pmatrix}, \mathbf{b}_j = \begin{pmatrix} T_i^{1,j} + T_h^{1,j} + T_d(1 - e^{-t/\tau}) \\ T_i^{2,j} + T_h^{2,j} \\ T_i^{3,j} + T_h^{3,j} \\ \vdots \\ T_i^{n-1,j} + T_h^{n-1,j} \\ T_i^{n,j} + T_h^{n,j} \end{pmatrix} \quad (4.40)$$

$$\mathbf{A} := \begin{pmatrix} 1-2r & r & & & \\ r & 1-2r & r & & \\ & r & 1-2r & r & \\ & \ddots & \ddots & \ddots & \\ & & r & 1-2r & r \\ & & & 2r & 1-2r \end{pmatrix} \quad (4.41)$$

with

$$r = \frac{\lambda_{Cu}(T_{Cu}^{(i,j)})}{\delta_{Cu} \cdot c_{p_{Cu}}(T_{Cu}^{(i,j)})} \frac{\Delta t}{(\Delta x)^2}, \quad (4.42)$$

$$T_i^{(i,j)} = \frac{\rho_{Cu}(T_{Cu}^{(i,j)}) \cdot i^2(t)}{\delta_{Cu} \cdot c_{p_{Cu}}(T_{Cu}^{(i,j)}) \cdot A_{Cu}^2} \cdot \Delta t, \quad (4.43)$$

$$T_h^{(i,j)} = \frac{p \cdot h \cdot [T_{Cu}^{(i,j)} - T_{He}]}{\delta_{Cu} \cdot c_{p_{Cu}}(T_{Cu}^{(i,j)}) \cdot A_{Cu}} \cdot \Delta t. \quad (4.44)$$

The matrix \mathbf{A} is tri-diagonal. Absolute stability is only given if the absolute eigenvalues η_ν of \mathbf{A} are lower than 1. To consider the dependencies of η_ν from r , one can write

$$\mathbf{A} = \mathbf{I} - r\mathbf{J} \quad (4.45)$$

with

$$\mathbf{J} := \begin{pmatrix} 2 & -1 & & & \\ -1 & 2 & -1 & & \\ & -1 & 2 & -1 & \\ & & \ddots & \ddots & \ddots \\ & & & -1 & 2 & -1 \\ & & & & -2 & 2 \end{pmatrix} \in \mathbf{R}^{n \times n} \quad (4.46)$$

The eigenvalues η_ν of \mathbf{A} are given by the eigenvalues ξ_ν of \mathbf{J} with $\eta_\nu = 1 - r\xi_\nu$, ($\nu = 1, 2, \dots, n$). The eigenvalues of \mathbf{J} are real, since \mathbf{J} is similar to a symmetric matrix $\tilde{\mathbf{J}} := \mathbf{D}^{-1}\mathbf{J}\mathbf{D}$ with $\mathbf{D} := \text{diag}(1, 1, \dots, \sqrt{2})$. Further, the eigenvalues of \mathbf{J} are positive and are not greater than 4. The matrix $\hat{\mathbf{J}} - 4\mathbf{I}$ is negative definite, whereas the value 4 is not an eigenvalue of $\hat{\mathbf{J}}$. Since $r > 0$, yields for the eigenvalues of \mathbf{A}

$$1 - 4r < \eta_\nu < 1$$

and the conditions for the absolute stability are fulfilled if

$$r \leq 1/2.$$

4.7.2 Heat Propagation along Bus-bar

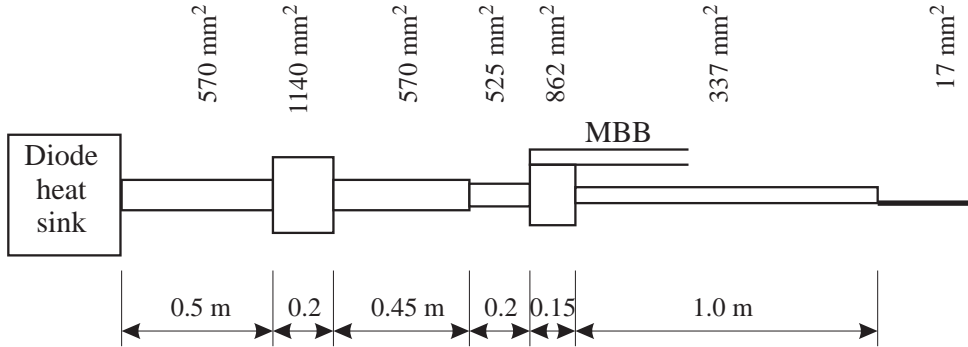


Figure 4.12: Bus bar dimensions for simulating heat propagation

The numerical calculation of the heat propagation along the bus-bar section from the diode triplet to the adjacent dipole (Fig. 5.26 and Fig. 4.12) considers:

- The diode heat sink is a heat source, heating according to the exponential function in Eq. (4.35).
- The initial temperature of the bus-bar is equal to the bath temperature of the surrounding helium (≈ 1.8 K).
- Above the critical temperature of the superconductor $T_c = f(I, B)$, Joule heating of the resistive section along the bus-bar supports the conductive heating.

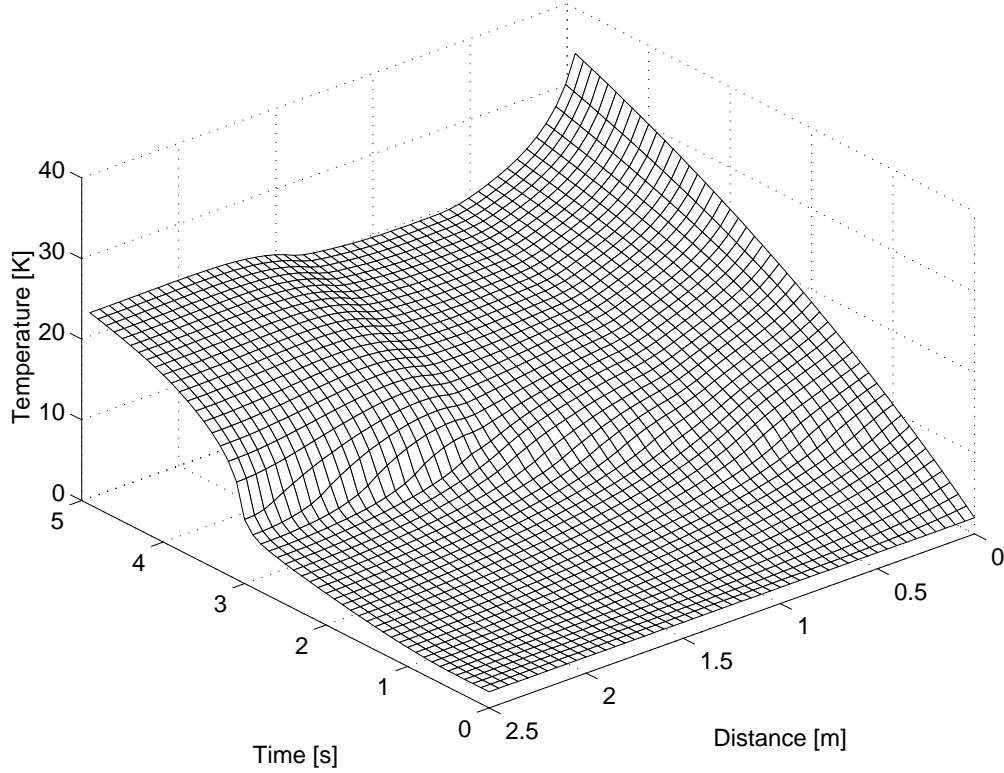


Figure 4.13: Temperature profile versus time across the bus-bar leading from the diode triplet to the adjacent dipole

- Heat transfer from the bus-bar to the surrounding helium is not considered in the simulation.

The result of the simulation is given in the time duration between heating up the front end of the bus-bar and exceeding the critical temperature (about 9 K) at the rear end of the bus-bar. This provokes a quench in the less stabilised cable section ($A_{Cu} \approx 17 \text{ mm}^2$), leading to the dipole coil. The simulation assumes an initial current of $I_0=13.1 \text{ kA}$, a final diode heat sink temperature $T_d=60 \text{ K}$, and a time constant $\tau=5 \text{ s}$. The values are deduced from the bus-bar temperature sensor *TT0325S1* during the quench propagation experiment at an initial current of 13.1 kA (see Fig. 5.32). Since the main bus-bar does not lead current after the quadrupole has been discharged, the influence in the temperature calculation can be neglected. By not considering the heat transfer to the surrounding helium, the rear end of the bus-bar becomes resistive after about 3 s, as shown in Fig. 4.13.

As shown in the experimental results of inter-magnet quench propagation (next chapter), the time between quenching the quadrupole and detecting a quench in the adjacent dipole magnet is about 20 times longer. The reason for this extension in time is the heat exchange between the bus-bar (hollow profile) with the helium.

Chapter 5

String Experiments and Test Results

This chapter describes the analysis of natural and heater-provoked quenches, performed both on a single dipole magnet and on the LHC Test String. The relevant parameters from the point of quench protection (max. voltages, hot-spot temperatures, current characteristics, coil resistances, etc.) are discussed.

In case of a magnet quench in a half-cell, heat propagates from the quenched magnet to the adjacent magnets. Inter-magnet quench propagation experiments have been performed to study the heating effects both along the bus-bar connections and through the coolant.

5.1 Measurement Errors

A measurement system is often made up of a chain of components, each of which is subject to individual inaccuracy. If y is a known function of n independent variables x_n , then

$$y = f(x_1, x_2, x_3, \dots, x_n). \quad (5.1)$$

The x 's are the measured quantities (instrument or component outputs) and are in error by $\pm\Delta x_1, \pm\Delta x_2, \pm\Delta x_3, \dots, \pm\Delta x_n$, respectively. These errors cause an error Δy in the computed result y .

An approximate solution valid for engineering purposes may be obtained by application of the Taylor series. Expanding the function f in a Taylor series gives

$$\begin{aligned} f(x_1 \pm \Delta x_1, x_2 \pm \Delta x_2, x_n \pm \Delta x_n) &= f(x_1, x_2, x_3, \dots, x_n) \\ &+ \Delta x_1 \frac{\partial f}{\partial x_1} + \Delta x_2 \frac{\partial f}{\partial x_2} + \dots + \Delta x_n \frac{\partial f}{\partial x_n} + \frac{1}{2} \left[(\Delta x_1)^2 \frac{\partial^2 f}{\partial x_1^2} + \dots \right] + \dots \end{aligned} \quad (5.2)$$

where all the partial derivatives are to be evaluated at the known values of x_1, x_2, \dots, x_n . In actual practice, the Δx 's will all be small quantities, and thus terms such as $(\Delta x)^2$ will be negligible. Then Eq. 5.2 may be given approximately as

$$\begin{aligned} f(x_1 + \Delta x_1, x_2 + \Delta x_2, x_n + \Delta x_n) \\ = f(x_1, x_2, x_3, \dots, x_n) + \Delta x_1 \frac{\partial f}{\partial x_1} + \Delta x_2 \frac{\partial f}{\partial x_2} + \dots + \Delta x_n \frac{\partial f}{\partial x_n}. \end{aligned} \quad (5.3)$$

The absolute error is given by

$$\Delta y = \left| \Delta x_1 \frac{\partial f}{\partial x_1} \right| + \left| \Delta x_2 \frac{\partial f}{\partial x_2} \right| + \cdots + \left| \Delta x_n \frac{\partial f}{\partial x_n} \right|. \quad (5.4)$$

5.1.1 Error Margin in Voltage Measurement

The relative error e_{rel} in voltage measurement

$$e_{rel} = \frac{u_M - u_T}{u_T} \quad (5.5)$$

is mainly determined by the isolation amplifier in the quench detector module (Fig. 5.1), whereas u_M is the measured value, and u_T is the true value.

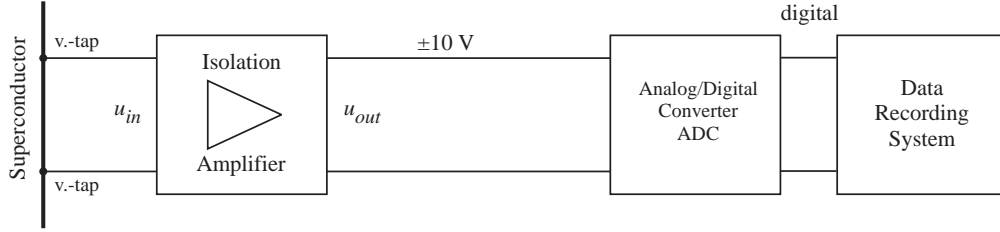


Figure 5.1: Chain of components for voltage measurement across coils and bus-bars

Table 5.1: Relative error in voltage measurement of a quench detector module (gain= 1.2)

u_M V	u_T V	e_{rel} %
0.024	0.024	1.66
0.122	0.12	1.41
1.217	1.2	1.40
2.437	2.4	1.53
6.087	6.0	1.45
12.168	12.0	1.39

Table 5.1 shows the relative error for different input voltages at a fixed gain of 1.2 [16]. The relative error of the isolation amplifier is about 1.7 %. The 16 bit Analog/Digital Converter operates in an input range of ± 10 V with an error of lower than 0.1 % at 1 V. Therefore, an average error in voltage measurement of ± 1.8 % FSR (Full Scale Range) can be assumed. The error does not take into account the systematic error of cabling due to the induced voltage in case of change in magnetic field. This effect should be minimised by use of twisted wire-pairs.

5.1.2 Error Margin in Temperature Measurement

The temperature measurement is based on the temperature dependencies of carbon and platinum resistors. By supplying a constant current, the voltage across the resistor is a function of temperature.

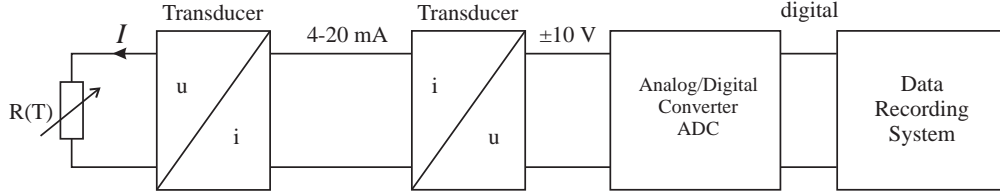


Figure 5.2: Chain of components for temperature measurement

The carbon resistors for temperature measurement, located in superfluid helium, have a resistance of $10000 \pm 100 \, \Omega$. A constant current source in the i/u transducer operates at $10 \pm 0.02 \, \mu\text{A}$.

The voltage drop across the temperature sensor at 1.8 K can be estimated with $10^{-5} \cdot 10^4 = 0.1 \, \text{V}$. For the voltage error follows

$$\begin{aligned} \Delta u &= \frac{\partial(I \cdot R)}{\partial I} \Delta I + \frac{\partial(I \cdot R)}{\partial R} \Delta R \\ \Delta u &= R \cdot \Delta I + I \cdot \Delta R \\ \Delta u &= 10^4 \, \Omega \cdot 10^{-8} \, \text{A} + 10^{-5} \, \text{A} \cdot 100 \, \Omega \\ \Delta u &= 1.1 \, \text{mV}. \end{aligned}$$

Then

$$u = 0.1 \, \text{V} \pm 1.1 \, \text{mV} \quad (5.6)$$

The error of the temperature transmitter and sensor element is about 1.1 % FSR. Considering an error margin of 0.1 % for each transducer in the chain and for the Analogue/Digital converter (Fig. 5.2), the temperature measurement is performed with an error of about $\pm 1.4 \, \%$ FSR.

5.2 Single Dipole Quench Behaviour

The LHC main dipole magnets contain two single aperture dipoles. The poles are formed of two layer coils which are connected electrically in series (see Fig. 5.3). Following the current through an aperture dipole, it enters the outer layer coil and flows over a splice to the inner layer coil of the same pole. A connection is necessary due to the different cable dimensions of the outer and inner layer coil. The inner layer coils of both poles are connected in series without changing the cable. In the second pole, the current flows over a contact back to the outer layer coil, from where it leaves the aperture dipole of the same magnet. The same

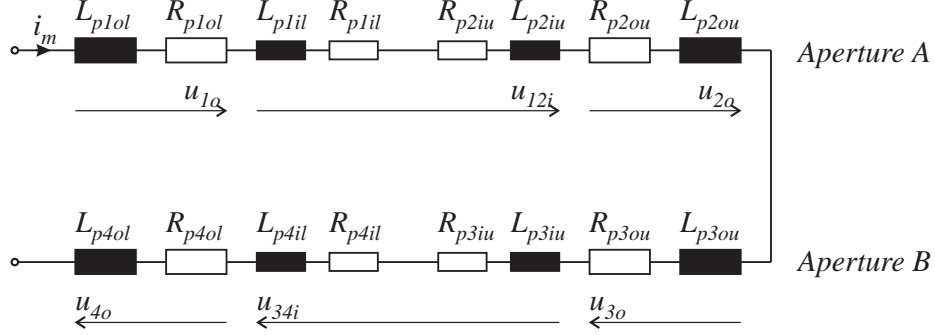


Figure 5.3: Electrical scheme of a twin-aperture LHC dipole

sequence is repeated in the other aperture dipole. The pole inductances are calculated as described in appendix A.1.

The subscripts of inductances and resistances have to be interpreted as follow:

- 1st: p ... pole;
- 2nd: 1, 2, 3, 4 ... pole number;
- 3rd: $i, (o)$... inner (outer) layer coil;
- 4th: $u, (l)$... upper (lower) pole.

In case of a detected quench, heater strips along the outer layer coils of the superconducting dipoles are fired in order to quench the magnet in its full length. The higher the magnet current, the lower is the critical temperature of the superconducting cable and the more efficient become the quench heaters. After firing the quench heaters, part of the generated heat in the heater strips will be distributed to the conductors on the outer layer coils, situated below the heater strips. A small part of the heat will be dissipated in the collars whereas at least the number of conductors below the heater strips quench. Due to quench back and quench propagation in transversal and radial direction, some more conductors become resistive.

Table 5.2: Experimental parameters of a heater provoked quench in dipole MB3 after the 2nd thermal cycle

Energy extraction:	no
Temperature:	1.76 K
Ramp rate (di/dt):	10 As ⁻¹
Quench current:	13994 A
Recording date:	21/04/1995
File number:	A0421160.207

Parameters for a representative experiment on a single magnet are listed in Tab. 5.2. Due to the increasing resistance in the normal conducting sections of the coil during a quench, the current decays in about 600 ms from 14 kA down to 0 A (Fig. 5.4). The current de-ramp rate of more than 60 kA per second (Fig. 5.5) may induce high voltages in the still superconducting coil sections.

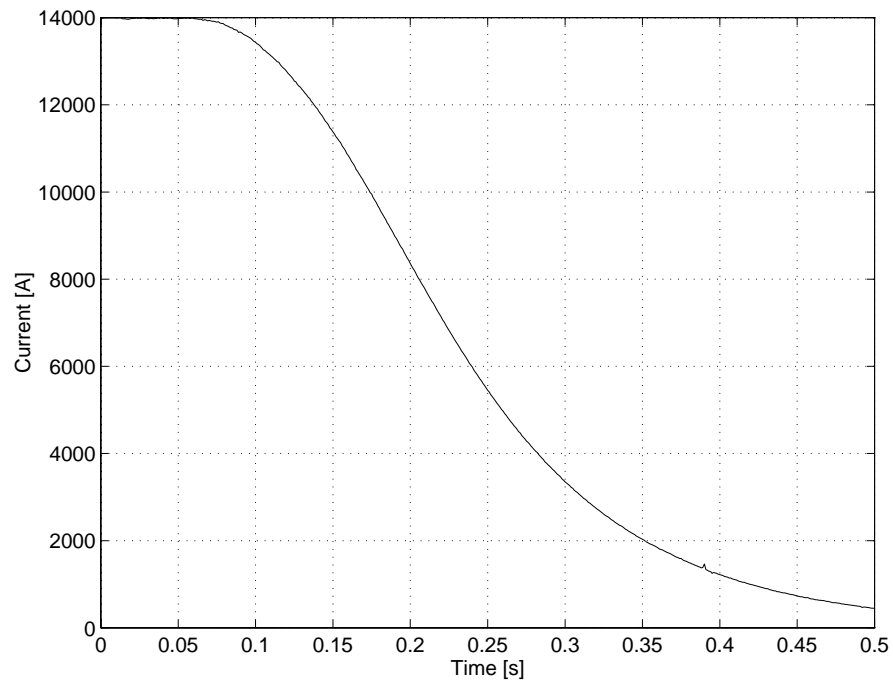


Figure 5.4: Measured magnet current versus time after a heater provoked quench in dipole MB3 at 13994 A

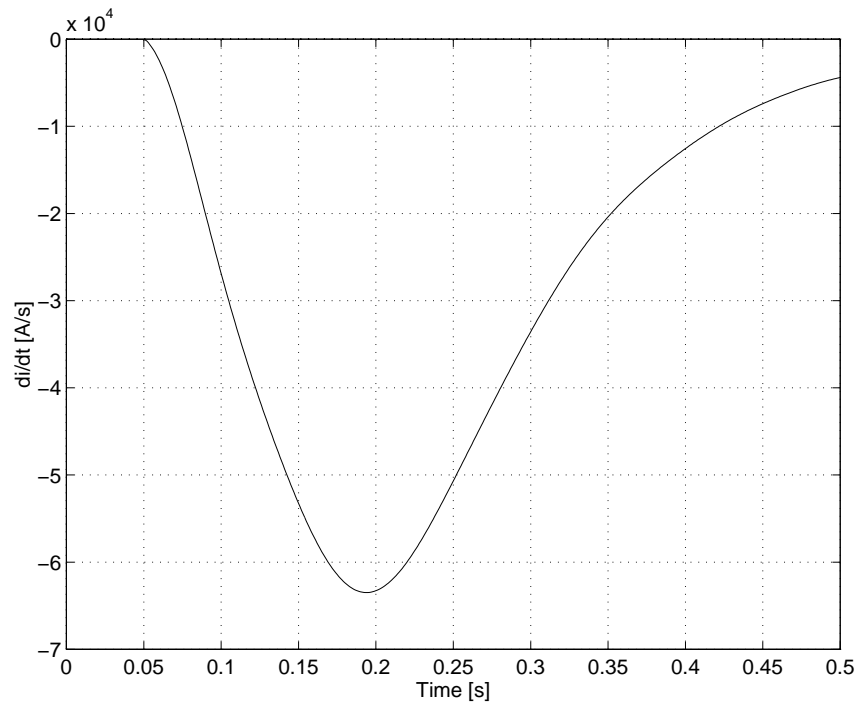


Figure 5.5: Deduced magnet current decay rate versus time after a heater provoked quench in dipole MB3 at 13994 A

The pure inductive voltage across a coil (outer layer or inner layer) can be evaluated via the current de-ramp rate

$$u_{L_{coil}} = L_{coil} \cdot \frac{di_m}{dt} \quad (5.7)$$

by considering the coil inductance L_{coil} as constant.

The resistive voltage

$$u_{R_{coil}} = u_{coil} - u_{L_{coil}}. \quad (5.8)$$

is the difference between the measured coil voltage U_{coil} and the pure inductive voltage $U_{L_{coil}}$ for the outer layer coil (Fig. 5.6 and for the inner layer coil Fig. 5.7).

The coil resistance becomes

$$R_{coil} = \frac{u_{R_{coil}}}{i_m} = \frac{u_{coil} - L \cdot \frac{di_m}{dt}}{i_m}, \quad (5.9)$$

as depicted for both layers of pole 1 in Fig. 5.8.

After exceeding the critical temperature of the superconductor, almost the entire current flows through the copper matrix of the cable. The electrical resistivity of copper is

$$\rho_{Cu} = \frac{R_{coil} \cdot A_{Cu}}{l_m \cdot w} = f(T, B, RRR) \quad (5.10)$$

with A_{Cu} the copper cross section, l_m the magnetic length, and w the assumed number of quenched conductors. Without considering the radial heat propagation into the conductor after firing the heater strips, the average coil temperature is shown in Fig. 5.9. In the very pessimistic assumption, only the conductors covered by the heater strips become resistive (Fig. 5.10, left picture). Therefore the temperature in the outer layer coil rises up to about 160 K while the inner layer coil remains superconducting. More realistic is the case depicted in the right picture of Fig. 5.10. Since quench propagation and quench back support the normal transition, the expected average coil temperature after the de-excitation is about 110 K in the outer layer coil and about 60 K in the inner layer coil. This effect is welcome since the average coil temperature becomes lower. Differences in temperature between the different coils in an aperture are possible due to differences in RRR of the conductors and differences in heater response time after initiating the quench.

During the current decay after a quench, high voltages can appear across the resistive coil sections in the magnet. In order not to endanger the magnet, the voltages have to be kept below the allowed coil insulation voltage. Coil voltages referred to ground (Fig. 5.11), are more representative to estimate the maximum voltage than the differential voltage measurement across magnet coils. A voltage distribution across dipole MB 3 is shown in Fig. 5.12 by interpolating linearly between the measurement points. In reality, the voltage distribution in the magnet depends on the location of resistive and superconducting sections inside the coils. With the number of voltage taps mounted on the magnet coils, a precise measurement cannot be performed. Therefore, a uniform resistance distribution of the resistive section in a coil has been assumed for the analysis.

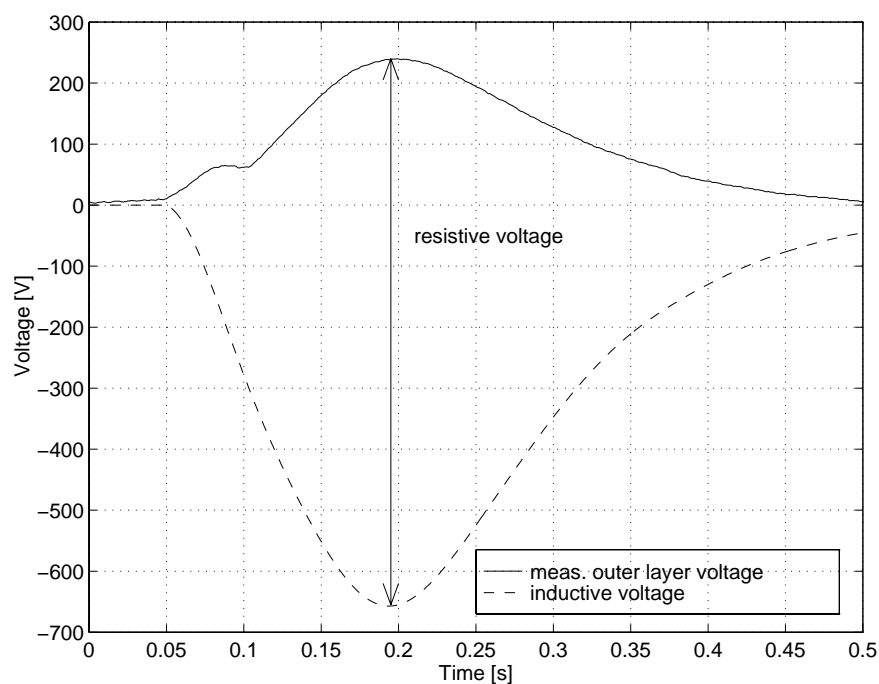


Figure 5.6: Voltage across the outer layer coil of pole 1 after a heater provoked quench at 13994 A (inductive voltage deduced from current decay)

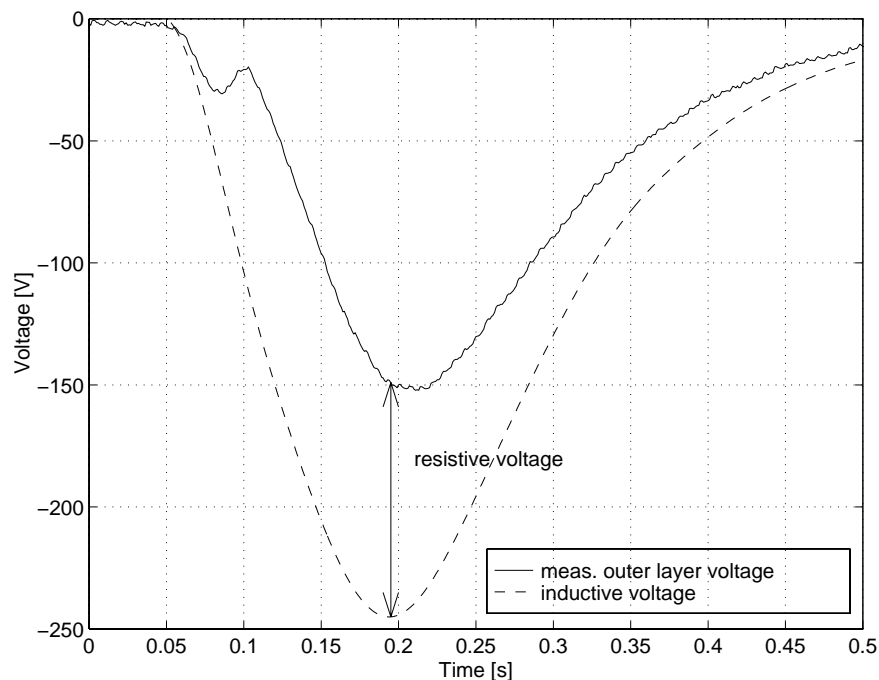


Figure 5.7: Voltage across the inner layer coils of pole 1 after a heater provoked quench at 13994 A (inductive voltage deduced from current decay)

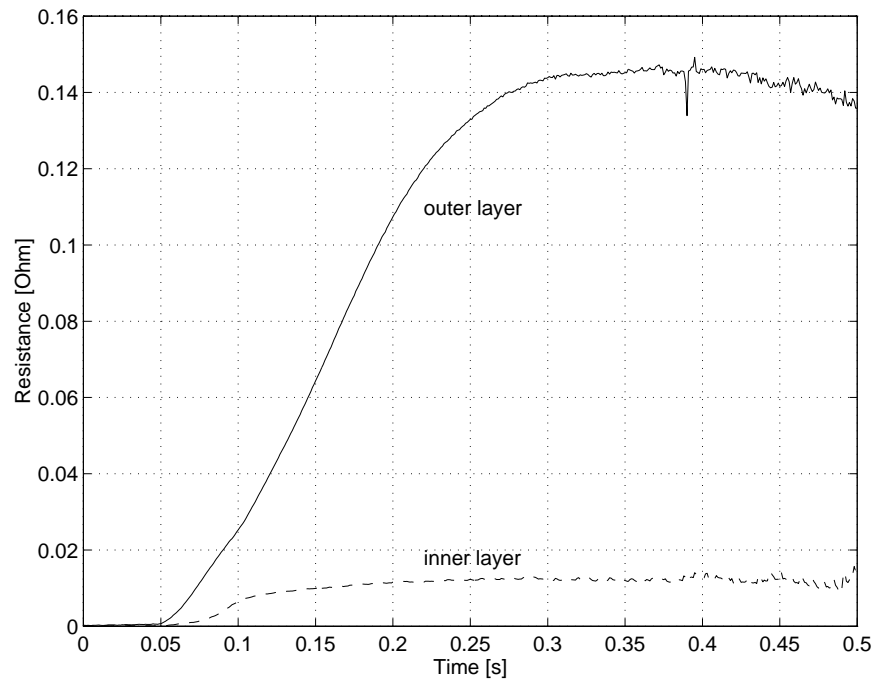


Figure 5.8: Resistance of the outer layer coil and the inner layer coil of pole 1 after a heater provoked quench at 13994 A

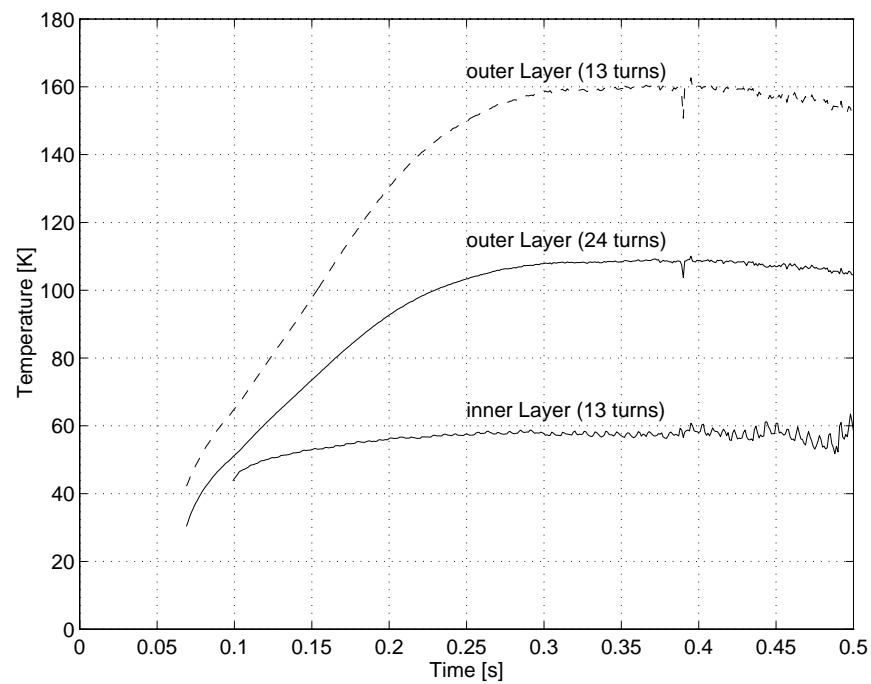


Figure 5.9: Deduced temperature versus time in the outer and inner layer coil after a heater provoked quench at 13994 A

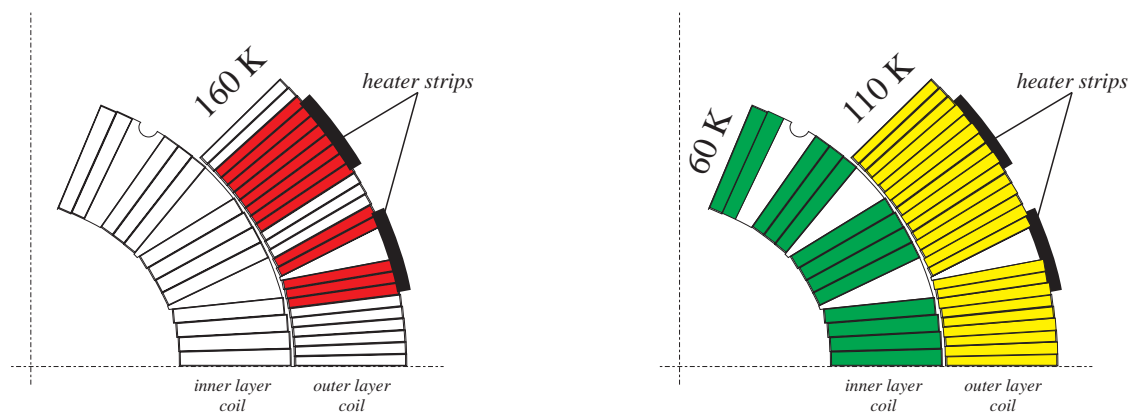


Figure 5.10: Possible number of resistive conductors in the dipole coils after a heater provoked quench at 13994 A

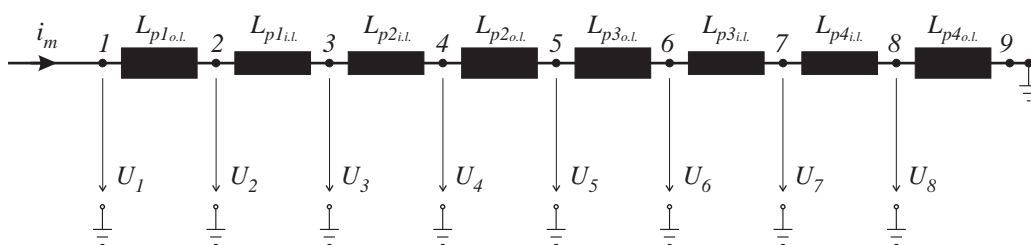


Figure 5.11: Simplified electrical scheme of a dipole magnet

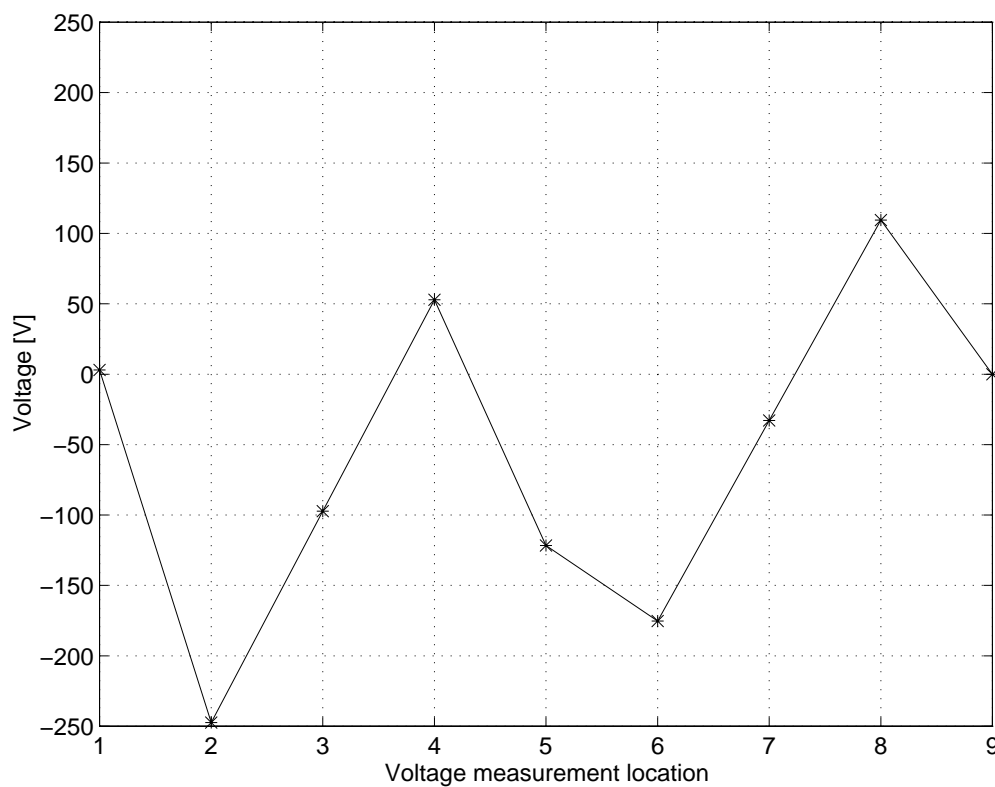


Figure 5.12: Coil voltage distribution in dipole MB 3 after a heater provoked quench at 13994 A

5.3 Quench Behaviour of the LHC Test String

5.3.1 Heater Provoked Quench

Measured Parameters

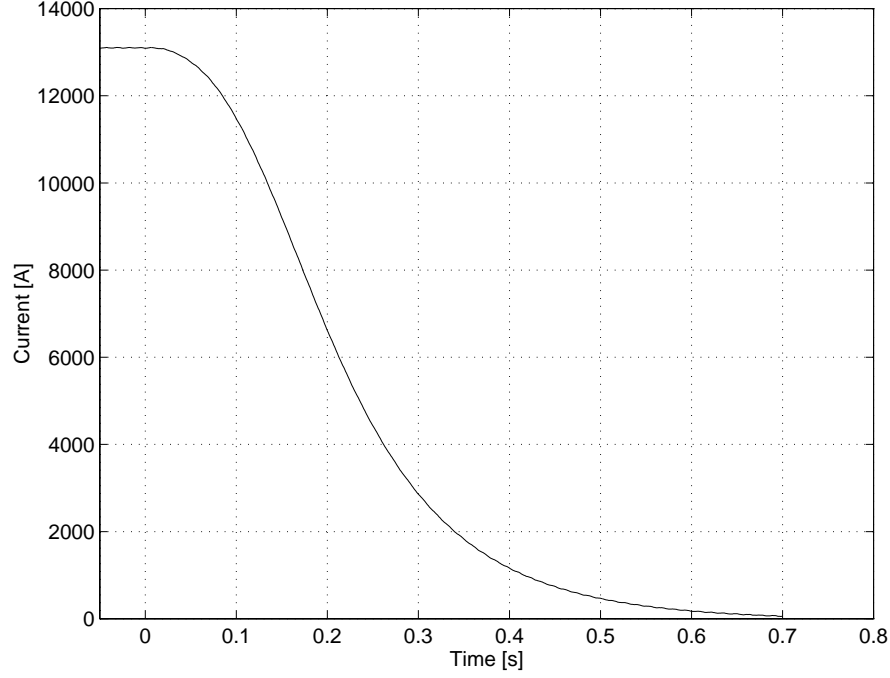


Figure 5.13: String current decay versus time after a heater provoked quench at 13.1 kA

After provoking a half-cell quench by firing the quench heaters in the magnets, heat propagates from the heater strips through the insulation to the conductors of the magnet outer layer coils. At least the conductors which are covered by the heater strips are assumed to become resistive. The magnet currents may decay faster than the string current in Fig. 5.13, by-passing the difference between string current and magnet current through the by-pass diode. As soon as a magnet voltage u_m reaches the turn-on voltage of the by-passing diode, this magnet voltage will be clamped to the diode forward voltage (see Fig. 5.14). Oscillations in the beginning (Fig. 5.15) are mainly caused by differences in heater response time, differences in RRR of copper in the superconducting cables (see Table 4.3), and quench propagation effects in longitudinal and transversal direction.

On the basis of a heater provoked half-cell quench at 13.1 kA in the LHC Test String (see Fig. 5.15), the magnet voltage development across the single magnets is described.

Interval -0.030 s to 0.000 s: The quench heaters are fired at the time step -0.030 s. The quadrupole voltage starts rising up first due to the short quench heater response time. Also the coils in dipoles MB2 and MB3 become partly resistive while dipole MB1 remains superconducting. Since dipole MB3 has lower RRR than dipole MB2, the resistive voltage in dipole MB3 increases faster.

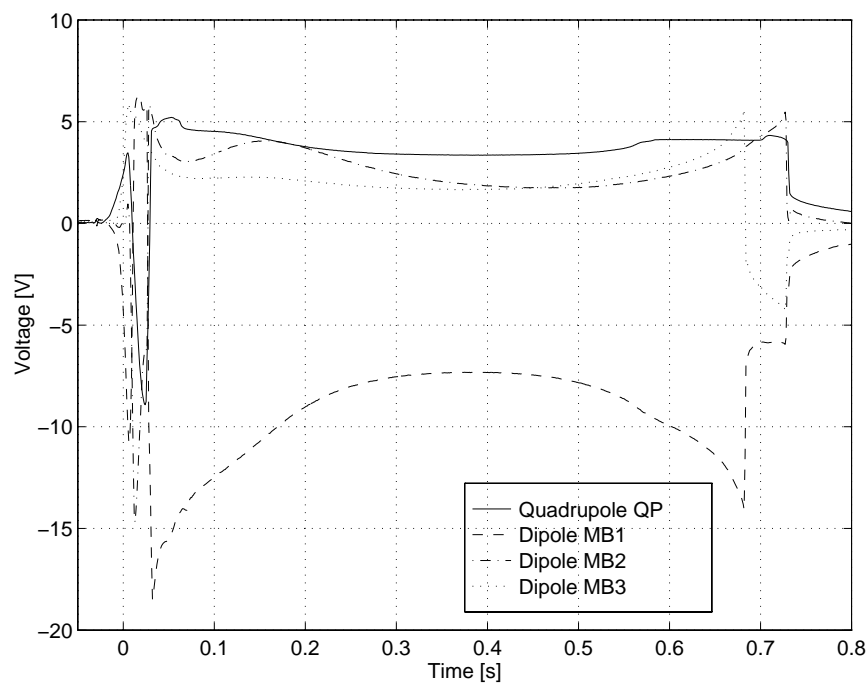


Figure 5.14: Magnet voltages versus time after a heater provoked quench at 13.1 kA

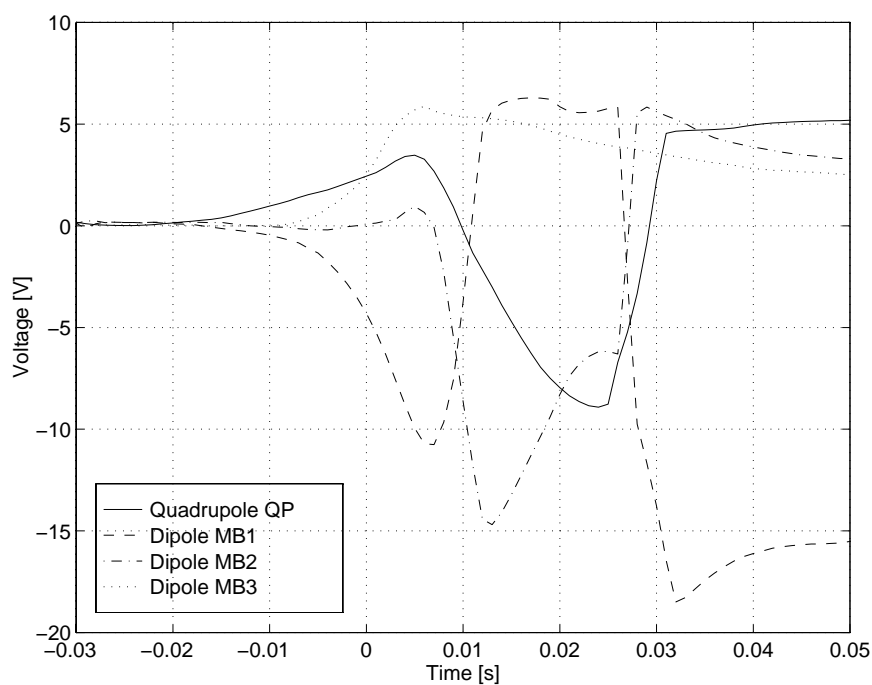


Figure 5.15: Development of magnet voltages after firing the quench heaters at 13.1 kA (zoom of Fig. 5.14)

Interval 0.000 s to 0.025 s: About 37 ms after firing the quench heaters, the resistive voltage in dipole MB1 becomes larger than the inductive voltage. The voltage across dipole MB1 rises up to the forward voltage of the by-passing diode. The fast increase of voltage in MB1 causes a drop down of the voltages across the quadrupole and across dipole MB2 to equilibrate the sum of voltages in the circuit to zero. As soon as the diode across dipole MB1 is turned on, the current in this magnet decays faster. The heat in the resistive sections grows with i_m^2 whereas less heat will be generated. The voltage across dipole MB2 starts rising up again.

Interval 0.025 s to 0.050 s: The current decay in Fig. 5.16 is a function of the inductances and coil resistances of the magnets in the LHC Test String. While in the dipole the inductive and resistive voltage have about the same value, but opposite sign, the resistive voltage in the quadrupole has majority because of the much smaller inductance. About 30 ms after firing the heaters, the resistive voltage across the quadrupole becomes large enough so that the by-passing diode turns on. Due to the fact that the average RRR in dipole MB2 is about 10 % lower than the average RRR in dipole MB1, more heat will be dissipated in dipole MB2 and the coil resistance increases faster than in dipole MB1. The decay rate of the string current becomes stronger whereas the forward voltage of the diode across dipole MB1 will be undershot and the diode starts blocking. At the same time the diode across dipole MB2 turns on and starts by-passing the current. The following voltage decay across dipole MB2 is caused by the temperature dependence of the diode forward voltage.

Deduced Parameters by Simulation

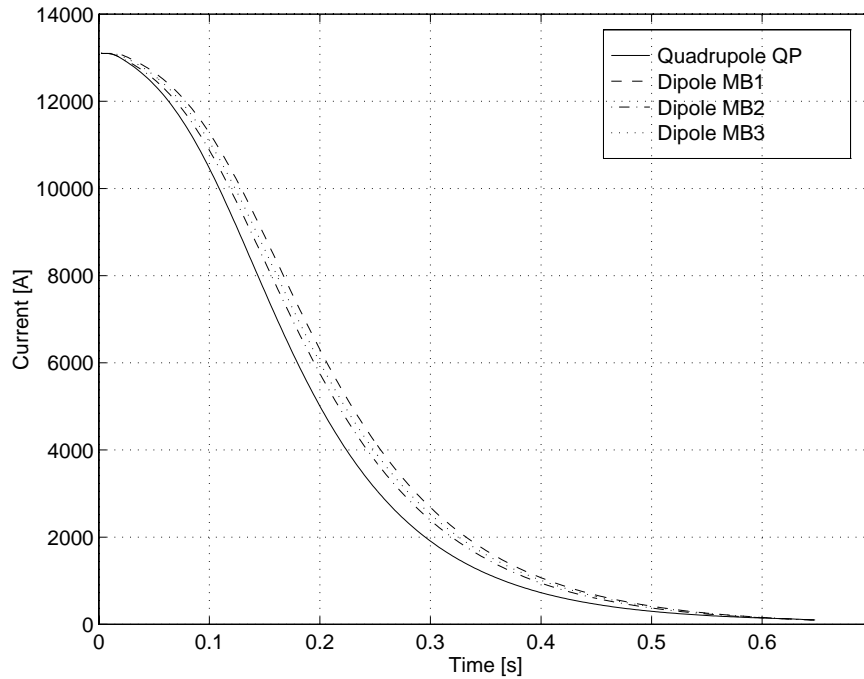


Figure 5.16: Simulated magnet currents versus time for a heater provoked quench at 13.1 kA

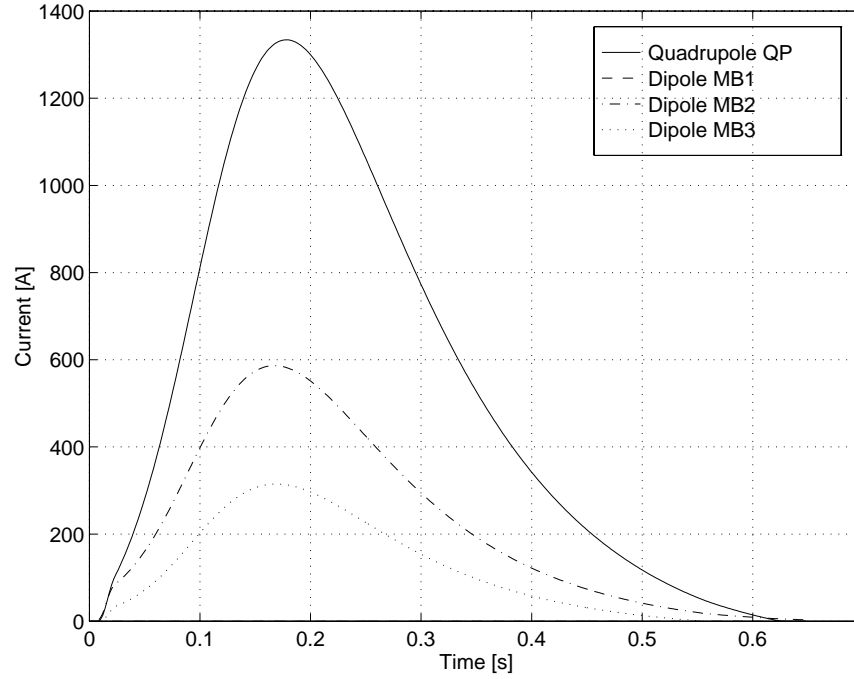


Figure 5.17: Simulated diode current versus time for a heater provoked quench at 13.1 kA (Note: Current across dipole MB1 is zero)

The simulation program is fed with the quench heater delay (see Table 4.3) and the initial current deduced from the experiment. It calculates the current decay in the single magnets (Fig. 5.16) as well as the current through the by-pass diodes (Fig. 5.17).

Fig. 5.18 shows the simulation of the average magnet resistance development in the magnets of the LHC Test String after a quench at 13.1 kA. The step at the beginning is given by the transition from the superconducting state to the resistive state. This worst case simulation considers only the conductors which are located below the quench heater strips as resistive (Fig. 5.10, left picture). The average temperature in the resistive coil sections is shown in Fig. 5.19. The more conductors are becoming resistive after a quench, the lower will be the final coil temperature. Table 5.3 lists some results, simulated for a heater induced quench at 13.1 kA. Since the voltage across the by-pass diode of MB1 is negative (Fig. 5.14), no energy is dissipated in this diode during the discharge.

If all dipoles in the LHC Test String would have the same properties (RRR, heater delay, inductances, etc.) and would be assembled without any differences in geometric dimensions and parameters, the diodes across the dipole magnets would not turn-on in case of a fast discharge. They would all have the same voltage

$$u_{m2(3,4)} = -\frac{1}{3} (U_{Dfw} + i_s \cdot R_c + u_{m1}) .$$

Since this is not the case, the string current decay is determined by the magnets which have not reached the turn-on voltage of their by-pass diode.

The coil resistance in a magnet with low RRR grows up faster than in a magnet with higher RRR.

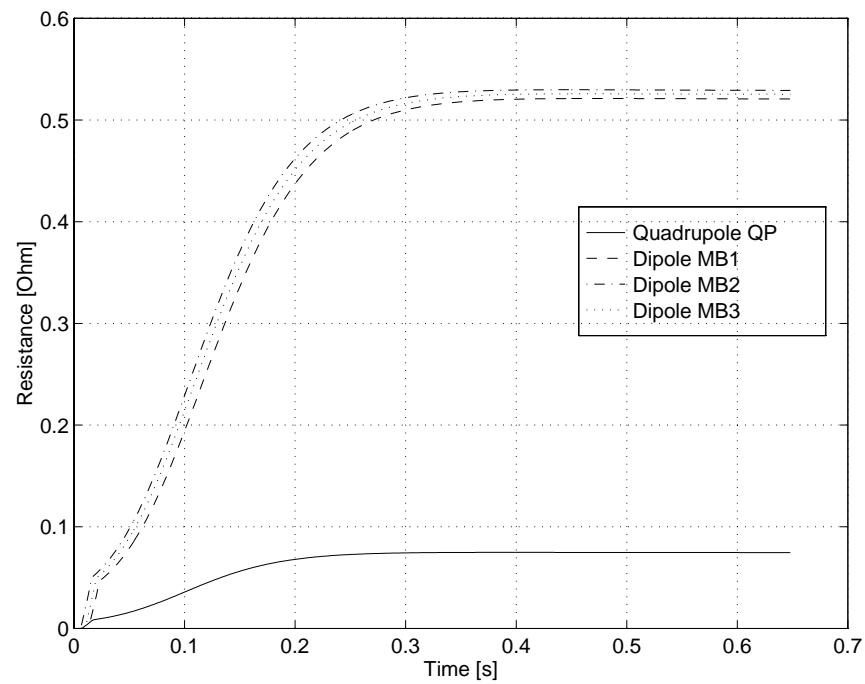


Figure 5.18: Simulated average magnet resistance versus time for a heater provoked quench at 13.1 kA

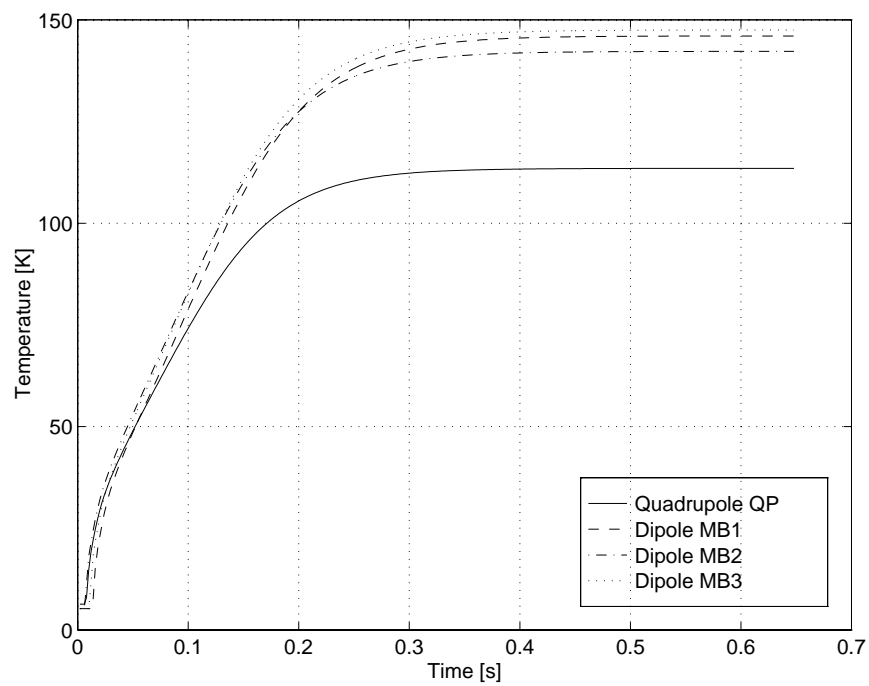


Figure 5.19: Simulated average temperature in the resistive sections of the magnet coils versus time for a heater provoked quench at 13.1 kA

Table 5.3: Results deduced from a simulation of a heater induced quench at 13.1 kA (*RUN0525*)

Magnet	av. magnet	av. coil	dissipated energy	
	resistance [Ω]	temperature [K]	magnet [MJ]	diode [MJ]
Quadrupole QP	0.075	114	0.6412	1.4977
Dipole MB1	0.521	146	4.8444	0.0000
Dipole MB2	0.530	144	4.8834	0.2848
Dipole MB3	0.525	148	4.8834	0.1549

A delayed firing of the quench heaters of one dipole in respect to the others results in a higher current through the diodes, connected parallel to the already resistive magnets. The string current i_s decays according Eq. 4.15 and is determined by the external resistance, the inductance of the still superconducting magnet, and the sum of forward voltages in the circuit, as shown in the electrical scheme Fig. 4.1.

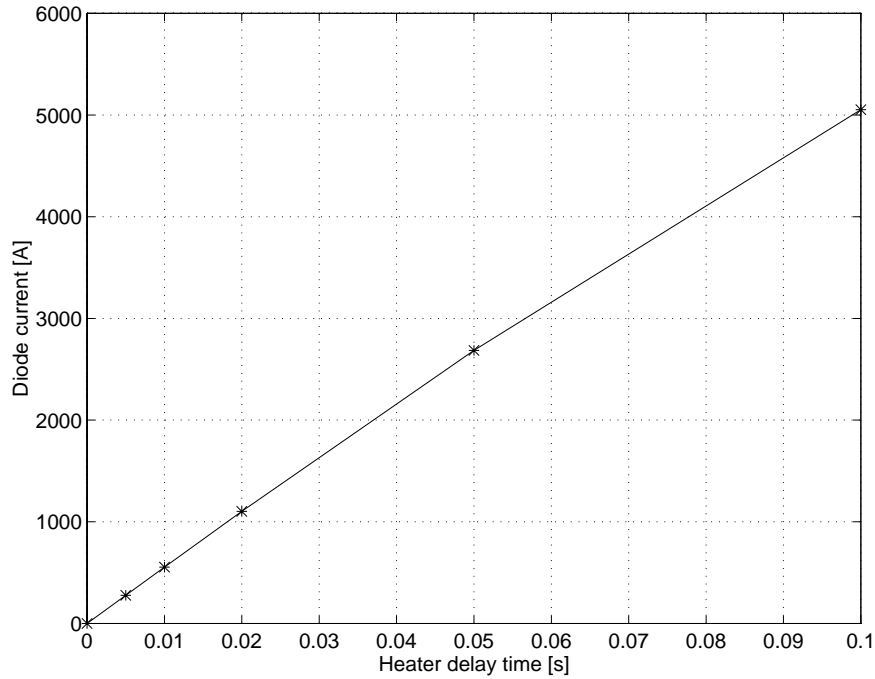


Figure 5.20: Simulated maximum bus-bar current versus heater delay time after a quench at 12400 A

A simulation has been performed. As shown in Fig. 5.20, the diode current rises almost linearly with increasing quench heater delay time. The adiabatic average temperature of the small cross-section auxiliary bus-bars, connecting the diodes parallel to the dipoles, depends on $\int i_D^2(t)dt$. Fig. 5.21 shows the final bus-bar temperature at different heater delays.

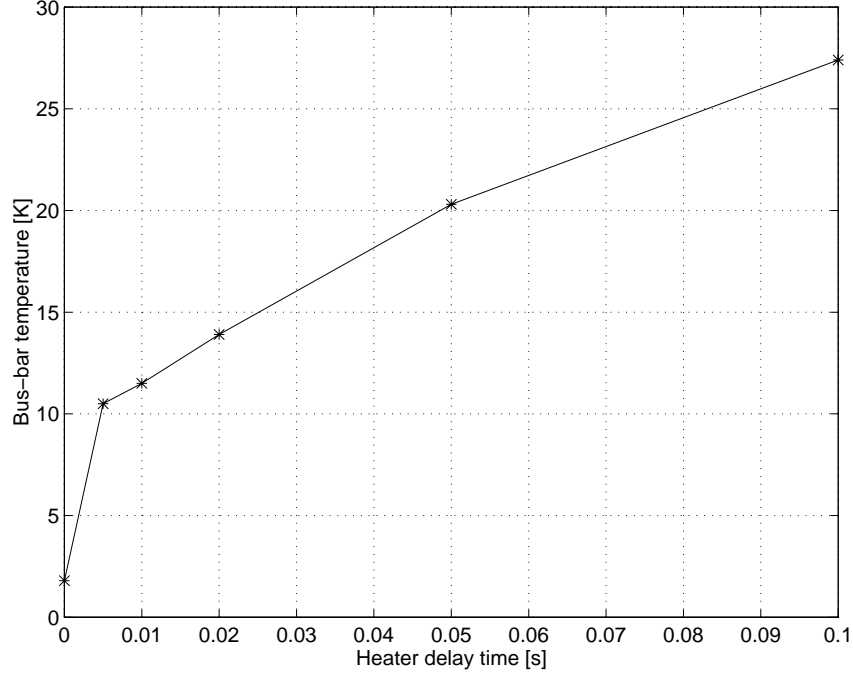


Figure 5.21: Simulated maximum temperature of the auxiliary bus-bar leads for different heater delay times after a quench at 12400 A

5.3.2 Natural Quench

In case of a natural quench in a superconducting dipole magnet for the LHC, the cable section around the quench origin has the highest temperature. By exceeding the minimum propagation zone, the normal zone starts growing in longitudinal direction, symmetrically about the quench origin (Fig. 2.4). At nominal current the high current density ($\approx 550 \text{ Amm}^{-2}$) in the LHC magnets, coupled with the relatively slow propagation speed (≈ 20 to 30 ms^{-1}) may lead to high temperatures around the quench origin [9]. The generated heat also penetrates through the coil insulation in transversal and radial direction.

As deduced from a natural quench experiment (*RUN1090*), the quench detector, observing the quenching section, becomes unbalanced (Fig 5.22) due to a resistive section in pole 1. Since the turn-on voltage of the by-pass diode across the quenching magnet has not been reached, until the heaters are fired at time step -0.013 s, the entire string current i_s flows through the magnet coils. The resistance in pole 1 is given with

$$R_{p1} = \frac{u_{qd}}{2 \cdot i_s} \quad (5.11)$$

where u_{qd} is the output voltage from the bridge quench detector (see Fig. 3.13). The factor 2 in Eq. 5.11 considers the voltage divider in the symmetrical bridge circuit. Fig. 5.23 shows the increase of resistance in the quenched pole before the quench heaters are fired.

Increasing the quench detector threshold level extends the time interval, until a quench is detected. As soon as the quench detector input voltage exceeds the threshold level, the

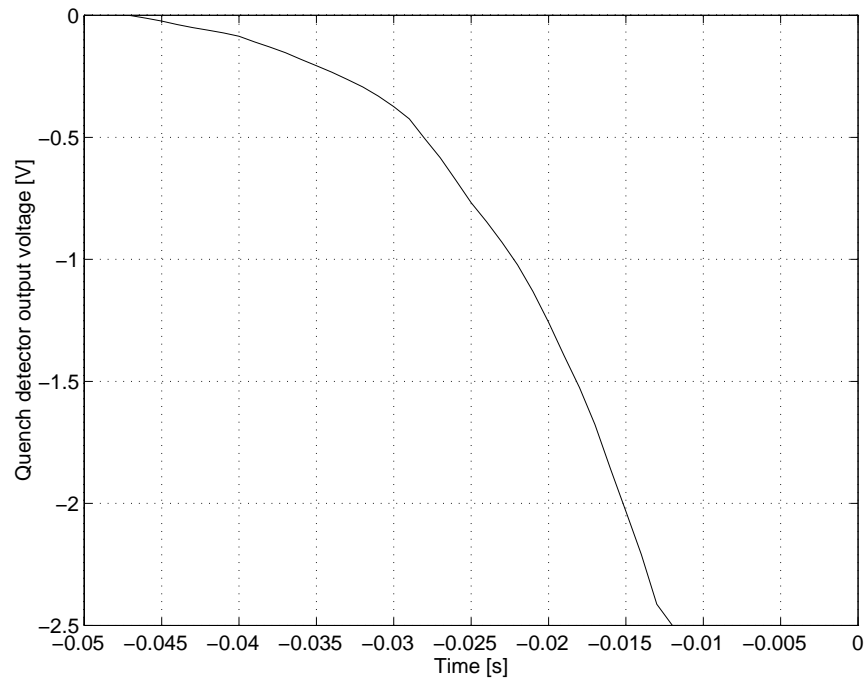


Figure 5.22: Measured output voltage of the bridge quench detector across aperture A of dipole MB2 during a natural quench at 13283 A

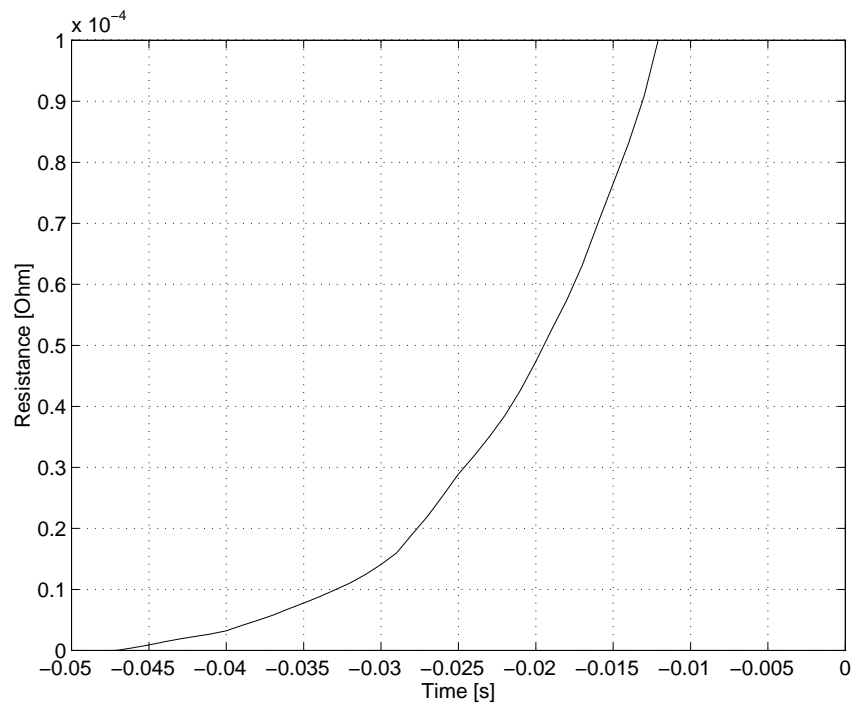


Figure 5.23: Resistance development in pole 1 of dipole MB2 during a natural quench at 13283 A

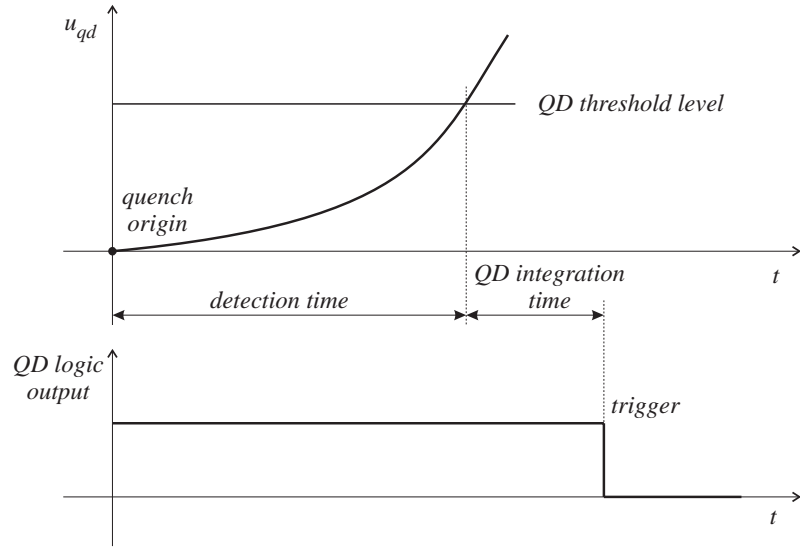


Figure 5.24: Chronology of quench detection

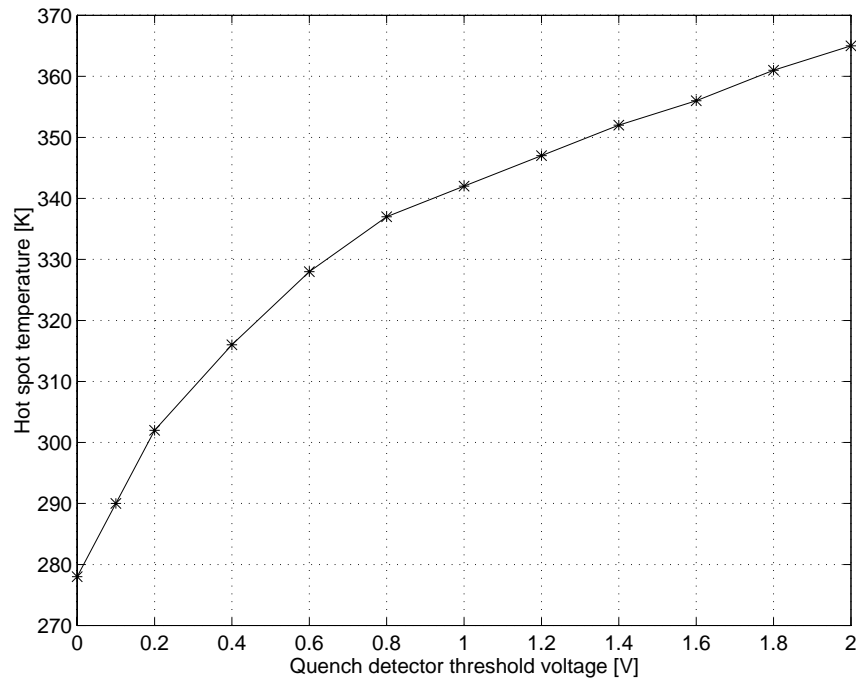


Figure 5.25: Adiabatically calculated hot-spot temperature in the outer layer coil at different quench detection levels after a natural quench at 13283 A

quench detector waits about 10 ms (quench detector integration time) in order to distinguish between a quench signal and a voltage spike (Fig. 5.24).

If the detector identifies the event as a quench, a trigger is sent to the interlock system. After the quench heaters are fired, the heat penetrates through the insulation to the coil. The time duration, between firing the heaters and exceeding the critical temperature of the superconductor is the heater response time. Until the magnet becomes resistive over the whole magnet length, the magnet current is almost constant. The hot-spot temperature in a quenched magnet depends on $\int i_m^2 dt$. Reducing the hot-spot temperature requires a fast detection of a quench and therefore a low detection level (Fig. 5.25). The hot-spot temperature is determined by considering adiabatic conditions which is the worst case. The relation between quench detection level and time is deduced from Fig. 5.22.

5.4 Inter-magnet Quench Propagation

The number of magnets quenching in an octant of the LHC should be limited to a minimum. It may be a dangerous for some elements of the magnet protection system because high reverse voltages might appear across a number of cold diodes. The cryogenic recovery of a quench of many magnets takes a long time. Typically, multiple or cascade quenching can be provoked by thermo-hydraulic quench propagation, by excessive negative di/dt , by beam losses, or by a global quench detection or control system error. It is essential to know if the quench in one of the LHC superconducting magnets will propagate to the neighbouring magnets and to understand possible mechanisms of a propagation [8].

5.4.1 Set-up of Quadrupole Quench Propagation Experiments

In the design of the LHC machine the quench protection acts at the magnet level. If a quench in one magnet is detected, the quench heaters only in the magnet concerned are fired. In order to study inter-magnet quench propagation in the LHC Test String, a special setting of the magnet protection electronics was necessary, since the quench heater strips in the quadrupole magnet have to be fired independently from the quench heater strips in the dipole magnets. Quench relief valves in the LHC Test String are located at the front end of the quadrupole and at the rear end of the third dipole magnet. Both relief valves can be opened automatically or manually if the pressure is below a defined threshold level of about 12 bar. The relief valve at the front end of the LHC Test String is situated below the superconducting coils. By opening this valve, vaporized and liquid helium will be extracted from the cold mass. The position of the quench relief valve at the rear end is located above the magnet coils, where mainly vaporized helium will be extracted by opening it after a quench.

The two essential effects on the inter-magnet quench propagation, which have to be considered, are the heat transport via helium and heat conduction through the metallic bus-bars. All quench protection diodes are directly immersed in the superfluid helium bath.

In case of a quench in the quadrupole, the current through it decays in less than a second. Almost the whole string current by-passes the quadrupole magnet through the diode triplet. The copper heat sinks around these diode packages heat up and distribute heat both to the surrounding helium and to the connected, highly copper stabilised, diode bus-bars.

Fig. 5.26 shows the location of the diode triplet and the bus-bars, located in the short straight section behind the quadrupole. In the serial chain of magnets the quadrupole is connected to the first dipole magnet via the main bus-bar MBB. Both the main bus-bar and the diode bus-bar are highly stabilised with copper, which facilitates the solid heat conductivity.

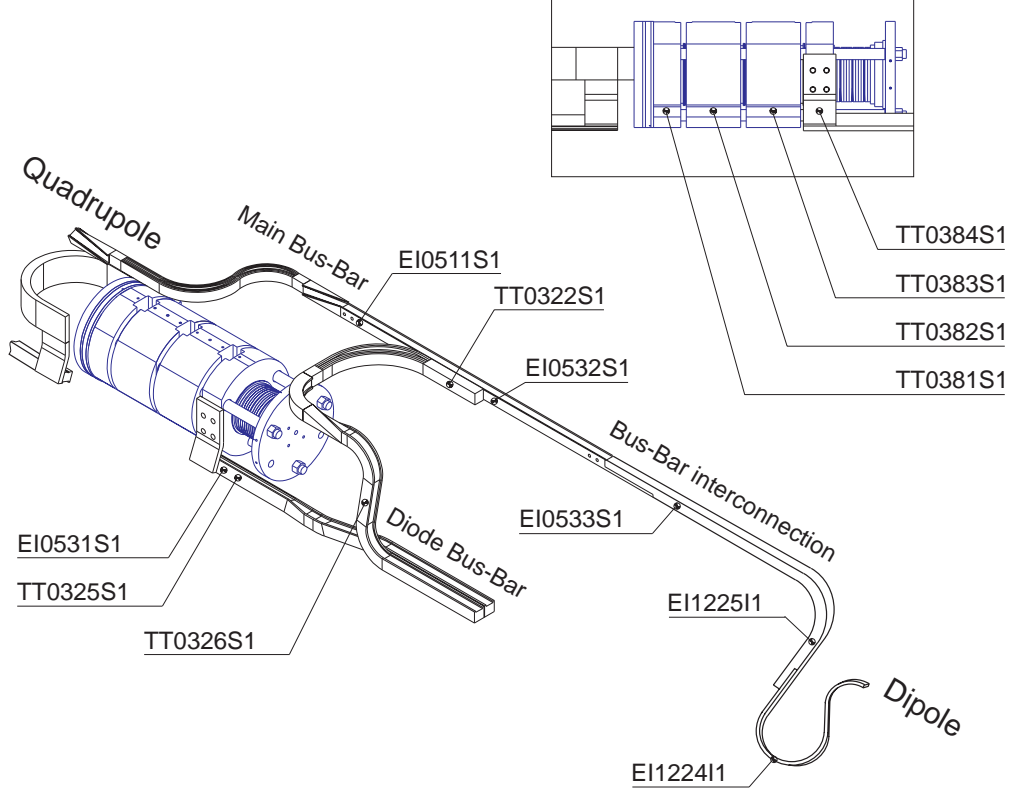


Figure 5.26: Short Straight Section with protection diodes and instrumentation

In order to measure the temperature development after a quadrupole quench, some carbon temperature sensors are located in the stabilisation copper of the bus-bars. TT0325S1 is mounted close to the diode triplet, TT0326S1 about in the middle between the diode triplet and the connection to the main bus-bar, and TT0322S1 is situated on the connection of the diode bus-bar to the main bus-bar. Platinum sensors (TT0381S1 to TT0384S1) on the heat sinks indicate the generated heat in the diode triplet. Pressure and temperature probes are located in the end volumes of each superconducting magnet. Voltage taps on the bus-bar permit the voltage drop measurements along the bus-bar from the quadrupole to the neighbouring dipole magnet. The voltage drop across the transition from the stabilised section to the non-stabilised section in the dipole magnet is of essential interest (Fig. 5.27).

5.4.2 Quadrupole Quench Propagation Experiments

All quench propagation test runs were performed at 1.9 K. Table 5.4 summarizes the parameters for the different quadrupole quench propagation experiments. For different initial currents quenches are provoked by firing the quench heater strips of the quadrupole only. At the same time the power converter switches off and the thyristor circuit-breaker opens.

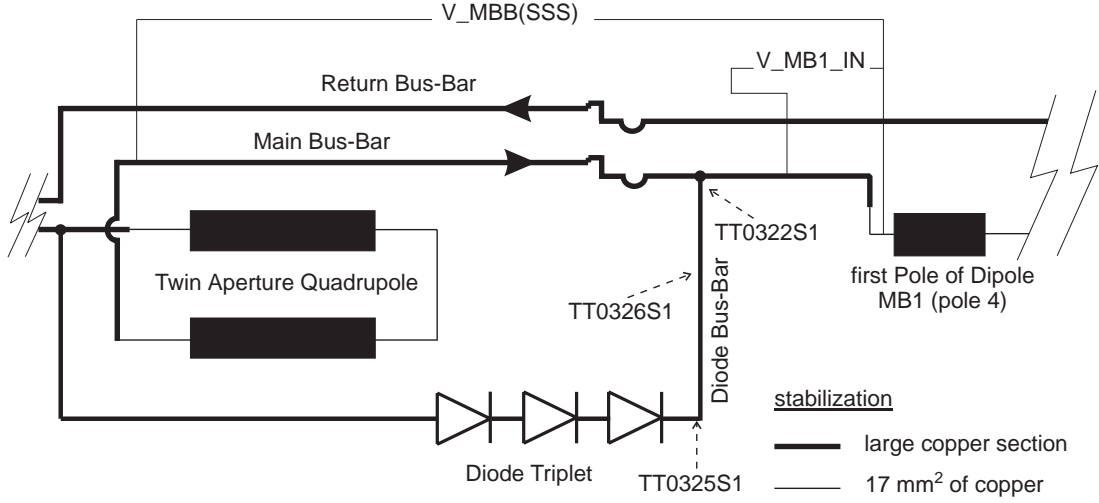


Figure 5.27: Simplified electrical scheme for quadrupole quench propagation experiments

While the quadrupole de-excites in less than a second, the current in the still superconducting dipole magnets decays with a time constant of about 100 s, governed by the sum of dipole inductances and the value of the external dump resistor, connected parallel to the thyristor switch.

Once a quench is detected in one of the dipole magnets, the quench heaters are fired in all dipoles and the current decays to zero within several hundred milliseconds. To fire just the quench heaters in the quenching dipole in the LHC Test String would overheat the auxiliary bus-bars of small copper cross section, connecting the by-pass diode across the quenched magnet.

Table 5.4: List of quench propagation experiments

run No.	initial current [A]	dipole quench at [A]	valve delay [s]	dipole quench after [s]	max. pressure [bar]
RUN702	5000	no quench	-	-	8.2
RUN704	7000	3350	overpressure	63	11.5
RUN713	7000	2600	35	79	7.9
RUN726	7000	3250	5	66	3.5
RUN749	9000	4920	5	59	1.3
RUN764	11000	6900	5	51	1.5
RUN781	11000	6600	25	54	8.1
RUN766	13100	9030	5	45	1.5

The diode triplet which by-passes the current across the quadrupole heats up to about 100 K at an initial quench current of 7 kA. Most of the heat will be exchanged with the surrounding helium, while part of it will propagate along the highly stabilised diode bus-bar.

Quench propagation experiments with manually delayed opening of the quench relief valves

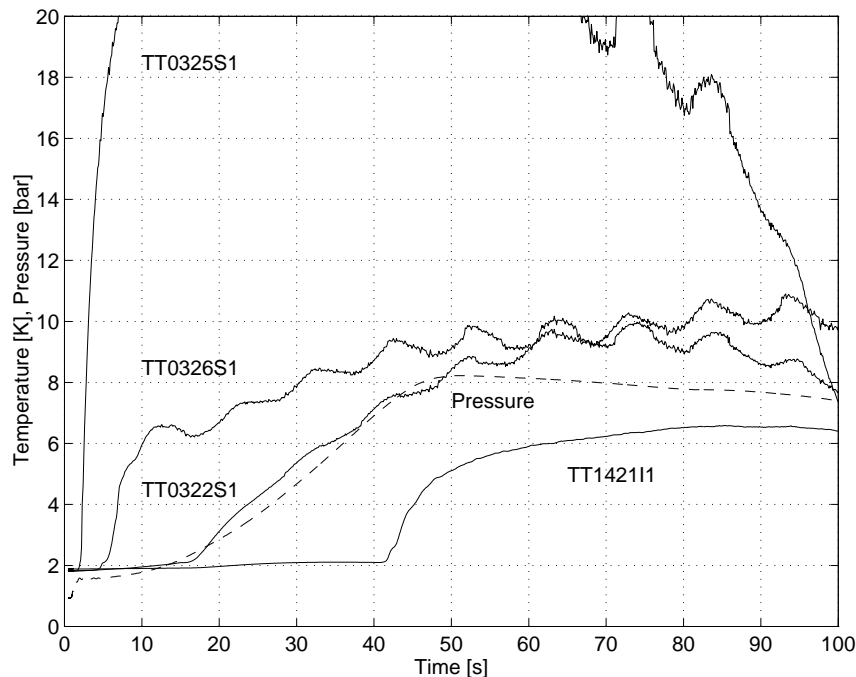


Figure 5.28: Pressure and temperature versus time for a quench at 5 kA and closed quench relief valves

If the pressure in the cold mass is below the threshold level of 12 bar, the quench relief valves can be opened manually. At an initial current of 5 kA the generated heat in the diode triplet and the quadrupole is too small to quench the neighbourhood dipole during the de-excitation procedure. The vaporized helium generates pressure in the cold mass up to about 8 bar, which is below the pressure threshold level of the quench relief valves (Fig. 5.28). The main bus-bar at the location of TT0322S1 becomes close to the critical temperature of the NbTi superconductor. Since the decaying string current i_s is rather small, the still surrounding helium starts cooling the bus-bar. The discharge finishes without quenching the dipole magnet.

Increasing the initial current to 7 kA leads to a quench of the neighbouring dipole magnet during the discharge. As long as the quench relief valves stay closed after provoking a quadrupole quench, the dissipated energy causes a pressure rise inside the cold mass. The helium becomes supercritical. The temperature sensor TT0325S1, located close to the triplet heat sink, indicates a fast increase in temperature up to about 30 K (see Fig. 5.29). The temperature of the main bus-bar starts rising up about 15 s after initiating the quench in the quadrupole and increases almost linearly with time.

In case of delayed opening of the quench relief valve at the rear end of the LHC Test String after 35 s and blocking the quench relief valve at the front end, a prolongation of the propagation time of about 10 % is possible. As long as the quench relief valves stay closed, the temperatures and the pressures rise up and the helium become supercritical, but it does not circulate. After opening the quench relief valve at the rear end of the LHC Test String,

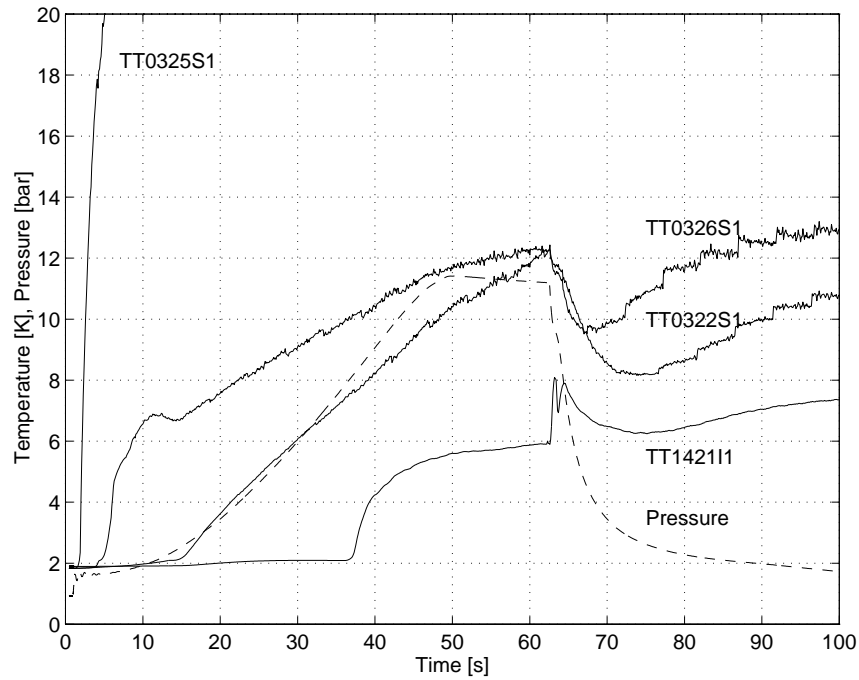


Figure 5.29: Pressure and temperature versus time for a quench at 7 kA by limiting the cold mass pressure to about 12 bar.

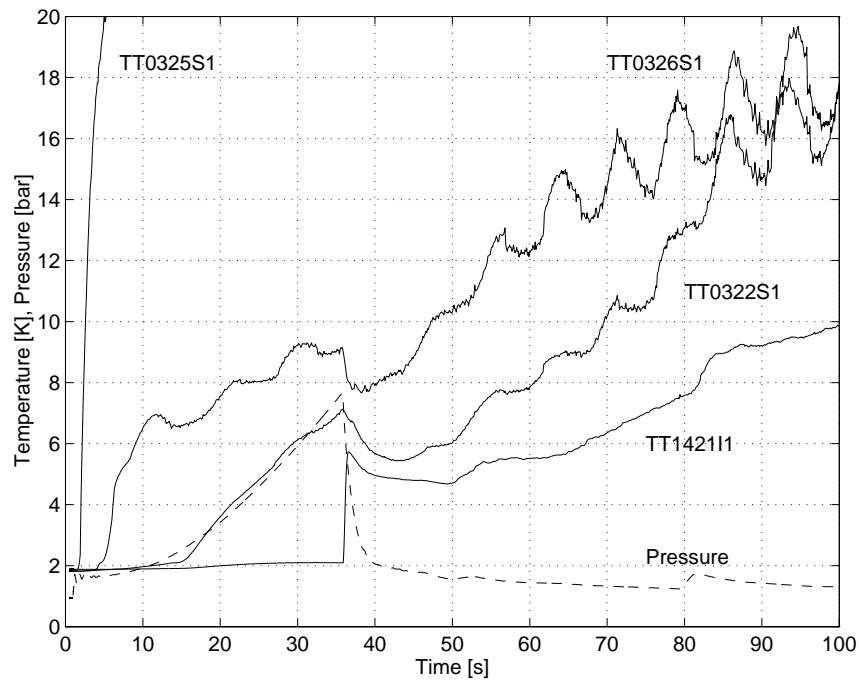


Figure 5.30: Pressure and temperature versus time for a quench at 7 kA by opening the relief valve on MB3 after 35 s.

the bus-bar temperature at TT0322S1 which is already close to the critical temperature of the NbTi superconductor decreases again (Fig. 5.30). Also the helium wave after opening the relief valve may cool again the bus-bar section.

After the liquid is vaporized, the bus-bar temperature increases again. The heat propagates along the bus-bar to the dipole magnet. The extension in delay time depends mainly on the re-cooling effect of the bus-bar after opening the relief valve.

Different opening delays of the quench relief valve on MB3 have shown only a weak correlation between the pressure in the cold masses of the magnets and the delay for the dipole to quench.

Quench propagation experiments with opened quench relief valves

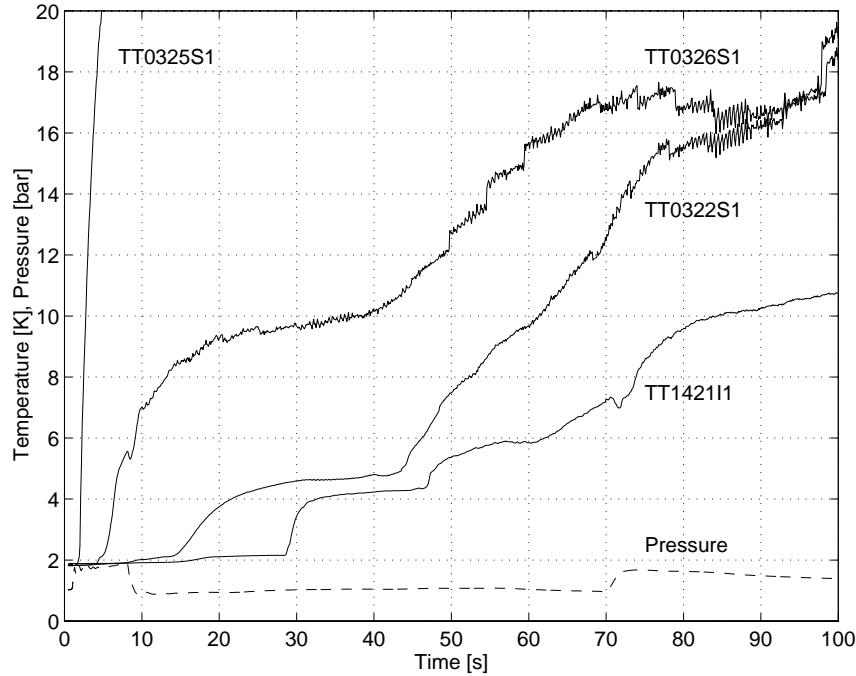


Figure 5.31: Pressure and temperature versus time for a quench at 7 kA and open relief valve on MB3

Most of the quench propagation experiments were performed with opened quench relief valve at the rear end of the LHC Test String about 5 s after the initiation of the quadrupole quench. This gives the possibility to study the effect of quench propagation from different initial current levels. After an initiated quadrupole quench at 7 kA, as shown in Fig. 5.31, the diode bus-bar at position TT0325S1 heat up immediately due to the closeness to the diode heat sink. TT0326S1, situated in the middle of the diode bus-bar, shows already a delay of about 5 s before heating becomes strong enough to vaporize superfluid helium. After 15 s the heat reaches the main bus-bar at TT0322S1. The section starts warming up from 1.9 K to helium I temperature of 4.2 K and stays at this level for some seconds until the surrounding helium is vaporized. The absence of helium II around the bus-bar diminishes the heat transfer from the latter to the bath. Propagation through the about 2 m long main bus-bar at the interconnection between the quadrupole and the first dipole magnet needs

about 15 s at this current level. The temperature in the main bus-bar, indicated with the temperature probe TT0322S1, exceeds the critical temperature of the NbTi superconductor, and hence it is the copper stabiliser which takes over the current. The signal from the voltage taps across the main bus-bar confirms this interpretation. Close to the dipole coil the copper section of the main bus-bar is reduced from about 300 mm² to 17 mm². A voltage measurement across this transition area (Fig. 5.27) shows a fast increase in voltage of about 2 mV just before it is detected in the dipole magnet. The voltage step is proportional to the current. It has been observed that the pole of the first dipole connected to the main bus-bar always quenched first. This is another indication for a quench propagation through the main bus-bar as the origin for the quench in the magnet.

Experiments at 9 kA, 11 kA, and 13.1 kA show results similar to the 7 kA tests. Due to the higher energy dissipated in the diode triplet and in the resistive bus-bar, the quench along the bus-bar propagates faster and time until the dipole quenches, becomes shorter.

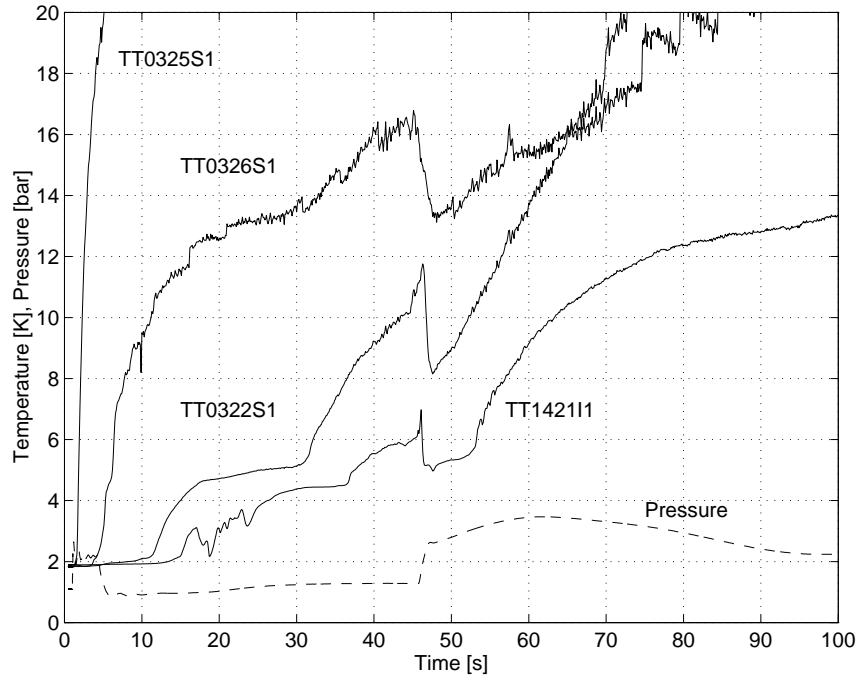


Figure 5.32: Pressure and temperature versus time for a quench at 13.1 kA by opening the relief valve on MB3 about 5 s after initiating a quench in the quadrupole

Fig. 5.32 shows the temperature profile of the bus-bar and the pressure in the short straight section, recorded for a quadrupole quench propagation test with an initial current of 13.1 kA.

As shown in Fig. 5.33, the dipole magnets quench during the de-excitation some tens of seconds later if the initial current is above 5 kA. The delay time is related to the initial current level.

The quench propagation velocity along the bus-bar is rather small. Assuming that the critical temperature of the superconducting cable is about 9 K, the heat needs more than 7 s to propagate from the position of TT0322S1 along the interconnection bus-bar to the

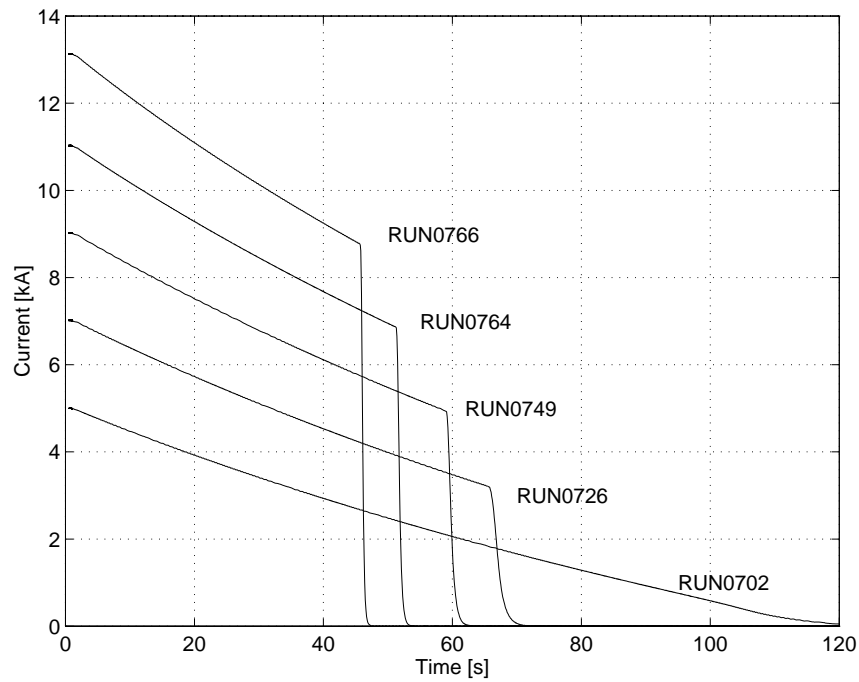


Figure 5.33: Current versus time after provoking a quadrupole quench with quench heaters at different initial current levels

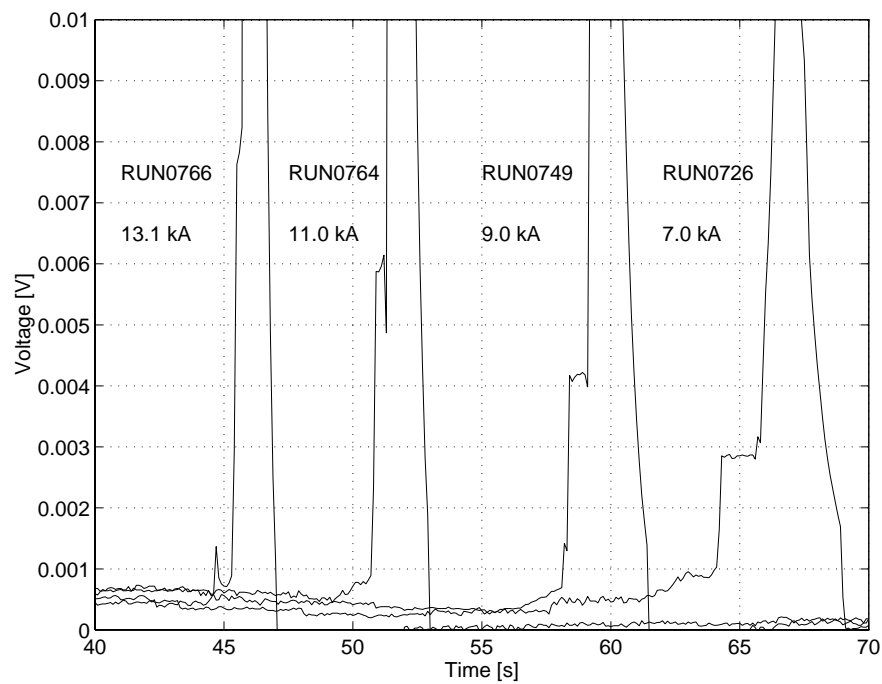


Figure 5.34: Voltage versus time across the transition of the stabilised and non-stabilised bus-bar section in the dipole at different initial current levels

less stabilised cable at the entrance of dipole MB1. At an initial current of 7 kA the quench propagation velocity is about 0.1 ms^{-1} . This is about 10 to 20 times lower than in the quench propagation model (see section 4.7) which does not consider the heat transfer between bus-bar and helium.

The voltage drop across the main bus-bar shows a constant signal as long as the bus-bar temperature is below the critical temperature of the superconductor (see Fig. 5.34). During the propagation along the interconnection bus-bar the voltage rises up slowly because of the high copper stabilisation. As soon as the weak stabilised part of the superconducting cable leading into MB1 quenches, the voltage increases rapidly to a higher level dependent on the level of the decaying current. Due to the cooling conditions of helium, the voltage stays constant at this level or rises up slowly until the heat is penetrated to the connected coil of the dipole magnet.

5.5 Quench Heater Performance Tests

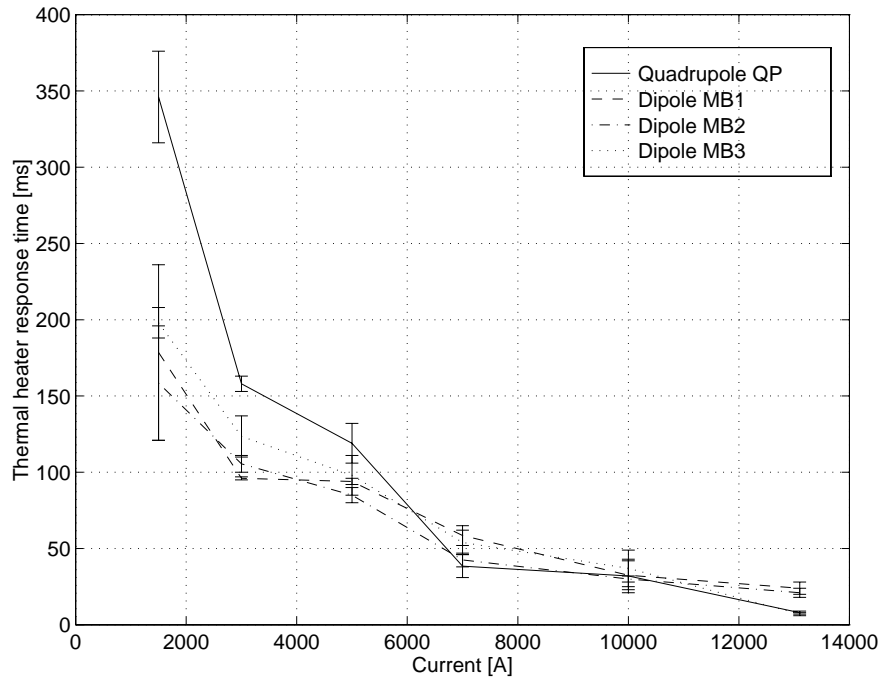


Figure 5.35: Measured time delays from protection heater firing until resistance in the superconducting coil appears

In the LHC Test String, one of the most crucial points for the magnet protection is given by the difference in minimum heater-provoked quenching current I_{hmin} between dipoles. If I_{hmin} is different for the dipoles, the small cross-section auxiliary diode leads (ADL2 to ADL4) in the by-pass circuit of each dipole could be damaged. This risk is strongly linked to the minimum current levels for which the heaters are still effective in one dipole and not in the others, and to the de-excitation time constant of the heater circuit.

The quench heater response time had been checked during heater induced quenches at different initial current levels. This was necessary to assure that the superconducting mag-

nets are quenchable by heating down to a certain current level, below which the maximum auxiliary lead temperature does not cause a damage of the auxiliary lead (see section 3.2.5).

Fig. 5.35 shows the thermal response time of the quench heaters in the different magnets as a function of initial magnet current. At high current levels the heater response time t_h is within 20 ms while at low current levels it can be one order of magnitude higher.

Differences in quench heater response time are usually not of electrical nature. They are mainly caused due to small deviations during the installation on the coil. The strips are mounted on the outer side of the conductors. Slightly different thickness of the polyimide insulation, local pressure differences during collaring, and superfluid helium in between cause in a longer time to penetrate from the heater strip to the coil conductor.

5.6 Balancing the Quench Detectors

Magnet coil quench detectors operate in bridge detection mode, while bus-bar quench detectors are switched in amplifier mode. Due to the high self inductances of the magnet coils, the quench detector circuits are sensitive to inductive voltages which appear during ramping and de-ramping. In discharge experiments without quenching the magnets, the bridge circuits can be well balanced.

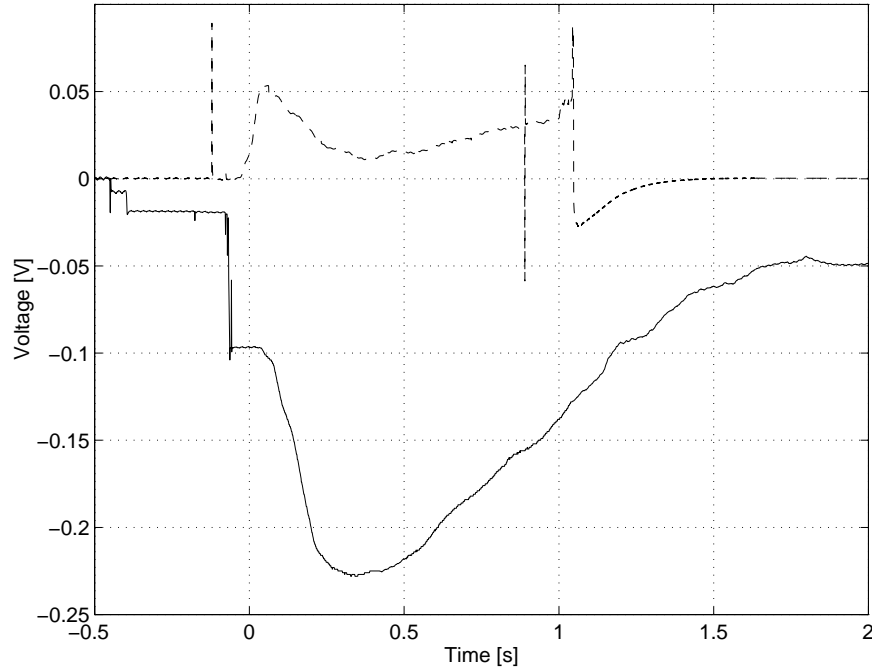


Figure 5.36: Quench detector output voltage signal versus time before (solid line) and after (dashed line) modification

Since these inductive voltages cannot be compensated in amplifier mode, the quench detectors across bus-bars send false trigger signals to the interlock system.

This problem has been solved by switching each dipole main bus-bar quench detector into bridge mode while compensating the inductive voltage with the voltage across the enclosed dipole pole (see Fig. 5.37).

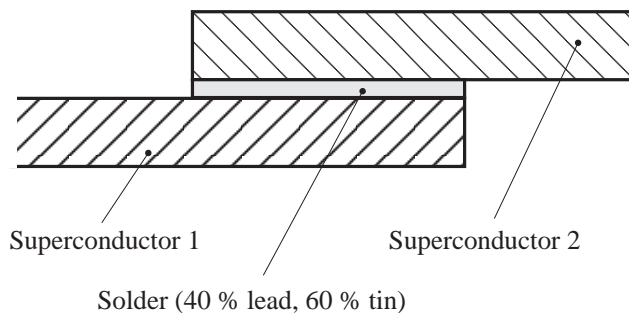


Figure 5.38: Connection of two superconducting cables by soldering

a critical field of about 0.3 T. The solder becomes resistive in most magnet situations. The electrical resistivity of solder is about $3 \cdot 10^{-9} \Omega\text{m}$, greater than that of copper which is $1.7 \cdot 10^{-9} \Omega\text{m}$ [33].

Most of the splices in the LHC Test String are soldered, only the connections to the positive and negative current lead are clamped. Fig. 5.39 shows the electrical circuit with all cable connections along the main circuit. About one quarter of all splices are located in regions of high magnetic flux density. These splices are necessary to connect the outer and inner layer cable in the dipoles, which have different cross sections. Most of the magnet, pole, and bus-bar connections are located outside the high magnetic field. The measurement was performed with two different methods in order to obtain more reliable values.

The electrical method to deduce the contact resistances is based on a current and voltage measurement. The calorimetric method evaluates the resistive heating in the superconducting connections from the difference in heat load at 1.9 K with and without current [17].

Table 5.5: Summary of the contact resistance measurement on the LHC Test String performed with electrical and calorimetric method

	Units	Values
Number of splices		44
<i>Electrical measurement:</i>		
Resistive heating	[W]	9.1 ± 1.3
Average resistance per splice	[nΩ]	1.3 ± 0.2
<i>Calorimetric measurement:</i>		
Resistive heating	[W]	10.3 ± 1.5
Average resistance per splice	[nΩ]	1.5 ± 0.2

The measurements, performed both by calorimetric and electrical methods, show a higher average resistance per splice than expected. The specified values for contact resistances in the yellow book [13] are given with 0.6 nΩ in low magnetic field regions (external splices) and 1.2 nΩ in high magnetic field regions (internal splices). This gives an average value of 0.85 nΩ per contact for the LHC Test String by considering 18 internal and 26 external splices. The value is smaller than the contact resistance deduced from measurements (Table 5.5).

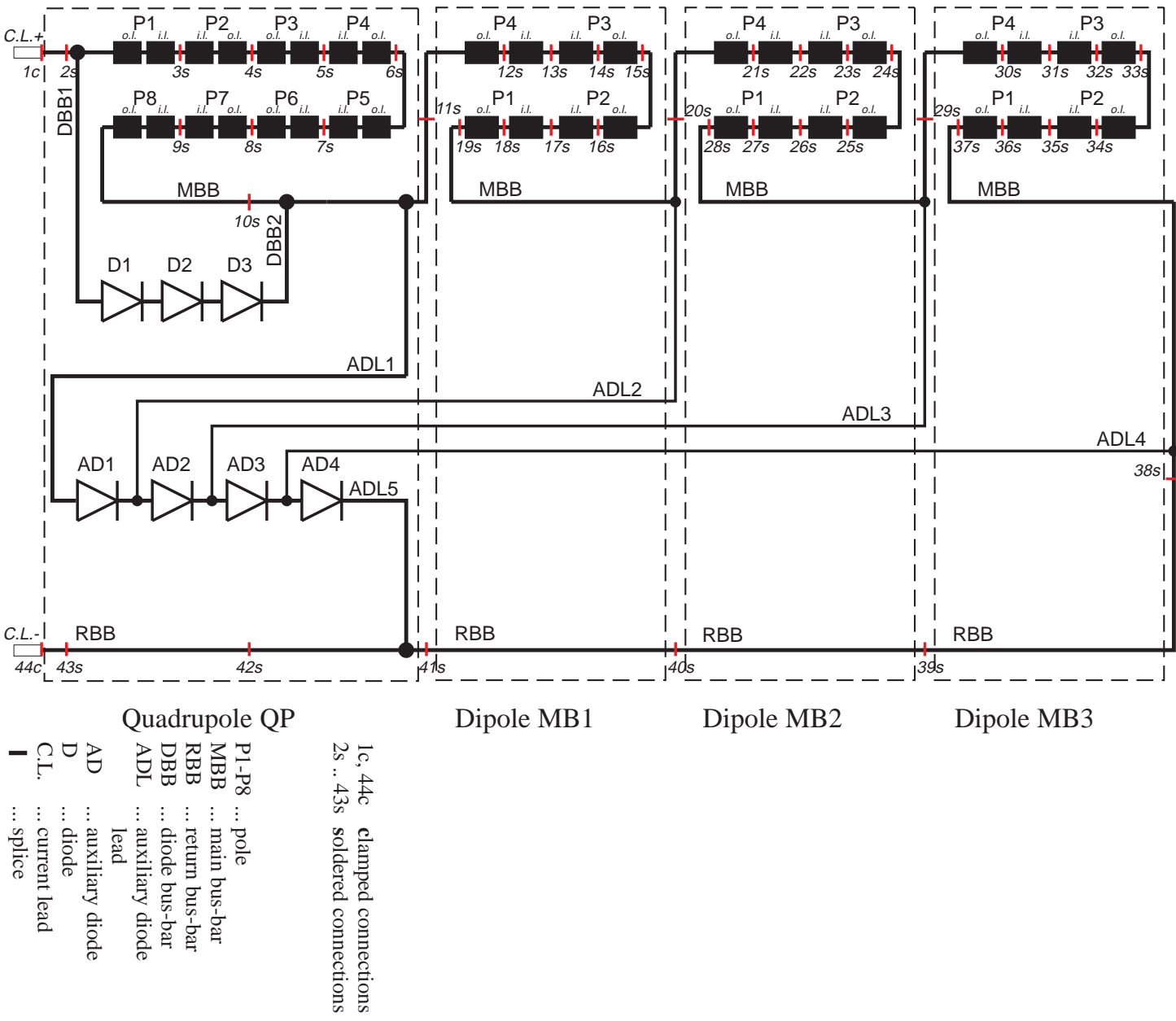


Figure 5.39: Electrical circuit of the LHC Test String with the number of splices along the main circuit

Chapter 6

Outlook for the LHC Magnet Protection

After validation of the transient model by string experiments, extrapolations have been performed to predict the behaviour of LHC magnets of the final version in case of a quench. With the variation of parameters, the influence of quench heater delay, residual resistivity ratio, and copper to superconductor ratio on hot-spot temperature and maximum voltages are simulated.

6.1 Final Design of Magnets for the LHC Machine

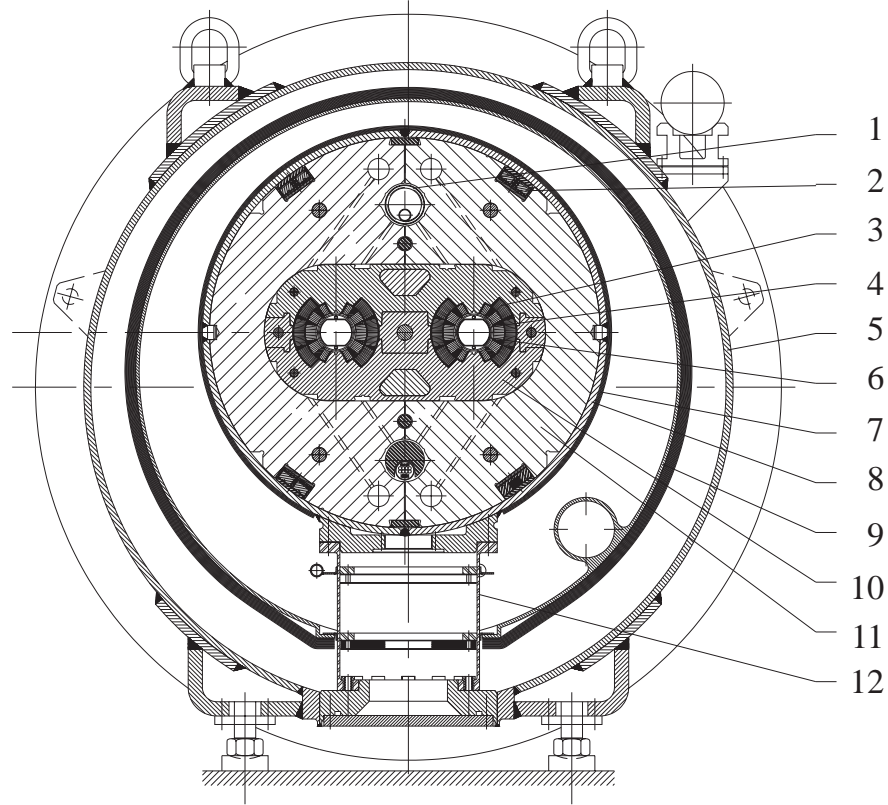
The superconducting accelerator magnets, used in the LHC machine, will be different from the magnets in the LHC Test String [13]. A cross section of the new dipole design is shown in Figure 6.1. In comparison to the dipoles of the first version, the new dipoles are about 50 % longer and the cryogenic lines are located outside the cryostat. The conductor cross section and the number of turns in the outer and inner layer coil will change. The copper to superconductor ratio in the outer layer coils of the dipole magnets will be increased from 1.8 to 1.9 (see Table B.2).

Each magnet will contain its protection diode in the same cryostat, connected across the magnet by use of highly copper stabilised bus-bars.

6.2 Extrapolation for the LHC Dipole Magnets

Critical values for the magnet protection are the hot-spot temperature T_{hs} of the superconductor and the maximum voltage U_{max} between conductor and ground. The parameters which essentially influence T_{hs} and U_{max} are the difference in heater response time Δt_h between aperture magnets, the difference in values of residual resistivity ratio ΔRRR , and the copper to superconductor ratio of the superconducting cable in the aperture dipoles.

The copper to superconductor ratio is well controlled during producing the superconducting cable. Since the values of RRR cannot be measured at room temperature, differences in values of RRR may be possible. Differences in quench heater response time are caused by differences in heat transfer from the heater strip to the coil through the insulation.



- | | |
|------------------------|-------------------------|
| 1. Heat exchanger tube | 7. Radiative insulation |
| 2. Bus-bars | 8. Shrinking cylinder |
| 3. Coils | 9. Thermal shield |
| 4. Beam pipe | 10. Collars |
| 5. Vacuum vessel | 11. Yoke |
| 6. Beam screen | 12. Support post |

Figure 6.1: Cross section of main lattice dipole (LHC version 4)

Differences in values of RRR and differences in heater response time between poles lead to unsymmetrical voltage distribution. A longer heater response time in aperture coils with higher values of RRR develops higher resistive voltages than the opposite case. Due to this fact, simulations consider only the first case.

The following parameter studies are performed on a single dipole model with a by-pass diode in parallel (see Figure 6.2).

6.2.1 Quench Simulations

The quench simulations consider a dipole quench at the nominal current of 11500 A [13]. The conductors in the outer layer coils become resistive about 50 ms after firing the heater strips. Due to quench back at current decay rates above 20 kAs^{-1} the inner layer coils are assumed to become resistive.

Three simulation runs show the influence of heater response time between aperture mag-

nets and different values of RRR of copper.

- a) Equal conditions for quench heater delays and values of RRR in both aperture dipoles.
- b) Different quench heater delay times in aperture dipoles at equal values of RRR.
- c) Different values of RRR in apertures dipoles at equal heater delays.

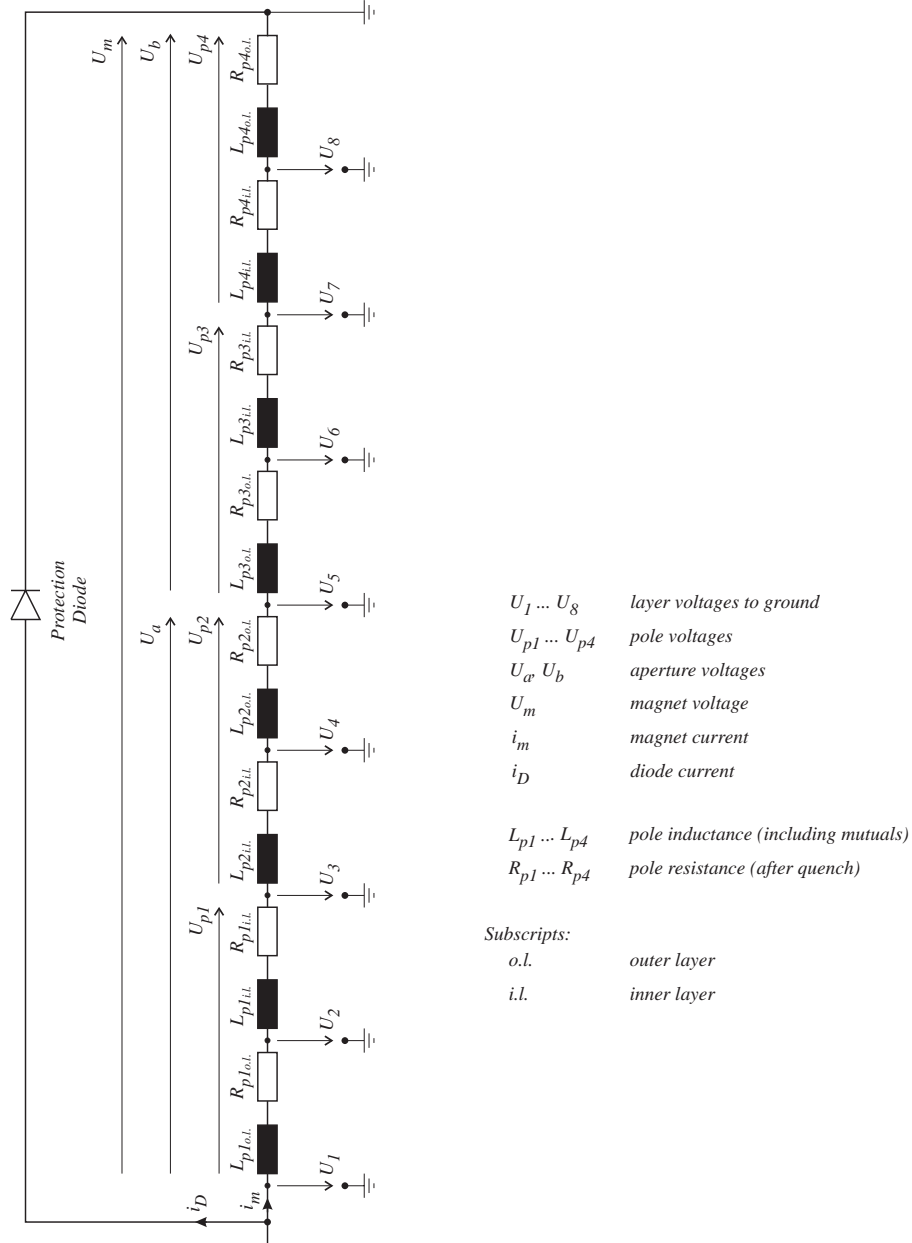


Figure 6.2: Electrical scheme of a single twin-aperture dipole magnet with a by-pass diode in parallel

a) Equal conditions for both aperture dipoles

The simulation, considering equal conditions for both apertures in a twin-aperture dipole, is a reference to compare simulations with different values of RRR and non-uniform heater delays in the dipole apertures.

Table 6.1: Input parameters for quench simulation by considering equal conditions for both aperture dipoles

	Units	Aperture A		Aperture B	
		outer layer	inner layer	outer layer	inner layer
Inductance	[mH]	18.74	8.27	18.74	8.27
No. of turns	[-]	52	30	52	30
Cross section	[mm ²]	19.244	24.943	19.244	24.943
Cu/Sc ratio	[-]	1.9	1.6	1.9	1.6
R_{Cu} at 300 K	[Ω]	1.81	0.86	1.81	0.86
RRR	[-]	100	100	100	100
Heater delay t_h	[ms]	50	50	50	50

The values of RRR, heater delay t_h , and copper to superconductor ratio α are the same in both aperture dipoles. The magnet current decay (Fig. 6.3) is determined by the magnet inductance and the raise of coil resistance. Due to the symmetrical conditions, the coil resistance distribution is the same in both apertures dipoles (Fig. 6.4).

The voltages at the odd points in the electrical scheme (Fig. 6.2) are almost zero. In the even points the voltage characteristic is determined by the different inductances (see section A.1) and the cable resistances of the outer and inner layer coils. The voltage distributions are shown in Fig. 6.5 for aperture dipole A and in Fig. 6.6 for aperture dipole B.

The average temperatures of the resistive sections for the outer and inner layer coils are calculated by assuming adiabatic conditions. After firing the quench heaters, the conductors in the outer and inner layer coils become resistive. Since the inner layer conductors contain more copper than the outer layer conductors, the final temperature of the inner layer coil is lower (Fig. 6.7).

The heater delay time determines the hot-spot temperature in the quench origin. The longer the heater delay after a quench, the higher becomes the temperature in the quench origin. The solid line in Fig. 6.8 shows the hot-spot temperature in case of a quench in the outer layer coil while the dashed line depicts the hot-spot temperature in case of a quench in the inner layer coil.

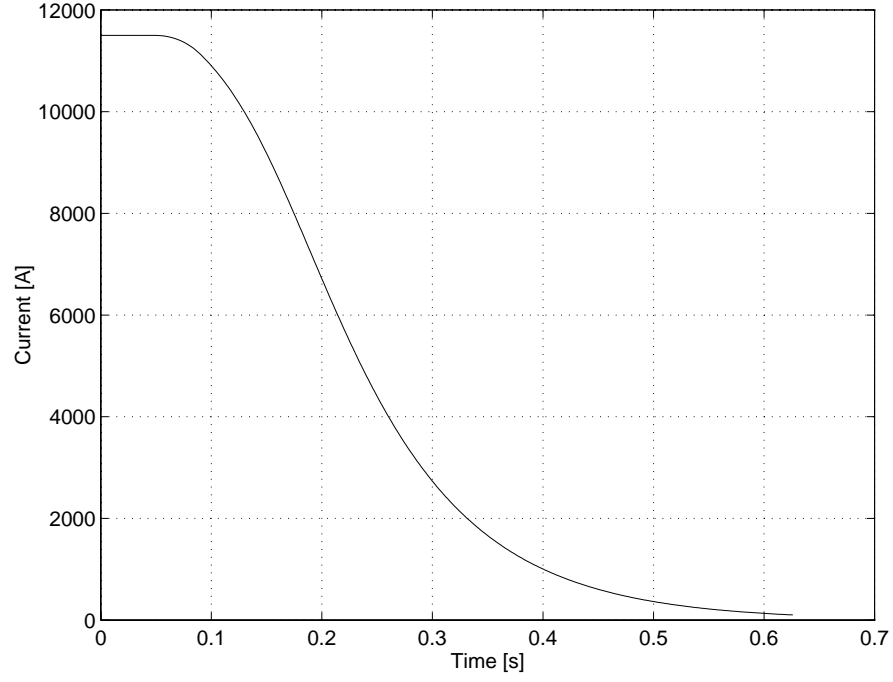


Figure 6.3: Magnet current versus time ($RRR_A = RRR_B = 100$, $t_{hA} = t_{hB} = 50$ ms)

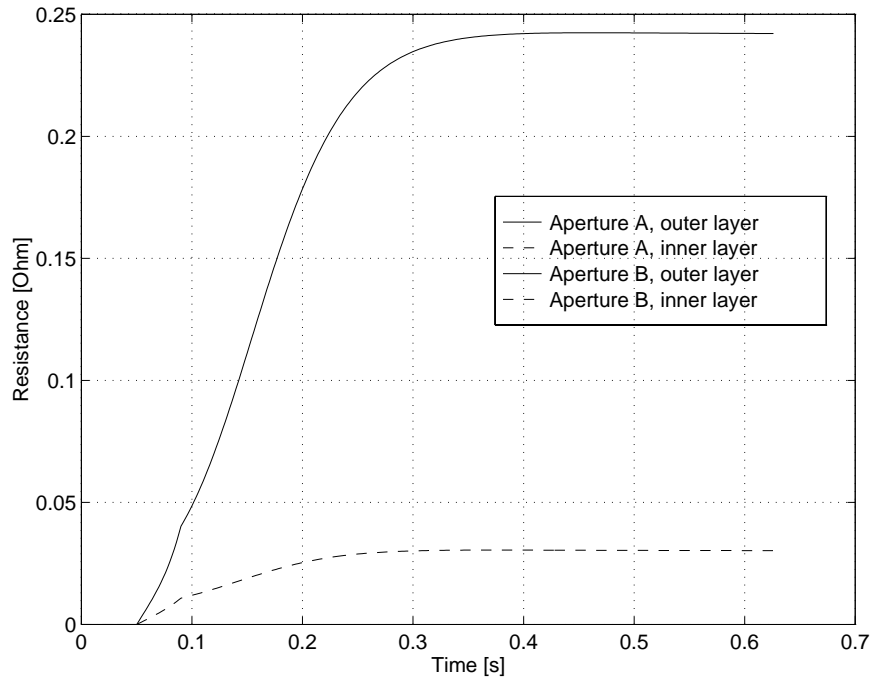


Figure 6.4: Average coil resistance of outer layer coils and inner layer coils versus time ($RRR_A = RRR_B = 100$, $t_{hA} = t_{hB} = 50$ ms)

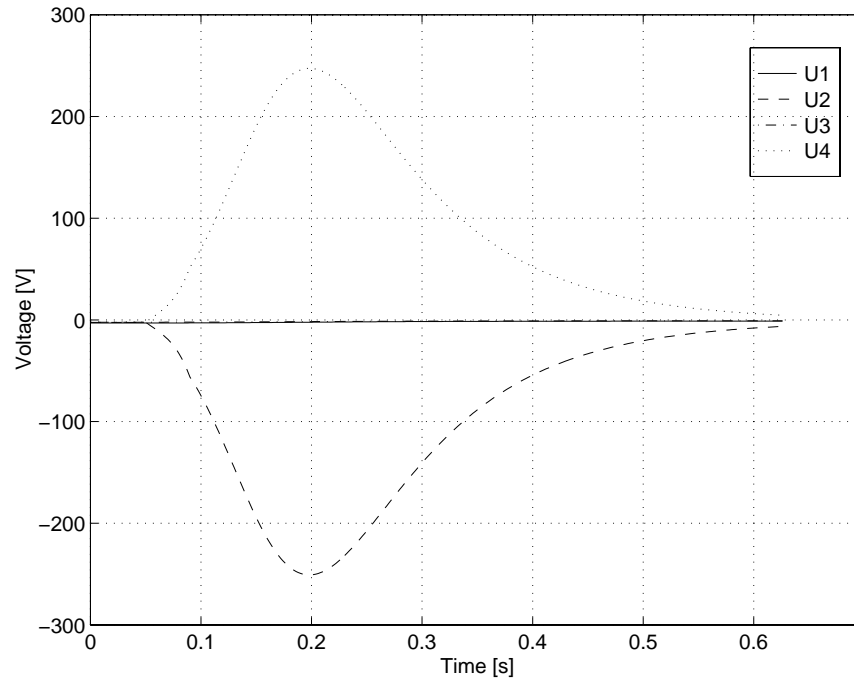


Figure 6.5: Voltages versus time in Aperture A ($RRR_A = RRR_B = 100$, $t_{hA} = t_{hB} = 50$ ms)

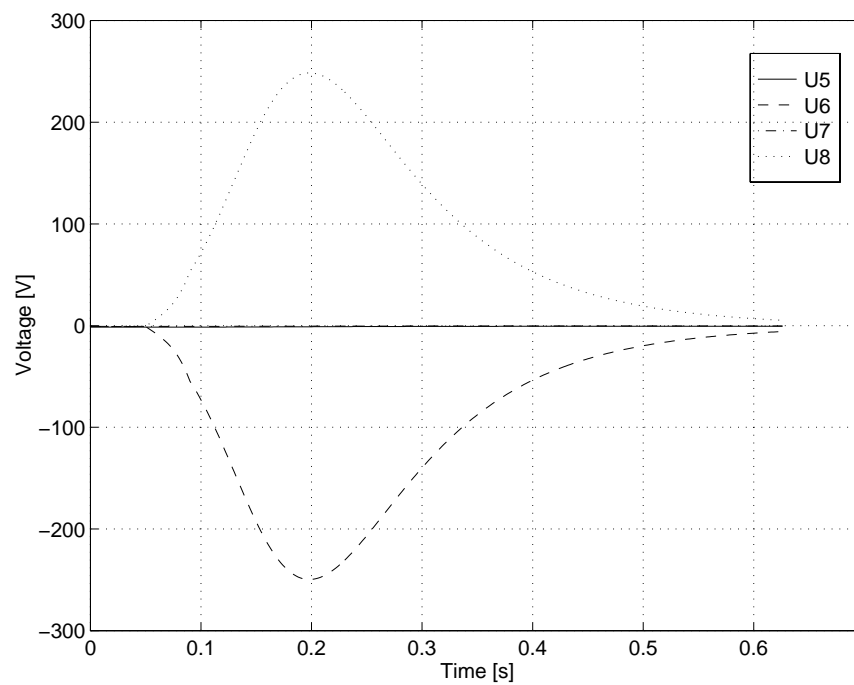


Figure 6.6: Voltages versus time in Aperture B ($RRR_A = RRR_B = 100$, $t_{hA} = t_{hB} = 50$ ms)

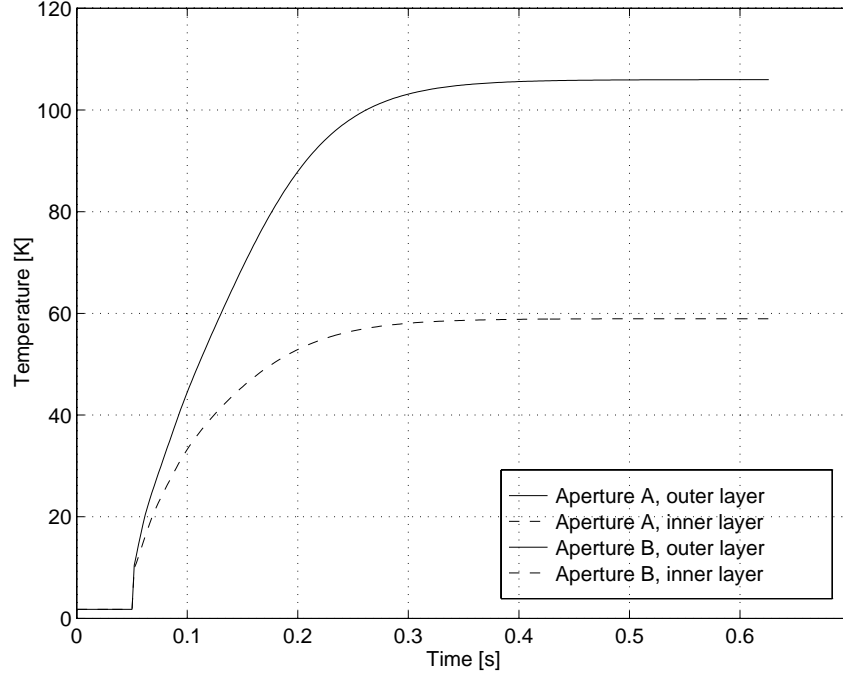


Figure 6.7: Average temperatures of outer layer and inner layer coils versus time ($RRR_A = RRR_B = 100$, $t_{hA} = t_{hB} = 50$ ms)

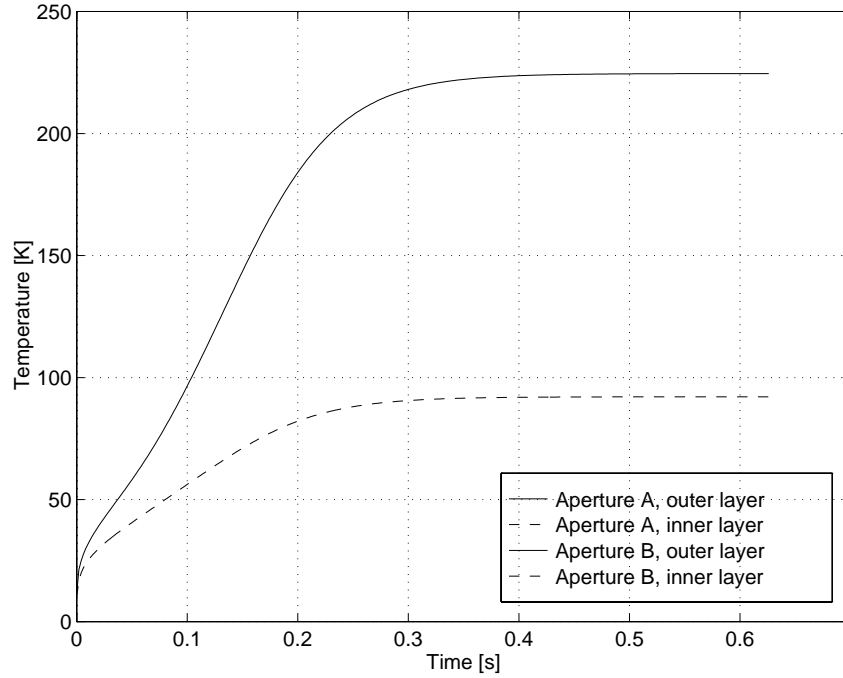


Figure 6.8: Hot-spot temperatures of outer layer and inner layer coils versus time ($RRR_A = RRR_B = 100$, $t_{hA} = t_{hB} = 50$ ms)

b) Differences in heater response time between aperture dipoles

In experiments on the LHC Test String, differences in heater response time between aperture dipoles in the range of 1 to 10 ms (see Table 4.3) were observed. Different heater delays t_h between the two aperture dipoles lead to an unsymmetrical temperature and voltage distribution.

Table 6.2: Input parameters for quench simulation by considering different heater delays for both aperture dipoles

	Units	Aperture A		Aperture B	
		outer layer	inner layer	outer layer	inner layer
inductance	[mH]	18.74	8.27	18.74	8.27
# of turns	[-]	52	30	52	30
Cross section	[mm ²]	19.244	24.943	19.244	24.943
Cu/Sc ratio	[-]	1.9	1.6	1.9	1.6
R_{Cu} at 300 K	[Ω]	1.81	0.86	1.81	0.86
RRR	[-]	100	100	100	100
t_h	[ms]	50	50	70	70

Aperture A becomes resistive earlier than aperture B. As long as the coil in aperture B is superconducting, the current decay (Fig. 6.9) is determined by the magnet inductance and the raise of coil resistances in aperture A. When the coils in aperture dipole B become resistive, the current decays faster.

Due to a longer heater response time in aperture B, the coil resistances in aperture A become higher than the coil resistances in aperture B (Fig. 6.10).

High voltage peaks between coil and ground may occur at the aperture dipole with the longer heater delay time. During the time interval $\Delta t_h = t_{hB} - t_{hA}$ the voltage drops across aperture B are only of inductive nature. The lower coil resistances lead to lower resistive voltages in aperture B (Fig. 6.12) than in aperture A (Fig. 6.11). The peaks in the voltage raise are caused by the change of the current decay rate when the aperture dipole with the longer heater response time becomes resistive. Without considering quench back in the inner layer coils, even higher voltages between coil and ground can be expected.

The average coil temperature in the coils of the aperture dipole with the longer heater delay is lower than in the other aperture dipole (Fig. 6.13).

The hot-spot temperatures in Fig. 6.14 are higher than in Fig. 6.8. This results from a slightly longer current decay which is caused by the lower dipole resistance.

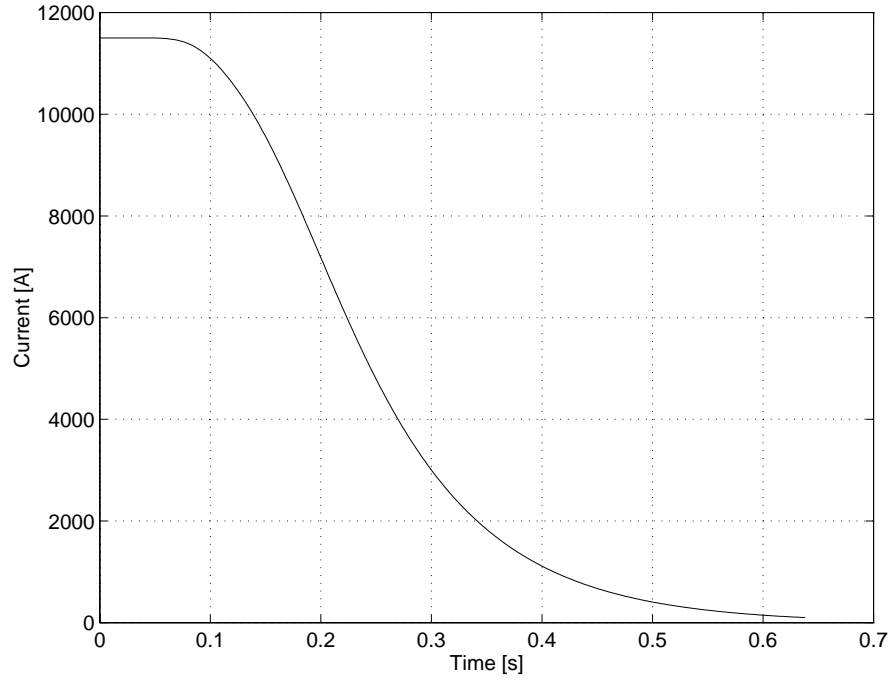


Figure 6.9: Magnet current versus time ($RRR_A = RRR_B = 100$, $t_{hA}=50$ ms, $t_{hB}=70$ ms)

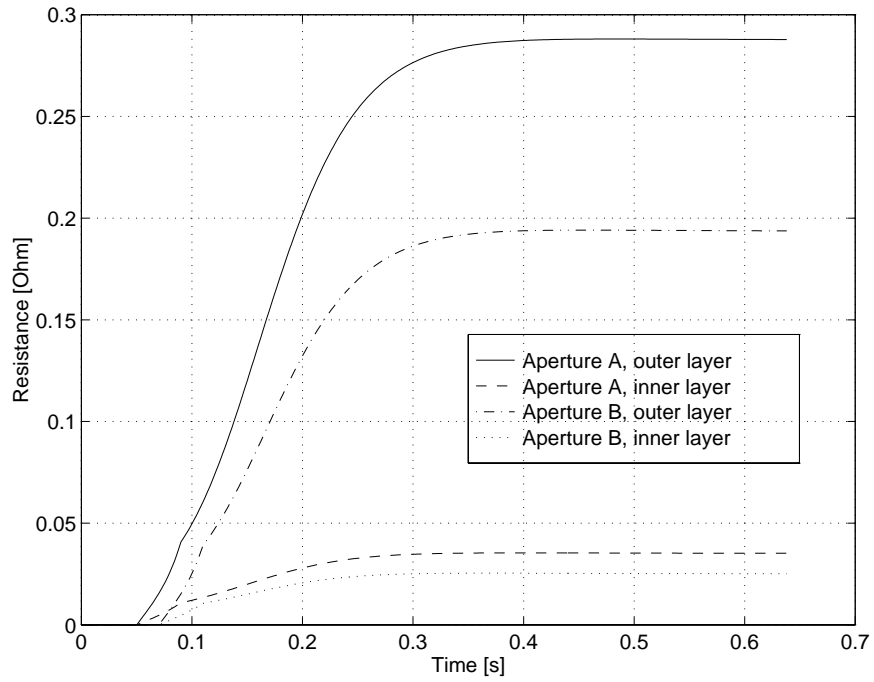


Figure 6.10: Average coil resistance of outer layer coils and inner layer coils versus time ($RRR_A = RRR_B = 100$, $t_{hA}=50$ ms, $t_{hB}=70$ ms)

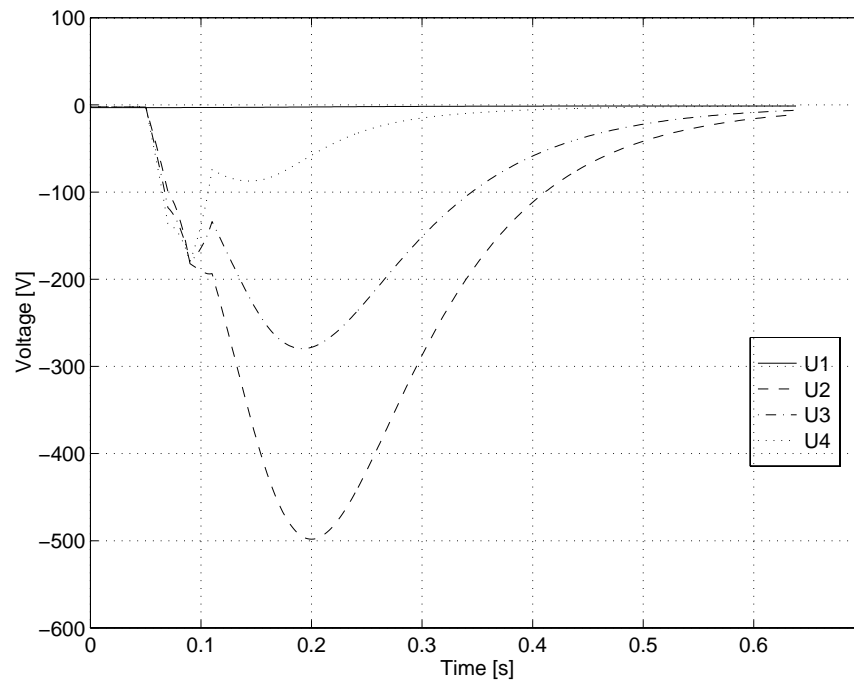


Figure 6.11: Voltages versus time in Aperture A ($RRR_A = RRR_B = 100$, $t_{hA}=50$ ms, $t_{hB}=70$ ms)

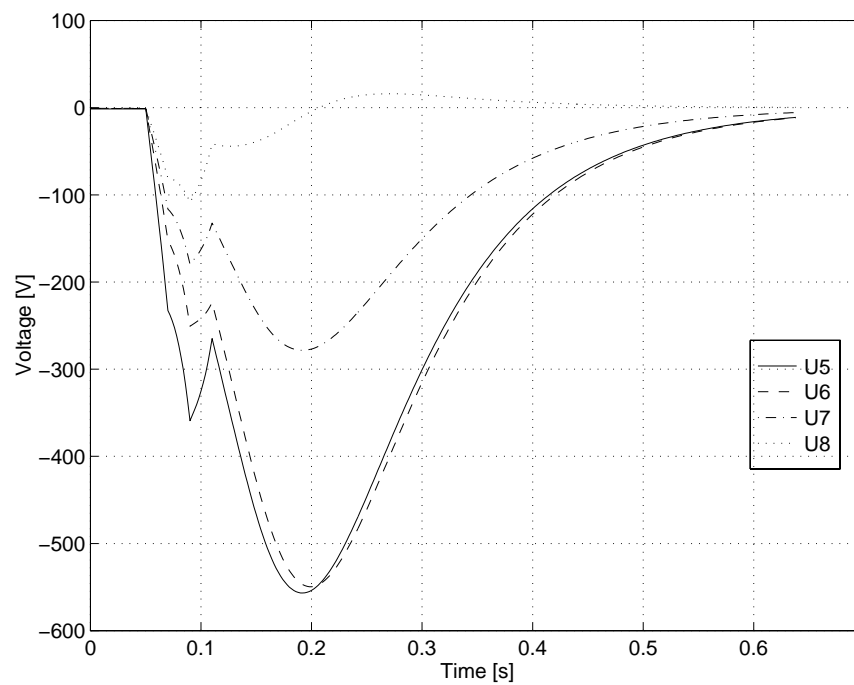


Figure 6.12: Voltages versus time in Aperture B ($RRR_A = RRR_B = 100$, $t_{hA}=50$ ms, $t_{hB}=70$ ms)

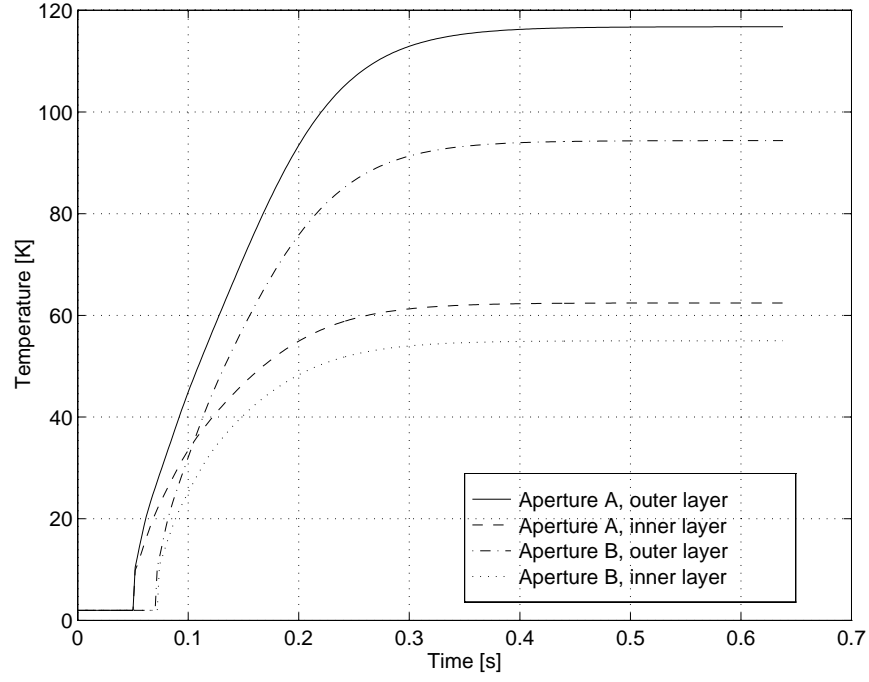


Figure 6.13: Average temperatures of outer layer and inner layer coils versus time ($RRR_A = RRR_B = 100$, $t_{hA}=50$ ms, $t_{hB}=70$ ms)

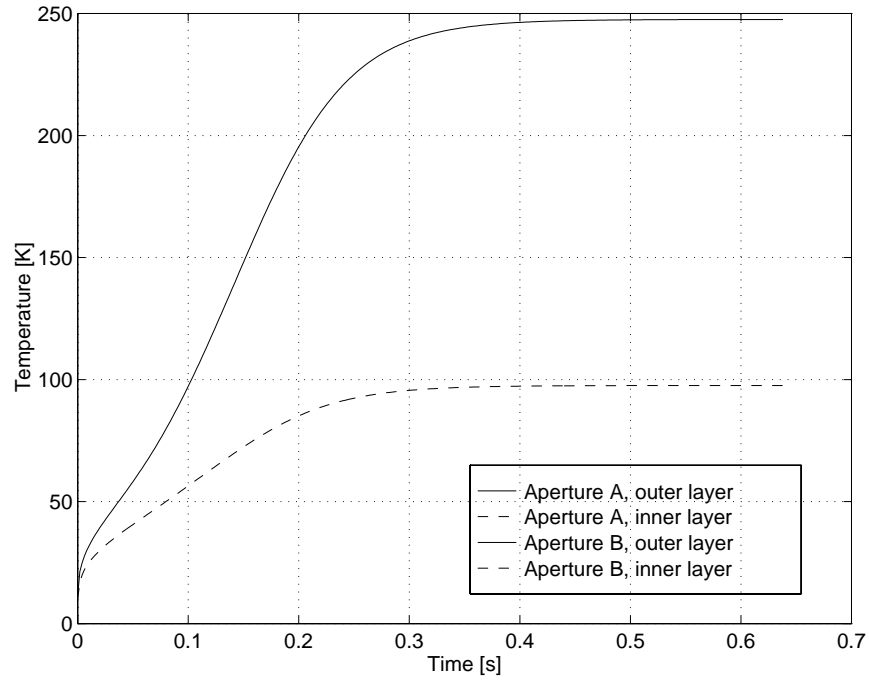


Figure 6.14: Hot-spot temperatures of outer layer and inner layer coils versus time ($RRR_A = RRR_B = 100$, $t_{hA}=50$ ms, $t_{hB}=70$ ms)

c) Different values of RRR in conductors of aperture dipoles

Differences in the values of RRR of copper in the aperture dipole coils lead to an unsymmetrical voltage distribution. The hot-spot temperature becomes higher in coils with lower values of RRR than in coils with higher values of RRR.

Table 6.3: Input parameters for quench simulation by considering different values of RRR for both aperture dipoles

	Units	Aperture A		Aperture B	
		outer layer	inner layer	outer layer	inner layer
inductance	[mH]	18.74	8.27	18.74	8.27
# of turns	[-]	52	30	52	30
Cross section	[mm ²]	19.244	24.943	19.244	24.943
Cu/Sc ratio	[-]	1.9	1.6	1.9	1.6
R_{Cu} at 300 K	[Ω]	1.81	0.86	1.81	0.86
RRR	[-]	70	70	130	130
t_h	[ms]	50	50	50	50

As shown in Fig. 6.16, the average resistance in coils with higher values of RRR (aperture dipole B) is lower than in coils with lower values of RRR (aperture dipole A). This leads to lower resistive voltages in coils with higher values of RRR compared to coils with lower values of RRR. The maximum voltage in aperture dipole B is higher than in aperture dipole A since the inductive voltages are the same in both aperture dipoles (Fig. 6.17 and Fig. 6.18).

Further, the average coil temperature in the aperture dipole with higher values of RRR becomes lower than in the aperture dipole with lower values of RRR (Fig. 6.19)

In case of a quench in the outer layer coil of the aperture dipole with the lower value of RRR, the hot-spot temperature grows to a higher value (Fig. 6.20).

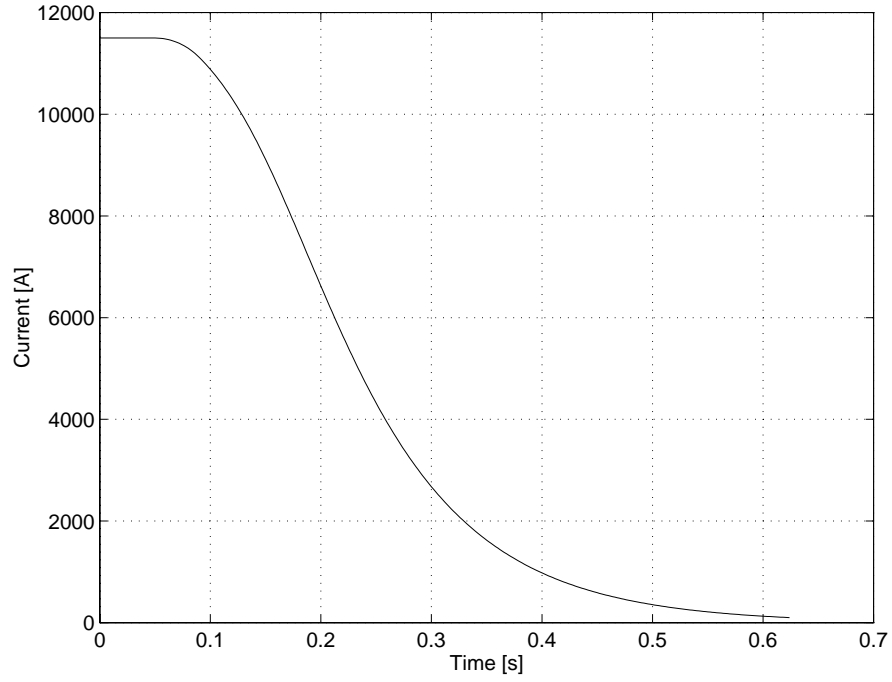


Figure 6.15: Magnet current versus time ($RRR_A = 70$, $RRR_B = 130$, $t_{hA} = t_{hB} = 50$ ms)

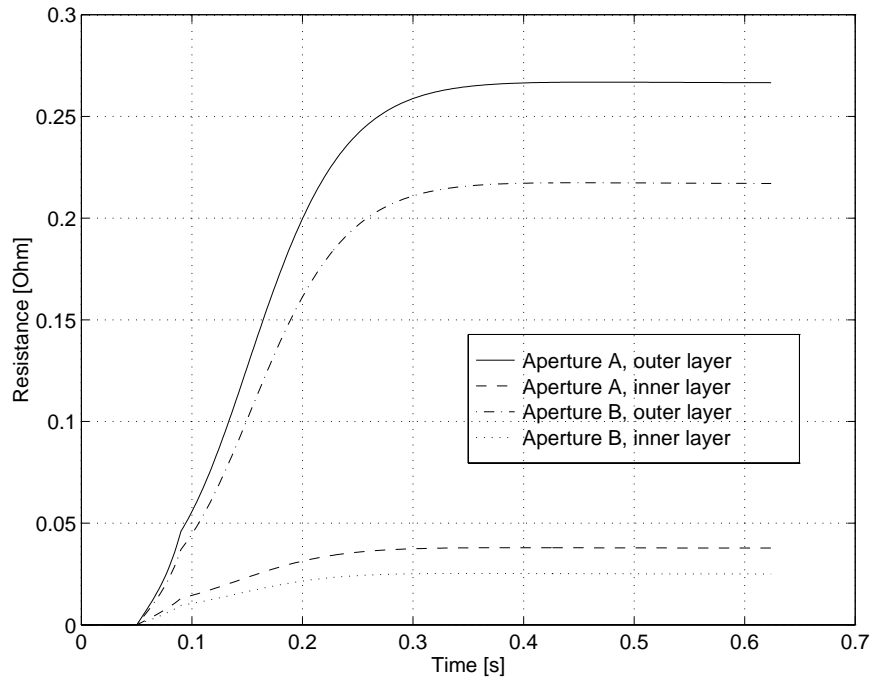


Figure 6.16: Average coil resistance of outer layer coils and inner layer coils versus time ($RRR_A = 70$, $RRR_B = 130$, $t_{hA} = t_{hB} = 50$ ms)

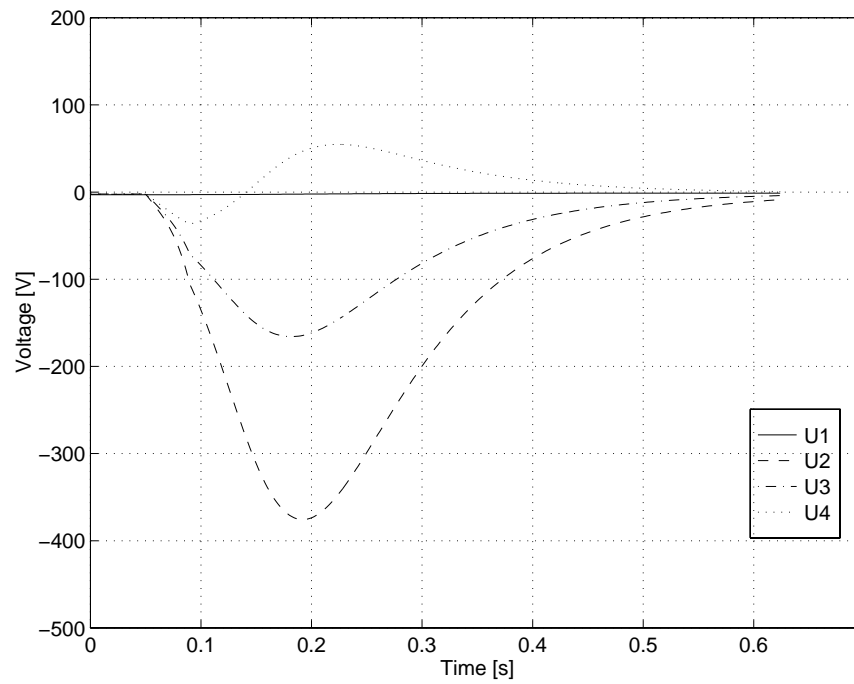


Figure 6.17: Voltages versus time in Aperture A ($RRR_A = 70$, $RRR_B = 130$, $t_{hA} = t_{hB} = 50$ ms)

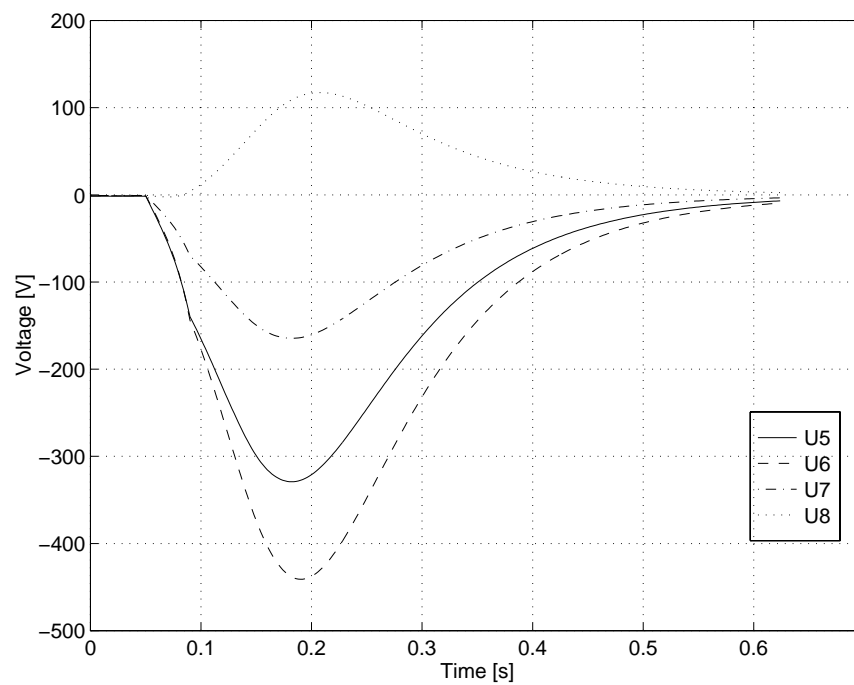


Figure 6.18: Voltages versus time in Aperture B ($RRR_A = 70$, $RRR_B = 130$, $t_{hA} = t_{hB} = 50$ ms)

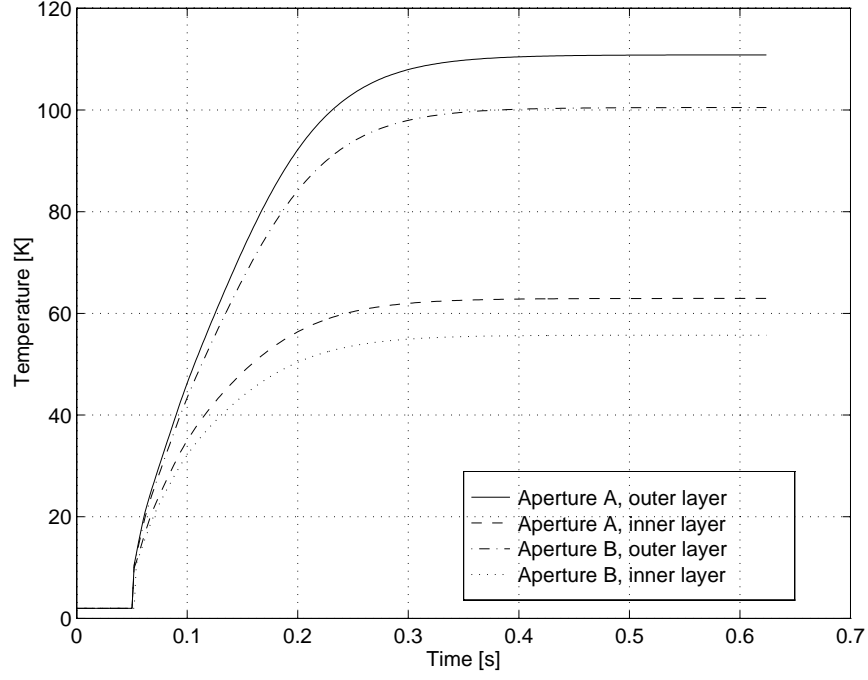


Figure 6.19: Average temperatures of outer layer and inner layer coils versus time ($RRR_A = 70$, $RRR_B = 130$, $t_{hA} = t_{hB} = 50$ ms)

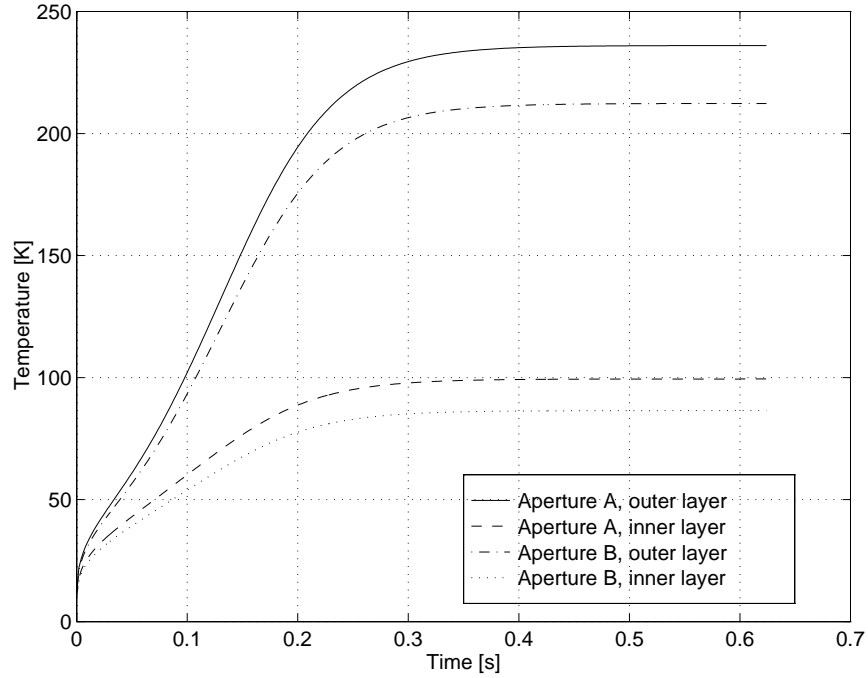


Figure 6.20: Hot-spot temperatures of outer layer and inner layer coils versus time ($RRR_A = 70$, $RRR_B = 130$, $t_{hA} = t_{hB} = 50$ ms)

6.2.2 Coil Voltage Distribution

Simulations of the coil voltage development (Fig. 5.11) after a quench at 11.5 kA are shown in Fig. 6.22 by assuming different heater response times and different values of RRR. In case of $RRR=100$ and a heater delay $t_h = 50$ ms in both apertures coils, the voltage distribution across the magnet shows a symmetrical shape. If $RRR_A=70$, $RRR_B=130$, and a difference in heater response time $\Delta t_h = 20$ ms in aperture B, the maximum voltage to ground across aperture exceeds 800 V.

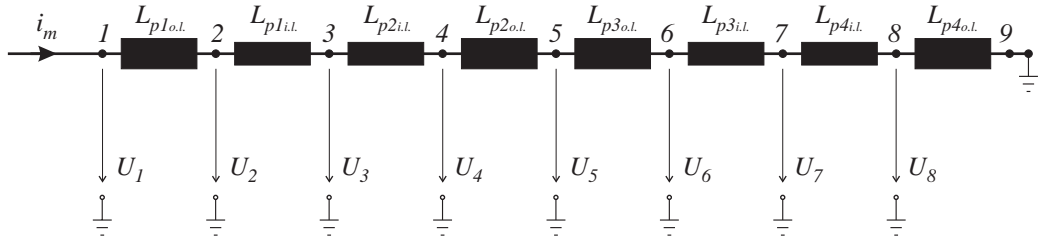


Figure 6.21: Electrical scheme of coil connections in a dipole magnet

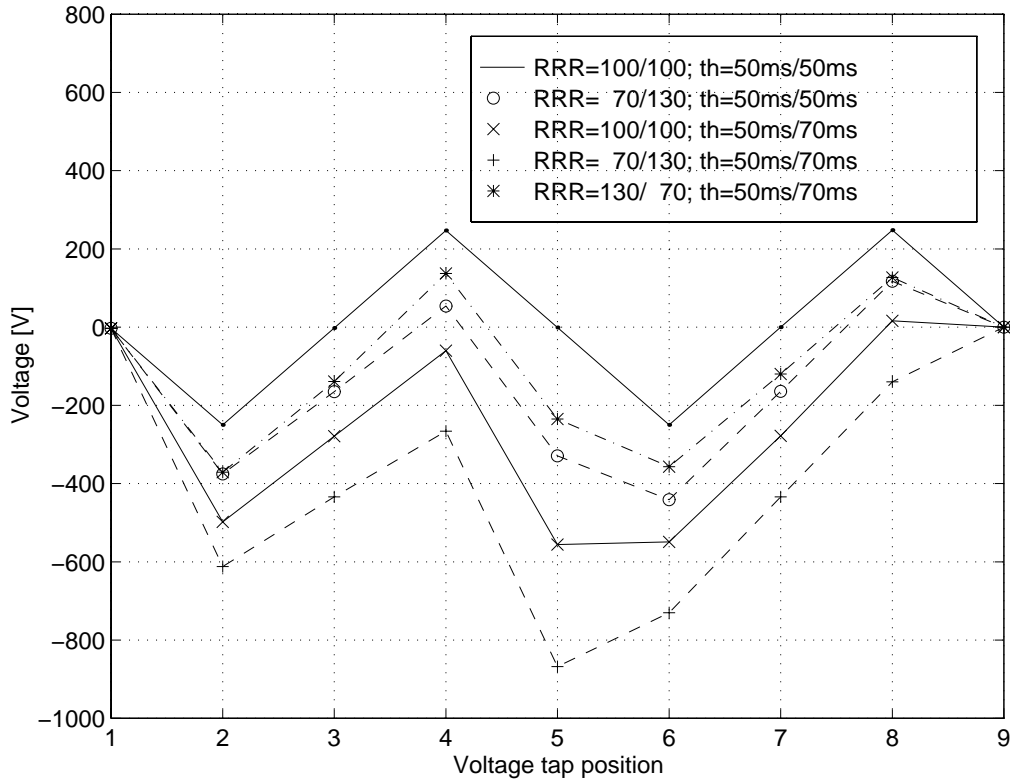


Figure 6.22: Simulated coil voltage distribution in a 14.2 m dipole magnet after a quench at 11.5 kA for different values of RRR and heater delay combinations

6.2.3 Variation of Parameters

From the point of quench protection, the most interesting parameters are the hot-spot temperature T_{hs} and the maximum voltage U_{max} between coil and ground.

The following studies show the dependencies of T_{hs} and U_{max} on

- a) differences in quench heater response time Δt_h between apertures,
- b) variation of values of residual resistivity ratios RRR,
- c) differences in values of residual resistivity ratio ΔRRR between apertures, and
- d) variation of copper to superconductor ratios Cu/Sc of the cable.

All simulations consider a dipole quench at 11.5 kA (nominal current). The initial heater delay for both apertures is assumed with 50 ms.

a) Different quench heater response time between apertures

The simulations to calculate the dependencies of hot-spot temperature T_{hs} and maximum voltage U_{max} consider an increasing delay in heater response time of aperture B with respect to aperture A.

If the values of RRR in the coils of both aperture dipoles are the same, then hot-spot temperature (Fig. 6.23) and maximum voltage (Fig. 6.24) depend mainly on the difference in heater response time of one aperture with respect to the other. Fig. 6.24 shows the maximum outer layer voltage to ground.

Different values of RRR in the aperture dipoles increase or reduce the hot-spot temperature T_{hs} and the maximum voltage U_{max} . If the coils with lower values of RRR have a shorter heater delay time than the coils with higher values of RRR, the hot-spot temperature and maximum voltage are higher. The opposite case reduces T_{hs} and U_{max} (Fig. 6.25 and 6.26).

A difference in values of RRR between aperture dipoles of 60 ($RRR_A=70$ and $RRR_B=130$) can be already considered as very high. In reality the hot-spot temperature and maximum voltages will be within the band, margined by the graphs $RRR=70/130$ and $RRR=130/70$, if the average value of RRR is assumed with 100.

b) Influence of Varying but Uniform Values of RRR

The study assumes the same value of RRR of copper in the cables of both aperture dipoles. After a quench, a higher value of RRR causes an increase of $\int i^2 dt$ due to a lower coil resistance at low temperatures. This leads to an almost linear raise of hot-spot temperature and coil temperature with increasing values of RRR. Since the coil resistance of the resistive sections of the cable raises with temperature, the voltages to ground become slightly higher with increasing values of RRR.

As shown in Fig. 6.27 and Fig. 6.28 the slope is rather small compared with the steps in hot-spot temperature and maximum voltage, performed by increasing the difference in heater response time between aperture dipoles.

c) Different Residual Resistivity Ratio RRR between apertures

At $\Delta\text{RRR}=0$, the hot-spot temperature and maximum voltage in Figures 6.29 and 6.30 are the same as in Figures 6.27 and 6.28, if the difference in heater response time Δt_h between aperture dipoles is zero. Keeping the average value of RRR in a dipole magnet constant by decreasing the value of RRR in one aperture and increasing the value of RRR in the other aperture lead to an almost linear rise of hot-spot temperature T_{hs} and maximum voltage U_{max} with increasing ΔRRR .

The slope depends on the average value of RRR in the magnet. Lower average values of RRR increase the slopes in the temperature and voltage graphs. The heater delay is assumed with 50 ms in both apertures.

d) Different Copper to Superconductor Ratio

The following graphs show the dependencies of hot-spot temperature T_{hs} and maximum voltage U_{max} on the copper to superconductor ratio Cu/Sc . The simulation considers the same copper to superconductor ratio in both apertures.

By assuming the same heater response time in both apertures ($t_h=50$ ms) and constant values of $\text{RRR}=100$, T_{hs} and U_{max} decreases with increasing copper to superconductor ratio (see Fig. 6.31 and Fig. 6.32).

An increase of heater response time in one aperture adds an offset to the hot-spot temperature. At low differences in heater response time, the layer voltage to ground exceeds the voltage across apertures (depicted as dashed line in Fig. 6.32). Since the balance between aperture voltages becomes unbalanced with increasing the difference in heater response time from one aperture in respect to the other, the aperture voltages become higher than the layer voltages (depicted as solid line in Fig. 6.32).

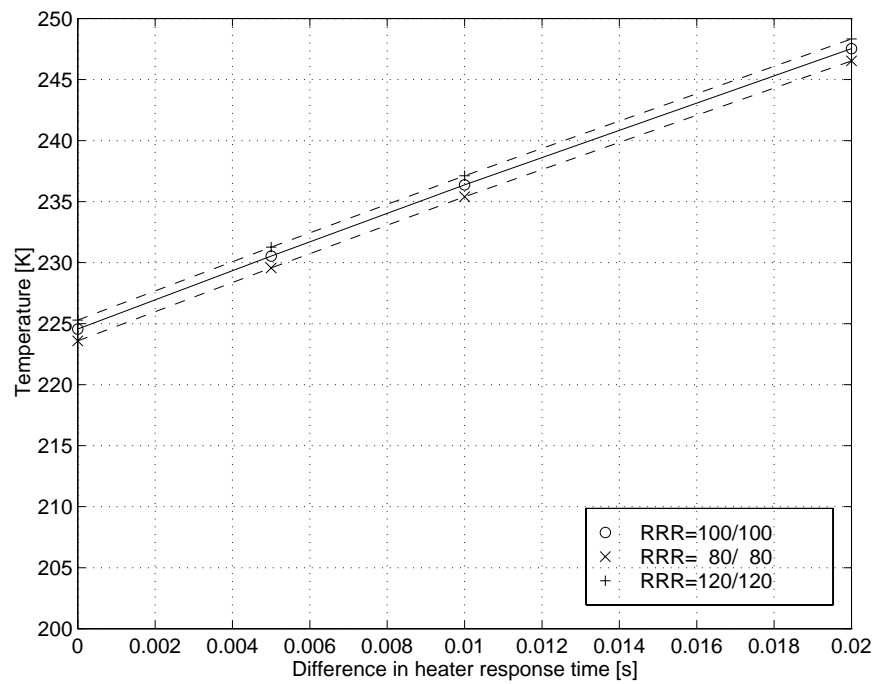


Figure 6.23: Hot-spot temperature versus differences in heater response time at different values of RRR (same in both apertures)

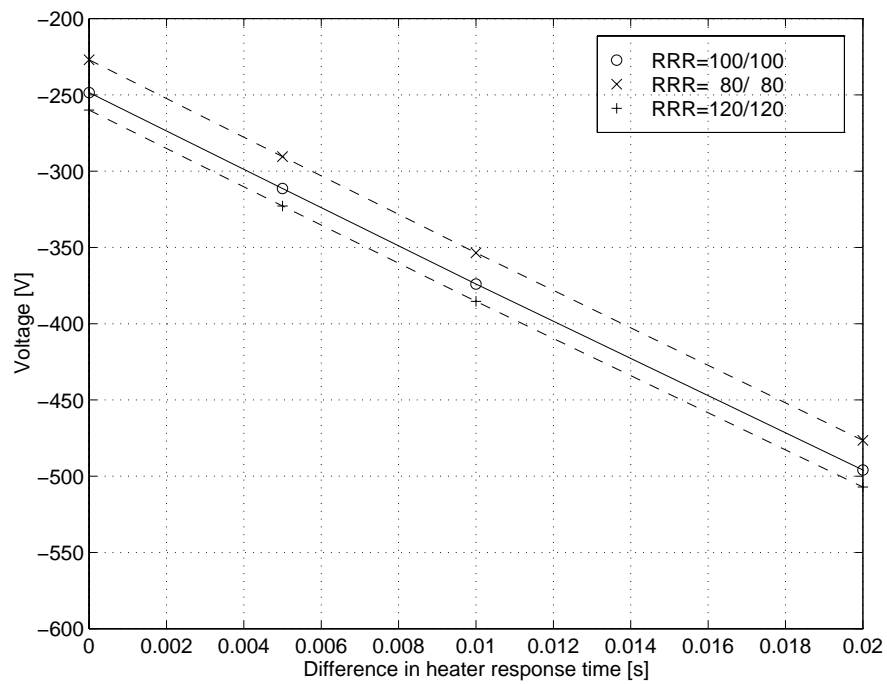


Figure 6.24: Maximum voltages versus differences in heater response time at different values of RRR (same in both apertures)

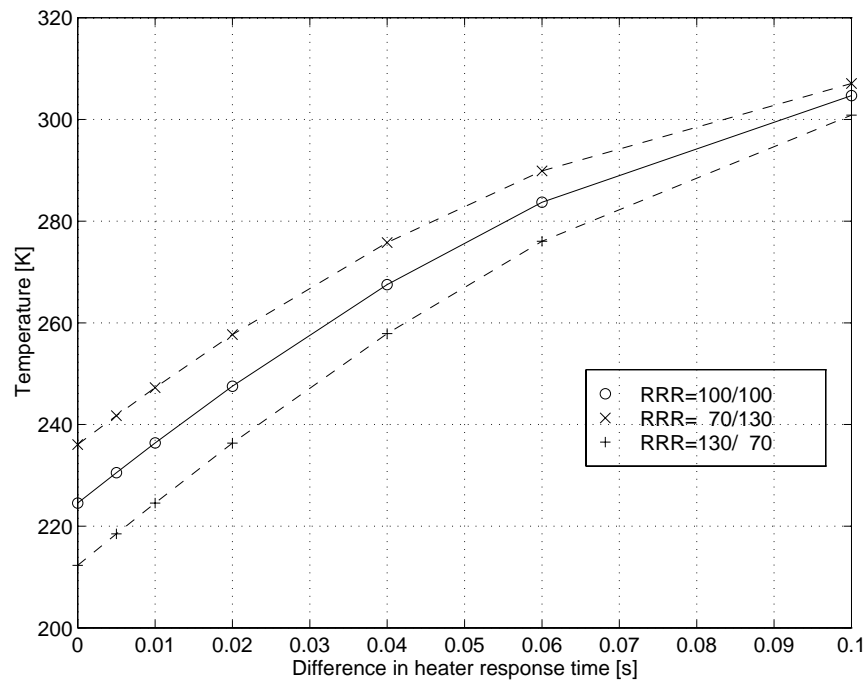


Figure 6.25: Hot-spot temperature versus differences in heater response time at an average RRR of 100 (different in apertures)

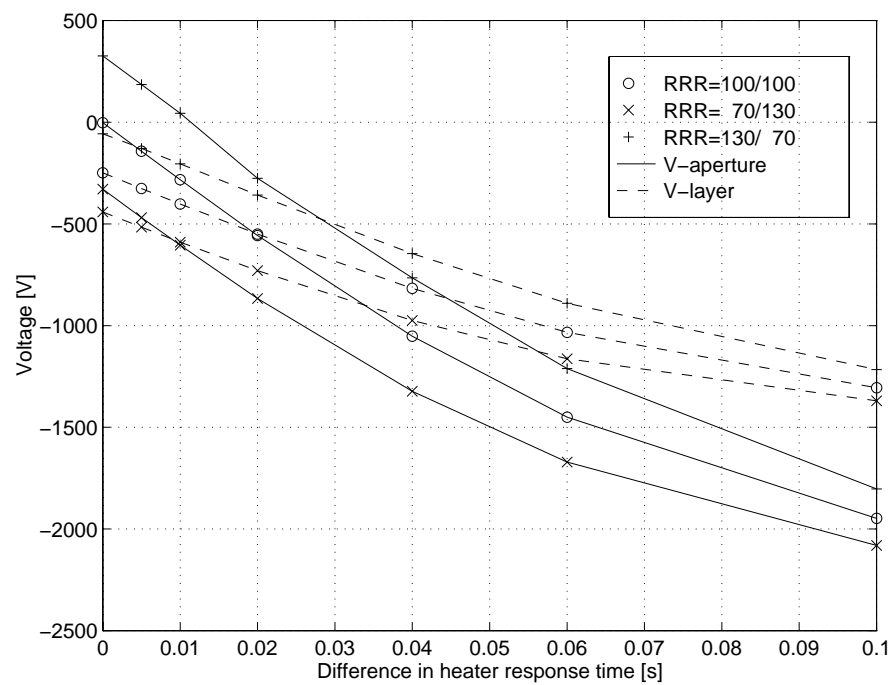
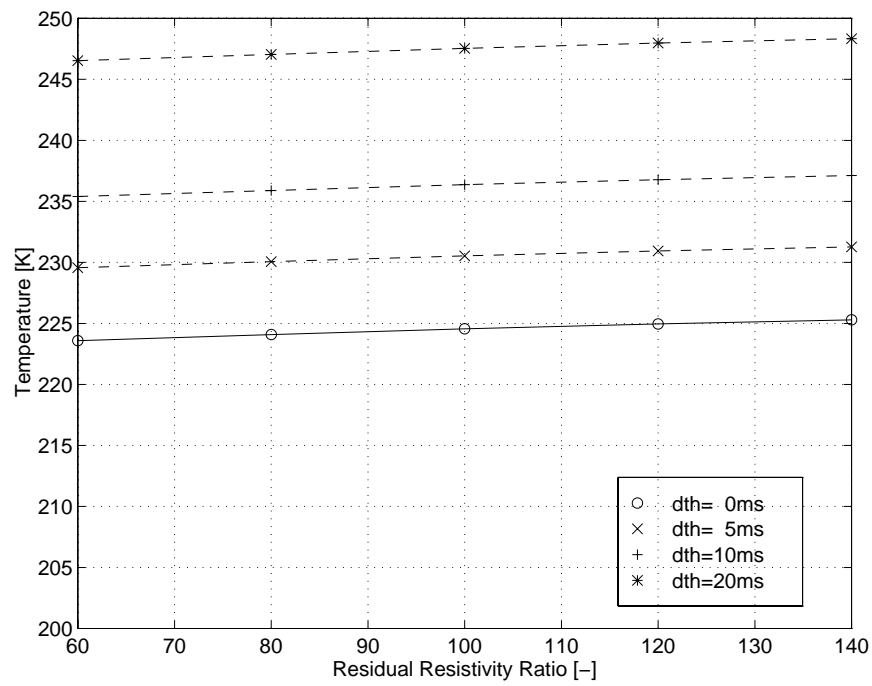
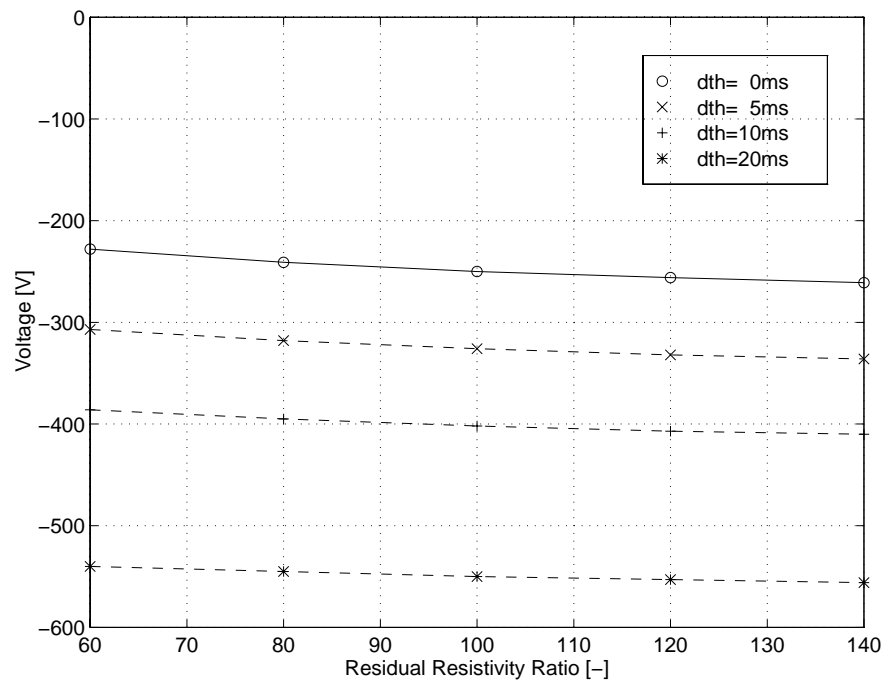


Figure 6.26: Maximum voltages versus differences in heater response time at an average RRR of 100 (different in apertures)

Figure 6.27: Hot-spot temperature versus RRR with Δt_h as parameterFigure 6.28: Maximum voltage versus RRR with Δt_h as parameter

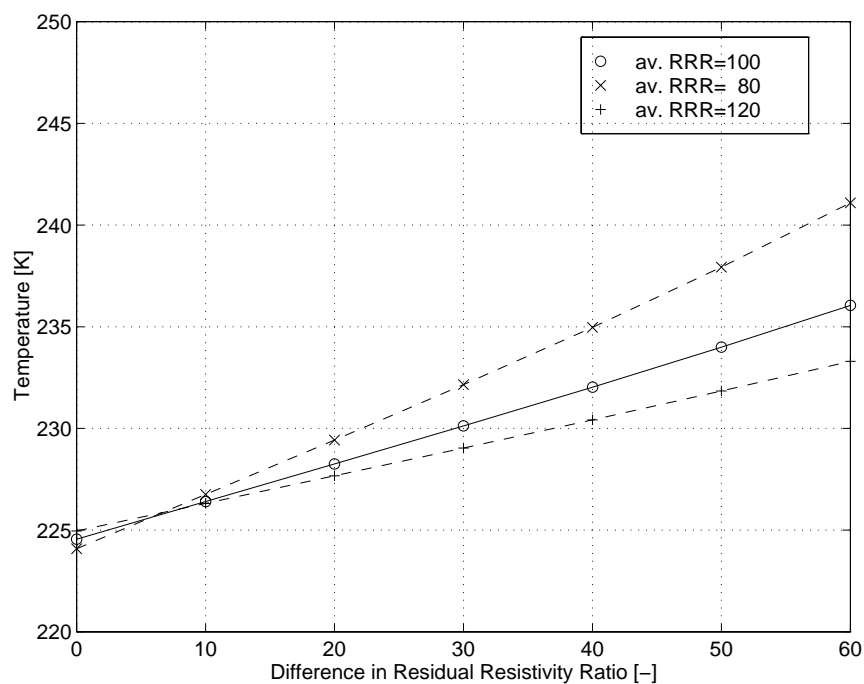


Figure 6.29: Hot-spot temperature versus ΔRRR with average RRR as parameter at uniform heater delay of $\Delta t_{hA} = \Delta t_{hB} = 50$ ms

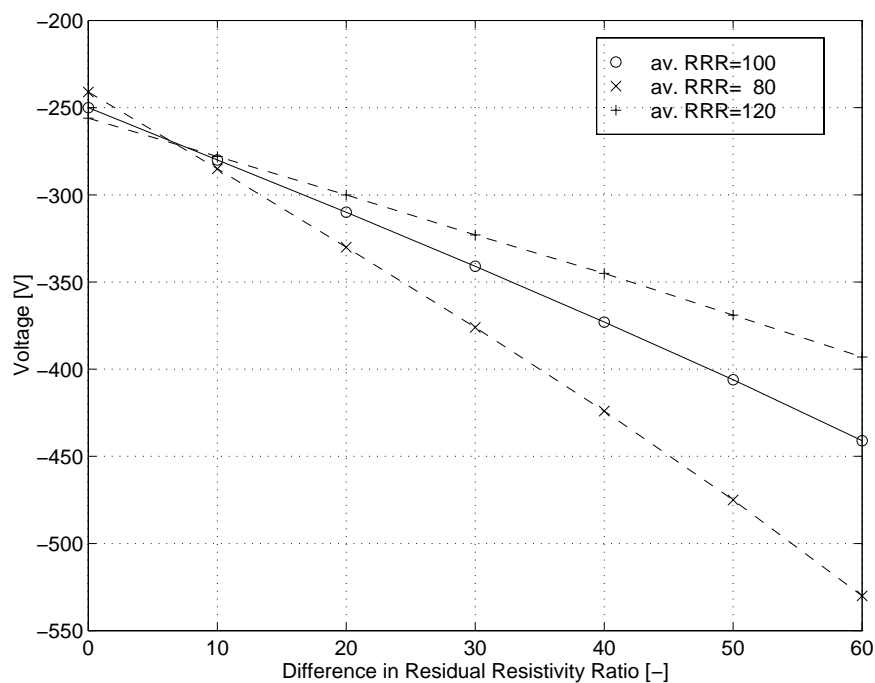
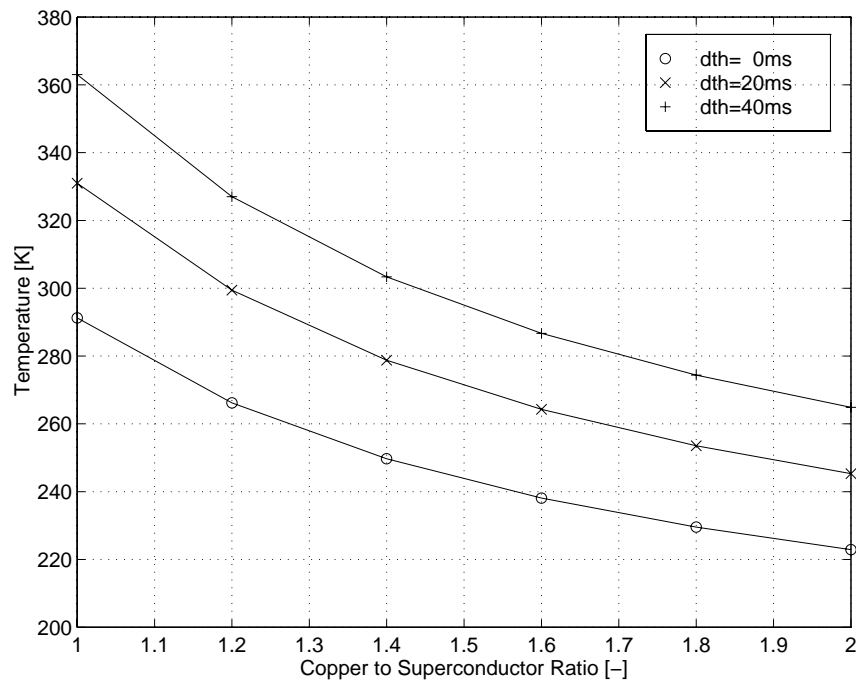
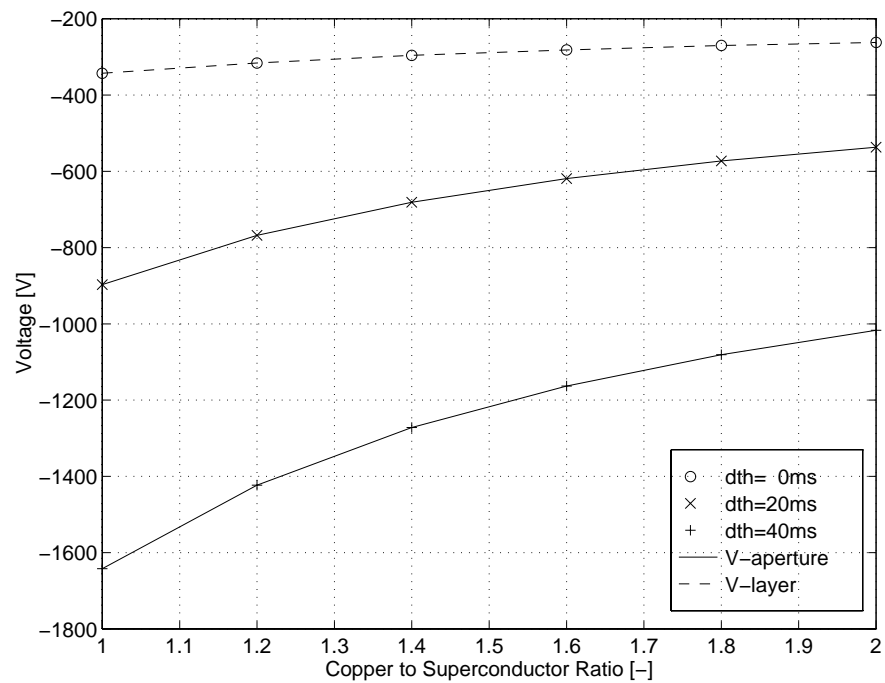
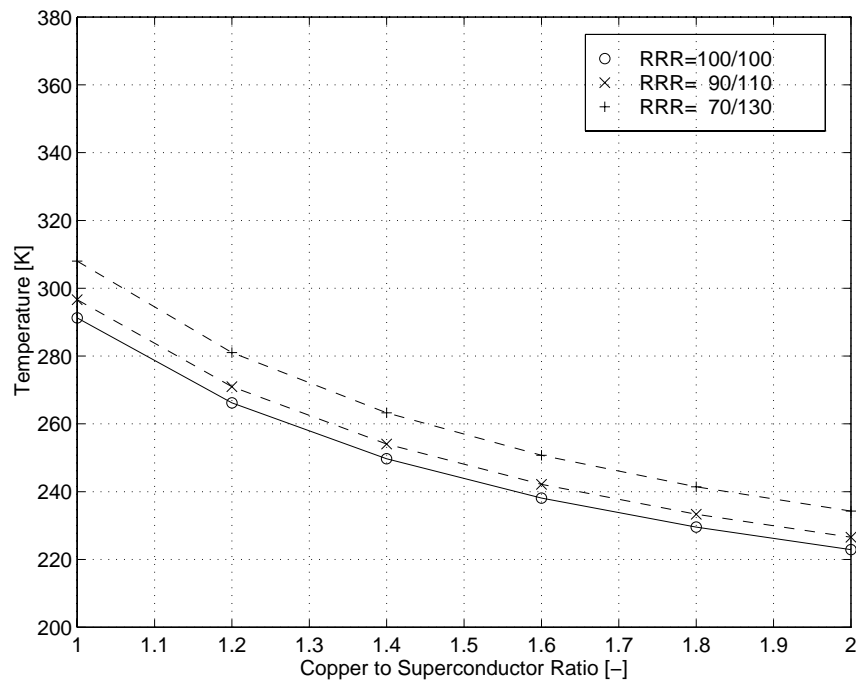
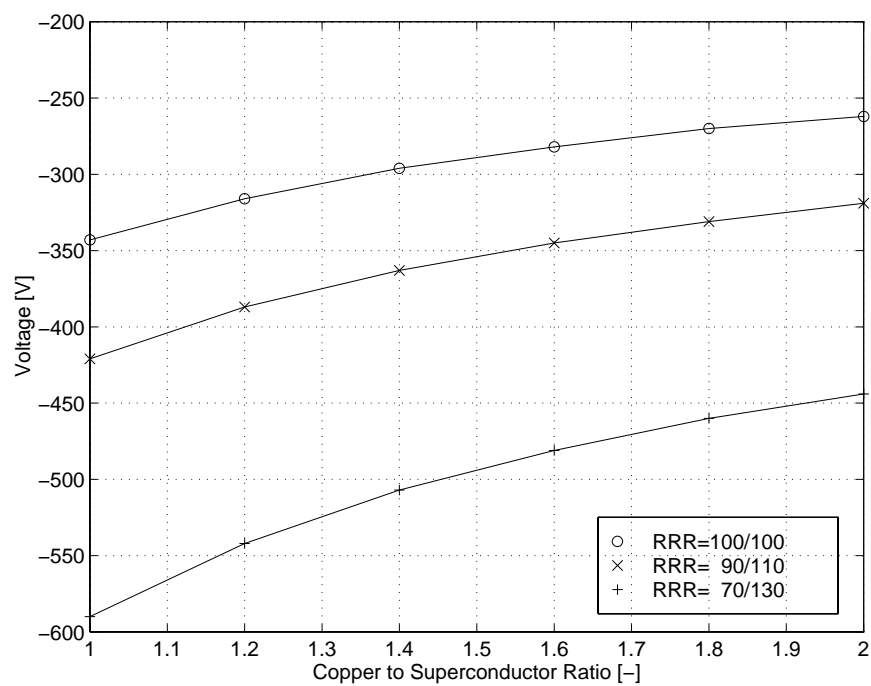


Figure 6.30: Maximum voltage to ground versus ΔRRR with average RRR as parameter at uniform heater delay of $\Delta t_{hA} = \Delta t_{hB} = 50$ ms

Figure 6.31: Hot-spot temperature versus Cu/Sc -ratio with Δt_h as parameterFigure 6.32: Maximum voltage versus Cu/Sc -ratio with Δt_h as parameter

Figure 6.33: Hot-spot temperature versus Cu/Sc -ratio with ΔRRR as parameterFigure 6.34: Maximum voltage versus Cu/Sc -ratio with ΔRRR as parameter

Conclusions

The influence of different values of RRR for aperture dipoles on the maximum voltage U_{max} is less important than the influence of differences in quench heater delay. The hot-spot temperature T_{hs} is more determined by the heater delay time t_h than by the differences in heater response time Δt_h and differences in values of RRR.

The higher the values of RRR, the longer becomes the current decay after a quench and the higher will be the raise of hot-spot temperature and maximum voltage. Hot-spot temperatures and maximum voltages to ground are more sensitive to different values of RRR the lower the absolute value of RRR is. A change of the value of RRR from 60 to 140 in the cables of both aperture dipoles leads to an increase in hot-spot temperature of about 3 K only. The peak voltages grow for about 30 V by increasing the values of RRR in the same range.

Differences in heater response time Δt_h between both apertures of 10 ms lead already to an increase in hot-spot temperature of about 10 K and an increase in maximum voltage to ground of about 150 V.

Chapter 7

Conclusions

The quench protection system of the LHC superconducting accelerator magnets is of essential importance for the LHC machine since all superconducting dipole magnets in a LHC octant will be electrically connected in series.

Practical experience has been attained on the LHC Test String, composed of one 3 m long superconducting twin-aperture prototype quadrupole and three 10 m long superconducting twin-aperture prototype dipoles. The protection diodes are housed in the cold mass of the short straight section. Auxiliary bus-bars, actually designed to supply corrector magnets, connect the diodes parallel to the dipoles. The copper cross-section of some auxiliary bus-bars is too small in order to by-pass the entire current for more than 1 s across the quenched dipole while the other magnets remain superconducting during the discharge. Therefore, the quench protection system on the LHC Test String acts on the half-cell level. If a quench is detected, the heater strips in all string magnets are fired in order to avoid damaging the auxiliary bus-bars. During the operation of the LHC Test String, magnet quenches have been provoked manually by firing the quench heaters or occurred naturally by exceeding the critical temperature or critical current density of the superconductor.

In order to understand the quench behaviour in the LHC Test String, a single magnet quench on the LHC test bench has been analysed. Studies on the electrodynamic behaviour have shown that after firing the heater strips not only the outer layer coils quench but also the inner coils become resistive. Unsymmetrical voltage distribution from coil to ground has been observed which is mainly caused by differences in heater response time Δt_h , differences in the values of RRR of copper, and differences in inter-strand resistance of the superconducting cable. To keep voltages limited across magnets in the LHC Test String, by-pass diodes are connected in parallel to each magnet.

Most of the data (current, magnet pole voltages, helium temperatures, helium pressures, etc.) could be measured while some parameters (magnet currents, diode currents, average coil temperatures, adiabatic hot-spot temperatures, dissipated energies, etc.) cannot be directly measured. A simulation program has been developed to calculate the missing data. The validation of the model has been performed by comparing measured and simulated values. The simulated values are of sufficient accuracy. Simulations, fed with parameters from experiments, show an almost equal energy distribution in the magnets of the LHC Test String after firing the quench heaters. This is mainly caused by firing the quench heaters simultaneously in all magnets. Deviations due to differences in heater response time and

different values of RRR have almost no influence on the energy distribution.

The LHC Test String quench protection system is working well. The detection levels are set sensitive between 80 and 160 mV. Deduced from an experiment, changing the quench detection level from 100 mV to 1 V leads to an increase of the adiabatic calculated hot-spot temperature from 290 K to 340 K.

In all quench experiments, the maximum voltages to ground were always below 250 V and did not endanger the electrical insulation. The adiabatic calculated hot-spot temperatures never exceeded 350 K. By assuming the maximum difference in heater response time Δt_h between apertures of the final LHC dipoles [13] with 10 ms as measured in the dipoles of the LHC Test String, the peak voltages between coil and ground during a discharge will not endanger the insulation.

The modelling of the quench behaviour of the final version of the LHC magnet shows that hot-spot temperatures and voltages to ground can be kept within safe limits as long as the variations in heater delay and values of RRR are not too large.

For the magnets, installed in the LHC machine, the quench propagation from magnet to magnet should be as slow as possible. If one dipole in a LHC octant quenches, an energy of about 7.2 MJ will be dissipated into the cryogenic system. The essential effects on quench propagation from the quenched magnet to the adjacent magnets are heat transport via helium and heat conduction through the metallic bus-bars. On the LHC Test String, quench propagation experiments between dipole magnets could not be performed because of the small copper cross section of the auxiliary bus-bars. Only the quench propagation by firing the heaters in the quadrupole have been studied.

Up to initial quench currents of 5 kA, the current decays faster than the quench propagates from the diode triplet across the quadrupole to the neighbour dipole. Initial quench currents above 5 kA lead to quenches in the adjacent dipole. Experiments have shown that the heat transport along the bus-bar, connecting the diode triplet to the adjacent dipole, has been responsible for a dipole quench and not the heat transport through the helium. Neither the dissipated heat in the quadrupole nor a helium pressure of 9 bar caused a quench in the adjacent dipole magnet.

Modelling the heat distribution along the bus-bar by neglecting the heat transfer to the surrounding helium has demonstrated that the cooling effect of helium is of essential importance. The influence of helium increases the time between quadrupole quench and dipole quench by about a factor 20.

In the final LHC machine, the by-pass diodes will be housed in the same cryostat as the magnets in order to avoid long auxiliary bus-bars. Based on the studies of magnet quench propagation, a modification on the LHC Test String is planned. The diode, by-passing the third dipole, will be replaced by a diode which will be housed in the cryostat between the second and the third dipole. The bus-bars will be dimensioned to carry the entire current during the decay. With such a configuration more realistic results for the quench behaviour of the final LHC machine are expected.

All experiments on the LHC Test String have been performed without destroying magnets or damaging quench protection elements as diodes and strip heaters. Some voltage taps on the quadrupole were lost maybe due to a helium pressure wave after a quench. It was possible to modify the quadrupole protection with the restriction of loosing redundancy.

Appendix A

Calculations

A.1 Inductance Calculation

Most of the superconducting accelerator magnets are designed as $\cos(m\phi)$ approximation magnets. The coil for this configuration consists of a long homogeneous straight section and two inhomogeneous coil ends. For field calculations adequate computer programs are available. They are time consuming if the iron saturation is taken into account. If the saturation effect of the iron can be almost neglected, simpler analytic methods give faster results.

The described method is based on *Biot-Savart's law* and calculates the mutual inductances in the straight sections of the coils. This is possible for the main dipole and quadrupole magnets because the straight parts of these coils are long in comparison to their aperture.

Since the coils for inner and outer layer as well as for the magnet poles are connected in series, each conductor carries the same current.

A simple arrangement for calculating the mutual inductance is given by two parallel double lines (see Fig. A.1). It is assumed that double line ab carries the current I , whereas double line cd is without current.

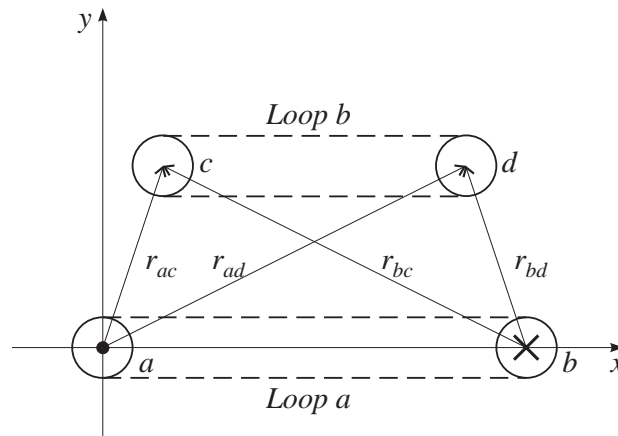


Figure A.1: Configuration of two parallel double lines to calculate the mutual inductance

The magnetic flux density \vec{B} in a distance r of a current carrying straight circular conductor is given with

$$|\vec{B}| = \mu \cdot |\vec{H}| = \frac{\mu \cdot I}{2 \cdot \pi \cdot r} e_r \quad (\text{A.1})$$

The particular flux through the surface cd , which is generated by the current I in conductor a , can be calculated by solving the integral

$$\Phi' = \int_{r_{ac}}^{r_{ad}} \frac{\mu \cdot I \cdot l}{2 \cdot \pi \cdot r} dr$$

which gives

$$\Phi' = \frac{\mu \cdot I \cdot l}{2 \cdot \pi} \ln \left(\frac{r_{ad}}{r_{ac}} \right) \quad (\text{A.2})$$

For the particular flux through the same surface cd , caused by the current $-I$ in conductor b , yields

$$\Phi'' = -\frac{\mu \cdot I \cdot l}{2 \cdot \pi} \ln \left(\frac{r_{bd}}{r_{bc}} \right) \quad (\text{A.3})$$

whereas l considers the length of the double line.

The flux of double line ab linked to double line cd is

$$\Phi_{cd} = \Phi' + \Phi'' = \frac{\mu \cdot I \cdot l}{2 \cdot \pi} \ln \left(\frac{r_{ad} \cdot r_{bc}}{r_{ac} \cdot r_{bd}} \right) \quad (\text{A.4})$$

and for the mutual inductance between double lines ab and cd follows in the Cylindrical co-ordinate system

$$M = \frac{\Phi_{cd}}{I} = \frac{\mu \cdot l}{2 \cdot \pi} \ln \left(\frac{r_{ad} \cdot r_{bc}}{r_{ac} \cdot r_{bd}} \right) \quad (\text{A.5})$$

which can be also depicted in the Cartesian co-ordinate system with

$$M = \frac{\mu \cdot l}{2 \cdot \pi} \ln \left(\frac{\sqrt{((x_d - x_a)^2 + (y_d - y_a)^2)} \cdot \sqrt{((x_c - x_b)^2 + (y_c - y_b)^2)}}{\sqrt{((x_c - x_a)^2 + (y_c - y_a)^2)} \cdot \sqrt{((x_b - x_d)^2 + (y_b - y_d)^2)}} \right) \quad (\text{A.6})$$

Usually the cables have a rectangular shape which makes the analytical calculation difficult. By permitting an error in the range of a few percent, the equation A.5 can be used if the distances r are measured between the centres of the rectangular shaped cables.

The influence of the iron yoke can be considered in the calculation by using the image-mirror method (see Fig. A.2). Therefore, not only the inductance of the line P is considered but also the inductance of the image mirror P' , which is mirrored into the iron yoke by the relation

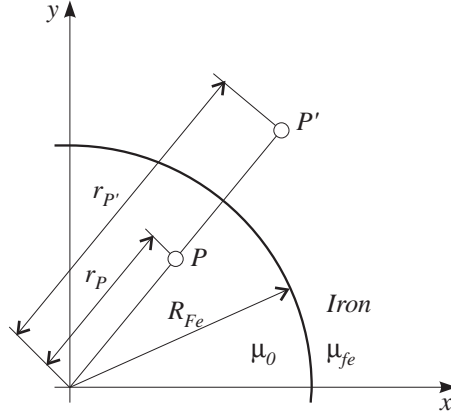


Figure A.2: Image mirror method to consider the effect of the iron

$$R_{Fe}^2 = r_P \cdot r_{P'} \quad (\text{A.7})$$

In the Cartesian co-ordinate system the image point P' is depicted with

$$x_{P'} = \frac{R_{Fe}^2}{\sqrt{x_P^2 + y_P^2}} \cos \left(\arctan \left(\frac{y_P}{x_P} \right) \right) = x_P \frac{R_{Fe}^2}{x_P^2 + y_P^2}$$

and

$$y_{P'} = \frac{R_{Fe}^2}{\sqrt{x_P^2 + y_P^2}} \sin \left(\arctan \left(\frac{y_P}{x_P} \right) \right) = y_P \frac{R_{Fe}^2}{x_P^2 + y_P^2}$$

The image current I' through the conductor is calculated by the expression

$$I' = I \frac{\mu_{Fe} - 1}{\mu_{Fe} + 1} \quad (\text{A.8})$$

Assuming the permeability of the iron yoke μ_{Fe} as infinite gives satisfied results. For more accurate calculations the saturation in each part of the iron yoke has to be taken into account. This can be performed by use of Finite-Element-Method (FEM) programs.

The aperture dipoles of a main dipole magnet are formed of two-layer coils with different conductor cross-sections for the outer and inner layer. The aperture quadrupoles of a main quadrupole magnet are formed of two-layer coils with the same type of cable for the outer and inner layer coils.

For simplifying the inductance calculation, the current is considered flowing in the centre of the conductors with the co-ordinates (Fig. A.3)

$$x_m = \frac{x_2 + x_4}{2} - \frac{h}{2} \cdot \sin \left(\arctan \left(\frac{y_4 - y_2}{x_2 - x_4} \right) \right) \quad (\text{A.9})$$

$$y_m = \frac{y_2 + y_4}{2} - \frac{h}{2} \cdot \cos \left(\arctan \left(\frac{y_4 - y_2}{x_2 - x_4} \right) \right). \quad (\text{A.10})$$

The Tables A.1 and A.2 contain the centre co-ordinates of the conductors in an aperture quadrant of a prototype dipole and a prototype quadrupole.

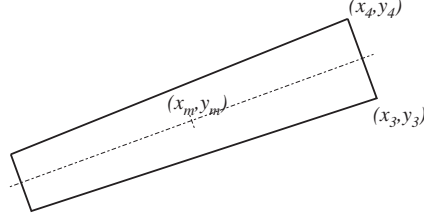


Figure A.3: Cross-section of the superconducting cable

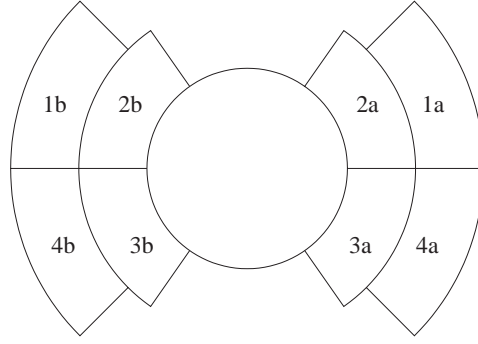


Figure A.4: Dipole coil designation for calculating self and mutual inductances

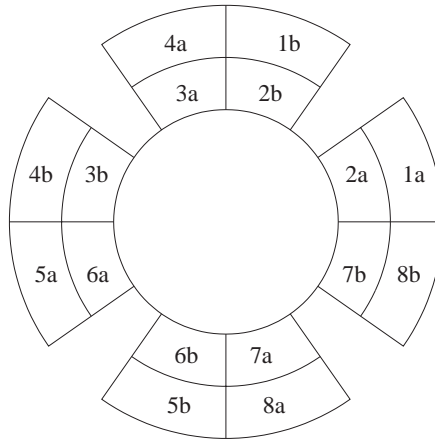


Figure A.5: Quadrupole coil designation calculating the self and mutual inductances

Table A.1: Centre co-ordinates of the conductors in the first quadrant of the LHC prototype dipole magnet

Inner Layer							
Block	Conductor	x2a	y2a	x4a	y4a	xm	ym
1	1	17.6309	38.3058	15.3825	39.3522	12.9199	31.1228
	2	15.1666	39.3112	12.8919	40.2991	10.6431	32.0087
2	1	28.9231	30.8383	26.9886	32.3902	22.6369	24.9841
	2	26.8768	32.5395	24.9029	34.0408	20.7443	26.5245
	3	24.7531	34.1410	22.7410	35.5907	18.7783	27.9694
3	1	38.6827	16.9112	37.5823	19.1337	30.5149	14.2511
	2	37.5000	19.2938	36.3425	21.4871	29.4039	16.4233
	3	36.1924	21.6103	34.9786	23.7730	28.1733	18.5313
	4	34.7059	23.8232	33.4365	25.9537	26.7691	20.5376
4	1	42.1711	0.1900	42.1390	2.6698	33.6557	1.3199
	2	42.0549	2.8476	41.9587	5.3258	33.5132	3.7568
	3	41.7314	5.4943	41.5710	7.9691	33.1690	6.1821
	4	41.1973	8.1206	40.9730	10.5904	32.6199	8.5866
Outer Layer							
Block	Conductor	x2a	y2a	x4a	y4a	xm	ym
5	1	56.0168	21.7434	55.2593	23.2092	48.0867	18.5741
	2	55.3195	23.4675	54.5320	24.9174	47.4563	20.1356
	3	54.5675	25.1662	53.0686	26.5996	46.0353	17.4189
	4	53.7623	26.8380	52.9158	28.2543	46.0429	23.1853
	5	52.9041	28.4817	52.0286	29.8802	45.2616	24.6708
	6	51.9941	30.0956	51.0899	31.4759	44.4316	26.1282
	7	51.0331	31.6785	50.1008	33.0396	43.5539	27.5563
	8	50.0222	33.2289	49.0620	34.5708	42.6294	28.9536
	9	48.9623	34.7456	47.9747	36.0675	41.6591	30.3191
	10	47.8589	36.2307	46.8443	37.5319	40.6484	31.6547
	11	46.7153	37.6848	45.6741	38.9648	39.6005	32.9613
	12	45.5304	39.1055	44.4631	40.3638	38.5144	34.2365
	13	44.3006	40.4876	43.2076	41.7237	37.3863	35.4753
	14	43.0266	41.8297	41.9084	43.0431	36.2169	36.6761
	15	41.7096	43.1306	40.5667	44.3206	35.0075	37.8379
6	1	60.0211	0.2000	60.0041	1.8499	51.5131	0.9375
	2	59.9844	2.0496	59.9335	3.6988	51.4630	2.6117
	3	59.8896	3.8971	59.8047	5.5449	51.3584	4.2837
	4	59.7353	5.7410	59.6165	7.3868	51.1979	5.9519
	5	59.5216	7.5796	59.3690	9.2225	50.9818	7.6147
	6	59.2487	9.4112	59.0622	11.0506	50.7099	9.2705
	7	58.9166	11.2340	58.6964	12.8683	50.3826	10.9164
	8	58.5255	13.0466	58.2717	14.6769	49.9997	12.5545
	9	58.0756	14.8471	57.7883	16.4719	49.5618	14.1796

Table A.2: Centre co-ordinates of the conductors in the first quadrant of the LHC prototype quadrupole magnet

Inner Layer							
Block	Conductor	x2a	y2a	x4a	y4a	xm	ym
1	1	41,1060	0,1695	41,0680	2,3228	32,5883	1,0961
	2	41,0231	2,5108	40,9093	4,6614	32,4780	3,1369
	3	40,8009	4,8437	40,6113	6,9889	32,2391	5,1679
	4	40,4364	7,1609	40,1714	9,2981	31,8684	7,1835
	5	39,9301	9,4552	39,5899	11,5818	31,3667	9,1757
	6	39,2824	11,7194	38,8675	13,8327	30,7341	11,1385
2	1	37,2248	17,2689	36,4639	19,2836	28,8925	15,2730
	2	36,1367	19,3573	35,3052	21,6997	27,7106	17,6850
Outer Layer							
Block	Conductor	x2a	y2a	x4a	y4a	xm	ym
3	1	54,9668	0,1696	54,9289	2,3228	48,4238	1,1313
	2	54,9054	2,5116	54,7915	4,6621	48,3325	3,2420
	3	54,7467	4,8489	54,5572	6,9942	48,1522	5,3474
	4	54,4885	7,1774	54,2235	9,3146	47,8805	7,4430
	5	54,1303	9,4928	53,7902	11,6193	47,5171	9,5255
	6	53,6728	11,7909	53,2579	13,9041	47,0626	11,5904
	7	53,1167	14,0676	52,6276	16,1649	46,5176	13,6343
	8	52,4629	16,3188	51,9002	18,3976	45,8832	15,6533
	9	51,7125	18,5405	51,0769	20,5981	45,1604	17,6435
	10	50,8667	20,7285	50,1590	22,7625	44,3502	19,6013
	11	49,9269	22,8790	49,1480	24,8868	43,4542	21,5229
	12	48,8947	24,9880	48,0455	26,9671	42,4738	23,4046

Table A.3: Self- and mutual inductances of the LHC dipole

	Units	First Version Dipole	Final Version Dipole
Input parameters:			
No. of outer layer turns	[-]	24	26
No. of inner layer turns	[-]	13	15
Inner iron radius	[m]	0.1005	0.101
Magnet length	[m]	9.0	14.2
Self inductances:			
L_{11}, L_{44}	[mH]	5.0193	8.8178
L_{22}, L_{33}	[mH]	0.8920	2.0286
Mutual inductances:			
M_{12}, M_{34}	[mH]	1.4849	3.1173
M_{13}, M_{24}	[mH]	1.0018	2.0203
M_{14}	[mH]	2.8439	4.7849
M_{23}	[mH]	0.4842	1.1044
Aperture inductance	[mH]	28.4256	54.0225
Magnet inductance	[mH]	56.8512	108.0437

Table A.4: Self- and mutual inductances of the LHC prototype quadrupole

	Units	Quadrupole
Input parameters:		
No. of outer layer turns	[-]	12
No. of inner layer turns	[-]	8
Inner iron radius	[m]	0.086
Magnet length	[m]	3.0
Self inductances:		
$L_{11}, L_{44}, L_{55}, L_{88}$	[mH]	0.3350
$L_{22}, L_{33}, L_{66}, L_{77}$	[mH]	0.1159
Mutual inductances:		
$M_{12}, M_{34}, M_{56}, M_{78}$	[mH]	1.4849
$M_{13}, M_{24}, M_{35}, M_{46}, M_{57}, M_{68}, M_{14}, M_{45}, M_{18}, M_{58}$	[mH]	0.0790
M_{15}, M_{48}	[mH]	-0.0424
M_{26}, M_{37}	[mH]	-0.0149
$M_{16}, M_{25}, M_{37}, M_{48}$	[mH]	-0.0243
M_{17}, M_{28}	[mH]	0.0322
$M_{23}, M_{36}, M_{67}, M_{27}$	[mH]	0.0301
Aperture inductance	[mH]	3.6700
Magnet inductance	[mH]	7.3400

A.2 Approximation of Diode Characteristics

Below 80 K the diode forward voltage $U_f(T)$ is strongly non linear with temperature. Forward voltage measurements at different temperatures and current levels are listed in Table A.5 for the triplet diodes and in Table A.6 for the quadruplet diodes [6]. Since it is not possible to measure U_f at high currents and 1.8 or 4.2 K and keeping the temperature constant, the measured values ($T > 4.2$ K) have been used. This has only little influence on the results.

Table A.5: Typical forward voltage measured on a single triplet diode versus temperature with the current as parameter

Initial Temp. [K]	U_f [V] at 460 A	U_f [V] at 3000 A	U_f [V] at 5000 A	U_f [V] at 8000 A	U_f [V] at 12000 A	U_f [V] at 15000 A
4.2	1.69	1.73	1.74	1.74	1.74	1.74
21	1.53	1.63	1.66	1.67	1.67	1.67
45	1.14	1.23	1.28	1.33	1.38	1.40
64	1.10	1.15	1.18	1.21	1.24	1.26
82	1.08	1.11	1.13	1.16	1.18	1.20
93	1.06	1.10	1.11	1.13	1.16	1.17
126	1.02	1.05	1.06	1.08	1.10	1.11
159	0.98	1.01	1.02	1.04	1.06	1.07
189	0.93	0.98	0.99	1.01	1.03	1.04
213	0.90	0.94	0.96	0.98	1.00	1.01
246	0.85	0.90	0.92	0.94	0.96	0.98
276	0.80	0.86	0.88	0.90	0.93	0.95
298	0.76	0.82	0.85	0.90	0.93	0.92

Table A.6: Typical forward voltage measured on a single quadruplet diode versus temperature with the current as parameter

Initial Temp. [K]	U_f [V] at 460 A	U_f [V] at 3000 A	U_f [V] at 5000 A	U_f [V] at 8000 A	U_f [V] at 12000 A	U_f [V] at 15000 A
1.8	3.443	3.403	3.439	3.474	3.528	3.631
4.2	3.287	3.364	3.402	3.436	3.466	3.498
77	1.104	1.242	1.338	1.471	1.634	1.766
200	0.950	1.080	1.170	1.280	1.410	1.500
295	0.794	0.923	0.993	1.081	1.185	1.264

The model approximates the diode characteristics by a non-linear fit of the voltage characteristics as a function of temperature and diode current

$$U_f(T, i_d) = (a_n + b_n \cdot i_d(t)) \cdot e^{-(c_n + d_n \cdot i_d(t)) \cdot T} \quad (\text{A.11})$$

with $n = 3$. Due to the different characteristics of the diode triplet and diode quadruplet, the fit parameters are evaluated for both types of diode configurations separately. The parameters a , b , c , and d are listed in Table A.7 for the diode triplet and in Table A.8 for the diode quadruplet. The diode characteristics were measured at similar cooling conditions as later in the LHC Magnet String.

Table A.7: Parameters to fit the diode triplet characteristics

n	a	b	c	d
1	3.2810^{-5}	0.7153	-1.3010^{-6}	0.0340
2	-1.0310^{-4}	-0.9183	7.0010^{-9}	0.0043
3	7.1510^{-5}	2.0251	1.0010^{-9}	0.0023

Table A.8: Parameters to fit the diode quadruplet characteristics

n	a	b	c	d
1	-0.4910^{-4}	2.5930	0.6010^{-6}	0.0336
2	0.3510^{-4}	-0.1677	3.8010^{-9}	0.0051
3	0.2910^{-5}	1.1380	-0.7010^{-9}	0.0009

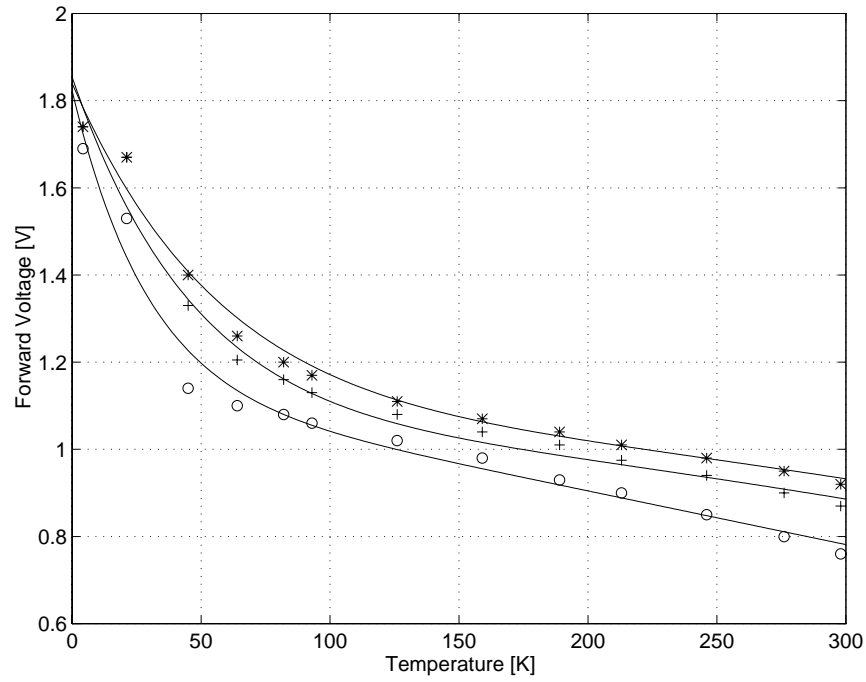


Figure A.6: Measured forward voltage versus temperature at different current levels for a single diode of the triplet; (o) $i = 460$ A, (+) $i = 8000$ A, (*) $i = 15000$ A and approximations

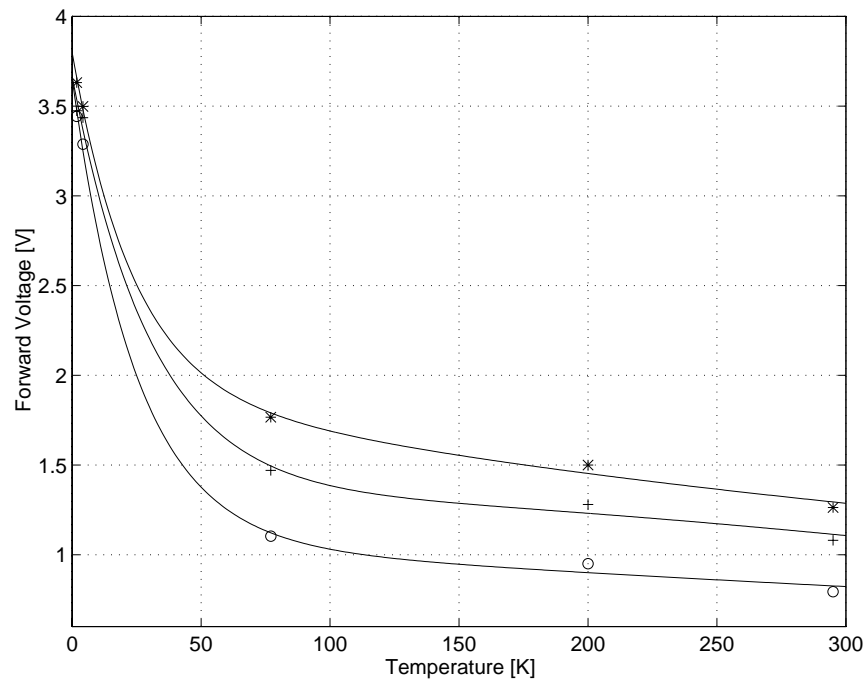


Figure A.7: Forward voltage versus temperature at different current levels for a single diode of the quadruplet; (o) $i = 460$ A, (+) $i = 8000$ A, (*) $i = 15000$ A and approximations

Appendix B

Magnet Parameters

Table B.1: Main quadrupole parameters for LHC version 1 and LHC version 4

	Units	Version 1	Version 4
Operational flux density gradient	[T m ⁻¹]	250	223
Peak field in the conductor	[T]	7.76	6.87
Coil aperture	[mm]	56	56
Magnetic length	[m]	3.05	14.2
Operating current	[A]	15060	11780
Operating temperature	[K]	1.9	1.9
<i>Coils (two-shells) construction</i>			
Coil inner diameter	[mm]	56	56
Coil outer diameter	[mm]	110.6	118.6
<i>Cable:</i>			
Number of turns per coil:			
Number of turns (inner layer)	[mm]	8	10
Number of turns (outer layer)	[mm]	12	14
Cable width	[mm]	13.05	15
Cable height	[mm]	1.70/2.16	1.34/1.60
Numbers of strands		24	36
Strand diameter	[mm]	1.09	0.825
Filament diameter	[μm]	5	6
Copper to superconductor ratio		1.8	1.9
<i>Structure:</i>			
Distance between aperture axis	[mm]	180	194
Outer collar diameter	[mm]	164	170
Yoke outer diameter	[mm]	444	456
<i>Other characteristics:</i>			
Stored energy (both channels)	[kJ]	890	784
Self inductance (both channels)	[mH]	8	11.4
Resultant e.m. forces in the first coil quadrant:			
$\sum F_x$	[MNm ⁻¹]		0.57
$\sum F_y$ (inner layer)	[MNm ⁻¹]		-0.75

Table B.2: Main dipole parameters for the first and final version of LHC magnets

	Units	first Version	final Version
Operational flux density	[T]	10	8.40
Coil aperture	[mm]	50	56
Magnetic length	[m]	9	14.2
Operating current	[A]	15060	11500
Operating temperature	[K]	1.9	1.9
<i>Coils (two-shells) construction</i>			
Coil inner diameter	[mm]	50	56
Coil outer diameter	[mm]	120.2	120.5
<i>Cable:</i>			
Inner shell:			
Turns per beam channel		26	30
Cable width	[mm]	17	15
Cable height	[mm]	2.02/2.48	1.72/2.06
Numbers of strands		26	28
Strand diameter	[mm]	1.29	1.065
Filament diameter	[μ m]	5	7
Copper to superconductor ratio		1.6	1.6
Outer shell:			
Turns per beam channel		48	52
Cable width	[mm]	17	15
Cable height	[mm]	1.30/1.65	1.34/1.60
Numbers of strands		40	36
Strand diameter	[mm]	0.840	0.825
Filament diameter	[μ m]	5	6
Copper to superconductor ratio		1.8	1.9
<i>Structure:</i>			
Distance between aperture axis	[mm]	180	194
Collar height	[mm]	201	192
Collar width	[mm]	381	396
Yoke outer diameter	[mm]	560	550
<i>Other characteristics:</i>			
Stored energy (both channels)	[MJ]	6156	7100
Self inductance (both channels)	[mH]	57	108
Resultant e.m. forces in the first coil quadrant:			
$\sum F_x$	[MNm ⁻¹]	2.27	1.7
$\sum F_y$ (inner layer)	[MNm ⁻¹]	-0.23	-0.14
$\sum F_y$ (outer layer)	[MNm ⁻¹]	-0.98	-0.60
Axial e.m. forces on magnet ends (both channels)	[MN]	0.70	0.50

Table B.3: Main parameters of the quench heater strips for the prototype quadrupole and prototype dipoles in the LHC Magnet String

	Units	Quadrupole	Dipole
Strips stainless steel type		AISI 302	AISI 304
Heater strip dimensions:			
Width	[mm]	12.7	15.0
Thickness	[μm]	25	25
Length	[m]	6	20
Pads		U-shaped	U-shaped
Copper plating:		no	yes
Thickness	[μm]	-	1 – 1.5
Cycle	[mm]	-	250 / 250
Sides		-	one side
Polyimide base	[μm]	125	125
Bonding		Loctite glue (spot)	Loctite glue (spot)
Number of covered turns (per pole, full length)		6	13
Heater arrangement		single strip	double strip
Powering:			
Unit strips per channel		1	1
Nominal voltage	[V]	400	800
eff. capacity per channel	[mF]	6.6	3.3
Strip resistance per channel (300 K / 1.9 K)	[Ω]	17 / 11	28 / 16
Discharge time constant	[ms]	73	50
Initial specific power per unit of heating surface	[Wcm ⁻²]	19	27
max. temperature (adiabatic)	[K]	175	160

Appendix C

Quench Detection Scheme

Table C.1: Threshold and gain adjustment of quench detector modules for the LHC Test String

Channel	Mode	Threshold [mV]	Gain	Description
V CL+	amplifier	100	40	detect. of positive current lead
V CL-	amplifier	100	40	detect. of negative current lead
V CL + SSS	amplifier	100	40	bus-bar detect. curr.lead+ to quad.
V SSS CL-	amplifier	100	40	bus-bar detect. quad. - curr.lead-
V MBB(SSS)	amplifier	100	40	quad. main bus-bar detector
V RBB(SSS)	amplifier	100	40	quad. return bus-bar detector
V MBB(MB1)	bridge	50	40	MTP1A1 main bus-bar detector
V RBB(MB1)	amplifier	100	40	MTP1A1 return bus-bar detector
V MBB(MB2)	bridge	50	40	MTP1A2 main bus-bar detector
V RBB(MB2)	amplifier	100	40	MTP1A2 return bus-bar detector
V MBB(MB3)	bridge	50	40	MTP1A3 main bus-bar detector
V RBB(MB3)	amplifier	100	40	MTP1A3 return bus-bar detector
QD PA(SSS)	bridge	40	4	quad. detector between poles 1+2 and 3+4
QD PB(SSS)	bridge	40	4	quad. detector between poles 5+6 and 7+8
QD A(SSS)	bridge	100	4	quad. detector between apertures A and B
QD PA(MB1)	bridge	80	4	MTP1A1 detector between poles 4 and 3
QD PB(MB1)	bridge	80	4	MTP1A1 detector between poles 2 and 1
QD A(MB1)	bridge	100	4	MTP1A1 detector between apertures A and B
QD PA(MB2)	bridge	80	4	MTP1A2 detector between poles 4 and 3
QD PB(MB2)	bridge	80	4	MTP1A2 detector between poles 2 and 1
QD A(MB2)	bridge	100	4	MTP1A2 detector between apertures A and B
QD PA(MB3)	bridge	80	4	MTP1A3 detector between poles 4 and 3
QD PB(MB3)	bridge	80	4	MTP1A3 detector between poles 2 and 1
QD A(MB3)	bridge	100	4	MTP1A3 detector between apertures A and B
QD M(MB1, MB2)	bridge	700	4	detector between MTP1A1 and MTP1A2
QD M(MB2, MB3)	bridge	700	4	detector between MTP1A2 and MTP1A3

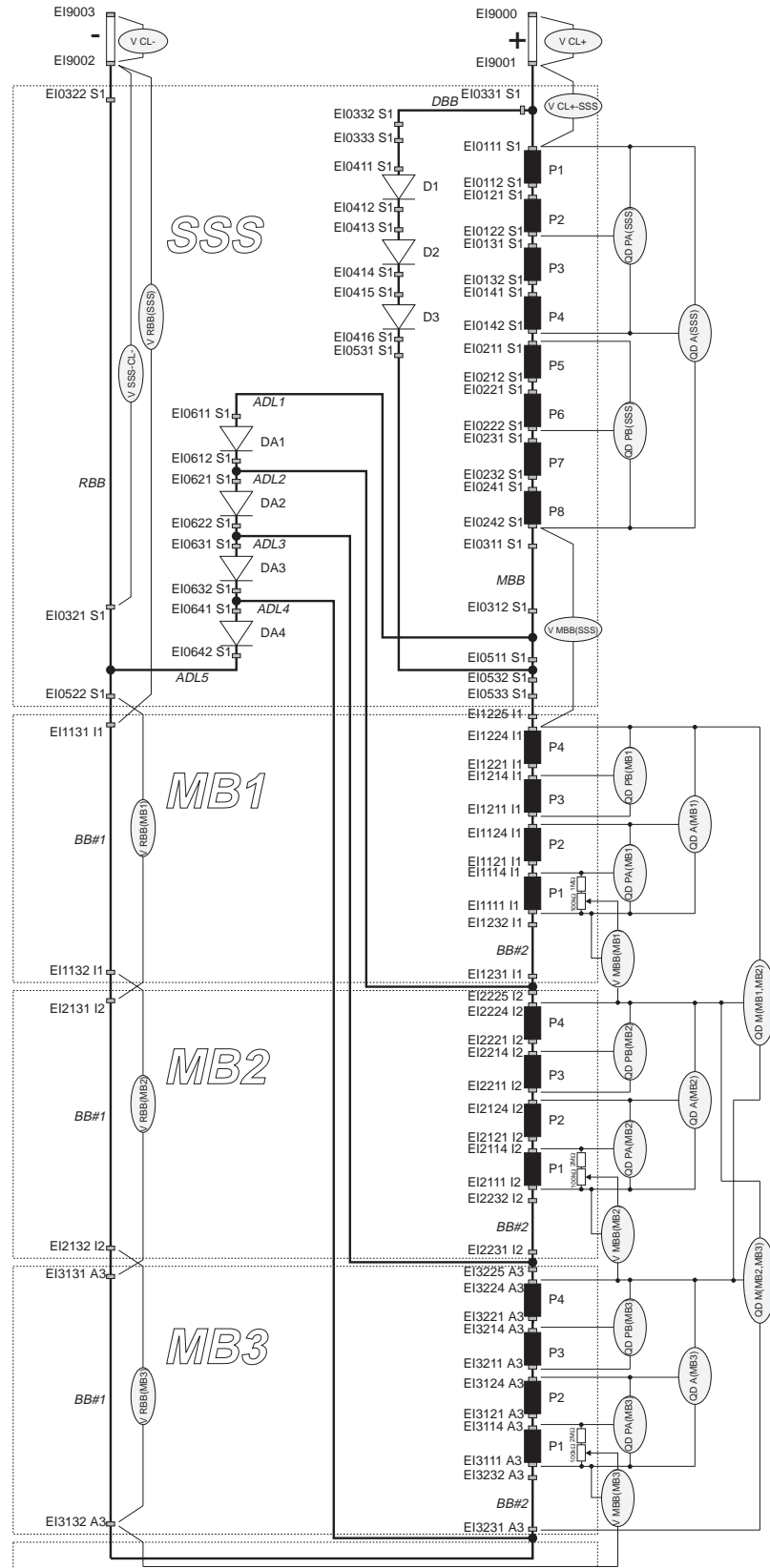


Figure C.1: Quench protection scheme for the LHC Test String

Appendix D

Material Properties

D.1 Specific Heat

The heat capacity is a fundamental state property of matter. It represents the amount of energy needed to raise the temperature of a material one degree. The heat capacity per unit mass is called the specific heat which is determined by the crystal lattice (T^3 -dependence), the free electrons (T -dependence), and the phase transitions undergone by the material.

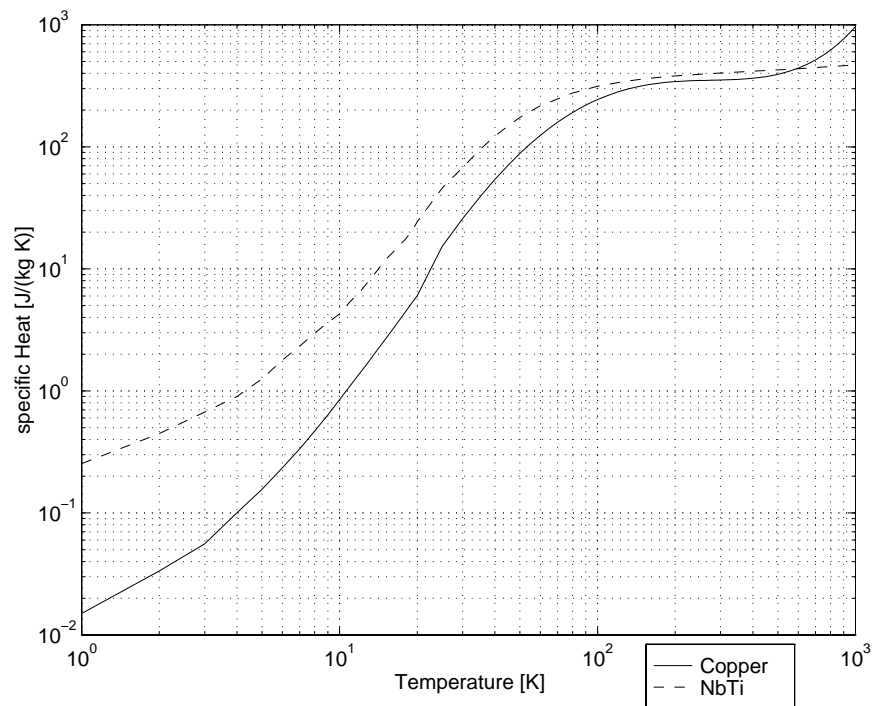


Figure D.1: Specific heat versus temperature for copper and niobium-titanium

D.2 Electrical Resistivity

The electrical resistivity of copper may thus be separated into two independent parts,

$$\rho_{Cu} = \rho_i + \rho_0$$

where ρ_i is the intrinsic resistivity (the electron-lattice interaction) and ρ_0 is the imperfection resistivity (the electron-imperfection interaction). While ρ_i is a function of temperature, ρ_0 is dependent on the type and concentration of the imperfections and is almost independent of temperature.

At very low temperatures ρ_0 is much greater than ρ_i , thus temperature change has little effect on the resistivity. The value of RRR (residual-resistivity-ratio) depends on the purity of copper. The higher the purity, the higher is the value of RRR and the lower becomes the electrical resistivity at very low temperatures. At high temperatures ρ_i is much greater than ρ_0 , thus the difference in electrical resistivity for various samples becomes relatively insignificant.

The electrical resistivity of copper is for instance calculated by use of the approximation formula

$$\rho_{Cu}(T, B) = \left[\frac{1.545}{RRR} + \frac{1}{\frac{2.32547 \cdot 10^9}{T^5} + \frac{9.57137 \cdot 10^5}{T^3} + \frac{1.62735 \cdot 10^2}{T}} \right] 10^{-8} + 0.5 \cdot 10^{-10} \cdot B \quad (D.1)$$

with an accuracy of better than a percent over the temperature range 0 to 1000 K [19]. The first term in Eq. (D.1) considers the temperature dependency of copper while the second term calculates the influence of magnetic field.

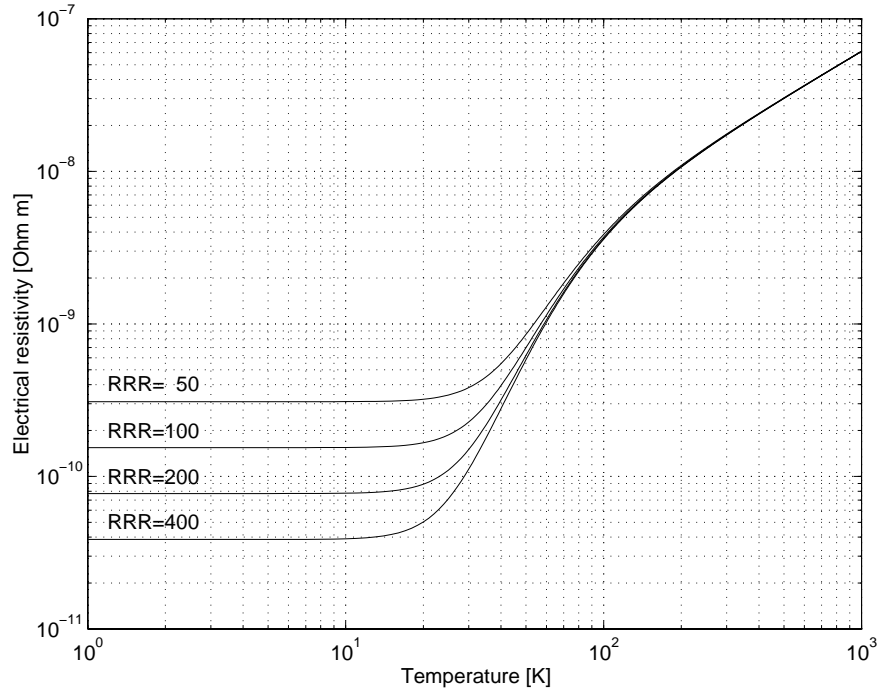


Figure D.2: Electrical resistivity versus temperature for copper with RRR as parameter

D.3 Thermal Conductivity

In a metal, the valence electrons with energies near the Fermi level act as conductors of thermal energy. Higher electrical conductivity is associated with higher thermal conductivity, the same number of conducting electrons being responsible for each. At higher temperatures, each conducting electron will carry, on average, higher thermal energy so that the ratio of thermal conductivity λ to electrical conductivity κ is proportional to absolute temperature [21]. This is summarised in the experimentally-determined *Wiedemann-Franz law*

$$L = \frac{\lambda}{\kappa \cdot T}. \quad (\text{D.2})$$

The theoretical value of L is $2.45 \cdot 10^{-8} \text{V}^2 \text{K}^{-2}$.

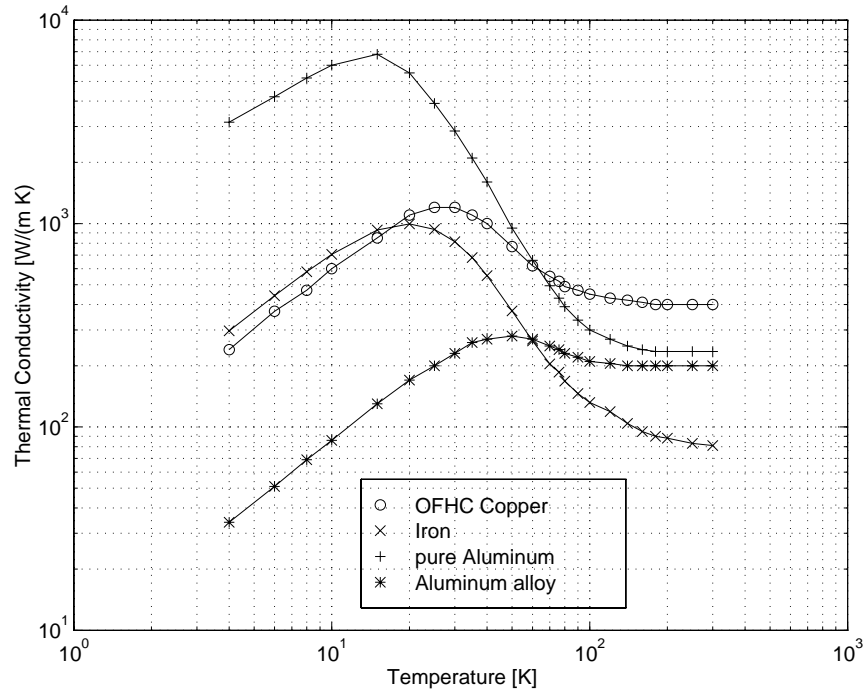


Figure D.3: Thermal conductivity versus temperature for different materials

Appendix E

List of Symbols

A	cross section area	$[\text{m}^2]$
A_{Cu}	copper cross section	$[\text{m}^2]$
A_{Sc}	superconductor cross section	$[\text{m}^2]$
B	magnetic flux density	$[\text{T}]$
B_c	critical magnetic flux density	$[\text{T}]$
c_p	specific heat	$[\text{Jkg}^{-1}\text{K}^{-1}]$
c_{pCu}	specific heat of copper	$[\text{Jkg}^{-1}\text{K}^{-1}]$
c_{pSc}	specific heat of superconductor	$[\text{Jkg}^{-1}\text{K}^{-1}]$
E	electric field	$[\text{Vm}^{-1}]$
f	frequency	$[\text{Hz}]$
f_c	characteristic frequency	$[\text{Hz}]$
G	gain of transfer function	$[\text{dB}]$
H	magnetic field	$[\text{Am}]$
I	current	$[\text{A}]$
I'	image current	$[\text{A}]$
I_0	initial current	$[\text{A}]$
i	transient current	$[\text{A}]$
i_d	diode current	$[\text{A}]$
i_m	magnet current	$[\text{A}]$
i_s	string current	$[\text{A}]$
J	current density	$[\text{Am}^{-2}]$
J_{av}	average current density	$[\text{Am}^{-2}]$
k	counter variable	$[-]$
l	length of conductor	$[\text{m}]$
l_{MPZ}	minimum propagation zone	$[\text{m}]$
L	self inductance	$[\text{H}]$
L_m	magnet inductance	$[\text{H}]$
m	mass	$[\text{kg}]$
\dot{m}_{He}	helium flow rate	$[\text{kg s}^{-1}]$
M	magnetisation	$[\text{Am}^{-1}]$
M	mutual inductance	$[\text{H}]$

n	index counter	[-]
P	power	[W]
\dot{q}	heat rate	[Js ⁻¹]
Q	joule heating	[J]
\dot{Q}	power loss	[W]
\dot{Q}_e	eddy current power loss	[W]
\dot{Q}_h	hysteretic power loss	[W]
r	radius	[m]
R	resistance	[Ω]
R_c	resistance of water cooled cable	[Ω]
R_d	resistance of dump resistor	[Ω]
R_e	resistance of external circuit	[Ω]
R_{Fe}	inner radius of magnet iron yoke	[m]
R_m	magnet coil resistance	[Ω]
R_{splice}	contact resistance	[Ω]
RRR	residual resistivity ratio	[-]
t	time	[s]
t_h	heater delay time	[s]
T	temperature	[K]
T_c	critical temperature	[K]
T_b	bath temperature	[K]
T_{hs}	hot-spot temperature	[K]
T_m	maximum temperature	[K]
u_a, u_b	magnet aperture voltage	[V]
u_L	inductive voltage	[V]
u_m	magnet voltage	[V]
U_{Dfw}	free-wheeling diode voltage	[V]
U_f	by-pass forward voltage	[V]
v	quench propagation velocity	[ms ⁻¹]
W	energy absorbed by the coolant	[J]
W_d	joule heat dissipated in by-pass diode	[J]
W_m	joule heat dissipated in magnet coils	[J]
x, y, z	Cartesian co-ordinates	[m]
Z_m	magnet impedance	[Ω]
δ_{Cu}	density of copper	[kgm ⁻³]
δ_{Sc}	density of the superconductor	[kgm ⁻³]
λ	thermal conductivity	[Wm ⁻¹ K ⁻¹]
μ_0	permeability of vacuum	[Hm ⁻¹]
μ_{Fe}	permeability of iron	[Hm ⁻¹]
ϕ	phase of transfer function	[deg]
ρ	electrical resistivity	[Ωm]
ρ_{Cu}	electrical resistivity of copper	[Ωm]
τ	discharge time constant	[s]

Bibliography

- [1] A. Bezaguët, D. Brahy, J. Casas-Cubillos, M. Grippeling, D. Lavielle, G. Leo, L. Madaro, A. Rijllart, and M. Skiadelli. The Control and Data Acquisition of the LHC Test String. *ICALPECS95*, 1995.
- [2] A. Bezaguët, A. J. Casas-Cubillos, B. Flemsaetter, B. Gaillard-Grenadier, T. Goiffon, H. Guinaudeau, P. Lebrun, M. Marguet, L. Serio, A. Suraci, L. Tavian, and R. van Weelderen. The Superfluid Helium Cryogenic System for the LHC Test String: Design, Construction and First Operation. *Cryogenics Engineering Conference*, 1995. Columbus, Ohio.
- [3] W. Burgett, L. Cromer, D. Haenni, M. Hentges, T. Jaffery, P. M. Kraushaar, Levin, A. McInturff, G. Mulholland, D. Richter, W. Robinson, D. Voy, J. Weisend, and J. Zatopek. Power Tests of a String of Magnets Comprising a Full Cell of the Superconducting Super Collider. *SSC-Note*, 1994.
- [4] E.W. Collings. *Applied Superconductivity, Metallurgy, and Physics of Titanium Alloys*, volume 2. Plenum Press, 1986.
- [5] L. Coull, P. Faugeras, P. Lebrun, A. Mathewson, P. Quesnel, and R. Saban, 1995. LHC Test String Workshop.
- [6] L. Coull and D. Hagedorn. Radiation Resistant Quench Protection Diodes for the LHC. *Cryogenics Engineering Conference*, 1993.
- [7] L. Coull, D. Hagedorn, G. Krainz, F. Rodriguez-Mateos, and R. Schmidt. Electrodynamic Behaviour of the LHC Superconducting Magnet String during a Discharge. *EPAC96*, 1996.
- [8] L. Coull, D. Hagedorn, G. Krainz, F. Rodriguez-Mateos, and R. Schmidt. Quench Propagation Tests on the LHC Superconducting Magnet String. *EPAC96*, 1996.
- [9] L. Coull, D. Hagedorn, V. Remondino, and F. Rodriguez-Mateos. LHC Magnet Quench Protection System. *Magnet Technology Conference (MT13)*, 1993.
- [10] A. Devred et al. Quench Start Localization in Full-length SSC R&D Dipoles. *SSC-N-214*, 1989. SSC, BNL, Fermilab, LBL.
- [11] E.I. Dyachkov, R. Herzog, I.S. Khukhareva, and A. Nichitiu. Thermal conductivity and electrical resistivity of Nb-Ti as a function of temperature and magnetic field. *Cryogenics*, 1981.

- [12] The LHC Study Group. *The Pink Book, Design Study of the Large Hadron Collider*. CERN 91-03, 1991.
- [13] The LHC Study Group. *The Yellow Book, LHC - The Large Hadron Collider - Conceptual Design*. CERN/AC/95-05(LHC), 1995.
- [14] D. Hagedorn. *Private communications*. CERN/LHC-ICP.
- [15] H. Hillmann. *Fabrication Technology of Superconducting Material*. Plenum Publishing Corp., superconducting materials science edition, 1981.
- [16] J. Kragh. *Measurement of Input/Output gain linearity of AD289 Isolation Amplifier Board*. CERN/LHC-ICP, 1996. unpublished.
- [17] G. Krainz, G. Riddone, and L. Serio. Contact Resistance of Superconducting Cable Splices on the LHC Prototype Magnet String. *CERN - LHC Project Note 61*, 1996.
- [18] D. Leroy et al. Test results on 10 T LHC superconducting one metre long dipole models. *12th International Conference on Magnet Technology*, 1991.
- [19] M. S. McAshan. MIITs Integrals for Copper and for Nb-46.5 wt% Ti. *SSC-N-468*, 1988.
- [20] A. McInturff, W. Burgett, H. Carter, T. Dombeck, J. Gannon, P. Kraushaar, G. Mulholland, T. Savord, G. Tool, W. Robinson, J.G. Weisend II, D. Voy, and J. Zbasnik. Test Results and Operational Characteristics of Prototype SSCL Half Cell. *IEEE Trans. on Magnetics*, 30(4), July 1994.
- [21] K.J. Pascoe. *Properties of Materials for Electrical Engineers*. J. Wiley & Sons, 1973.
- [22] R. Perin. Field, Forces and Mechanics of Superconducting Magnets. *CAS - Superconductivity in Particle Accelerators*, 1996. CERN 96-03.
- [23] R. Perin. Superconducting Magnets for the Large Hadron Collider. *LHC Project Report 52*, 1996. 10th General Conference of the European Physical Society Sevilla - Spain.
- [24] J. Perot. Special Magnets. *CAS - Superconductivity in Particle Accelerators*, 1996. CERN 96-03.
- [25] P. Proudlock. Electrical Powering Strategy of LHC First Design Study. *EPAC96*, 1996.
- [26] G. Riddone. Theoretical Modeling and Experimental Investigation of the Thermal Performance of the LHC Prototype Lattice Cryostats, 1997. Polytechnic of Turin - Italy.
- [27] W. Robinson, W. Burgett, T. Dombeck, J. Gannon, P. Kraushaar, A. McInturff, T. Savord, and G. Tool. Electrical Performance Characteristics of the SSC Accelerator System String Test. *Particle Accelerator Conference*, 1993.
- [28] F. Rodriguez-Mateos, L. Coull, K. Dahlerup-Petersen, D. Hagedorn, G. Krainz, A. McInturff, and A. Rijllart. Electrical Performance of a String of Magnets Representing a Half-cell of the LHC Machine. *Magnet Technology Conference (MT14)*, 1995.

- [29] T.P. Sheahen. *Introduction to High-Temperature Superconductivity*. Plenum Press, selected topics in superconductivity edition, 1994.
- [30] N. Siegel et al. Design Status of Superconducting Magnets for the LHC. *14th Conference on Charged Particle Accelerators*, 1994.
- [31] A.P. Verweij. Electrodynamics of Superconducting Cables in Accelerator Magnets, 1995. PhD-Thesis ISBN 90-9008555-6.
- [32] H. Wiedemann. *Particle Accelerator Physics, Basic Principles and Linear Beam Dynamics*. Springer-Verlag, 1993.
- [33] M.N. Wilson. *Superconducting Magnets*. Oxford University Press, 1983.
- [34] M.N. Wilson. Superconducting Materials for Magnets. *CAS - Superconductivity in Particle Accelerators*, 1996. CERN 96-03.